The Physical Properties and Cosmic Environments of Quasars in the First Gyr of the Universe

Chiara Mazzucchelli

Max-Planck-Institut für Astronomie

Heidelberg 2018

Dissertation in Astronomy
submitted to the
Combined Faculties of the Natural Science and Mathematics
of the Ruperto-Carola-University of Heidelberg, Germany
for the degree of
Doctor of Natural Sciences

put forward by

Chiara Mazzucchelli
born in Gallarate, Italy

Oral examination: 12 July 2018

The Physical Properties and Cosmic Environments of Quasars in the First Gyr of the Universe

Chiara Mazzucchelli

Max-Planck-Institut für Astronomie

Referees: Prof. Dr. Hans-Walter Rix
Prof. Dr. Jochen Heidt

Abstract

Luminous quasars at redshift $z \gtrsim 6$, i.e. $\lesssim 1$ Gyr after the Big Bang, are formidable probes of the early universe, at the edge of the Epoch of Reionization. These sources are predicted to be found in high–density peaks of the dark matter distribution at that time, surrounded by overdensities of galaxies. In this thesis, we present a search for and study of the most distant quasars, from the properties of their innermost regions, to those of their host galaxies and of their Mpc–scale environments. We search for the highest redshift quasars in the Panoramic Survey Telescope and Rapid Response System 1 (Pan-STARRS1, PS1), discovering six new objects at $z \gtrsim 6.5$. Using optical/near–infrared spectroscopic data, we perform a homogeneous analysis of the properties of 15 quasars at $z \gtrsim 6.5$. In short : 1) The majority of $z \gtrsim 6.5$ show large blueshifts of the broad C IV 1549 Å emission line, suggesting the presence of strong winds/outflows; 2) They already host supermassive black holes ($\sim 0.3 - 5 \times 10^9$ $M_\odot$) in their centers, which are accreting at a rate comparable to a luminosity–matched sample at $z \sim 1$; 3) No evolution of the Fe II/Mg II abundance ratio with cosmic time is observed; 4) The sizes of their surrounding ionized bubbles weakly decrease with redshift. We present new millimeter observations of the dust continuum and of the [C II] 158 μm emission line (one of the main coolant of the intergalactic medium) in the host galaxies of four quasars, providing new accurate redshifts and [C II]/infrared luminosities. We study the Mpc–scale environment of a $z \sim 5.7$ quasar, via observations with broad– and narrow–band filters. We recover no overdensities of galaxies. Among the potential explanations for these findings, are that the ionizing radiation from the quasar prevents galaxy formation, the sources in the fields are dust–obscured, or quasars do not live in the most massive dark matter halos. Finally, we report sensitive optical/near–infrared follow–up observations of gas–rich companion galaxies to four quasars at $z \gtrsim 6$, firstly detected with the Atacama Large Millimeter Array (ALMA). With the exception of one source, we detect no emission from the stellar population of these galaxies. Our limits on their stellar masses ($< 10^{10}$ $M_\odot$) and unobscured star formation rates (<few $M_\odot$ yr^{-1}) suggest that the companions are highly dust obscured and/or harboring a modest stellar content. In synthesis, in this thesis we show the large range of parameters of the most distant quasars, and the variety of their environments, with the aim of shading light on massive galaxy and black hole formation in the first Gyr of the universe.

Zusammenfassung

Leuchtstarke Quasare bei Rotverschiebungen $z \gtrsim 6$, also <1 Gyr nach dem Urknall, eignen sich wunderbar, um das frühe Universum zu untersuchen, kurz nach der Reionisationsepoche. Man vermutet, dass sich diese Objekte in den dichtesten Gebieten der damaligen Verteilung von dunkler Materie angesammelt haben und daher von vielen Galaxien umgeben werden sollten. In dieser Arbeit präsentieren wir eine Suche nach den weit entferntesten Quasaren und untersuchen die Eigenschaften der Galaxien und die Umgebungen der Quasare. Wir suchen die hoechst rotverschobenen Quasare in der Panoramic Survey Telescope and Rapid Response System 1 (Pan-STARRS1, PS1) und finden sechs neue Objekte bei $z \gtrsim 6.5$. Wir nutzen optische und infrarote Spektren, mit denen wir eine homogene Analyse der Eigenschaften von 15 Quasaren bei $z >$6,5 durchführen. Unsere Ergebnisse zeigen: 1) Die Mehrheit der Quasare zeigt grosse Verschiebungen zu blauen Wellenlängen der C IV 1549Å Emissionslinie, was auf starke Winde zurueckschliessen lässt. 2) Im Zentrum der Quasare befinden sich super massereiche schwarze Löcher ($\sim 0.3 - 5 \times 10^9$ $M_\odot$), die ähnliche Akkretionsraten aufweisen wie Quasare bei $z \sim 1$. 3) Wir finden keine Entwicklung des Verhältnisses von Fe II/Mg II mit zunehmender Rotverschiebung. 4) Die Größe der sie umgebende ionisierten Zone nimmt leicht ab mit zunehmender Rotverschiebung der Quasare. Zudem präsentieren wir neue Beobachtungen im Millimeter Wellenlängenbereich des Staubs und der [C II] Emissionslinie (welche hauptsächlich für die Kühlung des Intergalaktischen Mediums zuständig ist) in den Galaxien von vier Quasaren, die eine akkurate Bestimmung der Rotverschiebung und der [C II]/infraroten Helligkeiten erlauben. Wir untersuchen die Umgebung eines Quasars bei $z \sim 5.7$ auf Mpc Skalen durch Beobachtungen von Weit- und Schmalbandfiltern. Wir finden jedoch keine signifikant reichere Umgebung an Galaxien. Eine mögliche Erklärung für unsere Ergebnisse ist, dass die ionisierende Strahlung des Quasars die Entstehung von Galaxien verhindert, dass die Galaxien durch Staub verdeckt sind, oder dass sich Quasare nicht in besonders dichten Regionen befinden. Schlussendlich präsentieren wir optische und infrarote Beobachtungen von gasreichen Begleitgalaxien von vier Quasaren bei $z \gtrsim 6$, die zuerst mit dem Atacama Large Millimeter Array (ALMA) detektiert wurden. Mit Ausnahme eines Quasars, finden wir keine Emission einer Sternpopulation in diesen Galaxien. Unsere Einschränkungen für die Sternmassen ($< 10^{10}$ $M_\odot$) und Sternentstehungsraten ($<$ einige $M_\odot$ yr^{-1}) legen nahe, dass die Begleitgalaxien stark von Staub verdunkelt werden und/oder nur sehr wenige Sterne beherbergen. Zusammenfassend lässt sich sagen, dass wir in dieser Arbeit eine weite Spanne an Parameter der weit entferntesten Quasare und deren Umgebungen analysieren, um die Entstehung massereicher Galaxien und schwarzer Löcher im ersten Gyr unseres Universums zu verstehen.

Publications

Part of this work has appeared in the publications:

- Mazzucchelli, C., Bañados, E., Venemans, B. P., et al.,
Physical Properties of 15 Quasars at $z \gtrsim 6.5$, ApJ, 849, 91
- Mazzucchelli, C., Bañados, E., Decarli, R., et al.,
No overdensity of Lyman-Alpha Emitting Galaxies around a Quasar at $z \sim 5.7$, ApJ, 834, 83

A Mariano

Contents

List of Figures

List of Tables

Chapter 1

Introduction

In the following chapter, we summarize a few concepts and quantities to provide a useful background for this thesis. We describe the adopted cosmological model (§1.1), and the current observational and theoretical view of the Epoch of Reionization (§1.2) and of the first galaxies (§1.3). We then present the history and basic components of quasars (§1.4) and we explore recent efforts on the discovery and characterization of quasars at high–redshift (§1.5).

1.1 Elements of Cosmology

Here, we briefly set the cosmological framework of the present thesis. The following section makes use of material from Longair, 2008 and Ryden, 2003.

1.1.1 Cosmological Principles and Robertson-Walker Metric

As a first order approximation, we can consider the universe at the present epoch as isotropic and homogeneous. In such a universe, the *cosmological principle* postulates that any observer does not reside in a special location. Additionally, the *Weys postulate* assumes that no space–time geodesic intersects one another, as they all originated from a single point in the past. As a consequence, at each point in the universe only one geodesic is found. Considering the two points above, it is possible to define a system of *fundamental observers*, each at a specific *cosmic time*. In this framework, one can express the metric of the universe as follows.

In general, the distance between two points in a three-space isotropic universe can be formulated through the *Minkowski metric*:

$$\mathrm{d}s^2 = \mathrm{d}t^2 - \frac{\mathrm{d}l^2}{c^2} \tag{1.1}$$

with c the speed of light, and $\mathrm{d}t$ and $\mathrm{d}l$ the time and spatial increment, respectively. The latter can be expressed in spherical coordinates as:

$$dl^2 = dr_\mathrm{p}^2 + R_c^2 \sin^2\left(\frac{r_\mathrm{p}}{R_c}\right)\left[\mathrm{d}\theta^2 + \sin^2\theta \mathrm{d}\phi^2\right] \tag{1.2}$$

where r_p is the *proper radial distance* between two points, and R_c is the space curvature. If we consider an expanding universe that follows the cosmological principles reported above, then the distance between two fundamental observers (j and k) at two different epochs (t_1 and t_2) follows the relation:

$$\frac{r_{\mathrm{p,j}}(t_1)}{r_{\mathrm{p,k}}(t_1)} = \frac{r_{\mathrm{p,j}}(t_2)}{r_{\mathrm{p,k}}(t_2)} = \text{constant} \tag{1.3}$$

We can introduce a universal factor, the *scale factor*, that summarizes the evolution of this distance between two observers with time, $a(t)$. In this formalism, from eq. 1.3 we derive:

$$\frac{r_{\mathrm{p,j}}(t_1)}{r_{\mathrm{p,j}}(t_2)} = \frac{r_{\mathrm{p,k}}(t_1)}{r_{\mathrm{p,k}}(t_2)} = \text{constant} = \frac{a(t_1)}{a(t_2)} \tag{1.4}$$

The proper distance can also be expressed as:

$$r_{\mathrm{p}}(t) = a(t)r \tag{1.5}$$

with r being the *comoving radial distance* coordinate. Considering the evolution of the curvature as $R_c(t) = a(t)R_c(t_0) = a(t)R$, with R the curvature at present epoch, which is necessary to preserve the isotropy and homogeneity of the universe, the metric above becomes:

$$\mathrm{d}s^2 = \mathrm{d}t^2 - \frac{a(t)^2}{c^2}\left[\mathrm{d}r^2 + R^2 \sin^2\left(\frac{r}{R}\right)\left[\mathrm{d}\theta^2 + \sin^2\theta \mathrm{d}\phi^2\right]\right] \tag{1.6}$$

This is the so–called *Robertson-Walker metric*. It is important to notice that this metric is independent of the assumptions on the large scale dynamics of the universe, i.e. the physics of expansion, which is contained solely in the factor $a(t)$.

1.1.2 Cosmological Redshift

The cosmological redshift is the shift of emission lines to longer wavelengths associated with the isotropic expansion of the system of galaxies. Taking into account an emission line with emitted wavelength λ_e, and observed wavelength λ_o, the redshift z is calculated as:

$$z = \frac{\lambda_o - \lambda_e}{\lambda_e} \tag{1.7}$$

Interpreting the redshift as a galaxy's recession velocity, we can also write $z = v/c$ (in the approximation of small z). A crucial physical interpretation of the redshift comes directly from the Robertson-Walker metric. If one imposes a radial expansion (dθ=dϕ=0) on null cones (ds=0), it is possible to write:

$$\mathrm{d}t = \frac{a(t)}{c}\mathrm{d}r \tag{1.8}$$

Considering a wave packet of frequency ν_1, emitted during the time interval $[t_1, t_1 + \Delta t_1]$ and observed at $[t_0, t_0 + \Delta t_0]$, and integrating the relation above, one obtains:

$$\Delta t_0 = \frac{\Delta t_1}{a(t_1)} \tag{1.9}$$

which represents the dilation of time intervals. We can express this relation in terms of observed ($\nu_0 = \Delta t_0^{-1}$) and emitted ($\nu_1 = \Delta t_1^{-1}$) frequency, and hence:

$$\nu_0 = \nu_1 a(t_1) \tag{1.10}$$

All of these considerations lead to the following link between $a(t)$ and redshift:

$$a(t_1) = \frac{1}{1+z} \tag{1.11}$$

The redshift is therefore a measure of the scale factor of the universe at the time of the source emission.

In the present thesis, we will focus on cosmic epochs at z >5.5. In the following section, we will briefly show how the age of the universe and distance measures relate to redshift. First, we will shortly describe the cosmological model and parameters assumed in this thesis.

1.1.3 Hubble Law and Cosmological Parameters

A relation between the distance and recession velocity of nearby galaxies was initially observed by Hubble, 1929. This relation, expressed using the proper distance $r_{\rm p}$, is:

$$\frac{{\rm d}r_{\rm p}}{{\rm d}t} = Hr_{\rm p} \tag{1.12}$$

where H is the Hubble constant. One can also define the *density parameter* (Ω_x) of the different components of the universe, i.e. radiation (rad), matter (m) and dark energy (Λ), as:

$$\Omega_x = \frac{\rho_x}{\rho_c} = \rho_x \frac{8\pi {\rm G}}{3H_0} \tag{1.13}$$

with ρ_c the critical density of the universe, and H_0 the Hubble constant at present day. Considering the scale factor $a(t)$, the above defined density parameters and a model of the universe with no curvature, one obtains:

$$H(t) = \frac{\dot{a}}{a} = H_0 \left[\Omega_{\rm m} a^{-3} + \Omega_{\rm rad} a^{-4} + \Omega_\Lambda\right]^{1/2} \tag{1.14}$$

The radiation density parameter is negligible at the present epoch ($\Omega_{\rm rad} \sim 10^{-4}$). As for the remaining parameters, in this thesis we consider the matter density parameter ($\Omega_{\rm m}$) equal to 0.3, the dark energy density parameter (Ω_Λ) equal to 0.7, and H_0 =70 km s^{-1} Mpc^{-1}.

1.1.4 Age of the Universe

It is possible to obtain a measurement of the age of the universe (T) by integrating eq. 1.8:

$$T = \int {\rm d}t = \int \frac{a(t){\rm d}r}{c} \tag{1.15}$$

The current measurement of the age of the universe at present epoch, considering the cosmological models and parameters reported in eq. 1.1.3, is T_0 =13.462 Gyr. As reference for the work in this thesis, the age of the universe at z =5.5,6.0,6.5,7.0,7.5 is T =1.022, 0.914, 0.825, 0.748, 0.683 Gyr.

1.1.5 Cosmological Distances

We use several distance measurements in this thesis, that we define below.

Comoving and Proper Distance

The *comoving distance* ($d_{\rm c}$) is the distance between two points which takes into account the expansion of the universe. It does not change with the expansion of the universe, and it is

equivalent to the *proper distance* ($d_{\rm p}$) today:

$$d_{\rm c} = \frac{d_{\rm p}}{a(t)} = d_{\rm p}(1+z) \tag{1.16}$$

Luminosity Distance

The *luminosity distance* ($d_{\rm L}$) is the distance that light travels from the source to the observer:

$$d_{\rm L} = \left(\frac{L}{4\pi F}\right)^{1/2} = d_{\rm c}(1+z) = d_{\rm p}(1+z)^2 \tag{1.17}$$

with L and F the luminosity and flux of the source, respectively. Measurements of the luminosity distance are crucial in the understanding of the current expansion of the universe, through observations of standard candles, e.g. Type Ia Supernovae (Schmidt et al. 1998, Riess et al. 1998, Perlmutter et al. 1999).

Angular Diameter Distance

Considering an object at redshift z, with proper length d (perpendicular to the radial coordinate) and that subtends an angular size θ, the *angular diameter distance* can be expressed as:

$$d_{\rm A} = \frac{d}{\theta} \tag{1.18}$$

This quantity is linked to the comoving distance as:

$$d_{\rm A} = \frac{d_{\rm c}}{1+z} \tag{1.19}$$

Given the cosmological model and the parameters assumed here (see Section 1.1.3), an object with a perpendicular angular size of $1''$corresponds to a physical scale of 5.713 kpc at z=6. Considering the shallow evolution of $d_{\rm A}$ with redshift, this value does not drastically change in the cosmological times considered in this thesis, e.g. at z =5.5,7.5 the angular scale is 5.987,5.016 kpc/arcsec, respectively.

After defying our cosmological framework, we briefly depict in the next section (§ 1.2) the main transition phases of the universe, important in the context of this thesis.

1.2 The Epoch of Reionization

In Figure 1.1 we show a stylized picture of the history of the universe, from the initial Big Bang to the present day. Approximately ∼400 000 yr after the Big Bang, i.e. at redshift $z \sim 1100$, the temperature of the universe decreased to $\lesssim$3000 K, allowing protons and electrons to recombine and form neutral hydrogen and helium (*Epoch of Recombination*). Photons decoupled from barions in the primordial plasma, creating the first radiation that nowadays we observe as the *Cosmic Microwave Background* (CMB). This marked the beginning of the *Dark Ages*, when the diffuse material in the universe was mostly neutral. The gravitational collapse of material, modulated by the primordial density perturbations mapped into the CMB, gave birth to the first stars and galaxies. These sources started ionizing the neutral hydrogen in the intergalactic medium[1], firstly in "bubbles" surrounding these sources, and later expanding throughout the universe. This is the so–called *Epoch of Reionization* (EoR), which represents the last major transition phase of the universe (see e.g. Loeb and Barkana 2001, Fan, Carilli, and Keating 2006, McQuinn 2016 and Namikawa 2018 for reviews). At the end of this epoch, the universe emerged as virtually fully ionized, i.e. with a hydrogen neutral fraction of $x_{\rm HI} = n_{\rm HI}/n_{\rm H} \sim 10^{-5}$, as we see it nowadays. Despite the crucial importance of the EoR in the history of the universe, several questions are left unanswered. *When did reionization start, and how long did it last? What was its topology? Which were the sources primarily responsible for ionizing the universe?* In the last years, an extensive effort, both on a theoretical and observational ground, has been undertaken in order to address these issues.

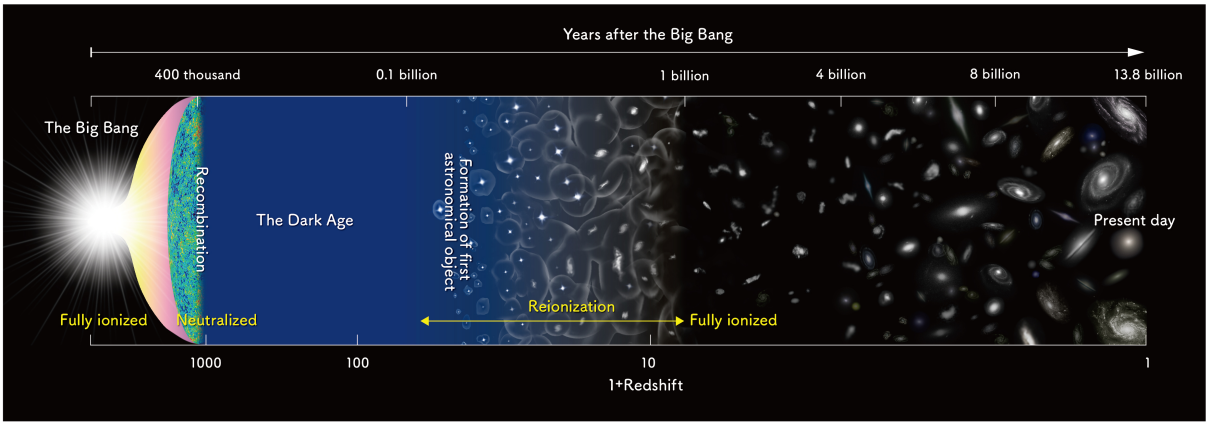

FIGURE 1.1: Simplified illustration of the history of the universe, from the Big Bang to the present epoch. The Epoch of Reionization marks the translation from a precedent neutral universe, i.e the Dark Ages, to a mostly ionized one (credits: NAOJ).

Mapping reionization through a theoretical approach is extremely challenging. Indeed, any simulation needs to take into account several physical scales. On the one hand, it is necessary to reproduce the physics of gas accretion and galaxy formation on sub−kpc scales, in order to characterize the properties (e.g. radiative feedback, metal pollution, star formation) of the first sources responsible for producing the initial ionizing radiation. On the other hand, these

[1]The reionization of helium takes place only afterwards, at $z \sim 3$, and it is believed to be mainly due to the hard radiation emitted by quasars (e.g. Sokasian, Abel, and Hernquist 2002, Furlanetto and Oh 2008; see Ciardi and Ferrara 2005 for a review).

galaxies need to be located in a cosmological framework, i.e. within the large scale (∼Mpc) dark–matter distribution, where typical inhomogeneities extend up to ∼100 Mpc. In the first case, combinations of N-body and hydrodynamical simulations are used, while, in the second case, radiative transfer techniques are commonly considered (for a recent review on these approaches see, e.g., Mesinger 2018).

From an observational perspective, current constraints are obtained from either "integral" probes, e.g. from the CMB or galaxies number counts, or individual sources that act as "lighthouses", that provide us information on specific lines of sight. As for the first case, recently, the Planck Collaboration et al., 2016 measured the Thomson scattering optical depth from the CMB, and set a redshift of z=8.8$^{+1.3}_{-1.2}$ for the EoR, under the assumption that reionization was instantaneous. Regarding the sources responsible for the initial re-ionization, a number of constraints from observations of large samples of UV–bright galaxies at $z > 6$ (see also Section 1.3) suggest that the main drivers for the EoR were faint star forming galaxies (e.g. Bouwens et al. 2015a and references therein; but see also, e.g. Giallongo et al. 2015, for an alternative view).

Luminous high–redshift quasars, i.e. the aforementioned "lighthouses", are key probes of the EoR. Indeed, observations of $z > 5.5$ quasars firstly set the end of reionization at $z \sim 6$ (e.g. Fan et al. 2006, McGreer, Mesinger, and D'Odorico 2015). Moreover, even one quasar found at $z > 7$ can provide stronger constraints on the hydrogen neutral fraction value, at one redshift and on one line-of-sight, than what obtained from CMB measurements (e.g. Bañados et al. 2018). In Section §1.5, we report in greater details the methods through which high–z quasars can constrain the onset, duration and morphology of reionization.
We start by summarizing the current census of the sources observed at the edge of the EoR ($z \gtrsim 6$) in the next Section (§ 1.3).

1.3 The First Galaxies

In the last years, several studies have been undertaken that search for the first galaxies.

One way of identifying such galaxies is through deep, extragalactic photometric surveys, which observe the rest–frame ultraviolet (UV) and/or optical emission from young stars and ionized nebular gas. Such searches can be performed via, e.g., the Lyman Break technique (identifying *drop-outs* or *Lyman Break Galaxies*, LBGs): absorption by intergalactic neutral hydrogen causes a break in the observed galactic spectrum, apparent from abrupt change in broad–band colors (e.g. Steidel et al. 1996). LBGs, selected with this method from ground–based facilities, are massive sources, characterized by strong UV stellar emission, and whose mass strongly correlates with the UV luminosity (e.g. González et al. 2011). On the other hand, suites of narrow and broad band filters efficiently identify *Lyα Emitters* (*LAE*), via the observations of the Lyα emission line. LAEs are believed to be mostly low-mass galaxies, spanning a range of stellar masses of $\sim 10^6 - 10^8$ M$_\odot$ and ages of $\sim$1−3 Myr (e.g. Pirzkal et al. 2007, Ono et al. 2010). However, a non negligible fraction of massive galaxies (with masses up to $\sim 10^{11}$ M$_\odot$), and galaxies hosting an older stellar population ($\sim$ 1 Gyr) has been also found among LAEs (e.g. Pentericci et al. 2009, Finkelstein et al. 2009, Finkelstein et al. 2015a). Recent theoretical and observational studies suggest that LBGs and LAEs trace a similar underlying galaxy

population, with the main difference between the two arising from the diverse selection methods (e.g. limits on the UV luminosity and equivalent width of the line; e.g. Garel et al. 2015).

Deep observations with the *Hubble Space Telescope* (*HST*) and the *Spitzer Space Telescope* were instrumental in shaping our knowledge of such galaxy population. More than 800 galaxy candidates have been identified with photometric redshifts at z ∼7–8 (e.g. Schmidt et al. 2014, Finkelstein et al. 2015b, Bouwens et al. 2015b), and even at z ∼9–10 (e.g. McLeod et al. 2015, Kawamata et al. 2016). Conversely, several ground–based surveys with narrow band filters at, e.g. the Subaru Telescope or the Very Large Telescope (VLT), detected a large number of LAEs at $z \sim 6-7$ (e.g. Ouchi et al. 2018, 2008, Ono et al. 2010, Hu et al. 2010). Nevertheless, only a small fraction of all these galaxies were spectroscopically confirmed at z >7 (e.g. Vanzella et al. 2011, Ono et al. 2012, Shibuya et al. 2012, Finkelstein et al. 2013, Zitrin et al. 2015, Roberts-Borsani et al. 2016).

The most distant galaxy was observed so far at z =11.09 (Oesch et al. 2016; see Figure 1.2). Even if this galaxy is extremely bright (i.e. its UV luminosity is 3×L* of z ∼7-8 dropouts[2]), its spectroscopic detection is still tentative, and little information on its physical properties can be derived from its observations. In general, the Lyα emission line is difficult to detect. It is highly affected by absorption and scattering (both in spatial and velocity space) by the intervening intergalactic medium (IGM), and the galactic interstellar medium (ISM). Its escape fraction from galaxies, and therefore our ability to detect it, is strongly dependent on the geometry, ionization state and composition of the ISM. The Lyα line is also rapidly absorbed by the IGM, even in case of low hydrogen neutral fraction (i.e. $x_{\rm HI} \gtrsim 10^{-4}$). Moreover, spectroscopic confirmation and study of other emission lines from the ISM of these very distant UV–selected galaxies is extremely challenging.

An alternative approach to uncover the first galaxies is through the emission of their cool gas and dust in the rest–frame far-infrared (FIR). Several blind surveys scanned the sky with e.g. the SCUBA camera at the James Clerk Maxwell Telescope (JCMT), and with MAMBO at the IRAM 30m telescope (e.g. Hughes et al. 1998,Ivison et al. 2000). These surveys detected multiple submillimeter galaxies (SMGs; e.g. Blain et al. 2002), characterized by large infrared (IR) luminosities ($L_{\rm IR} > 10^{12}$ L$_\odot$) from the dust emission, and large star formation rates (SFR ∼1000 M$_\odot$ yr^{-1}). The singly ionized [CII]158 μm emission line is an extensively used key diagnostics of galactic physics in these sources (see Carilli and Walter 2013 and Díaz-Santos et al. 2017 for reviews). The [CII] line is indeed one of the main coolant of the ISM, and it can be extremely bright, i.e. it can emit up to 1% of the total galactic infrared emission (e.g. see Herrera-Camus et al. 2018a,b). Further observations of this line and of the dust continuum with the Atacama Large Millimeter Array (ALMA), revealed that SMGs are extended (∼few kpc), heavily dust obscured and typically surrounded by companions/overdensities (e.g. Hodge et al. 2013, Zavala et al. 2017). These galaxies are fundamental in shaping our understanding of galaxy formation and in sampling the gas content and star formation activity in the early universe (e.g. Chapman et al. 2005). Indeed, they have been invoked as possible progenitors of massive, compact, "red and dead" galaxies, already observed at z >2 (e.g. van Dokkum et al. 2008) up to z ∼4 (e.g. Straatman et al. 2014). Indeed, these progenitor galaxies would undergo gas–rich,

[2]where L* is the characteristic luminosity, defined from the luminosity function (LF): $\phi(L) = (\phi^*/L^*)(L/L^*)^\alpha \exp -(L/L^*)$; see Bouwens et al. 2015b and Finkelstein et al. 2015b for LFs of z ∼7-8 galaxies.

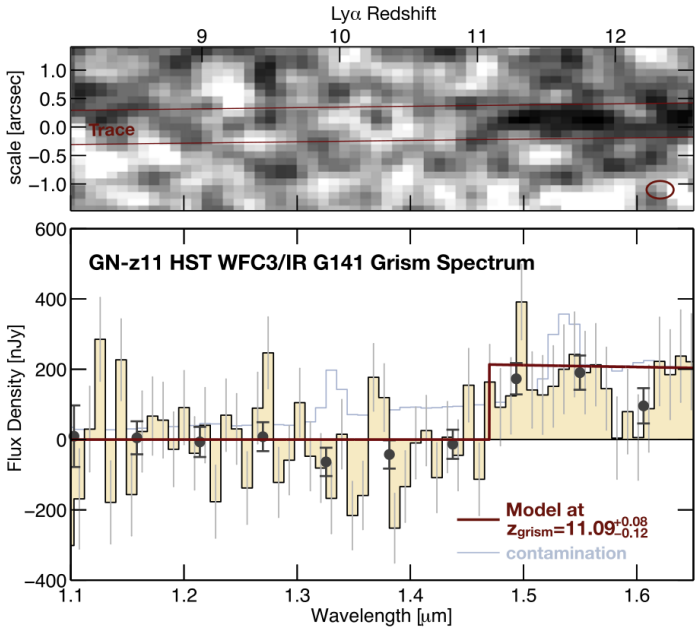

FIGURE 1.2: The 2D (*top*) and 1D (*bottom panel*) spectrum of GN-z11, the most distant galaxy with confirmed spectroscopic redshift so far, at z =11.09. The figure is taken from Oesch et al., 2016

massive mergers, that are expected to ignite powerful, heavily dust-enshrouded starbursts, with the possible formation of a central quasar. In later stages, the formation of new stars is prevented by the feedback from the quasar and/or by gas exhaustion; after the dissipation of the dust, and the dimming of the quasar, the central compact remnant can further redden and grow through dry mergers, building the observed "red and dead" galaxies (e.g. Hopkins et al. 2008, Wuyts et al. 2010, Toft et al. 2014).
However, up to now, only few SMGs, without a central active black hole, have been found at z >6. Riechers et al., 2013 found a dust-obscured, extremely star forming (SFR ∼3000 $M_\odot$ yr^{-1}) SMG at z=6.3; Fudamoto et al., 2017 recovered another SMG at z=6.03, slightly less star-forming (SFR ∼950 $M_\odot$ yr^{-1}). The highest redshift pair of massive SMGs has been observed by Marrone et al., 2018 at z ∼6.9 (see Figure 1.3). This very small sample is still too limited to study galaxy formation at early cosmic times.

Finally, quasars, due to their extreme brightness, have been observed up to z =7.5413 (Bañados et al. 2018, Venemans et al. 2017; see Figure 1.4). Their rest–frame UV spectra harbor a wealth of information regarding, e.g. the central black hole, their chemical abundance, and accretion mode. Moreover, their hosts galaxies are among the most massive, gas rich and star-forming sources in the early universe. Quasars are therefore not only unique probes of the state of the IGM in the EoR, but they can also shed light on the (co-)evolution of the first galaxies and black holes.

In the following section (§1.4), we summarize the discovery and basic physical components of quasars. In section §1.5, we report the main characteristics of z >5.5 quasars, and of their host galaxies and environments, prior to this work.

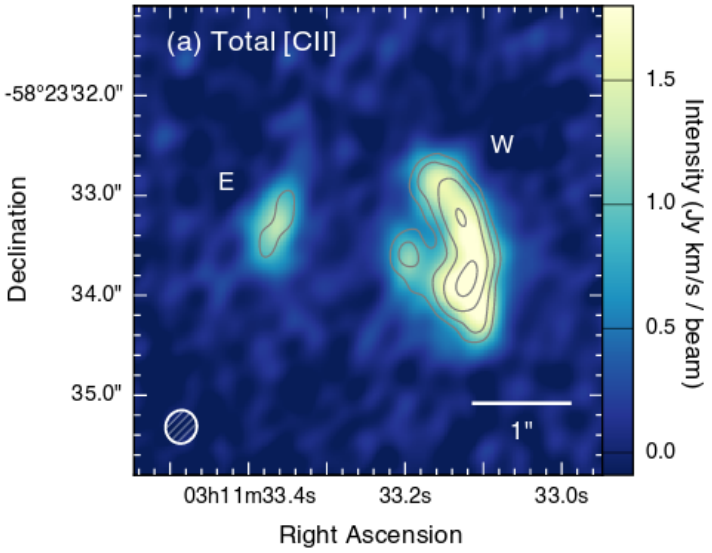

FIGURE 1.3: Map of the [CII] emission line (*color map*) and dust continuum (*contours*) in the highest redshift submillimeter galaxy, observed at $z \sim 6.9$ (figure adapted from Marrone et al. 2018).

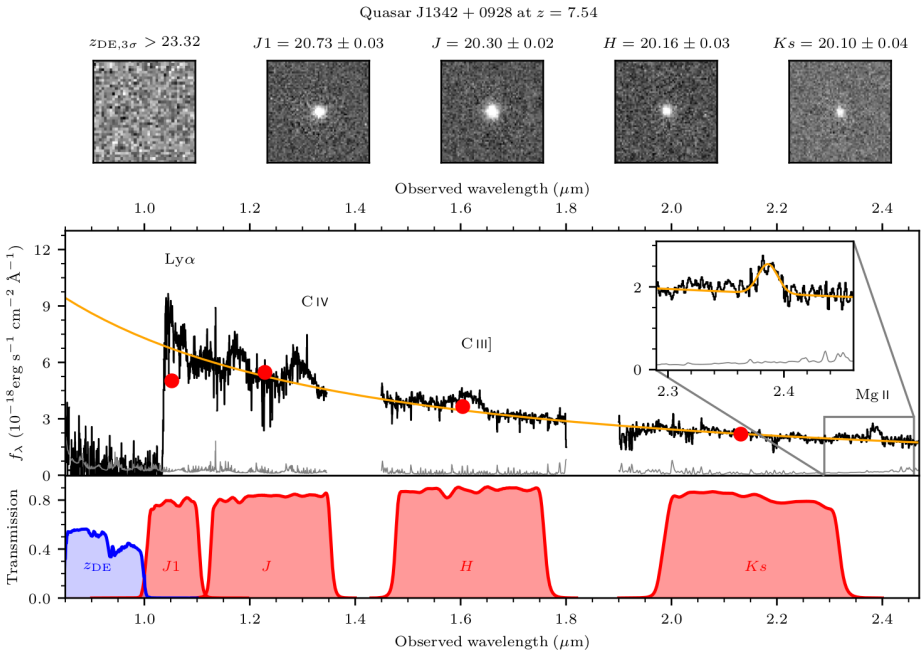

FIGURE 1.4: Rest–frame UV spectrum, and postage stamps, of the highest redshift quasar obseved so far, at z =7.5413. Figure adapted from Bañados et al., 2018.

1.4 Quasars: Discovery and Basic Elements

Quasars are among the most luminous, non-transient sources in the sky. The term "quasar" was first created as the acronym of "quasi–stellar radio source", due to the original, radio-based discoveries. When, in the following years, an increasing number of quasars with no radio emission was found (Sandage, 1965), the word "QSO", e.g. "quasi–stellar object", was introduced instead. Nowadays, the two terms are used as synonyms.

1.4.1 The Discovery of the First Quasars

The development of the first radio techniques for astronomy, during the fifties and sixties, opened a new window on the observable universe. The first radio surveys, such as the third Cambridge catalog of radio sources (3C; Edge et al. 1959), identified several radio sources distributed homogeneously over the sky, which were assumed to be of extragalactic origin (e.g. Baade and Minkowski 1954). Thanks to the technique of lunar occultations, Hazard, Mackey, and Shimmins, 1963 measured the location of the radio source 3C 273, with a, at that time unprecedented, uncertainty of 2″. Schmidt, 1963 identified a 13th magnitude "stellar–like" object as its optical counterpart. In the optical spectrum obtained at the Palomar 5m Telescope, he was able to reconstruct the Balmer emission line series redshifted at z =0.16 (see Figure 1.5). This result suggested that the source was located at large, cosmological distances, and it was characterized by extreme luminosities. 3C273 was the first discovered quasar (for a complete reconstruction of the events leading to this discovery, we refer to Hazard et al., 2018). Shortly afterwards, the object 3C48 was also identified as a similar point–like source at z =0.37 (Greenstein, 1963). In the same fashion, many more quasars were discovered from radio catalogs in the following years, followed by sources which were not characterized by any radio emission (e.g. Sandage 1965, Schmidt 1966). Quasars quickly revolutionized the understanding/view of the universe at that time, both greatly expanding the horizon of the observable universe (i.e. the first quasar at z ∼2 was discovered only 2 years after 3C273; Sandage 1965), and challenging the known physics, with compact sizes and significant luminosity variabilities that could not be explained by the sole stellar radiation (e.g. Smith and Hoffleit 1963). After significant observational and theoretical efforts, a good understanding of the structure and emission mechanism of quasars has been achieved.

1.4.2 Quasars Basic Components

Quasars are thought to be mainly composed by:

- A central, **supermassive black hole** (SMBHs; $10^7 \lesssim \mathrm{M_{BH}}/M_\odot \lesssim 10^{10}$)
- A surrounding **accretion disk**, i.e. material with non-null angular momentum, being accreted by the black hole and emitting a large amount of energy in the rest–frame UV/optical range.
- A **broad line region**, BLR, composed by high-velocity gas "clouds" in the proximities of the black hole.
- A **X-ray corona**, a hot (T$\gtrsim 10^7$ K) region above and below the accretion disk, strongly emitting in the X–ray regime.

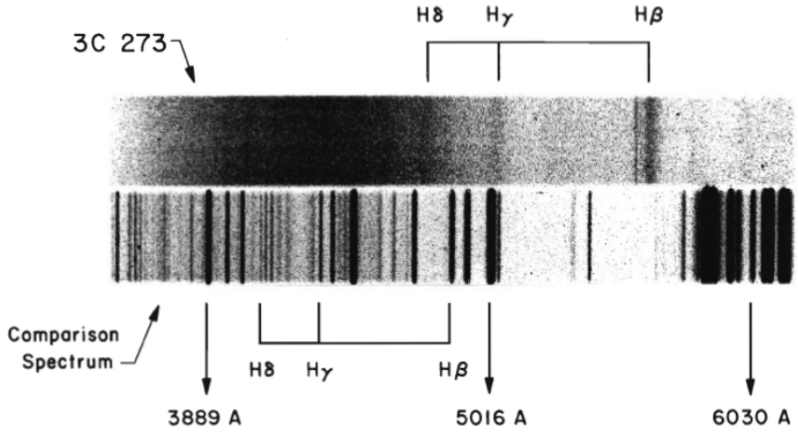

FIGURE 1.5: Discovery spectrum, acquired with the Palomar 5m Telescope, of the first quasar 3C273, at z =0.16. The figure is adapted from Hazard et al., 2018.

- An obscuring, dusty **torus**, found at several pc from the black hole, absorbing part of the energy from the accretion disk, and re-emitting it in the infrared ($\lambda \sim 3$ μm) range.
- A **narrow line region**, NLR, gas regions observed at larger distances ($\sim$0.1 kpc), moving at velocities of $\sim$300–500 km s^{-1}, and producing narrow emission lines in the UV/optical spectrum.
- Two powerful **jets**, which convey materials moving at relativistic speed; they are thought to be present in the 10%–20% of the objects.

All these elements are visually summarized in Figure 1.6.

In this thesis, we will mainly focus on the characterization of the central black holes and of the emission from the accretion disk and the BLR in high–redshift quasars, via observations of their rest–frame UV spectra. We provide here few additional details on the latter two components. This discussion is mainly adapted from Ghisellini, 2013 and Vanden Berk et al., 2001. We also list current methods of measuring M_{BH} in the next section (§ 1.4.3).

The accretion disk is composed of matter infalling into the central black hole, which, while loosing angular momentum, is emitting radiation as:

$$L_{\rm disk} = \epsilon \dot{M}_{\rm BH} c^2 \tag{1.20}$$

where ϵ is the radiative efficiency, usually around 10%, and $\dot{M}_{\rm BH}$ is the mass accretion rate. Assuming that this structure can be divided in annuli emitting black body radiation, than the total accretion disk emission can be modeled as a sum of black bodies with different temperatures, with higher temperatures closer to the black hole:

$$T(R) = \left[\frac{3R_{\rm S}L_{\rm disk}}{16\pi\sigma_{\rm MB}R^3}\right]^{1/4}\left[1-\left(\frac{3R_{\rm S}}{R}\right)^{1/2}\right]^{1/4} \propto R^{-3/4} \quad \text{if} \quad R >> R_{\rm S} \tag{1.21}$$

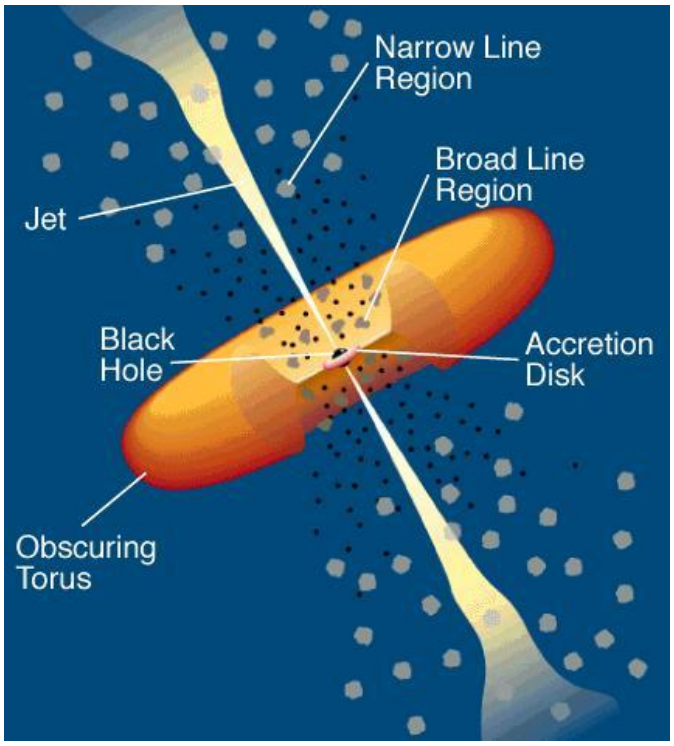

FIGURE 1.6: Schematic representation of an active galactic nucleus (AGN) basic components, which are listed in Section 1.4.2 (adapted from Urry and Padovani 1995).

where $\sigma_{\rm MB}$ is the Maxwell–Boltzmann constant, and $R_{\rm S} = 2M_{\rm BH}G/c^2$ is the Schwarzchild radius. No radiation is emitted from orbits with $R \leq 3R_{\rm S}$. Assuming that each annuli emits luminosity as:

$$dL = 4\pi R dR \sigma_{\rm MB} T^4 \tag{1.22}$$

and considering only the peak frequency corresponding to the black body temperature ($h\nu \propto kT$), one can derive:

$$L_{\rm disk} \propto \nu^{1/3} \tag{1.23}$$

This is valid up to the limit set by the maximum temperature, close to the internal radius ($R_{\rm in}$) of the accretion disk. In this case, we will observe only an exponential drop ($L_{\rm disk} \propto \exp^{h\nu/kT}$). On the other hand, only the Rayleigh-Jeans contribution will be observed at the outer radius ($R_{\rm out}$; $L_{\rm disk} \propto \nu^2$). We show all this components in Figure 1.7, *right*.
In the present work, we will model the emission from the quasars accretion disks with a power law relation (see Section 2.5.3).

Another important quantity is the *Eddington luminosity*, i.e. the theoretically maximum luminosity permitted for the quasar. This quantity is derived assuming that: *1)* the radiation pressure and the gravitational attraction are in equilibrium ($F_{\rm rad} = F_{\rm g}$); *2)* the radiation pressure acts on electrons through the Thomson scattering, while the gravitational force acts on the protons; *3)* the black hole accretion is spherically symmetric (i.e. Bondi accretion; Bondi 1952).

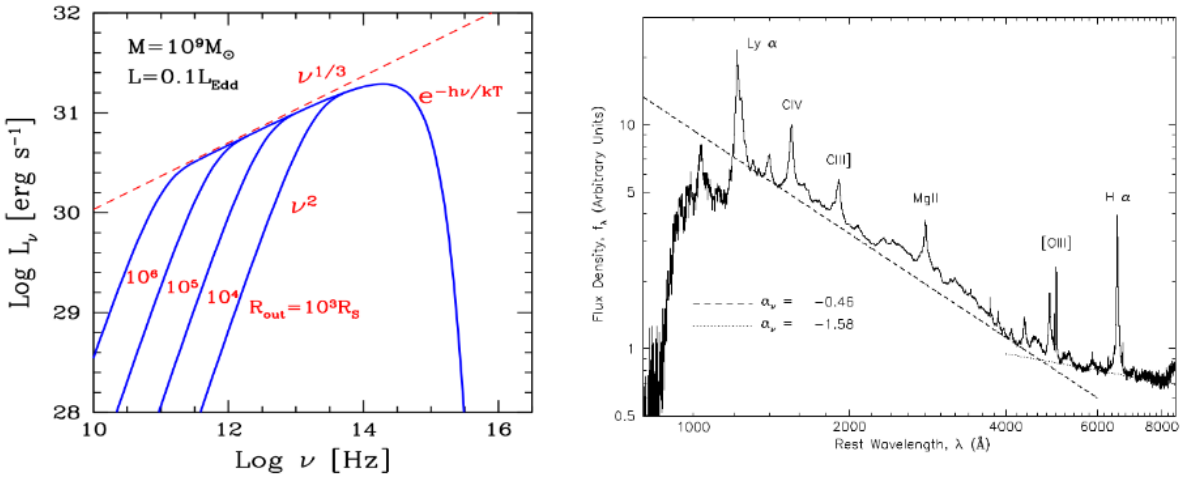

FIGURE 1.7: *Left*: Theoretical models of the spectrum of a quasar accretion disk, following a power law form, in case of different values of maximum radii. *Right*: Main broad (an narrow) emission lines in the UV/optical wavelength window, observed in the composite spectrum obtained using a sample of SDSS quasars. The figures are adapted from Ghisellini, 2013 and Vanden Berk et al., 2001.

From these assumptions, we can write:

$$\frac{L_{\rm Edd}\sigma_{\rm T}}{4\pi R^2 c} = \frac{GM_{\rm BH}m_{\rm p}}{R^2} \tag{1.24}$$

from which we derive

$$L_{\rm Edd} = \frac{4\pi G m_{\rm p}}{\sigma_{\rm T}} \cdot M_{\rm BH} = 1.3 \times 10^{38} \frac{M_{\rm BH}}{M_\odot} \tag{1.25}$$

with $\sigma_{\rm T}$ the Thomson scattering section and $m_{\rm p}$ the proton mass. Even considering the strict aforementioned assumptions, the Eddington limit seems to be generally respected among the observed AGNs, i.e. no black hole has been observed so far whose luminosity largely and securely surpasses the Eddington one (e.g. Trakhtenbrot, Volonteri, and Natarajan 2017; Bian and Zhao 2003). Also, one can define the *Eddington ratio*, i.e. the ratio between the bolometric ($L_{\rm bol}$) and the Eddington luminosity ($L_{\rm bol}/L_{\rm Edd}$). The Eddington ratio is commonly considered a proxy of the efficiency of matter accretion onto the central SMBH.
We will largely make use of $L_{\rm Edd}$ and its relation with the quasar bolometric luminosity in the present thesis.

In Figure 1.7, *left*, we show an example of emission from broad lines, overimposed to the continuous radiation from the accretion disk. In Table 1.1, we report the rest–frame wavelengths of the main emission lines, that we will utilize in the present work. The BLRs are composed by gaseous regions with a temperature of $\sim 10^4$ K, a density of $\sim 10^9 - 10^{11}$ cm^{-3}, and a covering factor of $\sim$0.1 (e.g. Ghisellini 2013). The full widths at half maximum (FWHM) of the lines are typically 1000–10,000 km s^{-1}, while the sizes of the BLRs are $R_{\rm BLR} \sim 0.1$pc (e.g. Peterson et al. 2004; see also Section 1.4.3)

TABLE 1.1: Main quasar broad emission lines observed in the rest–frame UV/optical spectrum. The laboratory wavelength of the rest frame emission and the relative strenght of the line with respect to that of Lyα are taken from Vanden Berk et al., 2001.

ID	$\lambda_{\rm rest}$ [Å]	**Relat. Flux** [$100\times F/F(Ly\alpha)$]
Lyβ	1025.72	9.615 ± 0.484
Lyα	1215.67	100.000 ± 0.753
NV	1240.14	2.461 ± 0.189
SiV	1396.76	8.916 ± 0.097
CIV	1549.06	25.291 ± 0.106
MgII	2798.75	14.725 ± 0.030
Hβ	4862.68	8.649 ± 0.030
Hα	6564.61	30.832 ± 0.098

1.4.3 Black Hole Masses Estimates

The mass of the central black hole can be estimated through direct (i.e. primary) or indirect (i.e. secondary) approaches. The black hole in our Galactic center is the closest and best studied one, and orbits of individual stars have been extensively used to measure its mass (e.g. Genzel, Eisenhauer, and Gillessen 2010). Among the primary methods, one can find high-resolution spectroscopic observations of gas and stars in the SMBH sphere of influence (e.g. Tremaine et al. 2002), or, alternatively, accurate water megamasers measurements (e.g. Miyoshi et al. 1995). However, these techniques can be applied only to very nearby and relatively low luminosity sources, for which the stellar emission from the host galaxy is not outshone by the central AGN (e.g. Vestergaard 2004). They are therefore unsuitable for surveys of luminous quasars at large cosmological distances.

Alternatively, one can rely on reverberation mapping (RM) techniques (e.g. Peterson et al. 2004, Peterson and Horne 2004). RM exploits the time delay (lag) between the flux variation observed in the emission from the continuum and that from the broad emission lines, in order to place constraints on the geometry and size of the BLR. RM campaigns in the local universe (e.g. Kaspi et al. 2005, Bentz et al. 2013) found that $R_{\rm BLR}$ strongly correlates with the source luminosity:

$$\mathrm{Log}\left(\frac{R_{\rm BLR}}{\mathrm{ltday}}\right) = K + \alpha \mathrm{Log}\left(\frac{\lambda L_\lambda}{10^{44}\,\mathrm{erg\,s^{-1}}}\right) \tag{1.26}$$

This method, together with the assumption that the BLR clouds are in virial equilibrium, allowed for the measurements of a large sample of black hole masses (e.g. Shen et al. 2016, Grier et al. 2017), up to redshift $z \sim 1$ (e.g. Shen et al. 2015). Nevertheless, its application at even larger cosmological distances is challenging. Indeed, on one hand, the time dilation renders the necessary observations much longer (i.e. years), and, on the other, the larger masses sampled at high redshifts are characterized by smaller, and therefore harder to detect, flux variations (e.g. Lira et al. 2018).

It is possible to measure $M_{\rm BH}$ in $z > 1$ quasars via observations of their single–epoch, rest–frame UV/optical spectra, and by adopting again the virial argument and the scaling relations

above. More specifically, under the assumption that the BLR dynamics is dominated by the central black hole gravitational potential, the virial theorem states:

$$M_{\rm BH} \sim \frac{R_{\rm BLR} v_{\rm BLR}^2}{G} \tag{1.27}$$

where $R_{\rm BLR}$ can be derived from the local $R_{\rm BLR}$–L scaling relation (e.g. eq. 1.26). The velocity of the BLR ($v_{\rm BLR}$) can be obtained instead from the FWHM of broad emission lines:

$$v_{\rm BLR} = f \times {\rm FWHM} \tag{1.28}$$

with f a geometrical factor accounting for projection effects (e.g. Decarli et al. 2008, Grier et al. 2013, Matthews, Knigge, and Long 2017). The emission lines commonly used are the Hβ, MgII and CIV (see Table 1.1), and the underlying continuum emission at 5100Å, 3000Å, and 1350Å, respectively. In particular, the MgII line and $\lambda L_{\lambda,3000}$, observed in the NIR range from ground-based telescopes at $6 \lesssim z \lesssim 7.5$, is commonly adopted to measure $M_{\rm BH}$ of high–redshift quasars.

In the present thesis, we will use the relation by Vestergaard and Osmer, 2009, to estimate masses of the black holes of $z \gtrsim 6.5$ quasars (see Section 2.5.6):

$$\frac{M_{\rm BH}}{{\rm M}_\odot} = 10^{6.86} \left(\frac{\rm FWHM}{10^3\,{\rm km\,s^{-1}}} \right)^2 \left(\frac{\lambda L_{\lambda,3000}}{10^{44}\,{\rm erg\,s^{-1}}} \right)^{0.5} \tag{1.29}$$

This relation has been obtained using thousands of high quality quasar spectra from Sloan Digital Sky Survey Data Release 3 (SDSS-DR3; Schneider et al. 2003), and has been calibrated on robust reverberation mapping mass estimates (Onken et al., 2004). The scatter on its zero point of 0.55 dex, which takes into account the uncertainty in the $R_{\rm BLR}$–L correlation, usually dominates the measured uncertainties on the black hole masses.

1.5 High–Redshift Quasars

In the present thesis, we refer to "high–redshift quasars" for the quasars at $z > 5.5$. Color selection techniques, which rely on multi-wavelength broad band observations, are among the most commonly used methods to find high–redshift quasars. The quasar flux at wavelengths shorter than the Lyα emission line is absorbed by the intervening neutral medium, causing an extremely red $(i - z)$ or $(z - y)$ color if the source is at $z \gtrsim 6$ ($i-$dropouts) or $z \gtrsim 6.4$ ($z-$dropouts), respectively. The main contaminants in such selection are cool stars in our own Galaxy, i.e. M/L/T Dwarf, which present similar red colors at shorter wavelength. In Figure 1.8 we show a representative spectrum of a quasar at z =6.3, together with an illustrative spectrum of a stellar contaminant. Information at longer wavelength, i.e. in the near-infrared (NIR) range, where the spectral signatures differ, are needed to reject any foreground Galactic contaminant. Moreover, high–redshift quasars are extremely rare. If one integrates the luminosity function provided by Willott et al. 2010b, at z =6, and down to an absolute UV magnitude at rest frame 1450 Å of $M_{1450} = -25$, one obtains a quasar number count of only $\sim$0.7 Gpc^{-3}. Therefore, in order to find high–redshift quasars, observations in the optical/NIR regime on a wide sky area are necessary.

The first quasar at z=5.5 was discovered $\sim$20 years ago by Stern et al., 2000. Since then, in the last two decades, 254 quasars have been discovered at $z > 5.5$. This was made possible by the advent of several large-area surveys:

- the *Dark Energy Camera Legacy Survey* (**DECaLS**, 1 quasar; Wang et al. 2017)
- the *Infrared Medium Deep Survey* (**IMS**, 1 quasar; Kim et al. 2015)
- the *Very Large Telescope Survey Telescope (VST) **ATLAS** Survey* (2 quasars; Carnall et al. 2015);
- the *NOAO Deep Wide-Field Survey* (**NDWFS**, 3 quasars; Cool et al. 2006, McGreer et al. 2006)
- the *UK Infrared Deep Sky Server* (**UKIDSS**, 9 quasars;Venemans et al. 2007, Mortlock et al. 2009, 2011, Bañados et al. 2018);
- the *Dark Energy Survey* (**DES**, 10 quasars; Reed et al. 2015, 2017);
- the *VISTA Kilo-Degree Infrared Galaxy Survey* (**VIKING**) and the *ESO public Kilo Degree Survey* (**KiDS**, 13 quasars in total; Venemans et al. 2013, 2015);
- the *Canada-France High-redshift Quasar Survey* (**CFHQS**, 20 quasars; Willott et al. 2007, 2009, 2010,b);
- the *Sloan Digital Sky Survey* (**SDSS**, 52 quasars; Fan et al. 2000, 2003, 2006, Zeimann et al. 2011, Jiang et al. 2016, Wang et al. 2016, 2017);
- the *Subaru Hyper Suprime-Cam-SPP Survey* (**HSC-SPP**, 64 quasars; Kashikawa et al. 2015[3], Matsuoka et al. 2016, 2018, 2018)

[3]This study used the Suprime-Cam.

- the *Panoramic Survey Telescope and Rapid Response System* (**Pan-STARRS1** or **PS1**, 78 quasars; Morganson et al. 2012, Bañados et al. 2014, 2015, 2016, Venemans et al. 2015b, Tang et al. 2017).

The current redshift record–holder, J1342+0928 at $z = 7.5$, was recently discovered by Bañados et al. (2018; see Figure 1.4). We refer to Section 2.2.1 for an further description of some of these surveys. The redshift distribution of all the z >5.5 quasars known at the time of this work is shown in Fig. 1.9.

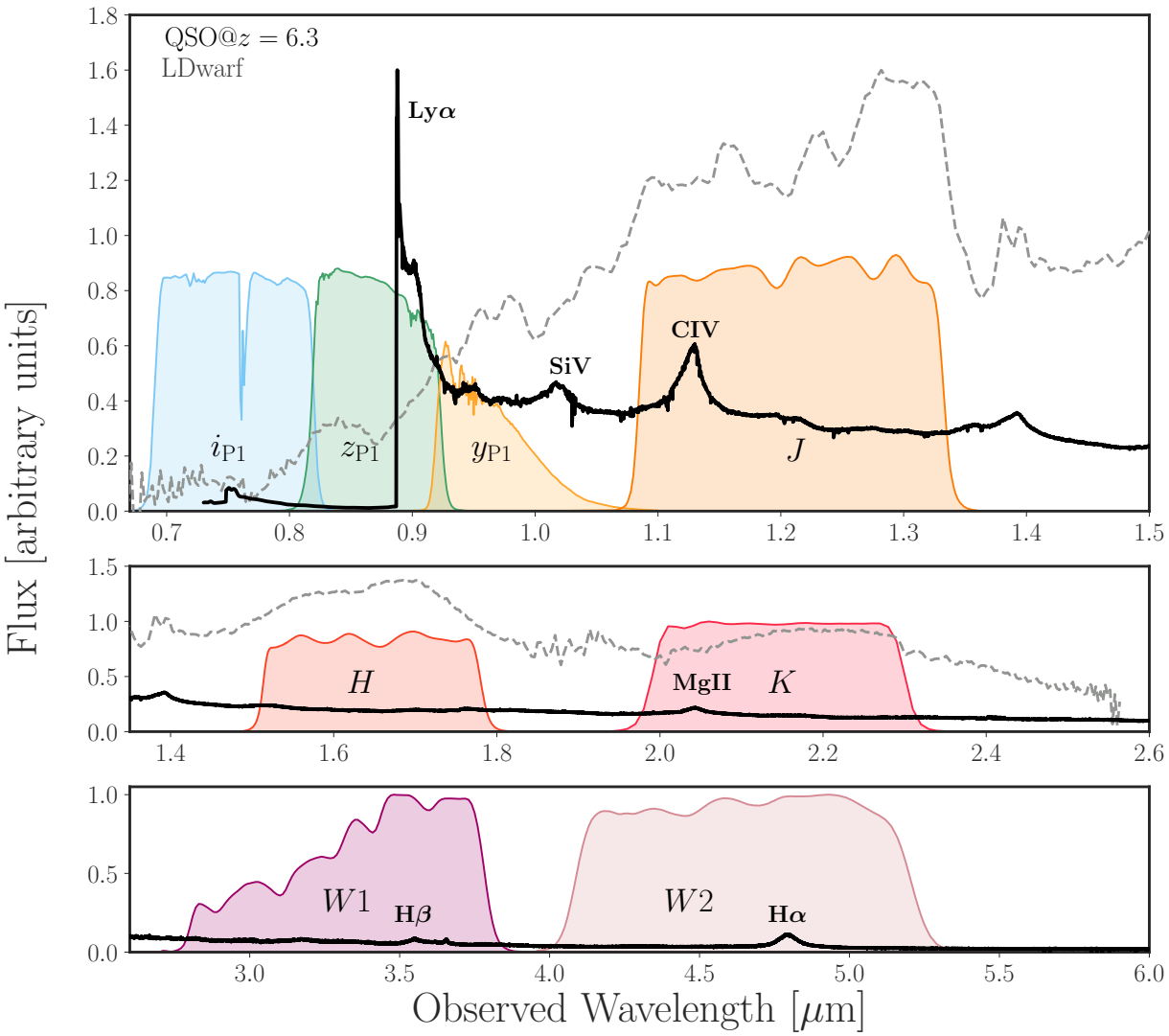

FIGURE 1.8: Representative spectrum of a quasar at z =6.3, obtained by shifting the lower−z template from Selsing et al., 2016. Overplotted, we show the spectrum of a cool dwarf star, one of the main contaminants in high–redshift quasar searches, and the response curves of the broad band filters primarily used in this work. The main broad emission lines (see Table 1.1) are also highlighted.

1.5.1 The First Supermassive Black Holes

High–z quasars already host SMBHs with $M_{BH} \gtrsim 10^9 M_\odot$ in their centers. These observations challenge current models of formation and evolution of early supermassive black holes

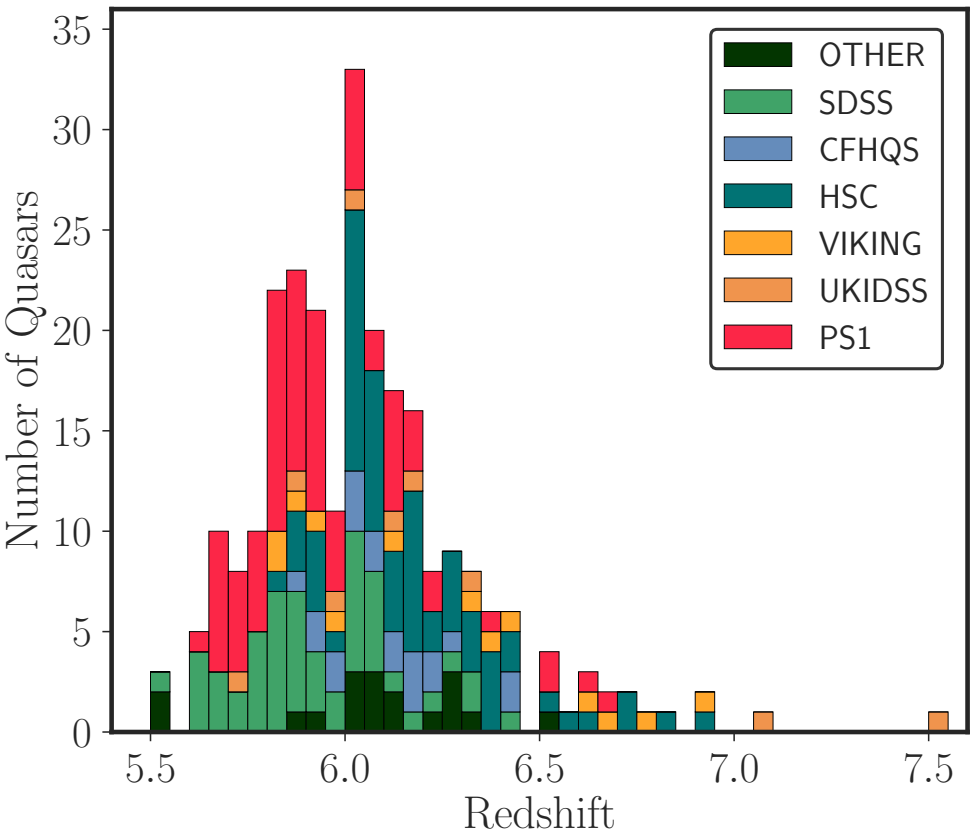

FIGURE 1.9: Redshift distribution of the quasars known at $z > 5.5$, as of May 2018. With "OTHER", we indicate the objects discovered by the remaining surveys listed in Section 1.5.

(e.g. Volonteri 2010, Latif and Ferrara 2016 for reviews). The current preferred models include the formation of black hole seeds from the direct collapse of massive gaseous reservoirs (e.g., Haehnelt and Rees 1993, Latif and Schleicher 2015), the collapse of Population III stars (e.g., Bond, Arnett, and Carr 1984, Alvarez, Wise, and Abel 2009, Valiante et al. 2016), the co-action of dynamical processes, gas collapse and star formation (e.g., Devecchi and Volonteri 2009), or the rapid growth of stellar-mass seeds via episodes of super-Eddington, radiatively inefficient accretion (e.g., Madau, Haardt, and Dotti 2014, Alexander and Natarajan 2014, Pacucci, Volonteri, and Ferrara 2015, Volonteri et al. 2016, Lupi et al. 2016, Pezzulli, Valiante, and Schneider 2016, Begelman and Volonteri 2017). While the black hole seeds from Pop III stars are expected to be relatively small ($\sim$ 100 $M_\odot$; e.g. Valiante et al. 2016), and to be formed at earlier times ($20 < z < 50$), direct collapse of massive clouds can lead to the formation of more massive seeds ($\sim 10^4 - 10^6$ $M_\odot$) at lower redshifts ($8 < z < 10$; e.g. Volonteri 2010). On the other hand, dynamical processes between stars and gas are expected to form 'intermediate seeds' ($\sim 10^3 M_\odot$) at intermediate times ($10 < z < 15$). From black hole growth theory, we know that black holes can evolve very rapidly from their initial seed masses, $M_{\rm BH,seed}$, to the final mass $M_{\rm BH,f}$. Indeed, we can express the black hole growth as:

$$M_{\rm BH,f} = M_{\rm BH,seed} \exp\left(\frac{t}{t_s} \times \frac{1-\epsilon}{\epsilon} \times \frac{L_{\rm bol}}{L_{\rm Edd}}\right) \tag{1.30}$$

with t_s =0.45 Gyr is the Salpeter time. Assuming accretion at the Eddington limit, i.e. $L_{\rm bol} = L_{\rm Edd}$, and a radiative efficiency of 10% (Volonteri and Rees, 2005), we obtain:

$$M_{\rm BH,f} \sim M_{\rm BH,seed}\, e^{9\times \frac{t\,[\rm Gyr]}{0.45}} \tag{1.31}$$

For instance, in the seemingly short redshift range $z \sim 6.0 - 6.5$, corresponding to $\sim$ 90 Myr, a black hole can grow by a factor of six. From an observational perspective, the discovery of quasars at $z \gtrsim$6.5 can give stronger constraints on the nature of black hole seeds than the quasar population at $z \sim 6$. In this thesis, we will derive $M_{\rm BH}$ estimates for a sample of $z >$6.5 quasars, and place constraints on the respective seed formation. Moreover, observations of the innermost regions of $z > 6$ quasars (i.e. the BLR) highlight how these objects have already metallicities close to solar (e.g., Barth et al. 2003, Stern et al. 2003, Walter et al. 2003, De Rosa et al. 2011, De Rosa et al. 2014). Here, we will derive an estimate of the BLR [metal/α elements] abundances from rest–frame UV spectra of $z \gtrsim$6.5 quasars.

1.5.2 The Host Galaxies of Distant Quasars

Most quasars at $z \sim$6 are already hosted in massive gas–rich galaxies. The bright, non thermal emission from the central engine outshines the stellar radiation from the host galaxy, hampering so far any attempt to recover the rest–frame UV/optical emission from such galaxies (e.g. Mechtley et al. 2012, Decarli et al. 2012). On the other hand, a large number of studies observed conspicuous amounts of cool gas and dust in quasars' hosts, thanks to the detection of the bright [CII]158 μm emission line and the underlying dust continuum, falling in the millimeter regime at $z \gtrsim 5.5$ (see Figure 1.10; e.g., Maiolino et al. 2009, Walter et al. 2009, Willott, Bergeron, and Omont 2015, Venemans et al. 2016, Venemans et al. 2017; for a review see Carilli and Walter 2013). These IR–luminous galaxies ($L_{\rm IR} \sim 10^{11} - 10^{12}$ L$_\odot$) show typical dust masses of $\sim 10^8 - 10^9 M_\odot$, dynamical masses of $\sim 10^{10} - 10^{11} M_\odot$, and star formation rates of few 100s $M_\odot$ yr^{-1} (e.g. Decarli et al. 2018). They are characterized by a variety of morphologies/kinematics, from rotation disks (e.g. Wang et al. 2013, Venemans et al. 2016), to disturbed/merger-like structures (e.g. Willott, Bergeron, and Omont 2017, Decarli et al. 2017), or compact, unresolved emissions (e.g. Venemans et al. 2017). In this thesis, we will present new mm–observations of four quasar host galaxies at $z \gtrsim 6.5$, and place their properties in the context of quasars and galaxies at low and high–redshifts.

1.5.3 Quasars as probes of the IGM in the EoR

Studies of $z \sim$5.7 quasars show that they live in a mostly ionized universe: Fan et al., 2006 pioneered the use of high–z quasars spectra as probes of the state of the early universe.
The most commonly used methods nowadays are:

- the measure of the *transmission spikes in the Lyα forest*, i.e. the absorption pattern in high–z quasars spectra bluewards of Lyα due to the intervening IGM. This technique permits to estimate the evolution of the Gunn-Peterson optical depth with redshift (e.g. Fan et al. 2006, Becker et al. 2015, Barnett et al. 2017), but it is hampered by the fast saturation of the Lyα emission line, which is already completely absorbed in case of a hydrogen neutral fraction of $x_{\rm HI} \sim 10^{-4}$. Analysis of the Lyβ and Lyγ forests are therefore necessary in order to probe environments with higher gas neutral fractions, i.e. well into the EoR.

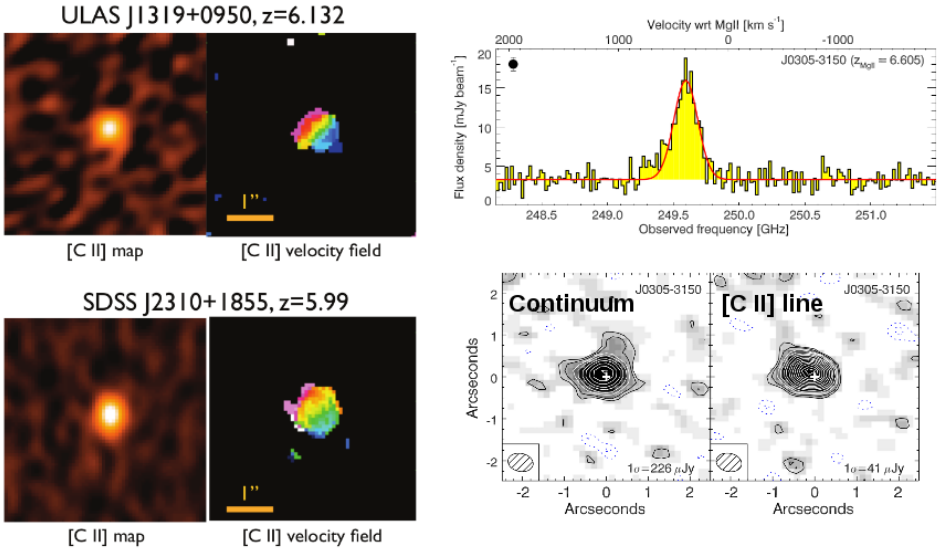

FIGURE 1.10: Examples of quasars host galaxies observed in the mm regime. *Left*: ALMA observations of the [CII] emission line total intensity map, and gas velocity map, of two $z \sim 6$ quasars (Wang et al., 2013). *Right*: Spectrum of the [CII] emission line of J0305 at $z = 6.6$ (*top*), and its [CII] and underlying continuum intensity map (*bottom*; Venemans et al. 2016).

- the study of the *Lyα power spectrum*, using a statistically significant sample of quasars (e.g., Palanque-Delabrouille et al. 2013).
- the analysis of the *damping wing* in quasars spectra. If the source is surrounded by mostly neutral gas, the 'Gunn-Peterson' absorption is detected, which is extended on the red side of the Lyα line mainly due to the intrinsic width of the line (e.g. Miralda-Escudé 1998). This signature has been observed in the spectra of the two highest redshift quasars known so far, J1120 and J1342, and, recently, it has been modeled in order to characterize the state of the surrounding IGM (e.g. Greig et al. 2017, Bañados et al. 2018, Davies et al. 2018). These studies determine hydrogen neutral fractions of $x_{\rm HI} \sim 0.4$ and > 0.33 at $z = 7.1$ and $z = 7.5$, respectively. This technique, even if very promising, is however only applicable to the few quasars where such signatures have been detected, and it is highly dependent on the assumptions considered in the model.
- the measurements of *near zone sizes*, i.e. regions around quasars which are ionized by the emission from the central objects. Their evolution with redshift has been studied to investigate the evolution of the IGM neutral fraction with cosmic time (e.g., Fan et al. 2006, Carilli et al. 2010, Venemans et al. 2015b). However, the modest-sized and non-homogeneous quasar samples at hand, large errors due to uncertain redshifts, and the limited theoretical models available have inhibited our understanding of these measurements to date. Recently, Eilers et al., 2017 addressed some of these caveats, deriving near zone sizes of 34 quasars at $5.77 \lesssim z \lesssim 6.54$. They find a less pronounced evolution of near zone radii with redshift than what has been reported by previous studies (e.g. Carilli et al. 2010 and Venemans et al. 2015b).

In this work, we will measure near zone sizes for quasars at $z \gtrsim 6.5$, and we will test whether the trend observed by Eilers et al., 2017 holds at higher redshift (see Section 2.5.10).

1.5.4 Quasars Environments

Current theoretical studies predict high–redshift quasars to be found in massive dark matter halos ($\sim 10^{13} M_{\odot}$; e.g. Lapi et al. 2006, Porciani and Norberg 2006, Wyithe and Loeb 2003), where a large number of galaxies are also expected to form (Overzier et al., 2009). These structures can eventually evolve into large gravitationally bound systems in the present universe (with a large scatter in mass, from groups to clusters, e.g. Springel et al. 2005, Overzier et al. 2009, Angulo et al. 2012).

UV–based Mpc–Scale Observations

Observational attempts to detect the rest–frame UV radiation of these high-redshift galaxies in the vicinities of high redshift quasars complement the aforementioned theoretical predictions. A number of studies investigated the presence of the theoretically expected galaxies around $z \sim$6 quasars, using the Lyman Break technique (see Section 1.3). However, the picture sketched out by observations is far from clear. For instance, Stiavelli et al., 2005 found an overdensity of LBGs in the field of the bright $z \sim$6.28 quasar SDSS J1030+0524, based on i_{775} and z_{850} images taken with the Advanced Camera for Surveys (ACS) at the *HST* (with a field of view of $\sim$ 11 arcmin^2, corresponding to an area of $\sim$65 comoving Mpc^2 [cMpc^2] at $z \sim$6). On the other hand, Kim et al., 2009 studied the environment of five $z \sim$6 quasars, again searching for LBGs through *HST* ACS imaging: they estimated that the fields around two quasars are overdense, two underdense and one consistent with a blank field. Simpson et al., 2014 investigated the quasar ULAS J1120+0641 at $z \sim$7, recovering no evidence for the presence of an overdensity of galaxies (using data from *HST* ACS). Studies on scales larger than ACS *HST* also do not provide an unambiguous scenario. Utsumi et al., 2010 found an enhancement in the number of LBGs in the field of the quasar CFHQS J2329-0301 ($z \sim$6.4), observed with the Suprime Camera at the Subaru Telescope, whose field of view covers an area of $\sim$900 arcmin^2($\sim$4600 cMpc^2). Morselli et al., 2014 showed that four $z \sim$6 quasars were situated in overdense environments, based on a search for LBGs with deep multi-wavelength photometry from the Large Binocular Camera (LBC) at the Large Binocular Telescope (LBT, whose field of view covers a wide area of $\sim$ 575 arcmin^2 $\sim$3100 cMpc^2). Recent additional imaging in the NIR regime for the field around one of these quasars, SDSSJ1030+0524, strengthens the significance of this overdensity ($> 4\sigma$; Balmaverde et al. 2017). Conversely, Willott et al., 2005 imaged three SDSS quasars at $z >$6 with GMOS-North on the Gemini-North Telescope (with a field of view of $\sim$ 30 arcmin^2, amounting to $\sim$170 cMpc^2 at $z \sim$6), recovering no clear signs for an overdensity of LBGs.

The different findings may be ascribed to different reasons, e.g. the depths reached in the observations, diverse techniques/selection criteria considered, different survey areas (and therefore scales) probed, and the diverse fields inspected, which may be intrinsically different. More importantly, the Lyman Break technique, using broad-band filters whose pass-bands normally span $\Delta\lambda \sim$ 1000 Å, does not provide an accurate redshift determination ($\Delta z \sim$1, equals to line of sight distances $\Delta d \sim$ 850 cMpc or 120 physical Mpc [pMpc] at $z \sim$6). Any possible overdensity may be diluted over this big cosmological volume (Chiang, Overzier, and Gebhardt, 2013), taking into account that the Universe is homogeneous at scales $\gtrsim$ 70-100 h^{-1} Mpc (Wu, Lahav, and Rees 1999, Sarkar et al. 2009). Samples of photometric LBGs, selected without a large number of broad band filters, are likely to be contaminated by foreground sources (e.g. lower-z, red/dusty galaxies).

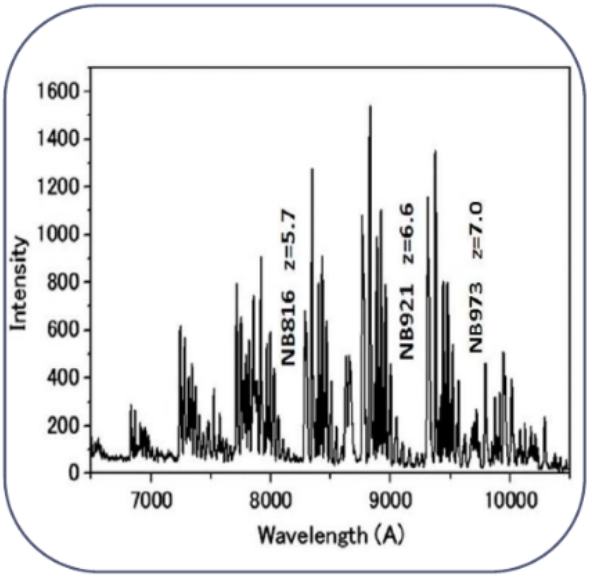

FIGURE 1.11: Intensity of the atmospheric emission in the red part of the optical spectrum. Ground based searches for LAEs with narrow band filters are limited to wavelength regions free of strong features, i.e. at redshift z ∼5.7, 6.6, 7.0. Figure taken from Dunlop, 2013.

A more secure approach to identify high redshift galaxies is to look for sources with a bright Lyα emission (LAEs; see Section 1.3). Such narrow line emission can be recovered by specific narrow band filters ($\Delta\lambda \sim 100$ Å). An immediate advantage, with respect to the LBG selection, is that the redshift range covered is much narrower ($\Delta z \sim 0.1$, corresponding to $\Delta d \sim 44$ cMpc$\sim$ 7 pMpc at $z \sim$6), i.e. an overdensity membership can be clearly established. For ground-based observations, the search for LAEs is possible only in wavelength regions clear of strong atmospheric emission, corresponding to windows at redshift z ∼3.1, 3.7, 5.7, 5.2, 6.6, 7.0 (see Figure 1.11; e.g. Dunlop 2013, Hu et al. 2010). Thanks to the fast expanding sample of quasars at $z >$5.5, this study is now made possible for several new sources.

Decarli et al., 2012 searched for Lyα emission around two $z >$6 quasars through narrow band imaging with *HST*: their study was limited to small scales (∼1 arcmin∼0.35 pMpc), and recover no Lyα emission in the proximity of these sources. Bañados et al., 2013 carried out the first search for LAEs at scales $\gtrsim$1 pMpc around a $z >$5.5 quasar. They used a collection of broad and narrow band filters at the VLT. No strong evidence was found for an enhancement in the number of LAEs with respect to the blank field. Recently, Farina et al., 2017 detect a LAE, 'smoking gun' of a rich environment, very proximate (∼12.5 kpc and ∼560 km s^{-1}) to a quasar at redshift z ∼6.6, using MUSE at the VLT.
In Chapter 3 of this thesis, we will present the second Mpc–scale search for LAEs around a $z \sim$ 5.7 quasar, performed using the FORS2 camera at the VLT.

IR–based kpc–Scale Observations

Very recently, Decarli et al., 2018 undertook an ALMA survey of the [CII] emission line and the underlying dust continuum emission in 27 quasar host galaxies at $z \gtrsim$6. Surprisingly, [CII]–

and infrared–bright companion galaxies have been serendipitously discovered in the field of four quasars, at projected separations of $\lesssim$60 kpc, and line-of-sight velocity shifts of $\lesssim$450 km s^{-1} (Decarli et al. 2017; see Figure 1.12). Additionally, Willott, Bergeron, and Omont, 2017, with ALMA observations at 0.″8 resolution, found a very close companion galaxy next to the quasar PSO J167.6415–13.4960 at z ∼6.5, at a projected distance of only 5 kpc and velocity separation of ∼300 km s^{-1} (see Figure 1.13). Analogous cases have been observed at z ∼5: indeed, Trakhtenbrot et al. 2017 detected [CII]–bright companion galaxies in three out of six fields imaged with ALMA, separated from the quasars by only $\lesssim$45 kpc and $\lesssim$450 km s^{-1}. These [CII]–bright companion galaxies spot rich environments, in line with the aforementioned theoretical predictions[4]. Characterized by high infrared luminosities ($L_{\rm IR} \gtrsim 10^{11}$ L$_\odot$) and harboring large reservoirs of dust (M$_{\rm dust} \gtrsim 10^8$ M$_\odot$), such galaxies have been considered (Decarli et al., 2017) as potential progenitors of the "read and dead" galaxies already observed at z ∼4 (e.g. Straatman et al. 2014; see Section 1.3). In this thesis, we present new sensitive optical/NIR follow-up observations specifically designed to probe four of these companion galaxies to $6 \lesssim z \lesssim 6.6$ quasars, obtained from several ground- and space-based facilities (see Chapter 4).

To summarize, in the following Chapter 2, we will report our search for the highest–redshift quasars ($z-$dropouts), and the analysis of their physical properties via optical/NIR spectra and mm observations, from their central SMBH/BLR to their host galaxies and near zones.
We will further present our investigation of the Mpc–scale environment around a quasar at z ∼5.7, searching for LAEs detected through a suit of broad and narrow–band filters (Chapter 3).
We will then focus on the follow–up observations of gas–rich galaxies observed in the proximities of four quasars at $z \gtrsim$6, and we will place them in the context of previous observations of high$-z$ star forming galaxies (Chapter 4).
Finally, in Chapter 5. we will list our conclusions and outlook.

[4]However, notice that other studies did not find overdensities of [CII]/dust continuum–emitting galaxies around a sample of $z \gtrsim$6 quasars (e.g. Venemans et al. 2016).

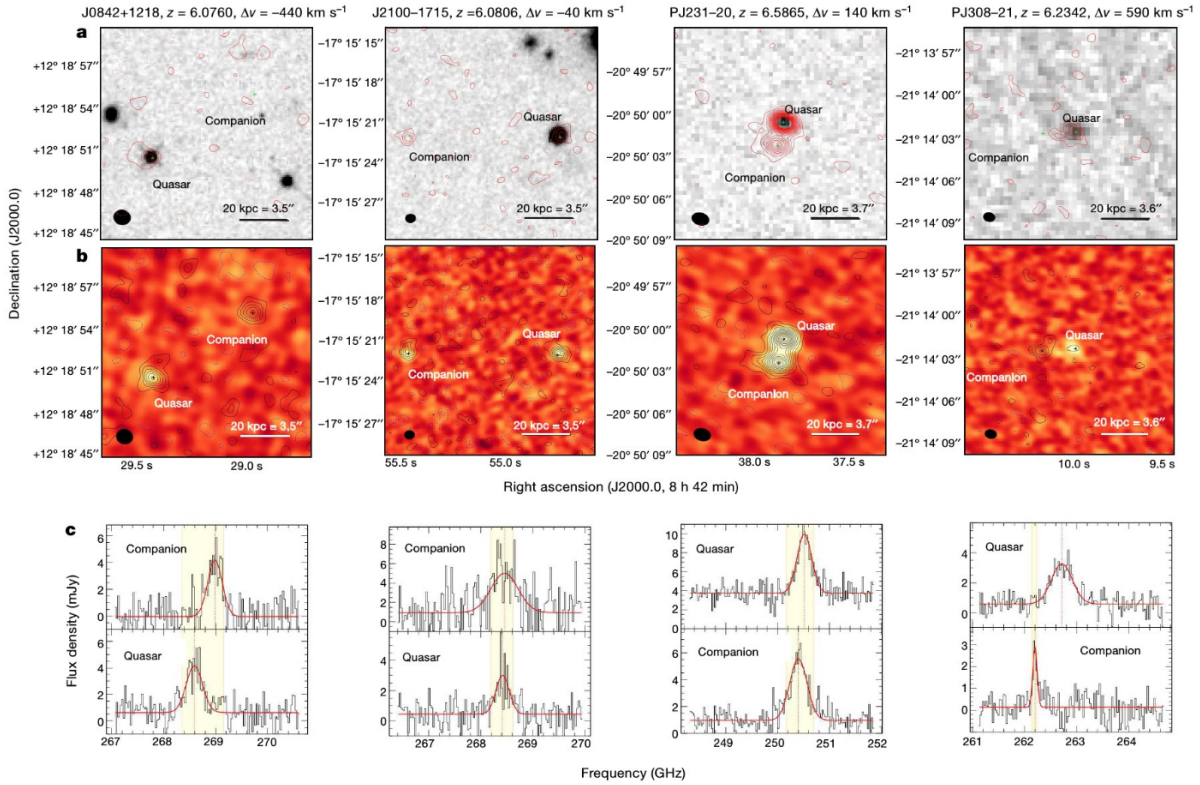

FIGURE 1.12: Gas–rich, massive companion galaxies, detected by ALMA around four $z \sim 6$ quasars, spot very rich environments. Despite their high IR and [CII] emission line luminosities (*center* and *bottom panels*), their emission in the rest–frame UV/optical range remained undetected (*top panel*). The figure is taken from Decarli et al., 2017.

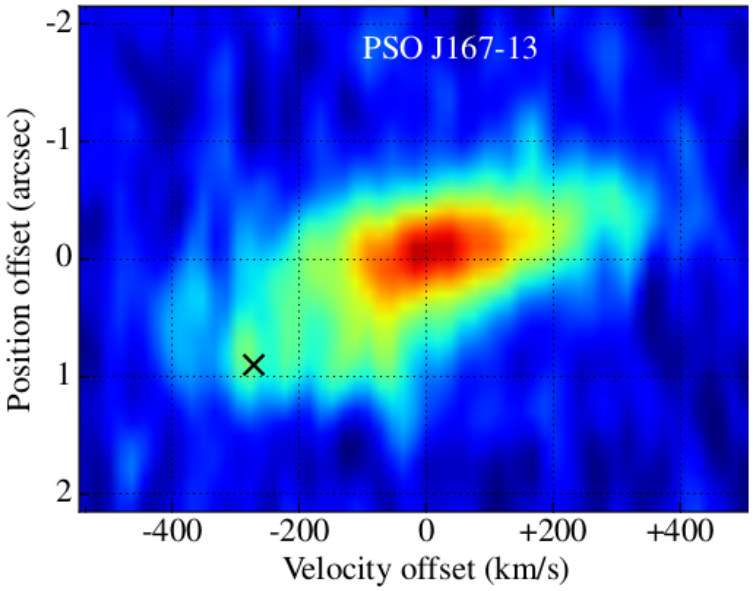

FIGURE 1.13: A further companion galaxy, in the very close proximity (5 kpc, i.e. 0.″9) of a quasar at $z \sim 6.5$, was recently observed by Willott, Bergeron, and Omont, 2017. In the position–velocity diagram reported here, it is possible to notice an extended emission connecting the quasar host galaxy and the companion (figure adapted from Willott, Bergeron, and Omont 2017).

Chapter 2

Physical Properties of 15 Quasars at z $\gtrsim$ 6.5[1]

In the following chapter, we present our search for the highest redshift quasars. We start by shortly describing the PS1 survey, on which we primarily base our quasar search (§ 2.1). We then report our candidate selection method (§ 2.2), follow–up imaging and spectroscopic observations (§ 2.3), and the newly discovered quasars (§ 2.4). We analyze several properties of 15 quasars at $z \gtrsim 6.5$, from their innermost regions, in the SMBH sphere of influence (§ 2.5.3–§ 2.5.8), to their host galaxies (§ 2.5.9), and their immediate ionized surroundings (§ 2.5.10).

2.1 The Pan–STARRS1 Survey

The *Panoramic Survey Telescope and Rapid Response System 1* (Pan-STARRS1 or PS1; Kaiser et al. 2002, 2010, Chambers et al. 2016, Magnier et al. 2016,a,b,c, Waters et al. 2016, Flewelling et al. 2016) carried out a 3π survey of the sky at Decl.$> -30°$, in five filters (g_{P1}, r_{P1}, i_{P1}, z_{P1}, y_{P1}; Stubbs et al. 2010, Tonry et al. 2012; see Appendix A). The main overall science goals include the monitoring of asteroids and Solar System objects, the measurement of precision photometry and astrometry for stars in the Milky Way and in the Local Group, and the investigations of the high–redshift universe.

The survey used the 1.4 Gigapixel camera (GPC1) mounted on the 1.8m Pan-STARRS1 telescope at the Haleakala Observatories in Hawaii. Data were collected over 5 years, from 2009-06-02 to 2014-03-31, with simultaneous observations in pairs of filters. Images in the g_{P1}, r_{P1} and i_{P1} bands were taken at the same time, while the corresponding z_{P1} and y_{P1} data were acquired 5-6 months later. This strategy was implemented in order to optimize the measurements of the stellar proper motion and parallaxes (Chambers et al., 2016).

The PS1 survey offers an excellent tool for the search for high–redshift quasars for several reasons.

1. PS1 is $\gtrsim$1 mag deeper than the SDSS survey, in particular in the red part of the optical spectrum.
2. Data acquired in the y_{P1} band allows for selection of quasars at $z \gtrsim 6.5$, overcoming the redshift limit of SDSS.
3. The survey provides coverage of a large fraction of the sky, in particular in the south, which was not previously explored by SDSS. Any quasar discovered in the southern

[1] This chapter is a version of the article Mazzucchelli et al., 2017b.

hemisphere represents an ideal target for multiwavelengths follow–up observations with facilities such as ALMA or VLT.

Bañados et al., 2016 carried out a search for quasars at $z \sim 6$ ($i-$dropouts), using the Pan-STARRS1 second internal release (PV2). This study lead to the discovery of 63 new sources, more than doubling the previously known sample.

The International Astronomical Union imposes in its naming convention that all non-transient sources discovered in the PS1 survey are named "PSO JRRR.rrrr±DD.dddd", with RRR.rrrr and DD.dddd right ascension and declination in decimal degrees (J2000), respectively. For simplicity, in this Chapter we will refer to the PS1 quasars as "PSORRR+DD", and to sources from other surveys, e.g. VIKING, UKIDSS and HSC, as "VIKhhmm", '"ULAShhmm" and "HSChhmm". We consider throughout this thesis the PS1 PSF magnitudes.

2.2 Candidate Selection

Here, we perform a search for $z-$dropouts in the Pan-STARRS1 survey using the PS1 third internal release (PV3) catalog. We follow and expand the selection illustrated both in Bañados et al., 2016, which was focused on lower redshift objects ($z \sim 6$), and in Venemans et al., 2015b. All the magnitudes reported here, and throughout this thesis, are in the AB system.

As reported in § 1.5, samples of high redshift quasar candidates selected through broad-band imaging and optical color criteria are highly contaminated by the numerous cool dwarf stars in our Galaxy (mainly M/L/T-dwarfs), which present similar colors and morphology. We therefore compile our sample and clean it from contaminants through the following steps:

- initial search based on the PS1 PV3 catalog and cross-match with known cool dwarf and quasar lists;
- cross-match with other infrared public surveys;
- forced photometry on the stacked and single epoch PS1 images;
- fit of the spectral energy distribution (SED); and
- visual inspection.

Afterwards, we follow up the selected candidates with dedicated photometric campaigns, followed by spectroscopy of the remaining targets to confirm (or discard) their quasar nature (see Section 2.3).

2.2.1 Catalog Search

Pan-STARRS1

The flux of high−redshift quasars at wavelengths shorter than the Lyα emission line is strongly absorbed by the intervening intergalactic medium (see also Section 1.2). Therefore, we expect to recover little or no flux in the bluer bands, and to observe a strong break of the continuum

emission. We base our selection of $z-$dropouts on the $y_{\rm P1}$ magnitude. We impose the following signal-to-noise (S/N) and colors requirements:

$$S/N(y_{\rm P1}) > 7 \tag{2.1}$$
$$S/N(g_{\rm P1}, r_{\rm P1}) < 3 \tag{2.2}$$
$$[S/N(i_{\rm P1}) < 5] \quad \text{or} \quad [S/N(i_{\rm P1}) > 5 \quad \text{and} \quad (i_{\rm P1} - y_{\rm P1}) > 2.2] \tag{2.3}$$

Furthermore, we require a $(z_{\rm P1} - y_{\rm P1})$ color criterion as:

$$[S/N(z_{\rm P1}) > 3 \quad \text{and} \quad z_{\rm P1} - y_{\rm P1} > 1.4] \quad \text{or} \tag{2.4}$$
$$[S/N(z_{\rm P1}) < 3 \quad \text{and} \quad z_{\rm P1,lim} - y_{\rm P1} > 1.4] \tag{2.5}$$

In order to reject objects with an extended morphology, we require:

$$|y_{\rm P1} - y_{\rm P1,aper}| < 0.3 \tag{2.6}$$

where $y_{\rm P1,aper}$ is the aperture magnitude in the PS1 catalog. This cut was implemented based on a test performed on a sample of spectroscopically confirmed stars and galaxies (from SDSS-DR12, Alam et al. 2015), and quasars at $z > 2$ (from SDSS-DR10, Pâris et al. 2014). Using this criterion, we are able to select a large fraction of point-like sources (83% of quasars and 78% of stars) and reject the majority of galaxies (94%; see Bañados et al. 2016 for more details on this approach).

Additionally, we discard objects based on the quality of the $y_{\rm P1}$ band image using the flags reported in the PS1 catalog (e.g., we require that the peak of the object is not saturated, and that it does not land off the edge of the chip or on a diffraction spike; for a full summary, see Bañados et al. 2014, Appendix A). We require also that 85% of the expected PSF-weighted flux in the $z_{\rm P1}$ and $y_{\rm P1}$ bands falls in a region of valid pixels (the catalog entry `PSF_QF` >0.85).

We exclude objects in regions of high Galactic extinction ($E(B-V) > 0.3$), following the extinction map of Schlegel, Finkbeiner, and Davis, 1998; we also exclude the area close to M31 (00:28:04<R.A.<00:56:08 and 37° <Decl.< 43°). We clean the resulting sample by removing known quasars at $z \geq$5.5 (see § 1.5, and Bañados et al. 2016, Table 7) and known L and T dwarfs (from Mace 2014, Lodieu, Boudreault, and Béjar 2014, Marocco et al. 2015 and Best et al. 2015). The total number of candidates at this stage is ∼781˙000. We take advantage of the information provided by other public surveys, when their sky coverage overlaps with Pan-STARRS1. We here further consider solely the sources with a detection in the ALLWISE catalog.

ALLWISE Survey

The ALLWISE catalog[2], results from the combination of the all-sky *Wide-field Infrared Survey Explorer* mission (*WISE* mission; Wright et al. 2010) and the NEOWISE survey (Mainzer et al. 2011). The 5σ limiting magnitudes are $W1$=19.3, $W2$= 18.9 and $W3$=16.5. We use a match radius

[2]http://wise2.ipac.caltech.edu/docs/release/allwise/

of 3″, requiring S/N>3 in $W1$ and $W2$. We further impose:

$$-0.2 < W1 - W2 < 0.86 \tag{2.7}$$

$$W1 - W2 > (-1.45 \times ((y_{\rm P1} - W1) - 0.1) - 0.6) \tag{2.8}$$

For candidates with S/N($W3$)> 3, we prioritize sources with $W2 - W3 > 0$. These selection criteria help exclude the bulk of the L-dwarf population (Bañados et al. 2016). The color criteria above were solely used to prioritize sources for follow-up observations, but not to reject them.

UKIDSS and VHS Surveys

We cross-match our sample using a 2″ matching radius with the UKIDSS Large Area Survey (UKIDSS LAS, Lawrence et al. 2007) data release 10[3], and the VISTA Hemisphere Survey (VHS, McMahon et al. 2013). UKIDSS and VHS provide Y, J, H and K images over areas of ∼4000 deg^2 and ∼8000 deg^2, respectively. The UKIDSS survey mapped regions of the sky within coordinates 00:32:04<R.A.<01:04:07 and -1.0° <Decl.<16°, and 00:32:04<R.A.<01:04:07 and 20° <Decl.<40°, to 5σ limiting magnitudes of Y=20.8, J=20.5, H=20.2, K=20.1. The VHS survey aims to cover the southern hemisphere, avoiding the Milky Way footprint, and to reach a depth ∼30 times fainter than 2MASS. In this work, we reject objects from our initial selection in case they were detected in these catalogs and had $Y - J > 0.6$ and/or $y_{\rm P1} - J > 1$ (e.g., typical colors of brown dwarfs; see Best et al. 2013).

DECaLS

The Dark Energy Camera Legacy Survey (DECaLS[4]) is an on-ongoing survey which will image ∼6700 deg^2 of the sky in the northern hemisphere, up to Decl.<30°, in $g_{\rm decam}$, $r_{\rm decam}$ and $z_{\rm decam}$, using the Dark Energy Camera on the Blanco Telescope. We consider the Data Release 2 (DR2[5]), which covers only a fraction of the proposed final area (2078 deg^2 in $g_{\rm decam}$, 2141 deg^2 in $r_{\rm decam}$ and 5322 deg^2 in $z_{\rm decam}$), but is deeper than PS1 ($g_{\rm decam,5\sigma} = 24.7$, $r_{\rm decam,5\sigma} = 23.6$, $z_{\rm decam,5\sigma} = 22.8$). We use a match radius of 2″. We reject all objects detected in $g_{\rm decam}$ and/or $r_{\rm decam}$, or that present an extended morphology (e.g. with catalog entry `type` different than 'PSF').

In Figure 3.4 we show one of the color-color plots ($y_{\rm P1} - J$ vs $z_{\rm P1} - y_{\rm P1}$) used at this stage of the candidate selection.

2.2.2 Forced photometry on PS1 images

Next, we perform forced photometry on both the stacked and single epoch images from PS1 of our remaining candidates. This is to confirm the photometry from the PS1 PV3 stacked catalog and to reject objects showing a large variation in the flux of the single epoch images which would most probably indicate spurious detections (for further details on the cuts used at this stage, see Bañados et al. 2014).

[3] http://surveys.roe.ac.uk/wsa/dr10plus_release.html
[4] http://legacysurvey.org/decamls/
[5] http://legacysurvey.org/dr2/description/

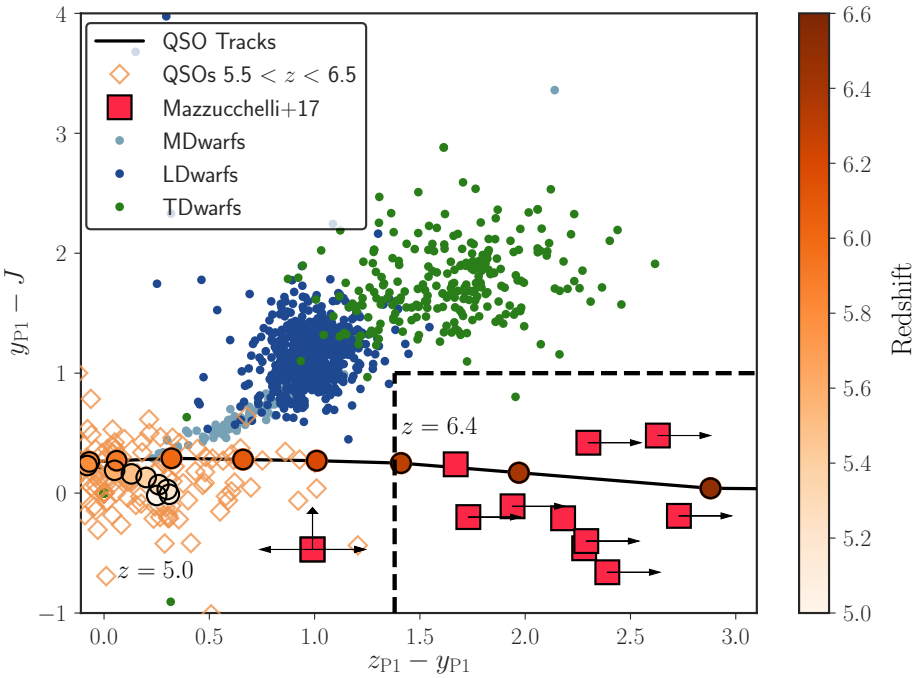

FIGURE 2.1: Color-color diagram ($y_{P1} - J$ vs $z_{P1} - y_{P1}$) used in our search for high−redshift quasars. We show the predicted quasar track (*black solid line* and *points* color-coded with respect to redshift, in steps of Δz =0.1), obtained by convolving the high−redshift quasar composite template reported by Bañados et al. (2016; see also Section 2.2.3) with the filters considered here. Observed colors of L/T dwarfs, taken from the literature (see Section 2.2 for references), are reported with *blue* and *green points*, while we consider for M dwarfs the colors calculated convolving a collection of spectra with the filters used here (see Section 2.2.3). We show also the location of known quasars at $5.5 < z < 6.5$ (*orange empty diamonds*; see Section 1.5 for references), and the objects studied in this work (*red squares* with *black right-pointing arrow* in case they only have lower limits in the z_{P1} band from the PS1 PV3 catalog, see Table 2.3). We do not show quasars from the VIKING survey, which are not present in the PS1 catalog, and PSO006+39, for which we do not possess J−band photometry. For HSC1205 we use the 3σ limits in z_{P1} and y_{P1} obtained from the forced photometry on the PS1 PV3 stacked images. Our selection box is highlighted with *dashed black lines*.

2.2.3 SED Fit

We implement a SED fitting routine to fully exploit all the multi-wavelength information provided by the surveys described in Sections 2.2.1.

We compare the observations of our candidates with synthetic fluxes, obtained by interpolating quasar and brown dwarf spectral templates through different filter curves, in the 0.7−4.6 μm observed wavelength range.
We consider 25 observed brown dwarf spectra taken from the SpeX Prism Library[6] (Burgasser 2014), and representative of typical M4-M9, L0-L9 and T0-T8 stellar types. These spectra cover the wavelength interval 0.65−2.55 μm (up to K band). The corresponding $W1$ (3.4 μm) and $W2$ (4.6 μm) magnitudes are obtained following Skrzypek et al., 2015, who exploit a reference sample of brown dwarfs with known spectral and photometric information to derive various color relations. For each brown dwarf template, we derive the *WISE* magnitudes using the

[6]http://pono.ucsd.edu/ adam/browndwarfs/spexprism/

synthetic K magnitude and scaling factors (K_W1 and $W1\_W2$) which depend on the stellar spectral type[7]. We apply the following relations:

$$W1 = K - K\_W1 - 0.783 \tag{2.9}$$

$$W2 = W1 - W1\_W2 - 0.636 \tag{2.10}$$

For the quasar models, we use four different observed composite spectra: the SDSS template, obtained from a sample of $1 \lesssim z \lesssim 2$ quasars (Selsing et al., 2016), and three composite of $z \gtrsim 5.6$ quasars by Bañados et al., 2016, the first one based on 117 sources (from PS1 and other surveys), the second obtained considering only the 10% of objects with the largest rest-frame Lyα+N v equivalent width (EW), and the last using the 10% of sources with smallest EW (Lyα+N v). These different templates allow us to take into account color changes due to the Lyα emission line strength. However, the three models from Bañados et al., 2016 cover only up to rest-frame wavelength $\lambda_{\rm rest} \sim 1500$ Å, so we use the template from Selsing et al., 2016 to extend coverage into the NIR region. We shift all the quasar templates over the redshift interval $5.5 \leq z \leq 9.0$, with Δz =0.1. We consider the effect of the IGM absorption on the SDSS composite spectrum using the redshift-dependent recipe provided by Meiksin, 2006. For the quasar templates from Bañados et al., 2016, we implement the following steps: we correct each of the three models for the IGM absorption as calculated at redshift z=$z_{\rm median}$ of the quasars used to create the composite, obtaining the reconstructed emitted quasar spectra. Then, we re-apply the IGM absorption to the corrected models at each redshift step, again using the method by Meiksin, 2006. The total number of quasar models is 140.

For each quasar candidate from our selection, after having normalized the brown dwarf and quasar templates to the candidate observed flux at $y_{\rm P1}$, we find the best models that provide the minimum reduced χ^2, i.e. $\chi^2_{b,min,r}$ and $\chi^2_{q,min,r}$, for brown dwarf and quasar templates, respectively. We assume that the candidate is best fitted by a quasar template if $R = \chi^2_{q,min,r}/\chi^2_{b,min,r} < 1$. In our search, we prioritize for further follow-up observations sources with the lowest R values. Though we do not reject any object based on this method, candidates with $R > 1$ were given the lowest priority. An example of the best quasar and brown dwarf models for one of our newly discovered quasars is shown in Figure 2.2.

Finally, we visually inspect all the stacked and single epoch PS1 frames, together with the images from the other public surveys, when available (∼4000 objects). This is to reject non-astronomical or spurious sources (e.g. CCD defects, hot pixels, moving objects), that were not removed by our automated routine. We then proceed with follow-up of the remaining targets (∼1000).

2.3 Observations

We first obtain imaging follow-up observations of our quasar candidates, and then we take spectra of the most promising objects.

[7]The scaling factors K_W1 and $W1\_W2$ for the different M/T/L stellar types can be found in Table 1 of Skrzypek et al., 2015.

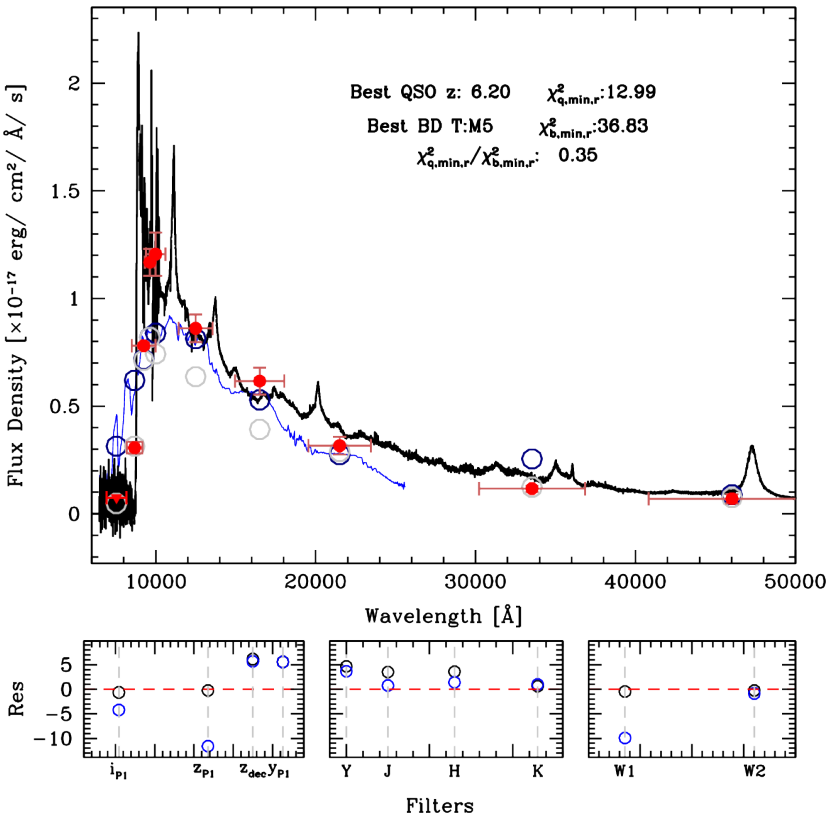

FIGURE 2.2: Example of SED fit for one of our candidates, confirmed to be a quasar at $z \sim 6.44$ (PSO183+05, see Table 2.5). In the *upper panel*, we show the photometric information taken from public surveys (*red points* and *down-pointing arrows* in case of non-detections at 3σ significance, see Section 2.2), the best quasar template (the weak-lined PS1 quasar template at $z = 6.2$; *black solid line*) and the best brown dwarf template (M5; *blue solid line*). The synthetic fluxes of the best quasar and brown dwarf templates, obtained by convolving the models to the filters considered here, are shown with *light grey* and *blue points*, respectively. In the *bottom panels*, the residuals, e.g. $(\text{flux}_{data,f} - \text{flux}_{bestmodel,f,q/b})/\sigma_f$, are displayed, for each f band used here. *Blue* and *black empty circles* indicate the best brown dwarf and quasar template, respectively.

2.3.1 Imaging and spectroscopic confirmation

We perform follow-up imaging observations in order to both confirm the catalog magnitudes, and to obtain missing NIR and deep optical photometry, crucial in identifying contaminant foreground objects.

We take advantage of different telescopes and instruments: MPG 2.2m/GROND (Greiner et al., 2008), NTT/EFOSC2 (Buzzoni et al., 1984), NTT/SofI (Moorwood, Cuby, and Lidman, 1998), du Pont/Retrocam[8], Calar Alto 3.5m/Omega2000 (Bailer-Jones, Bizenberger, and Storz, 2000), Calar Alto 2.2m/CAFOS[9]. In Table 2.1 we report the details of our campaigns, together with the filters used.

The data were reduced using standard data reduction procedures (Bañados et al., 2014). We

[8]http://www.lco.cl/telescopes-information/irenee-du-pont/instruments/website/retrocam
[9]http://www.caha.es/CAHA/Instruments/CAFOS/index.html

refer to Bañados et al., 2016 for the color conversions used to obtain the flux calibration in all these images. In case we collect new J band photometry for objects undetected or with low S/N in NIR public surveys, we consider as good quasar candidates the ones with $-1 < y_{P1} - J < 1$, while the sources with very red or very blue colors were considered to be stellar contaminants or spurious/moving objects, respectively. For a sources with good NIR colors (from either public surveys or our own follow-up photometry), we collected deep optical imaging, to confirm the continuum break.

We then took spectra of all the remaining promising candidates using VLT/FORS2 (Appenzeller et al., 1998), P200/DBSP (Oke and Gunn, 1982), MMT/Red Channel (Schmidt, Weymann, and Foltz, 1989), Magellan/FIRE (Simcoe et al. 2008) and LBT/MODS (Pogge et al., 2010) spectrographs. Standard techniques were used to reduce the data (see Venemans et al. 2013, Bañados et al. 2014, 2016, Chen et al. 2017). Six objects, out of nine observed candidates, were confirmed as high−redshift quasars: we present them and provide further details in Section 2.4. We list the spectroscopically rejected objects (Galactic sources) in Appendix B.

Further information on these observations, together with the additional spectroscopic observations for other objects in the quasar sample considered here (see Section 2.3.2), are reported in Table 2.2. In Table 2.3, we provide photometric data from catalogs for all the objects in our high−redshift quasars sample. Also, photometry from our own follow-up campaigns for the new six quasars is listed in Table 2.4. Table A.1 in Appendix A lists the information (central wavelength, λ_c, and width $\Delta\lambda$) of the various filters used in this work, both from public surveys and follow-up photometry.

TABLE 2.1: Imaging follow−up observation campaigns for PS1 high−redshift quasar candidates.

Date	Telescope/Instrument	Filters	Exposure Time
2014 May 9	CAHA 3.5m/Omega2000	z_{O2K}, Y_{O2K}, J_{O2K}	300s
2014 Jul 23−27	NTT/EFOSC2	I_E,Z_E	600s
2014 Jul 25	NTT/SofI	J_S	600s
2014 Aug 7 and 11−13	CAHA 3.5m/Omega2000	Y_{O2K}, J_{O2K}	600s
2014 Aug 22−24	CAHA 2.5m/CAFOS	i_w	1800s
2015 Feb 22	NTT/SofI	J_S	300s
2016 Jun 5−13	MPG 2.2m/GROND	g_G, r_G, i_G, z_G, J_G, H_G, K_G	1440s
2016 Sep 11−13	NTT/EFOSC2	I_E	900s
2016 Sep 16−25	MPG 2.2m/GROND	g_G, r_G, i_G, z_G, J_G, H_G, K_G	1440s
2016 Sep 18−21	du Pont/Retrocam	Y_{retro}	1200s

2.3.2 Spectroscopic follow-up of $z \gtrsim 6.44$ quasars

Once the high−redshift quasar nature of candidates is confirmed, we include them in our extensive campaign of follow-up observations aimed at characterizing quasars at the highest redshifts.

Here we present new optical/NIR spectroscopic data for nine quasars, the six objects newly discovered from PS1 and three sources from the literature (PSO006+39, PSO338+29 and HSC1205). These observations have been obtained with a variety of telescopes and spectrographs: VLT/FORS2, P200/DBSP, MMT/Red Channel, Magellan/FIRE, VLT/X-Shooter (Vernet et al., 2011), Keck/LRIS

(Oke et al. 1995 and Rockosi et al. 2010) and GNT/GNIRS (Dubbeldam et al., 2000). We take the remaining spectroscopic data from the literature. The details (i.e. observing dates, instruments, telescopes, exposure times and references) for all the spectra presented here are reported in Table 2.2. In case of multiple observations of one object, we use the weighted mean of the spectra. We scale the spectra to the observed J band magnitudes (see Table 2.3), with the exceptions of PSO006+39, for which we do not have this information, and PSO011+09 and PSO261+19, that only have optical spectral coverage; in these cases, we normalize the spectra to the $y_{\rm P1}$ magnitudes. We also correct the data for the Galactic extinction, using the extinction law provided by Calzetti et al., 2000. The reduced spectra are shown in Figure 2.3.

TABLE 2.2: Spectroscopic observations of the $z \gtrsim 6.5$ quasars presented in this study. We present optical/NIR spectra for all the newly discovered objects and for some known sources. We also gather data from the literature. The references are: (1) Venemans et al., 2013; (2) De Rosa et al., 2014, (3) Venemans et al., 2015b, (4) Chen et al., 2017, (5) Mortlock et al., 2011, and (6) this work.

Object	**Date**	**Telescope/Instrument**	**λ range** [μm]	**Exposure Time** [s]	**Slit Width**	**Reference**
PSO J006.1240+39.2219	2016 Jul 5	Keck/LRIS	0.55−1.1	1800	$1''.0$	(6)
PSO J011.3899+09.0325	2016 Nov 20	Magellan/FIRE	0.82−2.49	600	$1''.0$	(6)
	2016 Nov 26	Keck/LRIS	0.55−1.1	900	$1.''0$	(5)
VIK J0109–3047	2011 Aug-Nov	VLT/X-Shooter	0.56−2.48	21600	$0''.9-1''.5$	(1,2)
PSO J036.5078+03.0498	2015 Dec 22−29	VLT/FORS2	0.74−1.07	4000.	$1''.0$	(5)
	2014 Sep 4−6	Magellan/FIRE	0.82−2.49	8433	$0.''6$	(3)
VIK J0305–3150	2011 Nov −2012 Jan	Magellan/FIRE	0.82−2.49	26400	$0''.6$	(1,2)
PSO J167.6415–13.4960	2014 Apr 26	VLT/FORS2	0.74−1.07	2630	$1''.3$	(3)
	2014 May 30-Jun 2	Magellan/FIRE	0.82−2.49	12004	$0''.6$	(3)
ULAS J1120+0641	2011	GNT/GNIRS	0.90−2.48	–	$1''.0$	(5)
HSC J1205–0000	2016 Mar 14	Magellan/FIRE	0.82−2.49	14456	$0''.6$	(6)
PSO J183.1124+05.0926	2015 May 8	VLT/FORS2	0.74−1.07	2550	$1''.3$	(6)
	2015 Apr 6	Magellan/FIRE	0.82−2.49	11730	$0''.6$	(4,5)
PSO J231.6576–20.8335	2015 May 15	VLT/FORS2	0.74−1.07	2600	$1''.3$	(6)
	2015 Mar 13	Magellan/FIRE	0.82−2.49	9638	$0''.6$	(4,5)
PSO J247.2970+24.1277	2016 Mar 10	VLT/FORS2	0.74−1.07	1500	$1''.0$	(6)
	2016 Mar 31	Magellan/FIRE	0.82−2.49	6626	$0''.6$	(4,6)
PSO J261.0364+19.0286	2016 Sep 12	P200/DBSP	0.55−1.0	3600	$1''.5$	(6)
PSO J323.1382+12.2986	2015 Nov 5	VLT/FORS2	0.74−1.07	1500	$1''.0$	(6)
	2016 Aug 15	Magellan/FIRE	0.82−2.49	3614	$0''.6$	(6)
PSO J338.2298+29.5089	2014 Oct 19	MMT/Red Channel	0.67−1.03	1800	$1''.0$	(3)
	2014 Oct 30	Magellan/FIRE	0.82−2.49	7200	$0''.6$	(3)
	2014 Nov 27	LBT/MODS	0.51−1.06	2700	$1''.2$	(3)
VIK J2348–3054	2011 Aug 19−21	VLT/X-Shooter	0.56−2.48	8783	$0''.9-1''.5$	(1,2)

TABLE 2.3: PS1 PV3, $z_{\rm decam}$, J and *WISE* photometry and Galactic $E(B-V)$ values (from Schlegel, Finkbeiner, and Davis 1998) of the quasars analysed here. The limits are at 3σ significance. The $J-$band information is from (1) UKIDSS, (2) VHS, (3) Venemans et al., 2013, (4) Venemans et al., 2015b, (5) Matsuoka et al., 2016, (6) this work (in case we have follow up photometry on the quasar, we report the magnitude with the best S/N; see also Table 2.4). The $z_{\rm decam}$ information is taken from the last DECaLS DR3 release. The *WISE* data are from ALLWISE or, in case the object was present in DECaLS DR3, from the UNWISE catalog (Lang 2014 and Meisner, Lang, and Schlegel 2016). We note that the PS1 magnitudes of ULAS1120 are taken from the PV2 catalog, since the object is not detected in PV3, having S/N <5 in all bands. However, forced photometry on the $y_{\rm P1}$ PV3 stack image at the quasar position reveals a faint source with S/N=4.3. Also, the quasar HSC1205 does not appear in the PS1 PV3 catalog. The PS1 magnitudes are obtained by performing forced photometry on the $z_{\rm P1}$ and $y_{\rm P1}$ PV3 stacked images.

Name	$z_{\rm P1}$	$y_{\rm P1}$	$z_{\rm decam}$	J	$J_{\rm ref}$	$W1$	$W2$	$E(B-V)$
PSO J006.1240+39.2219	>23.02	20.06 ± 0.07	–	–	–	–	–	0.075
PSO J011.3899+09.0325	>22.33	20.60 ± 0.09	–	20.80 ± 0.13	(6)	20.19 ± 0.19	–	0.059
VIK J0109–3047	–	–	–	21.27 ± 0.16	(3)	20.96 ± 0.32	–	0.022
PSO J036.5078+03.0498	21.48 ± 0.12	19.30 ± 0.03	20.01 ± 0.01	19.51 ± 0.03	(4)	19.52 ± 0.06	19.69 ± 0.14	0.035
VIK J0305–3150	–	–	–	20.68 ± 0.07	(3)	20.38 ± 0.14	20.09 ± 0.24	0.012
PSO 167.6415–13.4960	>22.94	20.55 ± 0.11	–	21.21 ± 0.09	(4)	–	–	0.057
ULAS J1120+0641	>23.06	20.76 ± 0.19	22.38 ± 0.1	20.34 ± 0.15	(1)	19.81 ± 0.09	19.96 ± 0.23	0.052
HSC J1205–0000[10]	>22.47	>21.48	–	21.95 ± 0.21	(5)	19.98 ± 0.15	19.65 ± 0.23	0.0243
PSO J183.1124+05.0926	21.68 ± 0.10	20.01 ± 0.06	20.53 ± 0.02	19.77 ± 0.08	(6)	19.74 ± 0.08	20.03 ± 0.24	0.0173
PSO J231.6576–20.8335	>22.77	20.14 ± 0.08	–	19.66 ± 0.05	(6)	19.91 ± 0.15	19.97 ± 0.35	0.133
PSO J247.2970+24.1277	>22.77	20.04 ± 0.07	20.82 ± 0.03	20.23 ± 0.09	(6)	19.46 ± 0.04	19.28 ± 0.08	0.053
PSO J261.0364+19.0286	>22.92	20.98 ± 0.13	–	21.09 ± 0.18	(6)	20.61 ± 0.21	–	0.045
PSO J323.1382+12.2986	21.56 ± 0.10	19.28 ± 0.03	–	19.74 ± 0.03	(6)	19.06 ± 0.07	18.97 ± 0.12	0.108
PSO J338.2298+29.5089	>22.63	20.34 ± 0.1	21.15 ± 0.05	20.74 ± 0.09	(4)	20.51 ± 0.14	–	0.096
VIK J2348–3054	–	–	–	21.14 ± 0.08	(3)	20.36 ± 0.17	–	0.013

TABLE 2.4: Photometry from our follow-up campaigns for the newly discovered PS1 quasars; the limits are at 3σ. (see also Table 2.1 for a list of the observations).

Name	
PSO J011.3899+09.0325	i_G >23.36; z_G=22.38 ± 0.16; Y_{retro}=20.81 ± 0.07; J_G=20.80 ± 0.13
PSO J183.1124+05.0926	I_E=23.51 ± 0.21; Z_E=20.93 ± 0.09; J_S=19.77 ± 0.08
PSO J231.6576–20.8335	I_E >23.81; J_S=19.66 ± 0.05
PSO J247.2970+24.1277	i_w >22.36; i_{MMT} >22.69; z_{O2k}=20.89 ± 0.07; Y_{O2k}=20.04 ± 0.24; J_{O2k}=20.23 ± 0.09
PSO J261.0364+19.0286	i_G >23.40; I_E >24.01; z_G=22.18 ± 0.12; J_G=21.09 ± 0.18; H_G=20.92 ± 0.30
PSO J323.1382+12.2986	z_{O2k}=20.14 ± 0.05; Y_{O2k}=19.45 ± 0.07; J_S=19.74 ± 0.03

2.3.3 NOEMA observations

Four quasars in our sample (PSO323+12, PSO338+29, PSO006+39 and HSC1205) have been observed with the NOrthern Extended Millimeter Array (NOEMA): The NOEMA observations were carried out in the compact array configuration, for which the primary beam at 250 GHz is $\sim 20''$ (full width at half power). Data were processed with the latest release of the software clic in the GILDAS suite, and analyzed using the software mapping together with a number of custom routines written by our group.

PSO323+12 was observed in a Director's Discretionary Time program (project ID: E15AD) on 2015 December 28, with seven 15m antennae arranged in the 7D configuration. The source MWC349 was used for flux calibration, while the quasar 2145+067 was used for phase and amplitude calibration. The system temperature was in the range 110–160 K. Observations were performed with average precipitable water vapour conditions ($\sim$ 2.2 mm). The final cube includes 5159 visibilities, corresponding to 3.07 hr on source (7 antennas equivalent). After collapsing the entire 3.6 GHz bandwidth, the continuum rms is 0.146 mJy beam^{-1}.

PSO338+29 was observed on 2015 December 3 (project ID: W15FD) in the 7C array configuration. MWC349 was observed for flux calibration, while the quasar 2234+282 was targeted for phase and amplitude calibration. The typical system temperature was 85-115 K. Observations were carried out in good water vapour conditions (1.7-2.0 mm). The final data cube consists of 4110 visibilities, corresponding to 2.45 hr on source (7 antennas equivalent). The synthesized beam is $1''35 \times 0''69$. The rms of the collapsed data cube is 0.215 mJy beam^{-1}.

PSO006+39 was observed in two visits, on 2016 May 20 and 2016 July 7, as part of the project S16CO, with 5-7 antennae. The May visit was hampered by high precipitable water vapour ($\sim$3 mm) yielding high system temperature (200–300 K). The July track was observed in much better conditions, with precipitable water vapor (pwv) $\sim$ 1.3 mm and T_{sys}=105-130 K. The final cube consists of 2700 visibilities, corresponding to 2.25 hr on source (six antennas equivalent), with a continuum sensitivity of 0.178 mJy beam^{-1}. The synthesized beam is $1.19'' \times 0''61$.

HSC1205 was also observed as part of project S16CO, on 2016 October 29, using the full 8-antennae array. MWC349 was observed for flux calibration, while the quasar 1055+018 served as phase and amplitude calibrator. The precipitable water vapout was low ($\sim$ 1.3 mm), and the system temperature was 120-180 K. The final cube consists of 2489 visibilities, or 1.11 hr on source (8 antennae equivalent). The synthesized beam is $1.19'' \times 0''61$ and the continuum rms is 0.176 mJy beam^{-1}.

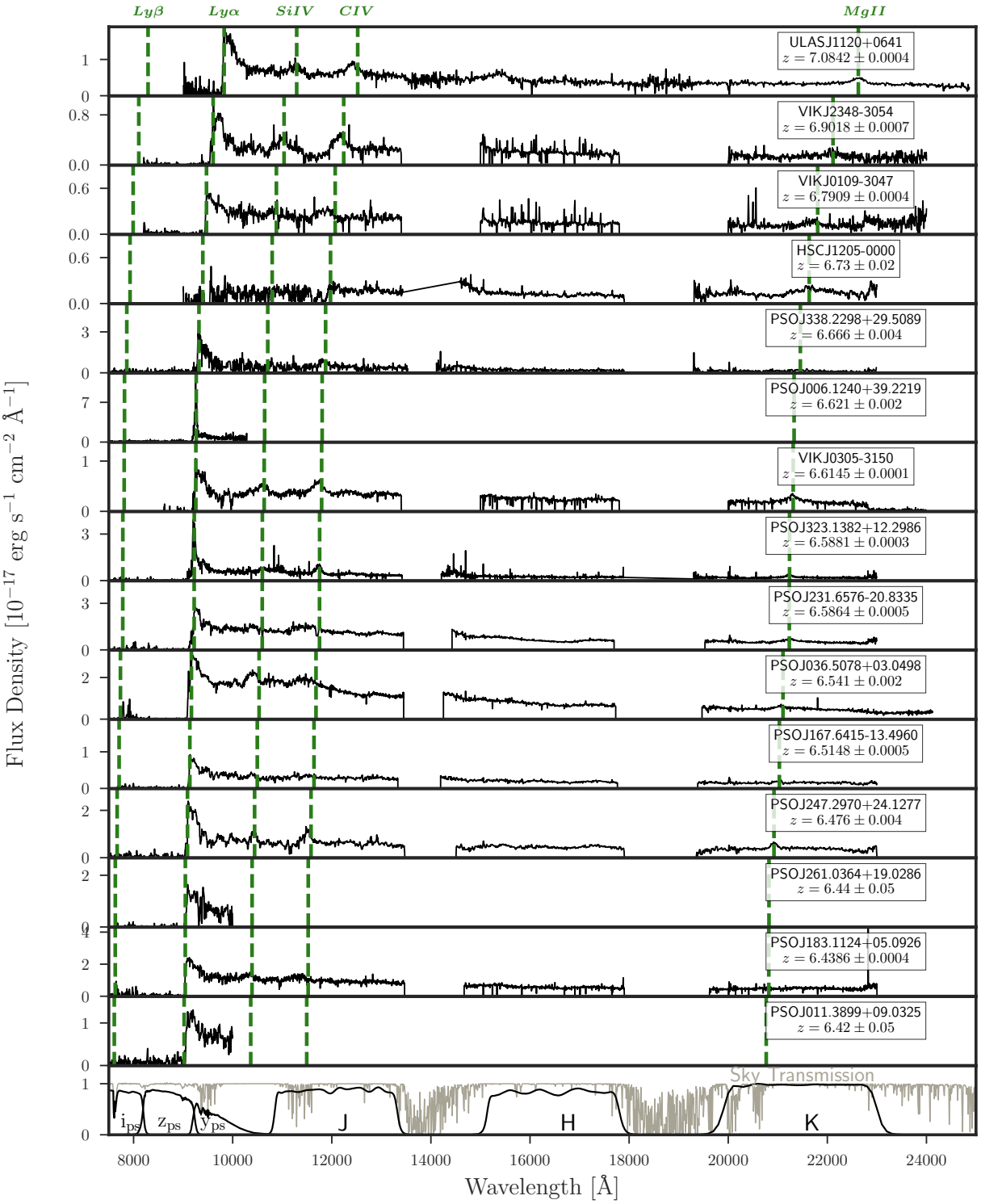

FIGURE 2.3: Binned spectra of the 15 $z \gtrsim 6.5$ quasars in the sample considered here. The quasars PSO323+12, PSO231-20, PSO247+24, PSO011+09, PSO261+19 and PSO183+05 are newly discovered from the PS1 PV3 survey; the other objects are taken from the literature (see Table 2.5). The locations of key emission lines (Lyβ, Lyα, Si IV, C IV and Mg II; see also Table 1.1) are highlighted with *dashed, green lines*.

2.4 Individual notes on six new quasars from PS1

We present six new quasars at $z \sim 6.5$ discovered from the PS1 survey: we here present brief observational summaries of each source.

PSO J011.3899+09.0325 @ z=6.42

Follow-up imaging data for PSO011+09 were acquired with MPG 2.2m/GROND and du Pont/Retrocam in September 2016; its quasar nature was confirmed with a short 600s low-resolution prism mode spectrum using Magellan/FIRE on 2016 November 20. We then obtained a higher S/N, higher resolution optical spectrum with Keck/LRIS. We consider in this work only the latter spectroscopic observation (see Figure 2.3) because the FIRE spectrum has a very limited S/N and over-exposed H and K bands. It is a relatively faint object, with $J_{\rm G}$=20.8, and presents a very flat $Y_{\rm retro} - J_{\rm G}$ color of 0.01 (see Table 2.4). This quasar does not show strong emission lines. Through a comparison with SDSS quasar templates (see Section 2.5.1), we calculate a redshift of $z = 6.42$, with an uncertainty of Δz=0.05.

PSO J183.1124+05.0926 @ z=6.4386

PSO183+05 was first followed up with the SofI and EFOSC2 instruments at the NTT, in February 2015. The discovery spectrum was taken with the Red Channel spectrograph at the MMT; higher quality spectra were later acquired with Magellan/FIRE and VLT/FORS2, in April and May 2015, respectively. Evidence was found for the presence of a very proximate Damped Lyman Absorber (DLA; $z \sim$6.404) along the same line-of-sight (see also Chen et al. 2017).

PSO J231.6576–20.8335 @ z=6.5864

The imaging follow-up for PSO231−20 was also undertaken with EFOSC2 and SofI at the NTT in February 2015. It was spectroscopically confirmed with Magellan/FIRE on the 2015 March 13, and we acquired a VLT/FORS2 spectrum on the 2015 May 15. With a $J-$band magnitude of 19.66, this quasar is the brightest newly discovered object, and one of the brightest known at $z > 6.5$, alongside with PSO036+03 and VDESJ0224-4711.

PSO J247.2970+24.1277 @ z=6.476

We acquired follow-up photometric observations of PSO247+24 with CAFOS and Omega2000 at the 2.2m and 3.5m telescope at CAHA, respectively. We confirmed its quasar nature with VLT/FORS2 in March 2016 and we obtained NIR spectroscopy with Magellan/FIRE in the same month. This quasar presents prominent broad emission lines (see Figure 2.3).

PSO J261.0364+19.0286 @ z=6.44

We used the 2.2m MPG/GROND and SofI at the NTT in June−September 2016 to acquire follow-up photometry for PSO261+19. Spectroscopic observations with the DBSP at the Palomar Observatory in September 2016 confirmed that the object is a quasar at $z = 6.44 \pm 0.05$ (redshift from SDSS quasar template fitting; see Section 2.5.1). Similar to PSO11+09, this is a relatively faint quasar, with $J_{\rm G} = 21.09$.

PSO J323.1382+12.2986 @ z=6.5881

Imaging follow-up of PSO323+12 was acquired with CAHA 3.5m/Omega2000 and NTT/SofI in August 2014 and February 2015, respectively. Spectroscopic observations with FORS2 at the VLT in December 2015 confirmed that the source is a high redshift quasar. The NIR spectrum was later obtained with Magellan/FIRE, in August 2016. This quasar is the one at the highest redshift among the newly discovered objects (z =6.5881; see Section 2.5.1) and presents another interesting case. In fact an additional object is present at a projected distance of only $\sim 1''$ from the quasar. Based on the photometric information at hands from the PS1 catalog, this source is most likely a galaxy at $z \sim 2$. Due to the very small projected distance, we might consider the hypothesis that the quasar is lensed by the foreground source. Assuming that this latter system is a massive object for which the Faber-Jackson relation holds, and whose dark matter potential is better described by a isothermal sphere, we obtain that $\sigma = \sigma* \sim 350$ km s^{-1}: the resulting Einstein radius is $\sim$1.38". This implies a magnification of $\sim$1.6. In case the lensing scenario would be confirmed, caution should be taken in calculating the quasar flux and interpreting its properties. In the following analysis, we although consider no magnification. A further accurate study of this system promise to shed new light on gas accretion onto high–z quasars (see Section 5.1.3).

2.5 Analysis

We next present a comprehensive study of the quasar population at the highest redshifts currently known ($z \gtrsim 6.42$). We consider a total sample of 15 quasars, six newly presented here and discovered in our search in the PS1 catalog (see Section 2.2 and 2.3) and 9 sources from the literature (one from UKIDSS, three from VIKING, four from PS1 and one from HSC). We report their coordinates, redshifts and discovery references in Table 2.5. Due to the variety of the data collected (e.g. we do not have NIR spectra or [CII] observations for all the objects in this work), we consider different sub-samples of quasars in the following sections, depending on the physical parameters that we could measure.

2.5.1 Redshifts

An accurate measurement of high$-z$ quasar systemic redshifts is challenging. Several techniques have been implemented, and previous studies have shown that redshift values obtained with different indicators often present large scatters or substantial shifts (e.g. De Rosa et al. 2014, Venemans et al. 2016).

In general, the most precise redshift indicators (with measurement uncertainties of $\Delta z < 0.004$) are the atomic or molecular narrow emission lines, originating from the interstellar medium of the quasar host galaxy. This emission, in particular the [CII] line, and the underlying, dust continuum emission is observable in the millimeter wavelength range at $z \sim 6$ (see Section 1.5). When available, we adopt $z_{[CII]}$ measurements for the objects in our sample (11 out of 15). We take advantage of our new NOEMA observations of four quasars (see Section 2.3.3) to estimate their systemic redshifts from the [CII]158 μm emission line. A flat continuum and a Gaussian profile are fitted to the spectra, as shown in Figure 2.4, allowing us to derive $z_{[CII]}$ for PSO006+39, PSO323+12 and PSO338+29. The frequency of the observations of HSC1205

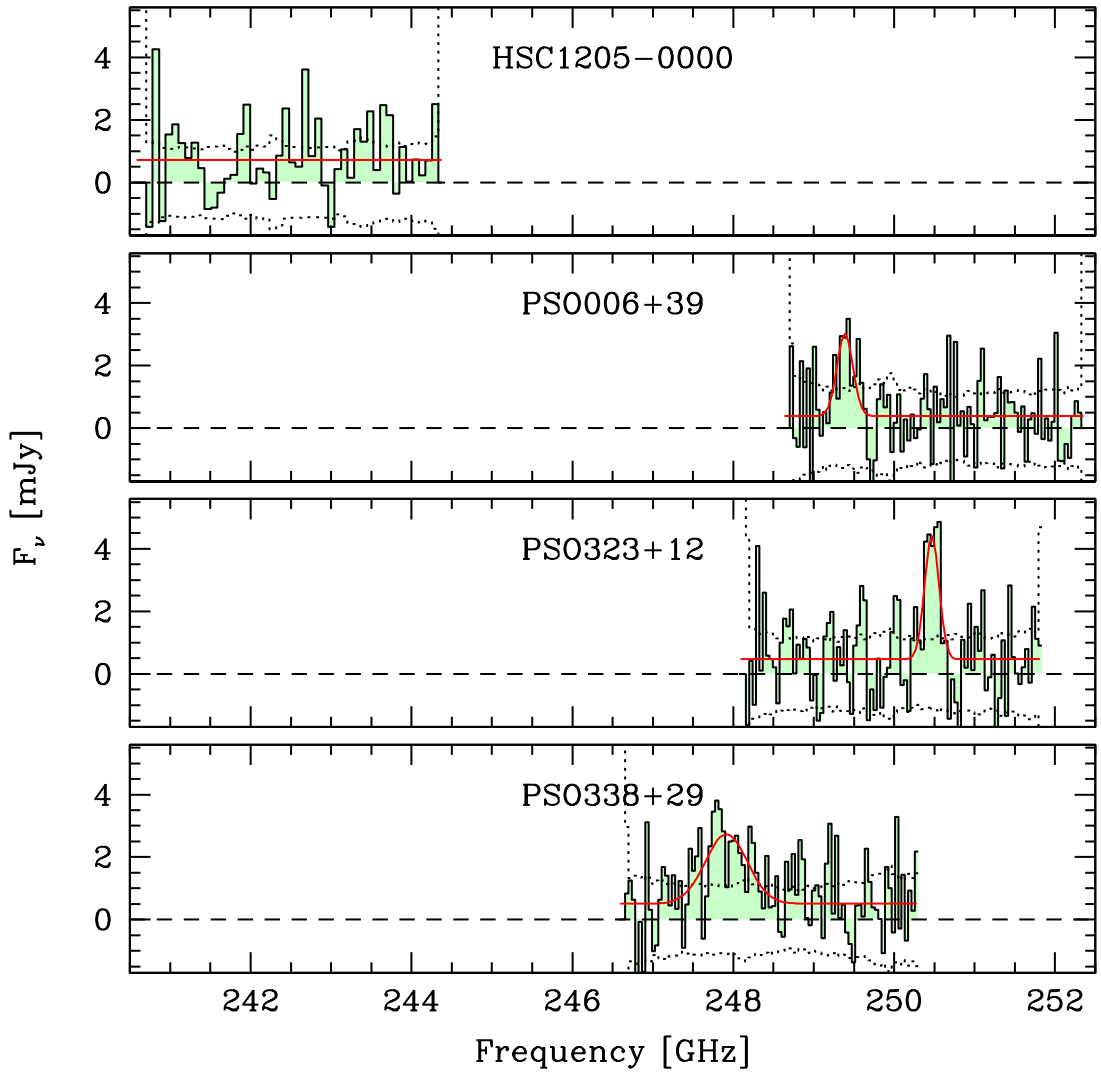

FIGURE 2.4: NOEMA 1.2 mm observations of the [CII]158 μm emission line and underlying dust continuum for four objects in our sample. The extracted spectra are fitted with a flat continuum and Gaussian function. We detect the [CII] emission for all the objects except HSC1205, whose observations were tuned based on the initial redshift range reported by Matsuoka et al., 2016: our Mg II emission line detection, consistent with the new redshift in Matsuoka et al., 2018a, positions its [CII] emission line out of the covered band (see text for details). We still detect the dust continuum from this quasar.

TABLE 2.5: Sample of quasars at $z \gtrsim 6.42$ considered in this study. The objects were discovered by several studies: (1) Mortlock et al., 2011, (2) Venemans et al., 2013, (3) Venemans et al., 2015b, (4) Matsuoka et al., 2016, (5) Tang et al., 2017 and (6) this work. In addition to this work (6), the redshifts measurements are taken from: (7) Venemans et al., 2012, (8) Venemans et al., 2016, (9) Bañados et al., 2015b, (10) Decarli et al., 2018.

Name	R.A.(J2000)	Decl. (J2000)	z	z_{err}	z method	Ref Discovery	Ref z
PSO J006.1240+39.2219	00:24:29.772	+39:13:18.98	6.621	0.002	[CII]	(5)	(6)
PSO J011.3899+09.0325	00:45:33.568	+09:01:56.96	6.42	0.05	template	(6)	(6)
VIK J0109–3047	01:09:53.131	–30:47:26.32	6.7909	0.0004	[CII]	(2)	(8)
PSO J036.5078+03.0498	02:26:01.876	+03:02:59.39	6.541	0.002	[CII]	(3)	(9)
VIK J0305–3150	03:05:16.916	–31:50:55.90	6.6145	0.0001	[CII]	(2)	(8)
PSO J167.6415–13.4960	11:10:33.976	–13:29:45.60	6.5148	0.0005	[CII]	(3)	(10)
ULAS J1120+0641	11:20:01.479	+06:41:24.30	7.0842	0.0004	[CII]	(1)	(7)
HSC J1205–0000	12:05:05.098	–00:00:27.97	6.73	0.02	Mg II	(4)	(6)
PSO J183.1124+05.0926	12:12:26.981	+05:05:33.49	6.4386	0.0004	[CII]	(6)	(10)
PSO J231.6576–20.8335	15:26:37.841	–20:50:00.66	6.5864	0.0005	[CII]	(6)	(10)
PSO J247.2970+24.1277	16:29:11.296	+24:07:39.74	6.476	0.004	Mg II	(6)	(6)
PSO J261.0364+19.0286	17:24:08.743	+19:01:43.12	6.44	0.05	template	(6)	(6)
PSO J323.1382+12.2986	21:32:33.191	+12:17:55.26	6.5881	0.0003	[CII]	(6)	(6)
PSO J338.2298+29.5089	22:32:55.150	+29:30:32.23	6.666	0.004	[CII]	(3)	(6)
VIK J2348–3054	23:48:33.334	–30:54:10.24	6.9018	0.0007	[CII]	(2)	(8)

was tuned for a redshift of z =6.85, in the range of redshifts originally reported in the discovery paper (Matsuoka et al., 2016). No [CII] emission line is detected from the quasar, possibly due to our frequency tuning not being centered on the true redshift of the source. This scenario is supported by our own new NIR observations of the Mg II line, which place HSC1205 at $z = 6.73 \pm 0.02$ (see below, Table 2.5 and Section 2.5.5). This is also consistent with the new redshift reported in Matsuoka et al. (2018; z=6.75). At this redshift, the [CII] emission line falls at an observed frequency of 245.87 GHz, outside the range probed in the NOEMA data (see top panel of Figure 2.4). The redshifts of PSO231-20, PSO167-13 and PSO183+05 are measured from the [CII] line, observed in our ALMA survey of cool gas and dust in $z \gtrsim 6$ quasars (Decarli et al. 2018). We take the values of $z_{[CII]}$ for ULAS1120, VIK2348, VIK0109, VIK0305 and PSO036+03 from the literature (Venemans et al. 2012, 2016, Bañados et al. 2015b).

The second best way to estimate redshifts is through the low-ionization Mg II broad emission line, which is observable in the $K-$band at $z >$6. This radiation is emitted from the BLR, and therefore it provides a less precise measurement than the narrow emission from the cool gas traced by the [CII] emission. Several studies, based on $z <$1 quasar samples, demonstrated that the Mg II emission is a far more reliable redshift estimator than other high-ionization emission lines (e.g. C IV and Si IV; see Table 1.1), and it has a median shift of only 97 $\pm$ 269 km s^{-1} with respect to the narrow [O III] λ5008.24 Å emission line (Richards et al., 2002). We provide z_{MgII} for HSC1205 and PSO247+24, for which we have no [CII] observations, as their best redshift estimates. We also calculate z_{MgII} for the remaining 9 quasars in our sample with NIR spectra (see Section 2.5.5 and Table 2.7). Our new values are consistent, within 1σ uncertainties, with the measurements from the literature for ULAS1120, VIK2348, VIK0109, VIK0305 (De Rosa et al., 2014), and PSO036+03, PSO167-13, PSO338+29 (Venemans et al. 2015b).

It has been recently shown that, at $z \gtrsim$6, the mean and standard deviation of the shifts between z_{MgII} and the quasar systemic redshift (as derived from the [CII] emission line), are significantly larger (480 $\pm$ 630 km s^{-1}) than what is found at low$-$redshift (see Venemans

et al. 2016). We can study the distribution of the shifts between the redshifts measured from Mg II and [CII] (or CO) emission lines, considering both the newly discovered and/or newly analyzed sources in this sample, and quasars at $z \gtrsim 6$ with such information from the literature (six objects; the values of $z_{\rm MgII}$ are taken from Willott et al. 2010a and De Rosa et al. 2011, while the $z_{\rm [CII]}$ measurements are from Carilli et al. 2010, Wang et al. 2011, Willott, Omont, and Bergeron 2013, 2015). The distribution of the shifts is shown in Figure 2.5. They span a large range of values, from +2300 km s^{-1} to -265 km s^{-1}. We obtain a mean and median of 485 and 270 km s^{-1}, respectively, and a large standard deviation of 717 km s^{-1}. These results are in line with what was found by Venemans et al., 2016, although we measure a less extreme median value (270 km s^{-1} against 467 km s^{-1}), and confirm that the Mg II emission line can be significantly blueshifted with respect to the [CII] emission in high−redshift quasars. This effect is unlikely to be due to the infalling of [CII] in the quasars' host galaxies: indeed, the gas free-fall time would be too short (∼few Myr, considering a typical galactic size of ∼2kpc and gas mass of $\sim 10^8$ M$_\odot$, e.g. Venemans et al. 2016) to allow the ubiquitous observation of [CII] in quasars at these redshifts. An alternative scenario explaining the detected blueshifts would be that the BLRs in these quasars are characterized by strong outflows/wind components (see also Section 2.5.4 for a further discussion on this point).

Finally, for PSO261+19 and PSO011+09, only the optical spectra are available. We derive their redshifts from a χ^2 minimization technique, comparing their spectrum with the low redshift quasar template from Selsing et al., 2016, and the composite of $z \sim 6$ quasars presented by Fan et al., 2006; for further details on this procedure see Bañados et al., 2016. The redshift measurements obtained in this case are the most uncertain, with Δz=0.05.
We report all the redshifts, their uncertainties, the different adopted techniques and references in Table 2.5.

2.5.2 Absolute magnitude at 1450Å

The apparent magnitude at rest-frame 1450 Å (m_{1450}) is a quantity commonly used in characterizing quasars. Following Bañados et al., 2016, we extrapolate m_{1450} from the J-band magnitude, assuming a power law fit of the continuum ($f \sim \lambda^{-\alpha}$), with $\alpha = -1.7$ (Selsing et al., 2016)[11]. We derive the corresponding absolute magnitude (M_{1450}) using the redshifts reported in Table 2.5. In Figure 2.6 we show the distribution of M_{1450}, a proxy of the UV-rest frame luminosity of the quasars, as a function of redshift, for the sources in our sample and a compilation of quasars at $5.5 \lesssim z \lesssim 6.4$ (see references in Bañados et al. 2016, Table 7, and Section 1.5). The highest-redshift objects considered here show similar luminosities to the ones at $z \sim 6$. In Table 2.6 we report the values of m_{1450} and M_{1450} for the quasars analyzed here.

2.5.3 Quasar continuum

The UV/optical rest-frame quasar continuum emission results from the superposition of multiple components: the non-thermal, power law emission from the accretion disk (see Section 1.4.2); the stellar continuum from the host galaxy; the Balmer pseudo-continuum; and the pseudo-continuum due to the blending of several broad Fe II and Fe III emission lines. In the

[11] For PSO006+39 we use the $y_{\rm P1}$−band magnitude, since we do not have J−band information.

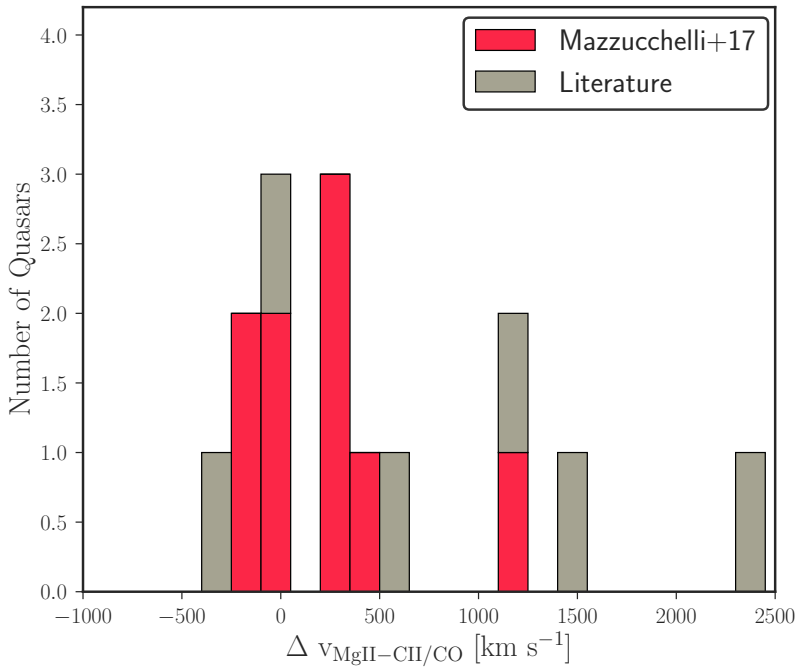

FIGURE 2.5: Difference between the velocity measurements obtained from Mg II and [CII] or CO emission lines for a sample of $z \gtrsim 6$ quasars. We consider 9 objects in this work for which we have both measurements (*red histogram*; see Tables 2.5 and 2.7) and six quasars from the literature (*grey histogram*; see text for references). The positive sign indicates the blueshift of the Mg II emission line. The offsets span a large range of values, with a mean and standard deviation of 485 $\pm$ 717 km s^{-1}, consistent with the results obtained by Venemans et al., 2016.

literature, the continua of very luminous quasars such as the ones studied here, have been generally reproduced with a simple power-law, since the host galaxy emission is outshone by the radiation from the central engine (see Section 1.5). Here, we first model the continuum with a single power law:

$$F_\lambda = F_0 \left(\frac{\lambda}{2500} \right)^\alpha \tag{2.11}$$

We consider regions of the rest-frame spectra which are free from strong emission lines: [1285−1295; 1315−1325; 1340−1375; 1425−1470; 1680−1710; 1975−2050; 2150−2250; and 2950−2990] Å (Decarli et al. 2010). We slightly adjust these windows to take into account sky absorption, residual sky emission and regions with low S/N. We use a χ^2 minimization technique to derive the best values and corresponding uncertainties for α and F_0 (see Table 2.6).

Vanden Berk et al., 2001 and Selsing et al., 2016 report typical slopes of $\alpha = -1.5$ and -1.7, respectively, for composite templates of lower redshift ($z \sim 2$) SDSS quasars. In our case, we find that α may significantly vary from object to object, with a mean of $\alpha = -1.6$ and a 1σ dispersion of 1.0. This large range of values is in agreement with previous studies of lower−redshift quasars ($z < 3$, Decarli et al. 2010; $4 \lesssim z \lesssim 6.4$, De Rosa et al. 2011, 2014). However, we notice that the quasars for which we only have optical spectral information are poorly reproduced by a power-law model, and the slopes obtained are characterized by large uncertainties (see Table 2.6). If we consider only the objects with NIR spectroscopy, we obtain a mean slope of $\alpha = -1.2$, with a 1σ scatter of 0.4.

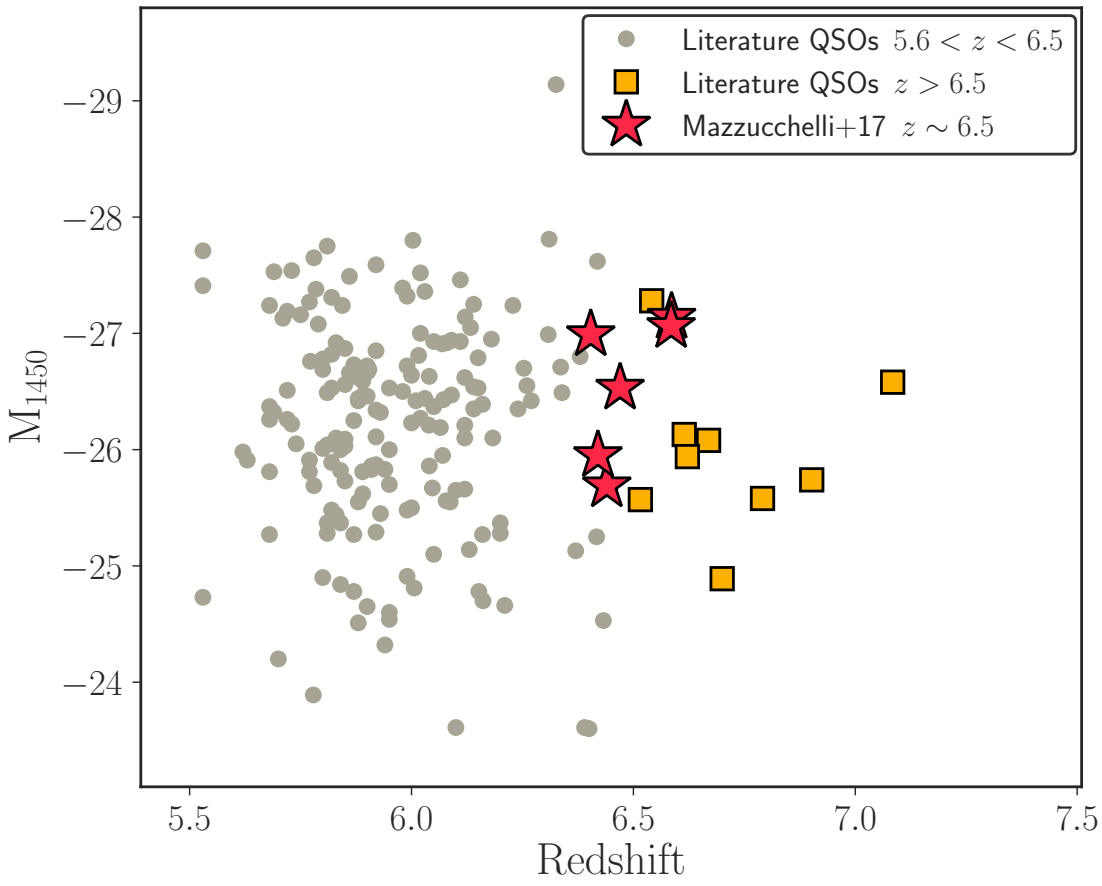

FIGURE 2.6: Absolute magnitude at rest frame wavelength 1450 Å, M_{1450}, against redshift, for quasars at $5.5 \lesssim z \lesssim 6.4$ from the literature (*grey circles*; see Section 1.5 and Bañados et al. 2016, Table 7, for references), and in the sample considered here, both taken from the literature (for references see Table 2.5; *yellow squares*) and newly discovered in this work (*red stars*). All the M_{1450} values were derived with a consistent methodology (see text). The magnitudes of the quasars presented here span a similar range as the ones at lower redshits.

We use these power law continuum fits in the modeling of the C IV broad emission line in our quasars with NIR coverage (see Section 2.5.4). Afterwards, we implement a more accurate modeling of the spectral region around the Mg II emission line, which, together with the Fe II emission and the rest-frame UV luminosity, is a key tool commonly used to derive crucial quasar properties, e.g. black hole masses (see Sections 1.4.3 and 2.5.6).

TABLE 2.6: Parameters (slope and normalization) obtained from the power law fit of the spectra in our quasar sample (see Section 2.5.3, eq. 2.11). We report also: the apparent and absolute magnitude at rest frame wavelenght 1450 Å (Section 2.5.2, plotted as a function of redshift in Figure 2.6); the C IV blueshifts with respect to the Mg II emission lines; the rest-frame C IV EW (Section 2.5.4).

Name	α	F_0 $[10^{-17}$erg s^{-1} cm$^{-2}]$	m_{1450}	$\mathbf{M_{1450}}$	$\Delta v_{\mathbf{CIV-MgII}}$ [km s^{-1}]	**C IV EW** [Å]
PSO J006.1240+39.2219	-3.92± 0.03	$0.060^{+1.86}_{-4.006}$	20.00	25.94[12]	–	–
PSO J011.3899+09.0325	$-3.75^{+3.91}_{-0.01}$	$0.051^{+0.06}_{-0.001}$	20.85	-25.95	–	–
VIK J0109–3047	$-0.96^{+2.71}_{-0.04}$	$0.141^{+0.09}_{-0.075}$	21.30	-25.58	4412±175	14.9±0.1
PSO J036.5078+03.0498	$-1.61^{+0.03}_{-0.07}$	0.610±0.05	19.55	-27.28	5386±689	41.5±1.1
VIK J0305–3150	$-0.84^{+0.02}_{-0.04}$	0.203±0.005	20.72	-26.13	2438±137	40.5±0.3
PSO J167.6415–13.4960	$-0.99^{+1.12}_{-0.68}$	$0.176^{+0.055}_{-0.175}$	21.25	-25.57	-	-
ULAS J1120+0641	$-1.35^{+0.24}_{-0.22}$	$0.248^{+0.086}_{-0.011}$	20.38	-26.58	2602±285	48.1±0.7
HSC J1205–0000	$-0.61^{+0.01}_{-0.48}$	$0.131^{+0.075}_{-0.275}$	21.98	-24.89	–	–
PSO J183.1124+05.0926	$-1.19^{+0.13}_{-0.15}$	$0.523^{+0.02}_{-0.05}$	19.82	-26.99	–	–
PSO J231.6576–20.8335	-1.59±0.06	$0.504^{+0.003}_{-0.075}$	19.70	-27.14	5861±318	23.0±1.2
PSO J247.2970+24.1277	$-0.926^{+0.15}_{-0.21}$	$0.350^{+0.102}_{-0.005}$	20.28	-26.53	2391±110	29.1±0.7
PSO J261.0364+19.0286	$-2.01^{+1.11}_{-0.01}$	$0.166^{+0.182}_{-0.024}$	21.12	-25.69	–	–
PSO J323.1382+12.2986	$-1.38^{+0.20}_{-0.18}$	$0.227^{+0.005}_{-0.115}$	19.78	-27.06	736±42	19.9±0.2
PSO J338.2298+29.5089	$-1.98^{+0.87}_{-0.60}$	$0.147^{+0.035}_{-0.055}$	20.78	-26.08	842±170	40.6±0.8
VIK J2348–3054	$-0.65^{+1.4}_{-0.6}$	$0.155^{+0.115}_{-0.134}$	21.17	-25.74	1793±110	45.8±0.3

2.5.4 C IV blueshifts

The peaks of high-ionization, broad emission lines, such as C IV, show significant shifts bluewards with respect to the systemic redshifts in quasars at low−redshift (e.g. Richards et al. 2002): this has been considered a signature of outflows and/or of an important wind component in quasars BLRs (e.g. Leighly 2004). Hints have been found of even more extreme blueshifts at high redshifts (e.g. De Rosa et al. 2014).

Here, we investigate the presence of C IV shifts in our high−redshift quasars by modeling the emission line with a single Gaussian function, after subtracting the continuum power law model obtained in Section 2.5.3 from the observed spectra. We report the computed C IV shifts with respect to the Mg II emission line in Table 2.6. We consider here the Mg II and not the [CII] line since we want to consistently compare our high−redshift sources to $z \sim 1$ quasars, for which the [CII] measurements are not always available. We adopt a positive sign for blueshifts. All quasars in our sample show significant blueshifts, from ∼730 to ∼5900 km s^{-1}. For the previously studied case of ULAS1120, the value found here is consistent with the ones reported in the literature (De Rosa et al. 2014, Greig et al. 2017). We neglect here: PSO167-13 and HSC1205, due to the low S/N; PSO183+05, for which we do not have a measurement of the Mg II redshift (see Section 2.5.5); and PSO011+09, PSO006+39 and PSO261+19, since we do not have NIR spectral coverage (see Section 2.3 and Figure 2.3); also, we include VIK2348, but with the

caveat that this object was flagged as a possible broad absorption line (BAL) quasar (De Rosa et al., 2014).

In Figure 2.7 we show the distribution of the blueshifts for high−redshift quasars in this work (*bottom panel*) and for a sample of objects at lower redshift taken from the SDSS−DR7 catalog (Shen et al. 2011; *upper panel*). For comparison, we select a subsample of objects at low redshift, partially following Richards et al., 2011. We consider quasars in the redshift range $1.52 < z < 2.2$ (where both the C IV and Mg II emission lines are covered), with significant detection of the broad C IV emission line ($\mathrm{FWHM_{C\,IV}} > 1000$ km s^{-1}; $\mathrm{FWHM_{C\,IV}} > 2\sigma_{\mathrm{FWHM_{C\,IV}}}$; $\mathrm{EW_{C\,IV}} > 5$ Å, $\mathrm{EW_{C\,IV}} > 2\sigma_{\mathrm{EW_{C\,IV}}}$; where σ_{FWHM} and σ_{EW} are the uncertainties on the FWHM and EW, respectively), and of the Mg II emission line ($\mathrm{FWHM_{Mg\,II}} > 1000$ km s^{-1}; $\mathrm{FWHM_{Mg\,II}} > 2\sigma_{\mathrm{FWHM_{Mg\,II}}}$; $\mathrm{EW_{Mg\,II}} > 2\sigma_{\mathrm{EW_{Mg\,II}}}$), and that are not flagged as BAL quasars (BAL FLAG=0). The total number of objects is ∼22700; the mean, median and standard deviation of the C IV blueshift with respect to the Mg II emission line in this lower−redshift sample are 685, 640 and 871 km s^{-1}, respectively. If we consider a sub sample of the brightest quasars (with luminosity at rest-frame wavelength 1350 Å $L_{\lambda,1350} > 3 \times 10^{46}$ erg s^{-1}; 1453 objects), we recover a higher mean and median values (994 and 930 km s^{-1}, respectively), but with large scatter (see Figure 2.7). We also draw a sub-sample of SDSS quasars matched to the $L_{\lambda,1350}$ distribution of the high−redshift sample (for details on the method with which we build this matched subsample, see Section 2.5.6). In this case, the mean and median values of the C IV blueshift are 790 and 732 km s^{-1}, respectively, with a standard deviation of 926 km s^{-1}. The high−redshift quasar population is characterized by a mean, median and standard deviation of 2940, 2438 and 1761 km s^{-1}; C IV blueshifts tend to be much higher at high−redshift, as already observed for the Mg II shifts with respect to the systemic quasars redshifts traced by CO/[CII] emission (see Section 2.5.1 and Figure 2.5).

In Table 2.6 we report the values of C IV rest-frame EW of the quasars in the sample of this work, which are plotted as a function of C IV blueshifts, together with objects at low−redshift, in Figure 2.8. Richards et al., 2011 show that C IV blueshifts correlate with C IV EW at $z \sim 1-2$: quasars with large EW are characterized by small blueshifts, while objects with small EW present both large and small blueshifts; no objects where found with strong C IV line and high blueshift. The high redshift quasars studied here follow the trend of the low−redshift objects, with extreme C IV blueshifts and EW equal or lower than the bulk of the SDSS sample. This is also in line with the higher fraction of weak emission line (WEL) quasars found at high redshifts (e.g. Bañados et al. 2014, 2016).

However, we note that C IV blueshifts scale with quasars UV luminosities: this is linked to the anti-correlation between luminosity and emission lines EW (i.e. Baldwin effect; e.g. Baldwin 1977, Richards et al. 2011). Also, the $z \gtrsim 6.5$ quasars presented here are biased towards higher luminosities (e.g. due to our selection criteria): we may then be considering here only the extreme cases of the highest redshift quasar population, and therefore missing the objects at lower luminosity and lower C IV blueshifts.

2.5.5 Mg II and Fe II emission modeling

We fit the quasar emission, in the rest-frame wavelength window $2100 < \lambda/[\text{Å}] < 3200$, as a superposition of multiple components:

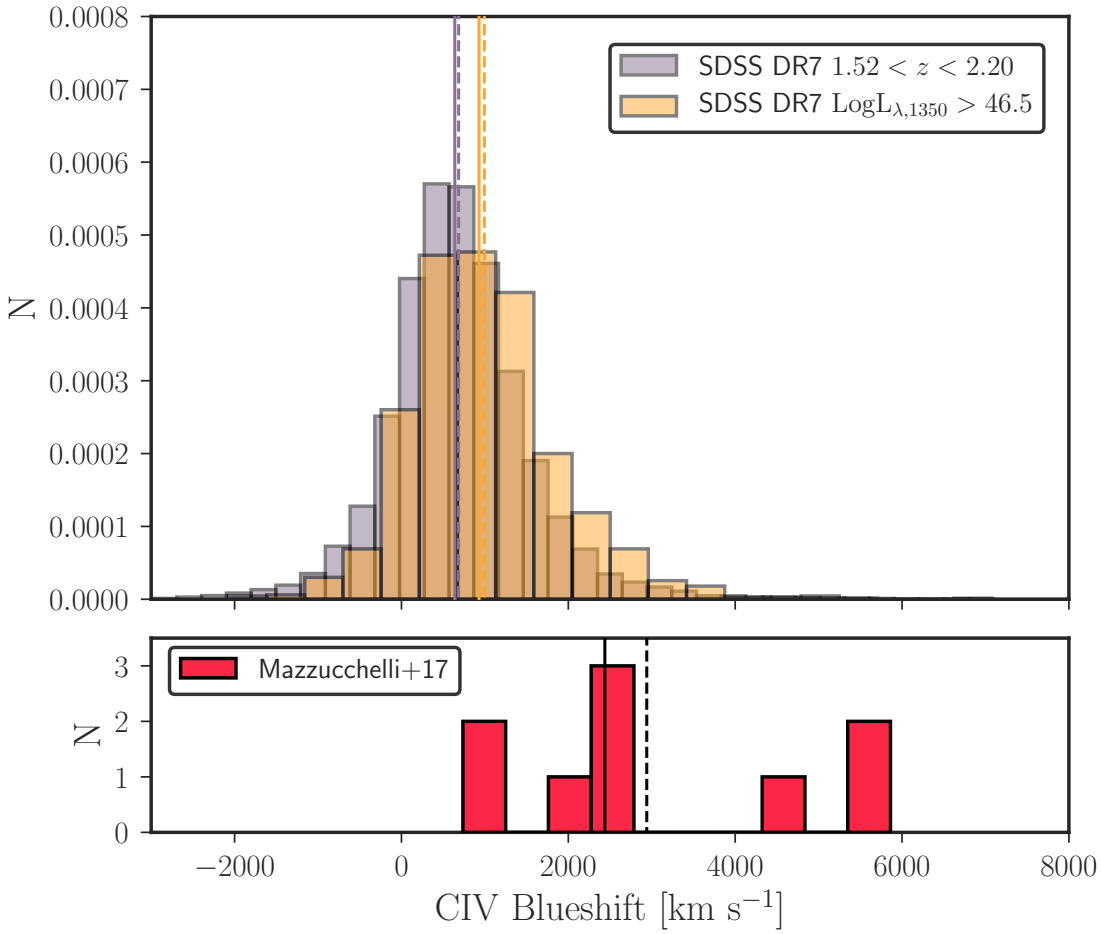

FIGURE 2.7: Histogram of C IV blueshifts with respect to the Mg II emission line, for the objects in our sample (*bottom panel*, *red histogram*) and a collection of $1.52 < z < 2.2$ quasars from the SDSS DR7 catalog (*upper panel*, *grey histogram*; see text for details). A sub-sample of low redshift quasars with higher luminosities ($L_{\lambda,1350} > 3 \times 10^{46}$ erg s^{-1}) is also reported (*orange histogram*). We adopt positive signs for blueshifts. The mean and median of the distributions are reported with *continuous* and *dashed lines*, respectively. Quasars at high redshift show much higher C IV blueshifts (with values up to ∼5900 km s^{-1}) with respect to the sample at lower redshift. The histograms reported in the upper panel are normalized such that the underlying area is equal to one.

- the quasar nuclear continuum emission, modeled as a power law (see eq. 2.11, and Section 1.4.2);
- the Balmer pseudo-continuum, modeled with the function provided by Grandi (1982; see their Eq 7) and imposing that the value of the flux at $\lambda_{\rm rest}$ =3675 Å is equal to 10% of the power law continuum contribution at the same wavelength;
- the pseudo-continuum Fe II emission, for which we use the empirical template by Vestergaard and Wilkes, 2001; and
- the Mg II emission line, fitted with a single Gaussian function.

We use a χ^2 minimization routine to find the best fitting parameters (slope and normalization) for the nuclear emission, together with the best scaling factor for the iron template; once we have subtracted the best continuum model from the observed spectra, we fit the Mg II emission

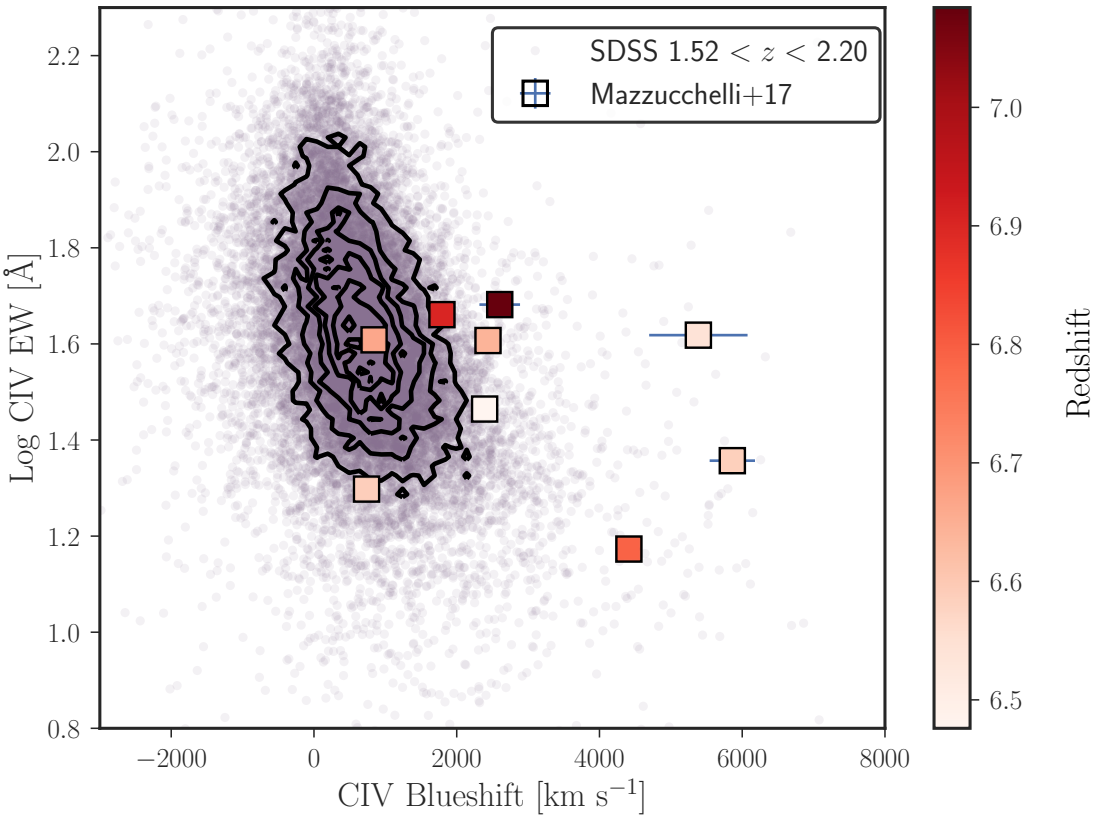

FIGURE 2.8: Rest frame C IV EW as a function of C IV blueshift, for the quasars in our sample (*big squares* color-coded with respect to redshifts) and a sample of quasars at lower redshift from SDSS DR7 (Shen et al. 2011; *grey points* and *black contours*; see text for details on the definition of this sub-sample). Quasars at low−redshift with very high blueshifts have small EW. The high redshift quasars are characterized by extreme blueshifts and small C IV EW, following the trend at $z \sim 1$ but with larger scatter.

line (see for further details Decarli et al. 2010). We apply this routine to all the quasars with NIR information in our sample. We exclude PSO183+05 from this analysis, since this source is a weak emission line quasar (see Figure 2.3) and the Mg II fit is highly uncertain.

We show the obtained fit for the 11 remaining objects in Figure 2.9. In Table 2.7, we list the derived monochromatic luminosities at rest-frame $\lambda_{\rm rest}$ =3000 (λL_{3000}), calculated from the continuum flux ($F_{\lambda,3000}$); the properties of the Mg II line (FWHM and flux); the flux of the Fe II emission and the redshift estimates $z_{\rm Mg\,II}$. We consider the 14th and 86th interquartiles of the χ^2 distribution as our 1σ confidence levels.

De Rosa et al., 2014 applied a similar analysis to the spectra of ULAS1120, VIK0305, VIK0109, VIK2348; their fitting procedures is however slightly different, since they fit all the spectral components at once, using the entire spectral range. Also, Venemans et al., 2015b analyzed the NIR spectra of PSO036+03, PSO338+29 and PSO167-13, considering solely the nuclear continuum emission fitted with a power law and modeling the Mg II emission line with a Gaussian function. The estimates that both studies obtain for $z_{\rm Mg\,II}$, black hole masses and bolometric luminosities are consistent, within the uncertainties, with the ones found here (see also Section 2.5.6 and Table 2.8).

TABLE 2.7: Quantities derived from the fit of the spectral region around the Mg II emission line: the monochromatic luminosity at rest-frame wavelength 3000 Å (λL_{3000}); FWHM, flux and redshift estimates of the Mg II line, and the Fe II flux.

Name	λL_{3000} $[10^{46}\mathrm{erg\,s^{-1}}]$	**MgII FWHM** $[\mathrm{km\,s^{-1}}]$	**MgII Flux** $[10^{-17}\mathrm{erg\,s^{-1}\,cm^{-2}}]$	**FeII Flux** $[10^{-17}\mathrm{erg\,s^{-1}\,cm^{-2}}]$	z_{MgII}
VIK J0109–3047	$1.0^{+0.1}_{-0.8}$	4313^{+606}_{-560}	$22.5^{+6.8}_{-6.2}$	$45^{+125}_{-0.15}$	6.763 ± 0.01
PSO J036.5078+03.0498	$3.9^{+0.4}_{-1.2}$	4585^{+691}_{-461}	$59.4^{+11.8}_{-9.2}$	147^{+221}_{-81}	$6.533^{+0.01}_{-0.008}$
VIK J0305–3150	$1.5^{+0.2}_{-0.7}$	3210^{+450}_{-293}	$41.0^{+7.2}_{-5.0}$	42^{+124}_{-15}	$6.610^{+0.006}_{-0.005}$
PSO J167.6415–13.4960	$0.9^{+0.3}_{-0.4}$	2071^{+211}_{-354}	$8.2^{+1.4}_{-0.8}$	<201	6.505 ± 0.005
ULAS J1120+0641	$3.6^{+0.4}_{-1.4}$	4258^{+524}_{-395}	$58.5^{+9.3}_{-7.8}$	61^{+225}_{-8}	$7.087^{+0.007}_{-0.009}$
HSC J1205–0000	$0.7^{+0.3}_{-0.4}$	8841^{+3410}_{-288}	$49.8^{+5.9}_{-52.4}$	< 182	$6.73^{+0.01}_{-0.02}$
PSO J231.6576–20.8335	$3.7^{+0.7}_{-0.9}$	4686^{+261}_{-1800}	$87.6^{+9.0}_{-28.2}$	216^{+204}_{-128}	$6.587^{+0.012}_{-0.008}$
PSO J247.2970+24.1277	$3.4^{+0.1}_{-1.5}$	1975^{+312}_{-288}	$40.2^{+4.4}_{-5.8}$	$54^{+234}_{-0.2}$	6.476 ± 0.004
PSO J323.1382+12.2986	$1.6^{+0.1}_{-1.0}$	3923^{+446}_{-380}	$45.9^{+7.4}_{-7.2}$	85^{+109}_{-45}	$6.592^{+0.007}_{-0.006}$
PSO J338.2298+29.5089	$0.8^{+0.4}_{-0.2}$	6491^{+543}_{1105}	$47.7^{+7.0}_{-9.0}$	76^{+44}_{-54}	$6.66^{+0.02}_{-0.01}$
VIK J2348–3054	$0.9^{+0.4}_{-0.3}$	5444^{+470}_{-1079}	$44^{+8.2}_{-8.5}$	95^{+41}_{-72}	6.902 ± 0.01

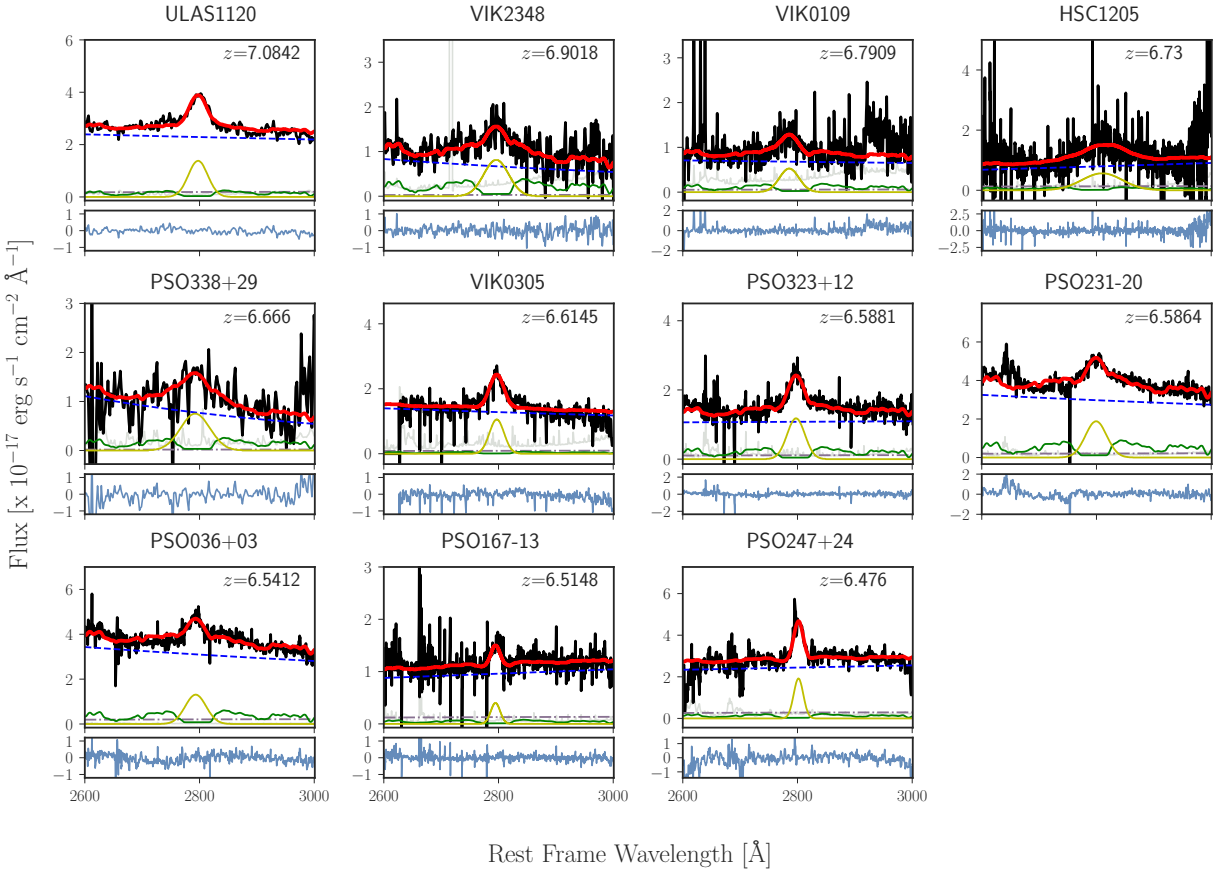

FIGURE 2.9: Best fit of the spectral region around the Mg II emission lines for the quasars in our sample for which we have K-band spectroscopy. We show the different components of the fit: the power law continuum (*dashed blue*), the Balmer (*brown dot-dashed*) and the Fe II pseudo-continuum emission (*solid green*) and the gaussian Mg II emission line (*yellow solid line*); the total fit is reported with a *solid red line*. In the *bottom panels* we show the residuals of the fit. The derived quantities are listed in Table 2.7.

2.5.6 Black Hole Masses

We can estimate the quasar black hole masses ($M_{\rm BH}$) from our single epoch NIR spectra using the broad Mg II emission line, $\lambda L_{\lambda,3000}$, and following Vestergaard and Osmer, 2009 (see Section 1.4.3 and eq. 1.29). We can also estimate the Eddington luminosity, using eq. 1.25, and the Eddington ratio (see Section 1.4.2). We calculate $L_{\rm bol}$ using the bolometric correction by Shen et al., 2008:

$$\frac{L_{\rm bol}}{\rm erg\,s^{-1}} = 5.15 \times \frac{\lambda L_{\lambda,3000}}{\rm erg\,s^{-1}} \tag{2.12}$$

The obtained values of black hole masses, bolometric luminosities and Eddington ratios for the quasars in our sample are shown in Table 2.8.

We notice that HSC1205, the faintest object in the sample, presents a very broad Mg II emission line: this leads to a high black hole mass ($\sim 5\times10^9$ M$_\odot$) and a low Eddington ratio of 0.06. However, HSC1205 is also characterized by a red $J-W1$ color of 1.97, suggesting that the quasar has a red continuum, due to internal galactic extinction. This could affect our measurement of the quasar intrinsic luminosity and therefore we could observe a value of the Eddington ratio lower than the intrinsic one. We test this hypothesis by comparing the observed photometric information of this source with a suite of quasar spectral models characterized by different values of internal reddening $E(B-V)$. We obtain these models by applying the reddening law by Calzetti et al., 2000 to the low−redshift quasar spectral template by Selsing et al., 2016, redshifted at $z = 6.73$ and corrected for the effect of the IGM absorption following Meiksin, 2006. We consider the J magnitude provided by Matsuoka et al., 2016, $W1$ and $W2$ from *WISE* (see Table 2.3) and H and K from the VIKING survey (H=21.38±0.21, K=20.77±0.14). A χ^2 minimization routine suggests that this quasar has a large $E(B-V)$=0.3 (see Figure 2.10). The corrected $\lambda L_{\lambda,3000}$ is 1.62×10^{46} erg s^{-1}, and the resulting black hole mass and Eddington ratio are 7.22×10^9 M$_\odot$ and 0.09, respectively. Therefore, even taking into account the high internal extinction, HSC1205 is found to host a very massive black hole and to accrete at the lowest rate in our sample.

We now place our estimates in a wider context, comparing them with those derived for low−redshift quasars. We consider the SDSS-DR7 and DR12 quasar catalogs, presented by Shen et al., 2011 and Pâris et al., 2017, respectively; we select only objects in the redshift range $0.35 < z < 2.35$. In the DR7 release, we take into account the objects with any measurements of $\lambda L_{\lambda,3000}$ and Mg II FWHM (85,507 out of ∼105,000 sources). We calculate $\lambda L_{\lambda,3000}$ for the quasars in the DR12 release, modeling a continuum power law with the index provided in the catalog (entry `ALPHA_NU`), and normalizing it to the observed SDSS i magnitude. We consider only the sources in DR12 with measurements of the power law index and of the Mg II FWHM, and not already presented in DR7. Thus, out of the 297,301 sources in DR12, we select 68,062 objects: the total number of sources is 153,569.

De Rosa et al., 2011 provide continuum luminosities and Mg II measurements for 22 quasars at $4.0 \lesssim z \lesssim 6.4$ (observations collected from several studies: Iwamuro et al. 2002, 2004, Barth et al. 2003, Jiang et al. 2007, Kurk et al. 2007, 2009); Willott et al., 2010a present data for nine lower luminosity ($L_{\rm bol} < 10^{47}$ erg s^{-1}) $z \sim 6$ quasars; finally, Wu et al., 2015 publish an ultra luminous quasar at $z \sim 6.3$. In order to implement a consistent comparison among the various data sets, we re-calculate the black hole masses for all the objects in the literature using eq. 1.29. In Figure 2.11 we show $M_{\rm BH}$ vs $L_{\rm bol}$, for the quasars presented here and the objects from the

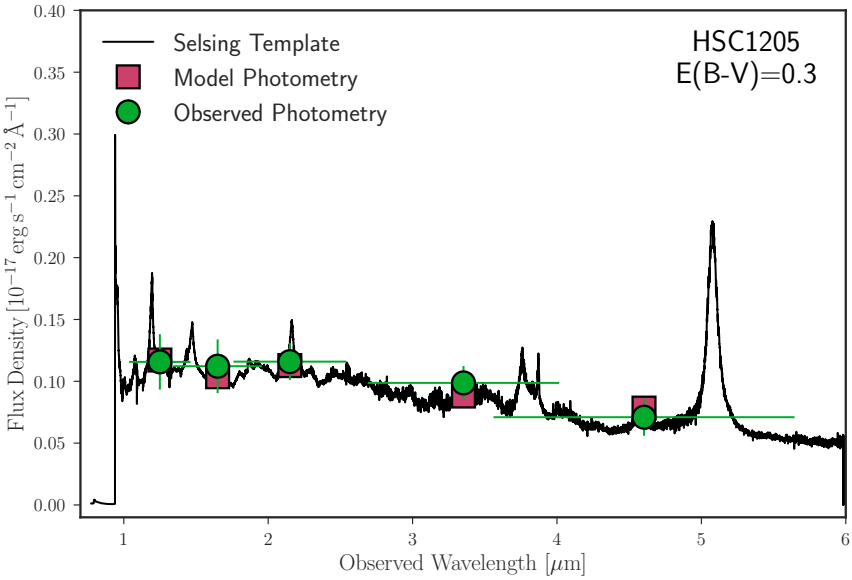

FIGURE 2.10: Fit of the broad band photometry of the quasar HSC1205, at z=6.73. The data are found to be consistent with a quasar model with internal reddening of $E(B-V)$=0.3

aforementioned studies. We highlight regions in the parameter space with constant Eddington ratio of 0.01, 0.1 and 1; we also show the typical errors on the black hole masses, due to the method uncertainties, and on the bolometric luminosities.

We note that the quasars at $z \gtrsim 4$ are generally found at higher bolometric luminosities ($L_{\rm bol} \gtrsim 10^{46}$ erg s^{-1}) than the objects at $z \sim 1$ (also due to selection effects, see below), but that the observed black hole masses span a similar range for both samples ($10^8 \lesssim M_{\rm BH}/{\rm M}_\odot \lesssim 5 \times 10^9$). The bulk of the low redshift ($z \sim 1$) quasar population shows lower Eddington ratios than the quasars at $z \gtrsim 4$. As for the objects at $z > 6.4$ presented in this sample, they occupy a parameter space similar to the sources from De Rosa et al., 2011, with a larger scatter in bolometric luminosities.

In order to provide a consistent comparison, we study the evolution of the black hole masses and Eddington ratios, as a function of redshift, for a quasar sample matched in bolometric luminosity. In order to reproduce the same luminosity distribution as the one of the high−redshift sources, we sample the low−redshift SDSS quasars by randomly drawing sources with comparable $L_{\rm bol}$ to $z \gtrsim 6.5$ quasars (within 0.01dex); we repeat this trial for 1000 times. We show in Figure 2.12 the black hole masses, bolometric luminosities and Eddington ratios, as a function of redshift, for the quasars presented in this work and for objects in one of the samples drawn at $z \sim 1$. The distributions of these quantities are also reported in Figure 2.13. We consider, as representative values for black hole mass and Eddington ratio of a bolometric luminosity matched sample at $z \sim$1, the mean of the means and the mean of the standard deviations calculated from the 1000 sub-samples. We then obtain $\langle \log(M_{\rm BH}) \rangle$=9.21 and $\langle \log(L_{\rm bol}/L_{\rm Edd}) \rangle$=-0.47, with a scatter of 0.34 and 0.33, respectively. These values are consistent, also considering the large scatter, with the estimates obtained for $z \gtrsim$6.5 quasars: $\langle \log(M_{\rm BH}) \rangle$=9.21 and $\langle \log(L_{\rm bol}/L_{\rm Edd}) \rangle$=-0.41, with a scatter of 0.34 and 0.44, respectively. Therefore, considering a bolometric luminosity matched sample, we do not find convincing evidence for an evolution of quasars accretion rate with redshift.

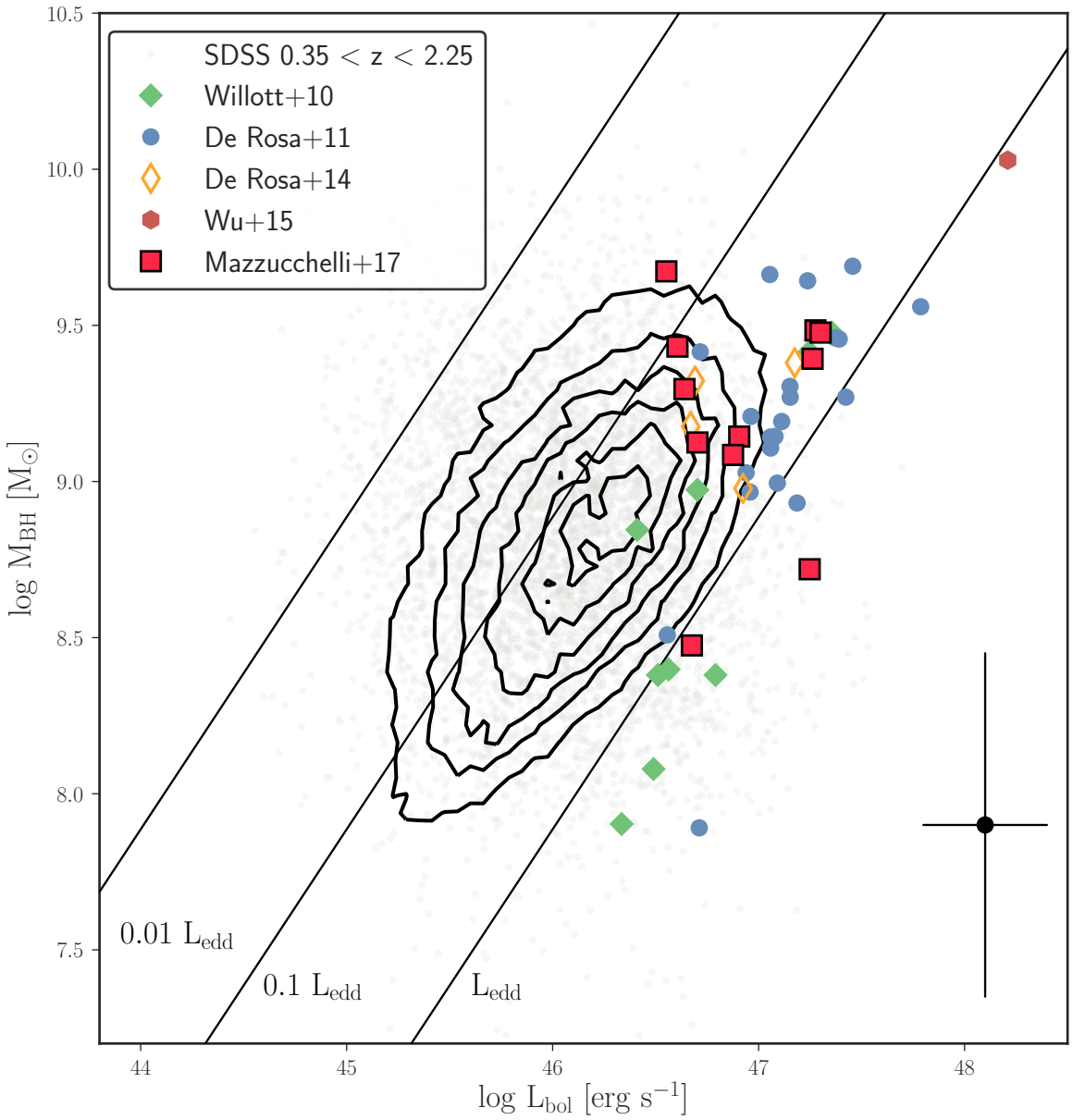

FIGURE 2.11: Black hole mass as function of bolometric luminosity for several quasar samples. We report a sub-sample from the SDSS-DR7 and DR12 quasar catalogs (Shen et al. 2011 and Pâris et al. 2017, respectively) at $0.35 < z < 2.25$ (*grey points* and *countours*). Also, we show measurements for quasars at higher redshifts, from Willott et al. (2010, $z \sim 6$; *green filled diamonds*), De Rosa et al. (2011, $4 < z < 6.4$; *blue points*), Wu et al. (2015, $z \sim 6.3$; *dark red hexagon*). The objects presented in this study are reported with *red, filled squares*. We notice that four quasars (VIK0109, VIK0305, VIK2348 and ULAS1120) have also been analyzed by De Rosa et al. (2014, *orange empty diamonds*): the two sets of measurements are consistent within the error bars. We show the method uncertainties on the black hole mass estimates and a representative mean error on the bolometric luminosity measurements (*black point*), and regions in the parameter space with constant Eddington luminosity (*black lines*). Quasars at high redshift are generally characterized by higher Eddington ratios than their lower−redshift counterparts, suggesting that they accreate at higher rates. However, the scatter in the $z \gtrsim 6.5$ sample is not negligible, with objects at $L_{\rm bol}/L_{\rm Edd}$ as low as ∼0.1.

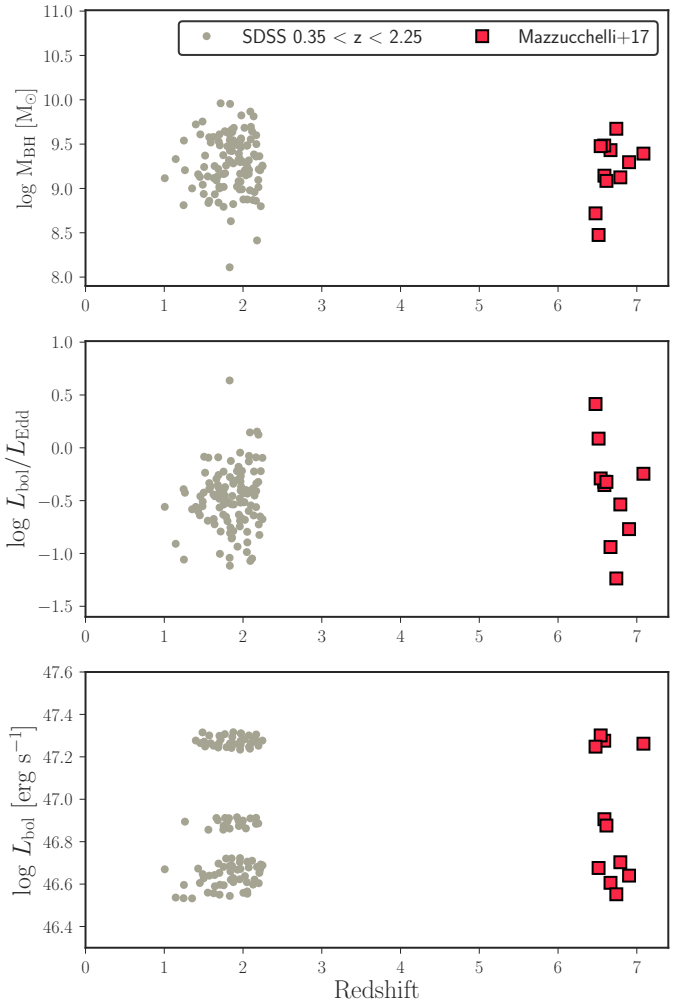

FIGURE 2.12: Black hole mass (*upper*), Eddington ratio (*central*) and bolometric luminosity (*lower panel*) against redshift, for a bolometric luminosity matched quasar sample (see text for details on the selection of the subsample at $z \sim 1$). We report the $z \gtrsim 6.5$ quasars presented in this work with *red squares*, and the ones at lower redshift ($0.35 < z < 2.25$) from SDSS-DR7+DR12 (Shen et al. 2011, Pâris et al. 2017) with *grey points*, respectively. The mean values of quasars black hole masses and Eddington ratios do not vary significantly with redshift (see also Figure 2.13).

Finally, we caution that we have witnessed evidence suggesting the presence of a strong wind component in the BLR (see Sections 2.5.4 and 2.5.1). In case of non-negligible radiation pressure by ionizing photons acting on the BLRs, the black hole masses derived by the simple application of the virial theorem might be underestimated (e.g. Marconi et al. 2008). This effect depends strongly on the column density (N_H) of the BLR, and on the Eddington ratio. Marconi et al., 2008 show that, in case of $0.1 \lesssim L_{bol}/L_{Edd} \lesssim 1.0$, as found in $z \gtrsim 6.5$ quasars, and for typical values of $10^{23} < N_H/[cm^{-2}] < 10^{24}$, the true black hole masses would be $\sim$2-10$\times$ larger than the virial estimates. This would lead to an even stronger challenge for the current models of primordial black holes formation and growth. An in depth discussion of this effect, given the uncertainties on the contribution of the possible wind and on the BLR structure itself, is beyond the scope of this work.

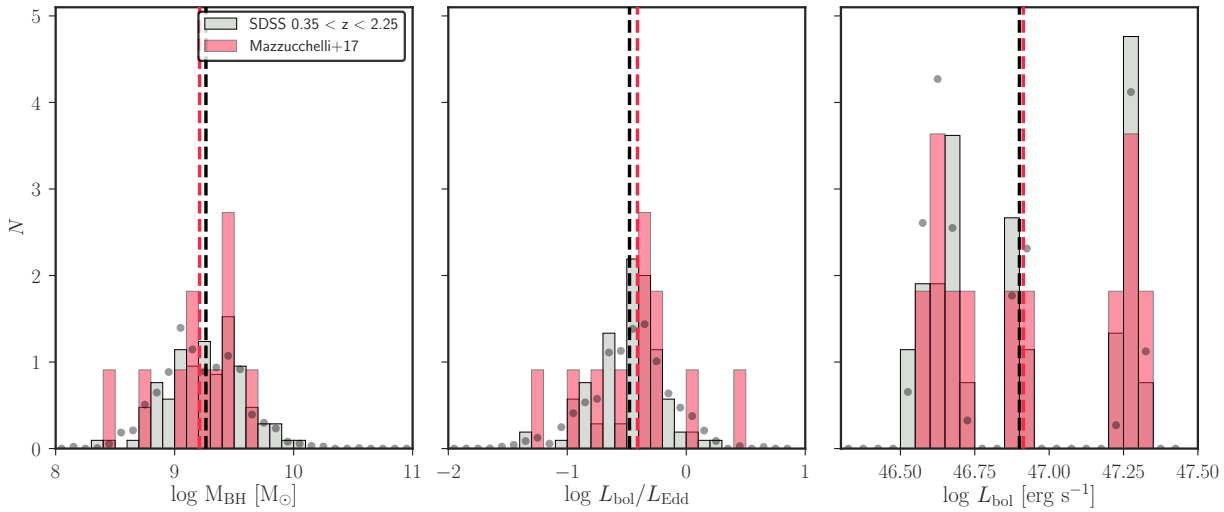

FIGURE 2.13: Distribution of black hole masses (*left*), Eddington ratios (*central*) and bolometric luminosities (*right panel*) for one of the 1000 bolometric luminosity matched sub-samples drawn from low−redshift SDSS quasars (*grey histograms*; Shen et al. 2011 and Pâris et al. 2017; see text for details), and for the $z \gtrsim 6.5$ quasars presented here (*red histograms*). The *grey points* represent the mean of black hole masses, Eddington ratios and bolometric luminosities in each bin, resulting from all the 1000 trials at $z \sim 1$. The mean of each quantity, for the low and high redshift populations, are shown in each panel with *black* and *red dashed lines*, respectively. We note that the mean black hole masses and Eddington ratios of the two samples are consistent, suggesting a non evolution of accretion rate with cosmic time. The histograms are normalized such that the underlying area is equal to one.

2.5.7 Black Hole Seeds

Measurements of black hole masses and Eddington ratios of high−redshift quasars help us in constraining formation scenarios of the first supermassive black holes in the very early universe. From eq. 1.30, we can derive that the time in which a black hole of mass $M_{\rm BH,f}$ is grown from an initial seed $M_{\rm BH,seed}$, assuming it accretes with a constant Eddington ratio for all the time, can be written as (see also,e.g. Shapiro 2005, Volonteri and Rees 2005):

$$\frac{t}{\rm Gyr} = t_{\rm s} \times \left[\frac{\epsilon}{1-\epsilon}\right] \times \frac{L_{\rm Edd}}{L_{\rm bol}} \times \ln\left(\frac{M_{\rm BH,f}}{M_{\rm BH,seed}}\right) \tag{2.13}$$

The average $M_{\rm BH}$ and $L_{\rm bol}/L_{\rm Edd}$ of all the $z \gtrsim 6.5$ quasars in the sample presented here (11 objects, not considering any luminosity cut, see Table 2.8) are 1.62×10^9 $M_\odot$ and 0.39, respectively. If we insert these values in Eq. 2.13, we can calculate the time needed by a black hole seed of $M_{\rm BH,seed} = [10^2, 10^4, 10^5, 10^6]$ $M_\odot$ to grow to the mean $M_{\rm BH}$ found here, assuming that it always accretes at an average Eddington rate of ∼0.39. We find that this time is t =[1.44,1.04,0.84,0.64] Gyr. As the age of the universe at z∼6.5 is only ∼0.83 Gyr (see Section 1.1), this implies that only very massive seeds (∼10^6 $M_\odot$) would be able to form the observed supermassive black holes.

Alternatively, we can invert eq. 2.13 and derive the initial masses of the black hole seeds required to obtain the observed black holes. This result depends on the assumptions made, e.g., on the redshift of the seed formation (z_i), on the accretion rate ($L_{\rm bol}/L_{\rm Edd}$), and on the radiative efficiency (ϵ; see eq. 2.13)[13]. We here consider different values for these parameters: We assume that the black holes accrete constantly with the observed Eddington ratios or with $L_{\rm bol}/L_{\rm Edd}$=1; also, we consider that they grow for a period of time equal to the age of the universe at their redshifts (i.e. $z_i \rightarrow \infty$), and from z_i=30 or 20. Finally, we assume an efficiency of 7% or 10%. The derived values of black hole seeds for all the combinations of these parameters are shown in Figure 2.14.

In all the cases considered here with ϵ=0.07 and Eddington accretion (and in case of ϵ=0.1, $z_i \rightarrow \infty$ and $L_{\rm bol}/L_{\rm Edd}$=1), the calculated seed masses ($\gtrsim10^2$ $M_\odot$) are consistent with being formed by stellar remnants. Alternatively, a scenario of higher efficiency (ϵ=0.1), later seeds birth (i.e. z =30 or 20), and accretion at $L_{\rm bol}/L_{\rm Edd}$=1, would require more massive seeds (∼10^{3-4} $M_\odot$) as progenitors of the observed $z \gtrsim$6.5 quasars.

2.5.8 Fe II/ Mg II

The estimates of the relative abundances of metals in high redshift sources act as useful proxies in the investigation of the chemical composition and evolution of galaxies in the early universe. In this context, the Mg II/Fe II ratio is of particular interest: α-elements, such as Mg, are mainly

[13]The efficiency depends in turn on the black hole spin and can be as high as ∼40% in the case of maximally spinning black holes. The spin is still an elusive parameter; it has been observationally measured only in ∼20 sources in the local Universe (through the relativistic broadening of the Fe Kα line; Brenneman et al. 2011 and Reynolds 2014). Thanks to stacked *Chandra* deep observations of ∼30 lensed quasars Walton et al., 2015 detected a broadened component of the Kα line up to z ∼4.5; however the low S/N prevented a measurement of the single quasars' black hole spins. Current semi-analytical models place only weak constraints on the spin value at $z \gtrsim$5, which depends on the gas accretion mode, galactic morphology and black hole mass (e.g. Sesana et al. 2014). However, since the spin decreases with black hole mass, we do not expect large values for our sample of quasars with $M_{\rm BH} \gtrsim 10^8$ $M_\odot$.

TABLE 2.8: Estimated quantities for the quasars in our sample: bolometric luminosities, black hole masses, Eddington ratios, Fe II-to-Mg II flux ratios.

Name	$L_{\rm bol}$ $[10^{47}{\rm erg\,s^{-1}}]$	$M_{\rm BH}$ $[\times 10^9 {\rm M}_\odot]$	$L_{\rm bol}/L_{\rm Edd}$	Fe II/Mg II
VIK J0109–3047	$0.51^{+0.05}_{-0.06}$	$1.33^{+0.38}_{-0.62}$	$0.29^{+0.88}_{-2.59}$	$2.02^{+5.56}_{-0.65}$
PSO J036.5078+03.0498	$2.0^{+0.22}_{-0.64}$	$3.00^{+0.92}_{-0.77}$	$0.51^{+0.17}_{-0.21}$	$2.47^{+3.71}_{-1.36}$
VIK J0305–3150	$0.75^{+0.10}_{-0.34}$	$0.90^{+0.29}_{-0.27}$	$0.64^{+2.20}_{-3.42}$	$1.03^{+3.04}_{-0.37}$
PSO J167.6415–13.4960	$0.47^{+0.16}_{-0.22}$	$0.30^{+0.08}_{-0.12}$	$1.22^{+0.51}_{-0.75}$	<3.1
ULAS J1120+0641	$1.83^{+0.19}_{-0.072}$	$2.47^{+0.62}_{-0.67}$	$0.57^{0.16}_{0.27}$	$1.04^{+3.84}_{-0.14}$
HSC J1205–0000	$0.36^{+0.18}_{-0.20}$	$4.7^{+1.2}_{-3.9}$	$0.06^{+0.32}_{-0.58}$	<0.50
PSO J231.6576–20.8335	$1.89^{+0.34}_{-0.45}$	$3.05^{+0.44}_{-2.24}$	$0.48^{+0.11}_{-0.39}$	2.64 ± 1.7
PSO J247.2970+24.1277	$1.77^{+0.06}_{-0.76}$	$0.52^{+0.22}_{-0.25}$	$2.60^{+0.08}_{-0.15}$	$1.33^{+5.82}_{-0.01}$
PSO J323.1382+12.2986	$0.81^{+0.07}_{-0.50}$	$1.39^{+0.32}_{-0.51}$	$0.44^{+1.09}_{-3.19}$	$1.85^{+2.37}_{-0.97}$
PSO J338.2298+29.5089	$4.04^{+2.14}_{-0.90}$	$2.70^{+0.85}_{-0.97}$	$0.11^{+0.71}_{-0.49}$	$1.29^{+2.1}_{-0.74}$
VIK J2348–3054	$0.43^{+0.20}_{-0.13}$	$1.98^{+0.57}_{-0.84}$	$0.17^{+0.92}_{-0.88}$	$2.13^{+0.93}_{-1.54}$

produced via type II supernovae (SNe) involving massive stars, while type Ia SNe from binary systems are primarily responsible for the provision of iron (Nomoto et al., 1997). Given that SNe Ia are expected to be delayed by ∼1 Gyr (Matteucci and Greggio 1986) with respect to type II SNe, estimating the relative abundances of α-elements to iron provides important insights on the stellar population in the galaxy, and on the duration and intensity of the star formation burst. Tracking the evolution of the Mg II/Fe II ratio as a function of redshift allows us to reconstruct the evolution of the galactic star formation history over cosmic time.

Many studies in the literature investigate the Mg II/Fe II ratio in the BLR of quasars, by estimating the ratio of the Fe II and Mg II fluxes ($F_{\rm Fe\,II}/F_{\rm Mg\,II}$), considered a first-order proxy of the abundance ratio (e.g. Barth et al. 2003, Maiolino et al. 2003, Iwamuro et al. 2002,2004, Jiang et al. 2007, Kurk et al. 2007, Sameshima et al. 2009, De Rosa et al. 2011,2014). In particular, De Rosa et al., 2011 and 2014 present a consistent analysis of ∼30 quasar spectra in the redshift range $4 \lesssim z \lesssim 7.1$, and find no evolution of their $F_{\rm Fe\,II}/F_{\rm Mg\,II}$ with cosmic time.

We estimate the Fe II and Mg II fluxes for the quasars in our study following De Rosa et al., 2014: for the former we integrate the fitted iron template over the rest-frame wavelength range $2200 < \lambda/\,[\text{Å}] < 3090$, and for the latter we compute the integral of the fitted Gaussian function (see Table 2.7 and 2.8 for the estimated flux values). In Figure 2.15, we plot $F_{\rm Fe\,II}/F_{\rm Mg\,II}$ as a function of redshift, for both the quasars in our sample and sources from the literature. We consider the sample by De Rosa et al., 2011 and 2014, and a sample of low−redshift quasars ($z \lesssim 2.05$) from Calderone et al., 2017. They consistently re-analyzed a sub-sample of quasars (∼70,000) from the SDSS-DR10 catalog, and provide measurements of the flux for Mg, Fe and the continuum emission at rest-frame $\lambda_{\rm rest}$ =3000 Å[14]. Here, we take only the sources with no flag on the quantities above (∼44,000 objects), and we correct the Fe II flux to account for the different wavelength ranges where the iron emission was computed[15].

[14] http://qsfit.inaf.it/

[15] Calderone et al., 2017 integrates the iron template in the rest-frame wavelength range $2140 < \lambda/[\text{Å}] < 3090$, while we use the range $2200 < \lambda/[\text{Å}] < 3090$.

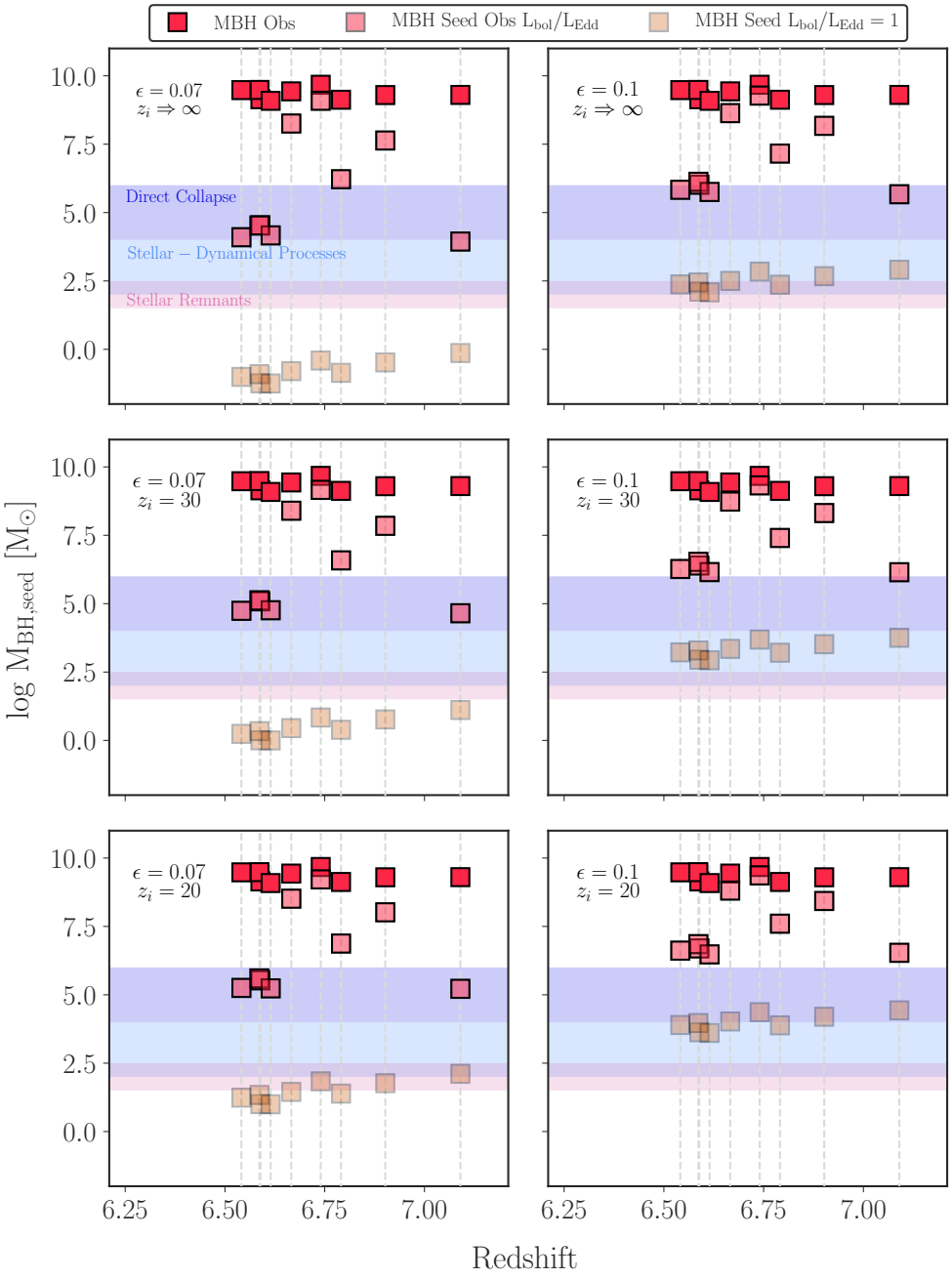

FIGURE 2.14: Masses of the black hole seeds required to obtain the observed black hole masses in our quasar sample (*dark red squares*). We here vary the efficiency (ϵ=0.07/0.1, *left* and *right columns*) and the redshift of the seed formation ($z \rightarrow \infty$/30/20, from *top* to *bottom*). For each case, we assume that the sources accrete constantly with the observed Eddington ratio (*light red squares*; see also Table 2.8), and at Eddington rate (*yellow squares*). The range of black hole seeds predicted by current theoretical models are shown in *orange*, *light blue* and *deep blue shaded areas* (see text for references). Black hole seeds with masses $\gtrsim 10^2$ $M_\odot$ can produce the observed high−redshift quasars in all cases with ϵ=0.07 and L_{bol}/L_{Edd}=1, and in case of [ϵ=0.1, L_{bol}/L_{Edd}=1 and $z_i \rightarrow \infty$]. If the radiative efficiency is higher (10%), and the seeds form at $z \sim$30−20, their predicted masses are correspondingly larger ($\sim 10^{3-4}$ $M_\odot$, at Eddington accretion).

From Figure 2.15, we see that the flux ratios of the quasars in our sample are systematically lower than those of the sources at lower redshift, both from De Rosa et al., 2011 and from

Calderone et al., 2017: this suggests a possible depletion of iron at $z \gtrsim 6.5$, and therefore the presence of a younger stellar population in these quasar host galaxies. However, our estimates are also characterized by large uncertainties, mainly due to the large uncertainties on the iron flux estimates (see Table 2.7). Within the errors, our measurements are consistent with a scenario of non−evolving $F_{\rm Fe\,II}/F_{\rm Mg\,II}$ over cosmic time, in agreement with De Rosa et al., 2014.

We test whether the systematic lower values of $F_{\rm Fe\,II}/F_{\rm Mg\,II}$ for the highest redshift quasar population is statistically significant. We associate to each of our measurements a probability distribution, built by connecting two half-Gaussian functions with mean and sigma equal to the calculated ratio and to the lower (or upper) uncertainty, respectively. We sum these functions to obtain the total probability distribution for the objects at high−redshift. We compare this function with the distribution of the $F_{\rm Fe\,II}/F_{\rm Mg\,II}$ values for the quasars at $z \sim 1$. We randomly draw nine sources from the two distributions (the number of objects in our sample excluding the limits) and we apply a Kolmogorov-Smirnoff test to check if these two samples could have been taken from the same probability distribution; we repeat this draw 10000 times. We obtain that the p-value is greater than 0.2 (0.5) in the 51% (27%) of the cases: this highlights that, considering the large uncertainties, we do not significantly measure a difference in the total probability distribution of $F_{\rm Fe\,II}/F_{\rm Mg\,II}$ at low and high−redshift.

Data with higher S/N in the Fe II emission line region are needed to place more stringent constraints on the evolution of the abundance ratio.

2.5.9 Infrared and [CII] luminosities in Quasar Host Galaxies

We observed four quasars in our sample with NOEMA (see Section 2.3). We extract their spectra, and fit the continuum+[CII] line emission with a flat+Gaussian function (see Figure 2.4). We estimate the line properties, e.g. the peak frequency, the width, amplitude and flux, and we calculate the continuum flux at rest frame wavelength 158 μm from the continuum map. We report these values in Table 2.9.

We can derive the far infrared properties of the observed quasars, following a number of assumptions commonly presented in the literature (e.g. Venemans et al. 2012, 2016). We approximate the shape of the quasar infrared emission with a modified black body: $f_\nu \propto B_\nu(T_d)(1-e^{\tau_d})$, where $B_\nu(T_d)$ is the Planck function and T_d and τ_d are the dust temperature and optical depth, respectively (Beelen et al., 2006). Under the assumption that the dust is optically thin at wavelength $\lambda_{\rm rest} > 40\mu$m ($\tau_d << 1$), we can further simplify the function above as $f_\nu \propto B_\nu(T_d)\nu^\beta$, with β the dust emissivity power law spectral index. We take $T_d = 47$ K and $\beta = 1.6$, which are typical values assumed in the literature (Beelen et al., 2006). We scale the modified black body function to the observed continuum flux at the rest frame frequency $\nu_{\rm rest} = 1900$ GHz; we then calculate the FIR luminosity ($L_{\rm FIR}$) integrating the template in the rest frame wavelength range 42.5 μm−122.5μm (Helou et al., 1988). The total infrared (TIR) luminosity ($L_{\rm TIR}$) is defined instead as the integral of the same function from 8 μm to 1000 μm. We note that these luminosity values are crucially dependent on the assumed shape of the quasar infrared emission. We can use the latter quantity to derive the star formation rate ($SFR_{\rm TIR}$) of

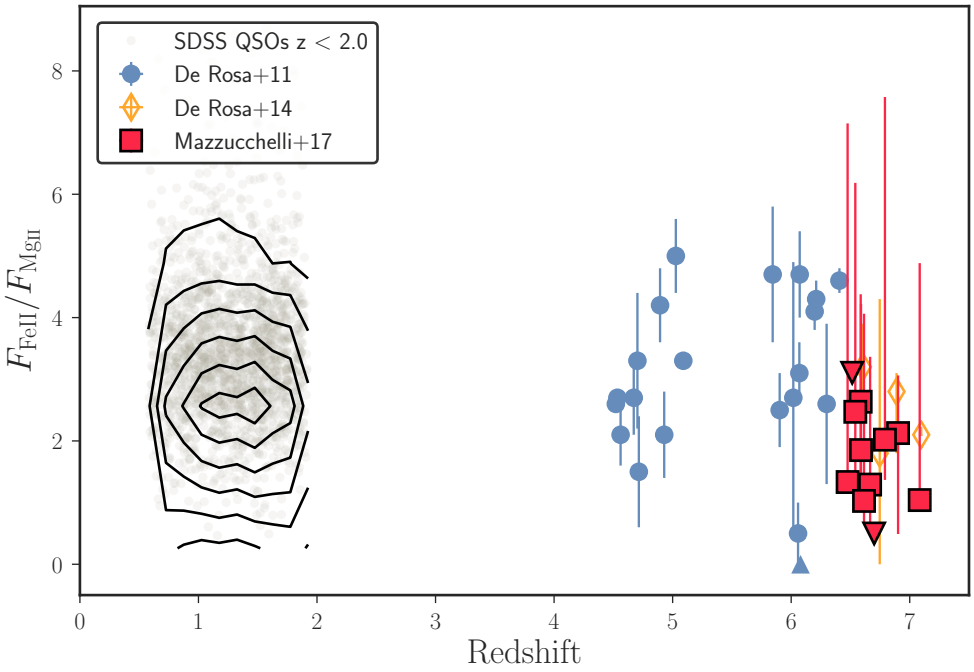

FIGURE 2.15: Fe II-to-Mg II flux ratio, considered as a first-order proxy for the relative abundance ratio, versus redshift. We show the quasars in our sample (*red squares* and, in case of upper limits, *down-pointing triangles*) and taken from the literature: De Rosa et al. 2011 (*blue points*) and $z \lesssim 2$ SDSS quasars (Calderone et al. 2017, *grey points* and *black contours*). We show with *orange empty diamonds* the measurements of De Rosa et al., 2014 for four of our quasars (VIK0109, VIK0305, VIK2348 and ULAS1120); they have been derived with a slightly different fitting routine (see text for details) but are consistent, within the errors, with the estimates obtained here. Our measurements are systematically lower than that of samples at lower redshifts; however, taking into account the large uncertainties, we find no statistical evidence for an evolution of the flux ratio with redshift.

the quasar host galaxy, through the relation calibrated by Murphy et al., 2011:

$$\frac{SFR}{[M_\odot\,\mathrm{yr}^{-1}]} = 3.88 \times 10^{-44} \frac{L_{\rm TIR}}{[\mathrm{erg\,s}^{-1}]} \tag{2.14}$$

Finally, we can estimate the total dust mass as (Magdis et al., 2011):

$$M_d = \frac{f_\nu D_{\rm L}^2}{(1+z)\,\kappa_\lambda B_\nu(\lambda, T_d)} \tag{2.15}$$

where $D_{\rm L}$ is the luminosity distance, $B_\nu(\lambda, T_d)$ and f_ν are the Planck function and continuum flux density, respectively, estimated at $\lambda_{\rm rest}$. κ_λ is the dust mass opacity coefficient, which can be expressed as $\kappa_\lambda = 0.77\,(850\mu\mathrm{m}/\lambda)^\beta\,\mathrm{cm}^2/\mathrm{g}$ (Dunne, Clements, and Eales, 2000).

We can also calculate the luminosity of the [CII] emission line ($L_{\rm [CII]}$) from the observed line flux ($S_{\rm [CII]}\Delta v$; Carilli and Walter 2013):

$$\frac{L_{\rm [CII]}}{L_\odot} = 1.04 \times 10^{-3} \frac{S_{\rm [CII]}\,\Delta v}{\mathrm{Jy\,km\,s}^{-1}} \left(\frac{D_{\rm L}}{\mathrm{Mpc}}\right)^2 \frac{\nu_{\rm obs}}{\mathrm{GHz}} \tag{2.16}$$

where $\nu_{\rm obs}$ is the observed frequency. Several studies in the literature find a correlation between $L_{\rm [CII]}$ and the SFR, and providing different recipes to derive $SFR_{\rm [CII]}$, which have been calibrated on a variety of data sets (De Looze et al. 2011, 2014, Sargsyan et al. 2012a, Herrera-Camus et al. 2015). We consider here the formula obtained by De Looze et al. 2014, who used a sample of high redshift ($z > 0.5$) galaxies:

$$\frac{SFR_{\rm [CII]}}{[M_\odot\,{\rm yr}^{-1}]} = 3 \times 10^{-9} \left(\frac{L_{\rm [CII]}}{L_\odot}\right)^{1.18} \tag{2.17}$$

The observed scatter of this relation is ∼0.40 dex. We note that, using the relations from De Looze et al., 2011 (Herrera-Camus et al., 2015), calibrated on local star forming galaxies, we obtain values of the $SFR_{\rm [CII]} \sim \times 2$ (5) lower. This difference may be due to the diverse luminosity range of the sources analyzed in this study ($L_{\rm FIR} \gtrsim 10^{12}\,M_\odot$) and the ones considered in the literature ($L_{\rm FIR} < 10^{12}\,M_\odot$; see also the discussion in Venemans et al. 2016). In Table 2.9, we list our estimates for the [CII] , FIR and TIR luminosities, $SFR_{\rm TIR}$, $SFR_{\rm [CII]}$ and dust masses.

In Figure 2.16, we plot $L_{\rm [CII]}\,/L_{\rm FIR}$ vs $L_{\rm FIR}$ for the quasars studied here and for a variety of sources from the literature. At low redshift ($z < 1$) both star-forming galaxies (Malhotra et al. 2001, Sargsyan et al. 2012a) and more extreme objects, e.g. LIRGS and ULIRGS (Díaz-Santos et al. 2013, Farrah et al. 2013), show lower luminosity ratios at higher FIR luminosities: this phenomenon is known as the "CII-deficit". At $z > 1$, the scenario is less clear, where the scatter in the measurements of $L_{\rm [CII]}\,/L_{\rm FIR}$ for star-forming galaxies (Stacey et al. 2010, Brisbin et al. 2015, Gullberg et al. 2015), SMGs and quasars increases.

Quasars at $z > 5$ present a variety of $L_{\rm [CII]}\,/L_{\rm FIR}$ values, mostly depending on their far-infrared brightness. Walter et al., 2009 and Wang et al., 2013 observe quasars with high $L_{\rm FIR}$, and show that they are characterized by low luminosity ratios, comparable to local ULIRGS ($\langle \log(L_{\rm [CII]}\,/L_{\rm FIR})\rangle \sim -3.5$). On the other hand, quasars with lower far infrared luminosities and black hole masses ($M_{\rm BH} < 10^9$ M$_\odot$; Willott, Bergeron, and Omont 2015) are located in a region of the parameter space similar to that of regular star forming galaxies ($\langle \log(L_{\rm [CII]}\,/L_{\rm FIR})\rangle \sim -2.5$). In the literature, the decrease of $L_{\rm [CII]}$ in high-redshift quasars has been tentatively explained invoking a role of the central AGN emission, which is heating the dust. The problem is however still under debate, and several other alternative scenarios have been advocated, e.g. C^+ suppression due to X-ray radiation from the AGN (Langer and Pineda, 2015), or the relative importance of different modes of star formation on-going in the galaxies (Graciá-Carpio et al., 2011).

The quasars whose new infrared observations are presented here, with $L_{\rm FIR} \sim 10^{12}$ L$_\odot$, are characterized by values of the luminosity ratio in between those of FIR bright quasars and of the sample by Willott, Bergeron, and Omont (2015; $\langle \log(L_{\rm [CII]}\,/L_{\rm FIR})\rangle \sim -3.0$). This is similar to what was found by Venemans et al. (2012, 2017) for ULAS1120, and suggests that the host galaxies of these quasars are more similar to ULIRGS.

TABLE 2.9: Results from our NOEMA observations: we report the [CII] line and continuum emission quantities obtained from our fit (i.e. flux and line width); the [CII] line, FIR and TIR luminosities; the [CII] and TIR SFR, and the dust masses.

	HSC J1205-0000	**PSO J338.2298+29.5089**	**PSO J006.1240+39.2219**	**PSO J323.1283+12.2986**
$z_{[CII]} - z_{MgII}$ [km s^{-1}]	–	818^{+168}_{-138}	–	230 ± 13
[CII] line width [km s^{-1}]	–	740^{+541}_{-313}	277^{+161}_{-141}	254^{+48}_{-28}
[CII] flux [Jy km s^{-1}]	–	$1.72^{+0.91}_{-0.84}$	$0.78^{+0.54}_{-0.38}$	$1.05^{+0.33}_{-0.21}$
Continuum flux density [mJy]	0.833 ± 0.176	0.972 ± 0.215	0.548 ± 0.178	0.470 ± 0.146
$L_{[CII]}$ [$\times 10^9\, L_\odot$]	–	2.0 ± 0.1	$0.9^{+0.6}_{-0.4}$	$1.2^{+0.4}_{-0.2}$
L_{FIR} [$\times 10^{12}\, L_\odot$]	1.9 ± 0.4	2.1 ± 0.5	1.1 ± 0.4	1.0 ± 0.3
L_{TIR} [$\times 10^{12}\, L_\odot$]	2.6 ± 0.5	2.8 ± 0.6	1.5 ± 0.5	1.3 ± 0.4
$L_{[CII]}\,/L_{FIR}$ [$\times 10^{-3}$]	–	$0.98^{+0.55}_{-0.52}$	$0.77^{+0.59}_{-0.45}$	$1.2^{+0.54}_{-0.45}$
SFR_{TIR} [M$_\odot$ yr^{-1}]	381 ± 76	413 ± 91	231 ± 75	196 ± 61
$SFR_{[CII]}$ [M$_\odot$ yr^{-1}]	–	285^{+175}_{-138}	108^{+89}_{-62}	153^{+57}_{36}
M_d [$\times 10^8$ M$_\odot$]	2.6 ± 0.5	2.7 ± 0.6	1.5 ± 0.5	1.3 ± 0.4

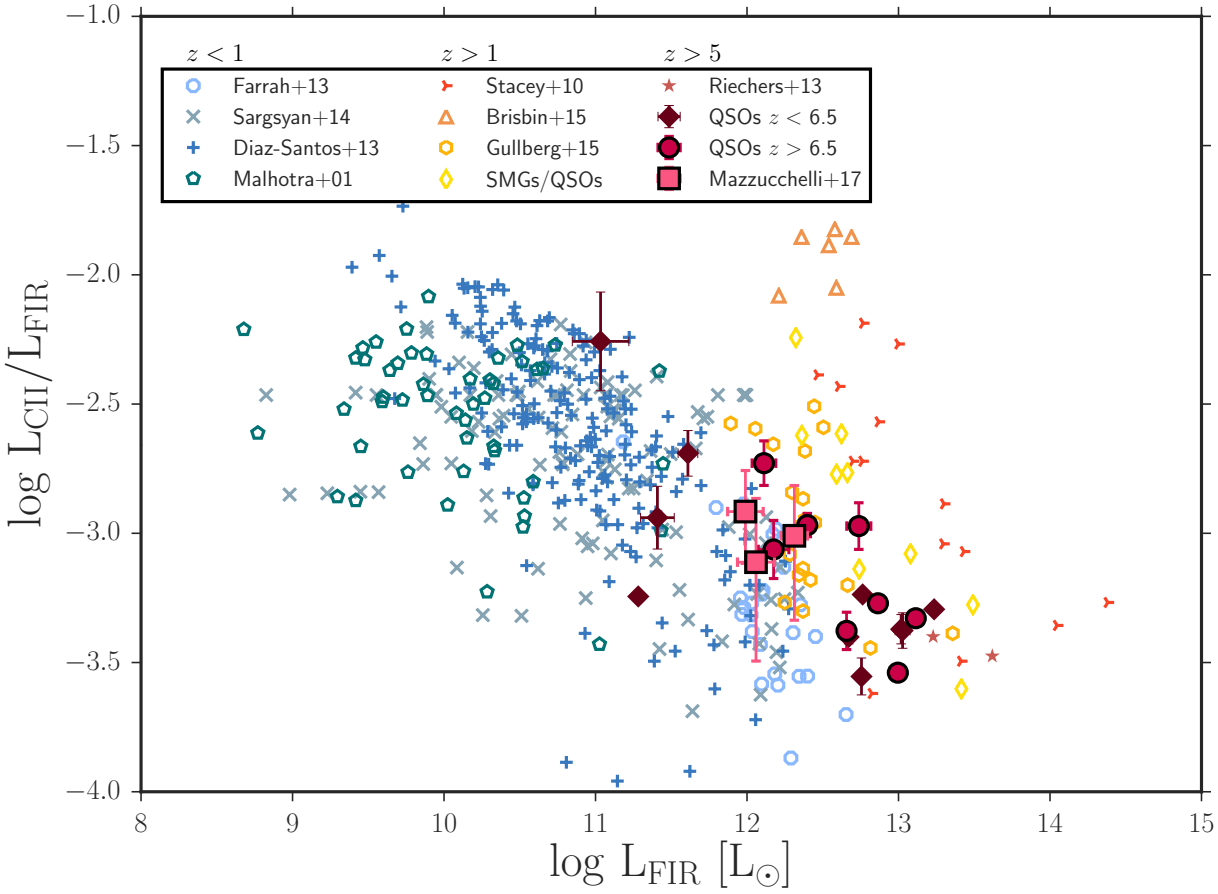

FIGURE 2.16: [CII] -to-FIR luminosity ratio as function of FIR luminosity. With *open blue/green symbols* we report objects at $z < 1$: star-forming galaxies (Malhotra et al. 2001, Sargsyan et al. 2012a), LIRGs (Díaz-Santos et al., 2013) and ULIRGS (Farrah et al., 2013). Values for sources at $1 < z < 5$ are shown with *open yellow/orange symbols*: star-forming galaxies (Stacey et al. 2010, Brisbin et al. 2015, Gullberg et al. 2015) and a collection of $3 \lesssim z \lesssim 5$ sub-millimeter galaxies and quasars (Cox et al. 2011,Wagg et al. 2010, 2012, Ivison et al. 2010, De Breuck et al. 2011, Valtchanov et al. 2011, Walter et al. 2012, Maiolino et al. 2009). The $z = 6.3$ SMG presented in Riechers et al., 2013 is shown as a *light-red star*. Quasars at $5 \lesssim z \lesssim 6.5$ (Maiolino et al. 2005, Wang et al. 2013, Willott, Bergeron, and Omont 2015) are shown with *filled dark-pink diamonds*. Quasars in the sample presented here are reported with *filled light-pink squares* (new observations for PSO338+29, PSO323+12, PSO006+39), and with *filled pink circles* (data taken from the literature; ULASJ1120, Venemans et al. 2012; PSO036+03, Bañados et al. 2015b; VIKJ0109, VIKJ0305, VIKJ2348, Venemans et al. 2016; PSO231-20, PSO183+05,PSO167-13, Decarli et al. 2018). Local sources show a decrease in the [CII] -to-FIR ratio at high FIR luminosities, whereas the values of this ratio for the high redshift sample have a large scatter. The $z > 6$ quasars whose mm observations are presented in this work are characterized by values of $L_{[CII]}$ / L_{FIR} comparable to local ULIRGs. The range of [CII] -to-FIR luminosity ratio of the general population of $z > 6$ quasars however hints to an intrinsic diversity among their host galaxies.

2.5.10 Near Zones

Near zones are regions surrounding quasars where the IGM is ionized by the UV radiation emitted from the central source (see Section 1.5). Taking into account several approximations, e.g. that the IGM is partially ionized and solely composed of hydrogen, and that photoionization recombination equilibrium is found outside the ionized region (Fan et al., 2006), the radius of the ionized bubble can be expressed as:

$$R_s \propto \left(\frac{\dot{N}_Q t_Q}{f_{\rm HI}} \right)^{1/3} \tag{2.18}$$

where $\dot{N}_Q$ is the rate of ionizing photons produced by the quasar, t_Q is the quasar lifetime, and $f_{\rm HI}$ is the IGM neutral fraction.

Several studies provide estimates of near zone radii for samples of $z > 5$ quasars, and investigate its evolution as a function of redshift, in order to investigate the IGM evolution (Fan et al. 2006, Carilli et al. 2010, Venemans et al. 2015b, Eilers et al. 2017; see Section 1.5.4). However, it is not straightforward to derive the exact values of R_s from the observed spectra; instead, we calculate here the near zone radii ($R_{\rm NZ}$) for the sources in our sample. We follow the definition of Fan et al., 2006, i.e. $R_{\rm NZ}$ is the distance from the central source where the transmitted flux drops below 0.1, once the spectrum has been smoothed to a resolution of 20 Å. The transmitted flux is obtained by dividing the observed spectrum by a model of the intrinsic emission.

We here model the quasar emission at $\lambda_{\rm rest} < 1215.16$ Å using a principal component analysis (PCA) approach. In short, the total spectrum, $q(\lambda)$, is represented as the sum of a mean spectrum, $\mu(\lambda)$, and $n = 1, .., N$ principal component spectra (PCS), $\xi_n(\lambda)$, each weighted by a coefficient w_n:

$$q(\lambda) = \mu(\lambda) + \sum_{n=1}^{N} w_n \xi_n(\lambda) \tag{2.19}$$

Pâris et al., 2011 and Suzuki, 2006 apply the PCA to a collection of 78 $z \sim 3$ and 50 $z \lesssim 1$ quasars from SDSS, respectively. In our study, we follow the approach by Eilers et al., 2017, mainly referring to Pâris et al., 2011 who provide PCS functions within the rest frame wavelength window $1020 < \lambda/[\text{Å}] < 2000$. After normalizing our spectra to the flux at $\lambda_{\rm rest} = 1280$ Å, we fit the region redwards than the Lyα emission line ($\lambda_{\rm rest} > 1215.16$ Å) to the PCS by Pâris et al., 2011, and we derive the best coefficients by finding the maximum likelihood. We then obtain the best coefficients which reproduce the entire spectrum by using the projection matrix presented by Pâris et al., 2011. For further details on this modeling procedure, see Eilers et al., 2017. We show in Figure 2.17 an example of PCA for one of the quasars in our sample. Also, in this way we provide an analysis of the near zone sizes consistent with Eilers et al., 2017, making it possible to coherently compare the results obtained from the two data sets.

The near zone sizes depend also on quasar luminosity (through the $\dot{N}_Q$ term in eq. 2.18): if we want to study their evolution with redshift, we need to break this degeneracy. We rescale the quasar luminosities to the common value of M_{1450}=-27 (following previous studies, e.g Carilli et al. 2010, Venemans et al. 2015b), and we use the scaling relation obtained from the most recent numerical simulations presented in Eilers et al., 2017 and Davies et al., 2018. They

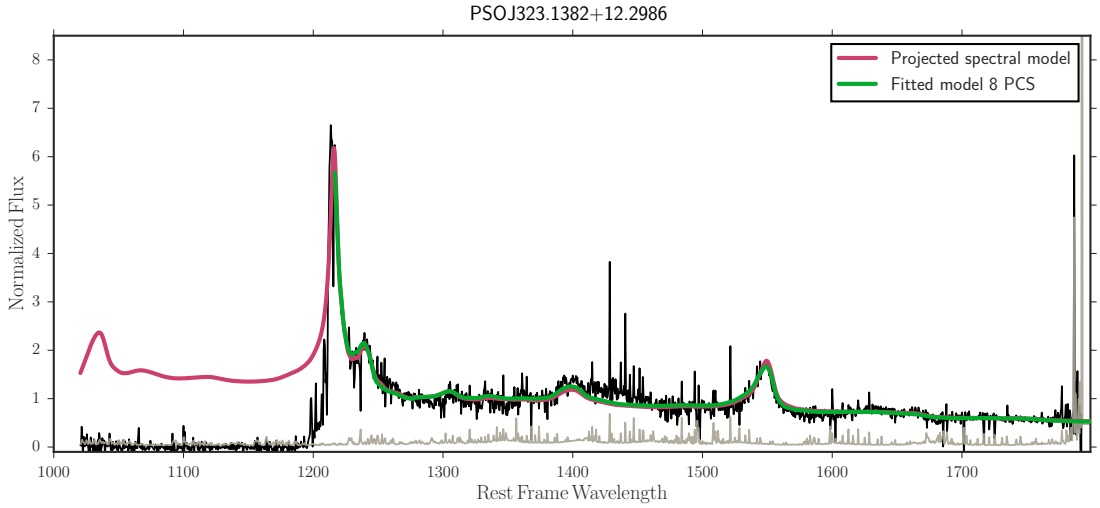

FIGURE 2.17: Example of quasar continuum emission fit with the PCA method for one of the sources in our sample (PSO323+12). We show the fitted model at wavelength greater than the Lyα emission line (with 8 PCAs; *green line*), and the projected model on the entire spectrum (*purple line*).

simulate radiative transfer outputs for a suite of z =6 quasars within the luminosity range -24.78<M_{1450} <-29.14, and constantly shining over $10^{7.5}$ yr, considering two scenarios in which the surrounding IGM is mostly ionized (see Sections 1.5 and 1.2; e.g. McGreer, Mesinger, and D'Odorico 2015) or mostly neutral. They obtain comparable results for the two cases, which are both in agreement with the outcome obtained by fitting the observational data (see Eilers et al. 2017, Figure 5). Following the approach of Eilers et al., 2017, we consider the case of a mostly ionized IGM: they fit the simulated quasar near zone sizes against luminosity with the power law:

$$R_{\rm NZ} = 5.57\,{\rm pMpc} \times 10^{0.4(M_{1450})/2.35} \tag{2.20}$$

from which they derive the following scaling relation, that we also use here:

$$R_{\rm NZ,corr} = R_{\rm NZ}\, 10^{0.4(27+M_{1450})/2.35} \tag{2.21}$$

We report in Table 2.10 the derived quantities, and the transmission fluxes are shown in Figure 2.18. We do not consider in our analysis the following quasars: HSC1205, due to the poor quality of the spectrum in the Lyα emission region (see Figure 2.3); PSO183+05, since this quasar is believed to present a proximate ($z \approx 6.404$) DLA (see Chen et al. 2017, Banados et al. subm); PSO011+09 and PSO261+19. The redshift measurements of these latter two objects are provided by the Lyα emission line: the lack of any other strong emission line, and the broad shape of the Lyα line, do not permit us to rule out that these quasars are BAL objects. The redshifts of the remaining objects are mainly derived from [CII] observations (see Table 2.10).

We show the evolution of $R_{\rm NZ,corr}$ as a function of redshift in Figure 2.19. We compare our data with estimates at lower redshift ($5.6 \lesssim z \lesssim 6.6$) presented by Eilers et al., 2017. The best fit of the evolution of $R_{\rm NZ,corr}$ with z, modeled as a power law function, gives the following:

$$R_{\rm NZ,corr} = (4.49 \pm 0.92) \times \left(\frac{1+z}{7}\right)^{-1.00\pm0.20} \tag{2.22}$$

TABLE 2.10: Near zone sizes of 11 quasars in the sample presented here. The corrected vaues have been calculated with Eq. 2.21, and take into account the dependency on their luminosity. We also report the number of PCS adopted in the continuum fit.

Name	$R_{\mathbf{NZ}}$ [Mpc]	$R_{\mathbf{NZ,corr}}$ [Mpc]	$R_{\mathbf{NZ,corr,err}}$ [Mpc]	**PCS**
PSO J006.1240+39.2219	4.47	6.78	0.09	5
VIK J0109–3047	1.59	2.78	0.03	8
PSO J036.5078+03.0498	4.37	3.91	0.08	8
VIK J0305–3150	3.417	4.81	0.006	10
PSO J167.6415–13.4960	2.02	3.55	0.03	8
ULAS J1120+0641	2.10	2.48	0.02	9
PSO J231.6576–20.8335	4.28	4.05	0.03	8
PSO J247.2970+24.1277	2.46	2.96	0.24	5
PSO J323.1382+12.2986	6.23	6.09	0.01	8
PSO J338.2298+29.5089	5.35	7.68	0.25	5
VIK J2348–3054	2.64	4.33	0.05	8

The values obtained are consistent, within the errors, with the results of Eilers et al., 2017[16]. In agreement with both measurements from observations and radiative transfer simulations presented by Eilers et al., 2017, we find a weak evolution of the quasar near zone sizes with cosmic time: this evolution is indeed much shallower than what was obtained by previous works (Fan et al. 2006, Carilli et al. 2010, Venemans et al. 2015b), which argued that the significant decrease of $R_{\rm NZ}$ with redshift could be explained by a steeply increasing IGM neutral fraction between $z \sim$5.7 and 6.4[17].

The different trend of near zone sizes with redshift with respect to what was found in the literature may be due to several reasons, i.e. we consider higher quality spectra and a larger sample of quasars, we take into consideration a consistent definition of $R_{\rm NZ}$ and we do not exclude the WEL quasars at $z \sim$6 (see Eilers et al. 2017 for an in depth discussion of the discrepancies with previous works). We argue that the shallow evolution is due to the fact that $R_{\rm NZ,corr}$ does not depend entirely or only on the external IGM properties, but it correlates more strongly with the quasar characteristics (e.g. lifetime, regions of neutral hydrogen within the ionized zone), which are highly variable from object to object.

2.6 Discussion and Summary

In this work we present our search for $z-$dropouts in the third internal release of the Pan-STARRS1 stacked catalog (PS1 PV3), which led to the discovery of six new $z \sim$6.5 quasars.

We complement these newly found quasars with 9 other $z \gtrsim 6.5$ quasars known to date, and perform a comprehensive analysis of the highest redshift quasar population. In particular, we provide new optical/NIR spectroscopic observations for the six newly discovered quasars and for three sources taken from the literature (PSO006+39, PSO338+29 and HSC1205). We

[16] $R_{\rm NZ,corr} \approx 4.87 \times [(1+z)/7]^{-1.44}$; see also their Figure 6.

[17] We note that these studies considered a smaller and lower$-z$ quasar sample, whose redshift measurements (mainly from the Mg II or Lyα emission lines, with only a minority of objects observed in CO or [CII]) have larger errors, and that they fit the redshift evolution of the near zone sizes with a linear relation.

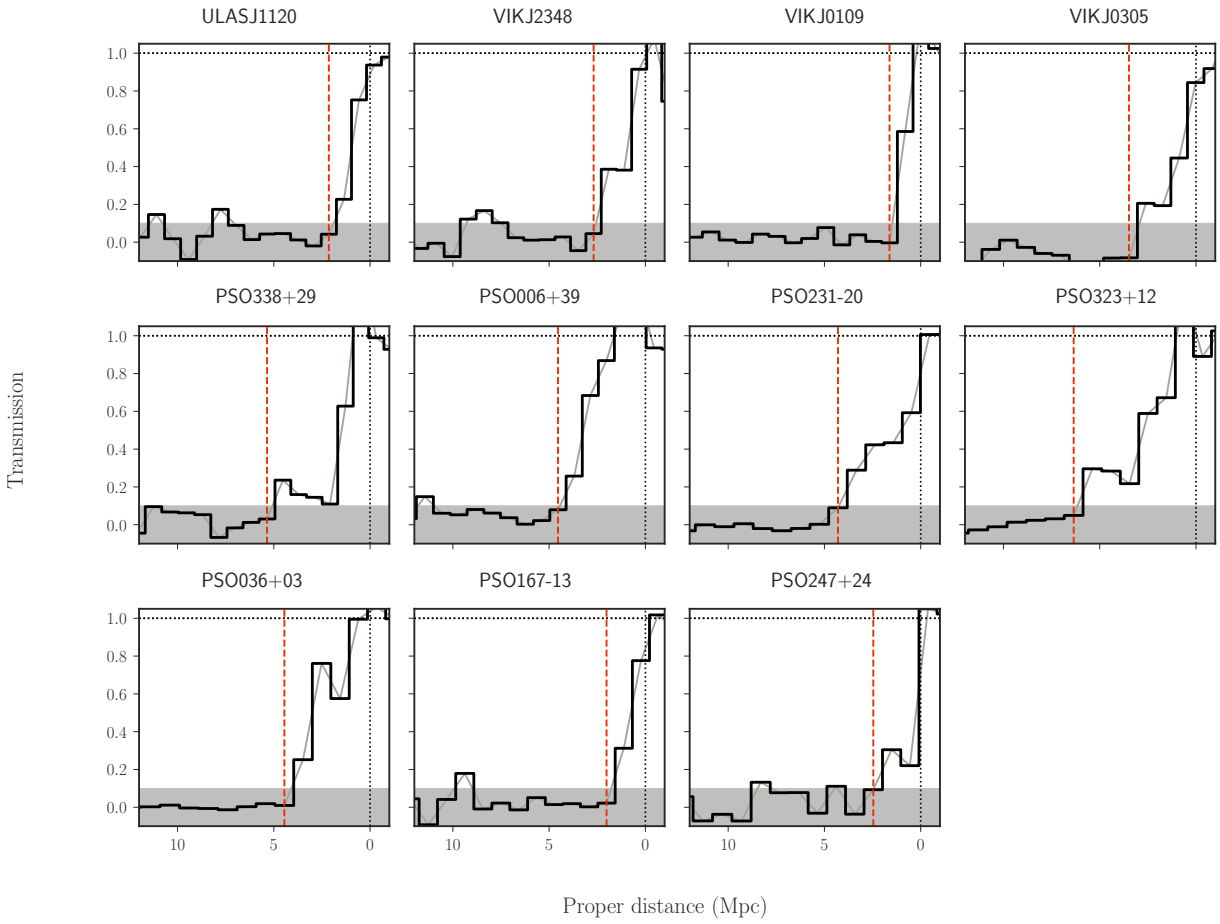

FIGURE 2.18: Transmission fluxes of the quasars in our sample, obtained normalizing the observed spectra by the emission model from the PCA method (see Section 4), as a function of proper distance from the source. We identify the near zone radius (*dashed red line*) as the distance at which the flux drops below 10%, after smoothing each spectrum to a common resolution of 20 Å. We do not consider in our analysis HSC1205, PSO183+05, PSO011+09 or PSO261+19 (see text).

also present new millimeter observations of the [CII] 158 μm emission line and the underlying continuum emission from NOEMA, for four quasars (PSO006+39, PSO323+12,PSO338+12 and HSC1205).

Our main results are:

- We calculate C IV rest−frame EWs, and blueshifts with respect to the Mg II emission line, for 9 sources in our sample. We derive that all the $z \gtrsim 6.5$ quasars considered here show large blueshifts (740−5900 km s^{-1}), and they are outliers with respect to a comparison SDSS quasar sample at $z \sim 1$; they also have EW values equal or lower than those of the low−redshift quasars. This evidence hints to a strong wind/outflows component in the BLRs of the highest redshift quasars known.

- We derive bolometric luminosities, black hole masses and accretion rates estimates by modeling the Mg II emission line region ($2100 < \lambda/[\text{Å}] < 3200$) for 11 objects with available NIR spectroscopic observations. Comparing those measurements with the ones of a bolometric luminosity matched quasar sample at lower redshift ($0.35 < z < 2.35$), we find that high−redshift quasars accrete their material at a similar rate, with a mean of

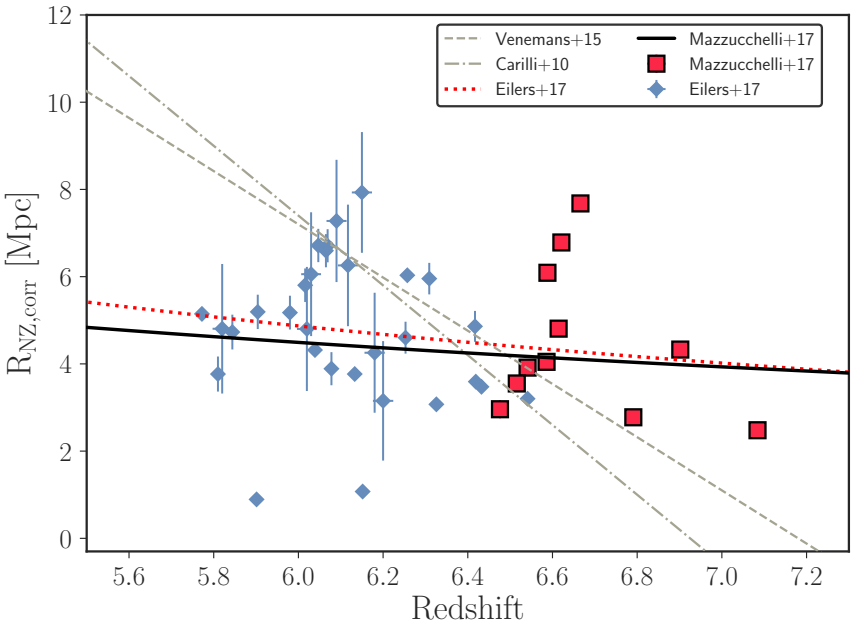

FIGURE 2.19: Near zone sizes as a function of redshift for the objects in our sample (*red squares*), and the ones taken from Eilers et al. (2017; *blue diamonds*). The errors plotted are only due to the uncertainties on the redshifts, and for the quasars in this work are particularly small due to our precise $z_{[CII]}$ measurements (see Table 2.10). We fit the data with a power law function (*solid black line*): the amplitude and slope values obtained are in line with the results presented by Eilers et al. (2017; *red dotted line*; see text and eq. 2.22). We find a redshift evolution of the near zone radii much shallower than that obtained in previous literature, e.g. by Carilli et al. (2010; *dot-dashed line*) and by Venemans et al. (2015; *grey dashed line*). This could be explained by the fact that $R_{NZ,corr}$ depends more strongly on the individual quasar properties which vary from object-to-object, rather than on the overall characteristics of the IGM.

$\langle \log(L_{bol}/L_{Edd}) \rangle \sim -0.41$ and a 1σ scatter of $\sim$0.4 dex, than their low−redshift counterparts, which present a mean of $\langle \log(L_{bol}/L_{Edd}) \rangle \sim -0.47$ and a scatter of $\sim$0.3 dex. A more homogeneous coverage of the quasar parameter space at high redshift will help us investigating this evolution in the future.

- We estimate the black hole seed masses ($M_{BH,seed}$) required to grow the observed $z \gtrsim$6.5 quasars studied here, assuming that they accrete at the constant observed Eddington ratio or with an Eddington ratio of unity, for a time equal to the age of the universe at the observed redshift, and with a constant radiative efficiency of 7%. In the first case, we derive $M_{BH,seed} \gtrsim 10^4$ $M_\odot$ (higher than what is expected in the collapse of Pop III stars), while in the second case we obtain a lower value, consistent with all current theoretical models; this is valid even in the scenario where the seeds are formed at z=20. Also, in the case the black hole seeds accrete at the Eddington rate with an efficiency of 10% from the beginning of the universe, their predicted masses are consistent with being formed by Pop III stars. Alternatively, we calculate that, if they seeds are created at $z \sim 20-30$ and accrete with ϵ=0.1, they would need to be as massive as $\gtrsim 10^{3-4}$ $M_\odot$ (see Figure 2.14).

- We calculate the Fe II/Mg II flux ratio, as a first-order proxy of the abundance ratio. We derive values systematically lower than the ones obtained for lower redshift quasars, implying a decrease of the iron abundance at $z \gtrsim 6.4$. However our measurements are

hampered by large uncertainties, and, within these errors, we are consistent with a scenario of no evolution of the abundance ratio with redshift, as previously found by De Rosa et al. (2011, 2014) from a smaller sample of high−redshift quasars.

- From new millimeter observations reported here for four objects, we derive precise redshift estimates ($\Delta z \lesssim 0.004$), and [CII] emission line and continuum luminosities, from which we obtain near infrared and total infrared luminosities. We study the $L_{[CII]}/L_{FIR}$ ratio as a function of L_{FIR} for these sources, and we place them in the context of present measurements from the literature, for both high and low redshift objects, normal star forming galaxies, LIRGS, ULIRGS and quasars. We find that the values obtained cover a parameter space similar to the one of ULIRGS.

- We calculate the near zone sizes of 11 objects. We study these measurements, together with the ones for a $5.6 \lesssim z \lesssim 6.5$ quasar sample from Eilers et al., 2017, as a function of redshift. The two data sets are analyzed with a consistent methodology; in agreement with Eilers et al., 2017, we find a much shallower evolution of the near zone sizes with cosmic times than what was found by previous work (e.g. Carilli et al. 2010, Venemans et al. 2015b). This result is also in line with recent radiative transfer simulations (Davies et al., 2018), and, as argued by Eilers et al., 2017, may be due to the much stronger dependency of the near zone sizes on the particular quasar characteristics (e.g. age and/or islands of neutral gas located inside the ionized spheres) than on the general IGM properties.

Chapter 3

The Environment of a z∼5.7 Quasar[1]

In the following chapter, we study the Mpc–scale environment around a quasar at z ∼5.7, by searching for LAEs in the field with a suite of broad– and narrow–band filters observations.

The sections below are organized as follows: in § 3.1 we describe the quasar target of this study, our observations and data reduction; in § 3.2 and § 3.3 we present our LAEs selection criteria, and the derived properties of our LAE candidates, respectively. In § 3.4, we study the environment of the quasar on the base of the candidates found; in § 3.5 we simulate a population of z ∼5.7 LAEs to which compare our results, and in § 3.6 we place our work in the context of the current clustering studies. Our selection of Lyman Break Galaxy is also reported in § 3.7. Finally, we discuss our findings in § 3.8.

3.1 Observations and Data Reduction

We present a search for LAEs in the field around the BAL quasar PSO J215.1512−16.0417 (hereafter PSO J215−16; Morganson et al. 2012). It has a bolometric luminosity of 3.8×10^{47} erg s^{-1}, with 0.2 dex of uncertainty, and a black hole mass of 6.7×10^{9} M$_{\odot}$, with an uncertainty of 0.3 dex. The redshift is z=5.732±0.007, measured from the O I emission line ($\lambda_{\rm rest}$ = 1307 Å). This line is the brightest and clearest among the emission lines observed in the spectrum of the quasar. As a further check, other emission lines were fitted (N V, S II, C II). The redshift estimates obtained are consistent (with a scatter of ∼0.02) within the astrophysical systematic uncertainties (all these estimates are taken from Morganson et al. 2012).

We obtained multi-wavelength photometry of the field around this quasar with the FOcal Reducer/low dispersion Spectrograph 2 (FORS2, Appenzeller and Rupprecht 1992) at the VLT. The observations were obtained over nine nights in 2013, June, July and August. We used the red sensitive detector consisting of two 2k×4k MIT CCDs. In order to decrease the read out time and noise, we adopted a 2×2 binning. The resulting pixel size is 0.25 arcsec/pixel and the total field of view is equal to 6.8×6.8 arcmin^2, i.e. 2.38×2.38 pMpc^2.

We collected images in two broad band filters R_SPECIAL (R, with a central wavelength λ_c = 6550 Å, and a width $\Delta\lambda$ = 1650 Å) and z_GUNN (z, λ_c = 9100 Å, $\Delta\lambda$ = 1305 Å), and in the narrow band filter FILT815_13+70 (NB, λ_c = 8150 Å, $\Delta\lambda$ = 130 Å). The filters allow us to select LAEs at redshifts between $5.66 \lesssim z \lesssim 5.75$ ($\Delta z \sim 0.1$), i.e. at the precise redshift of the black hole in the center of the quasar studied here. Using the broad filters, LBGs can be selected

[1]This chapter is a version of the paper Mazzucchelli et al., 2017a.

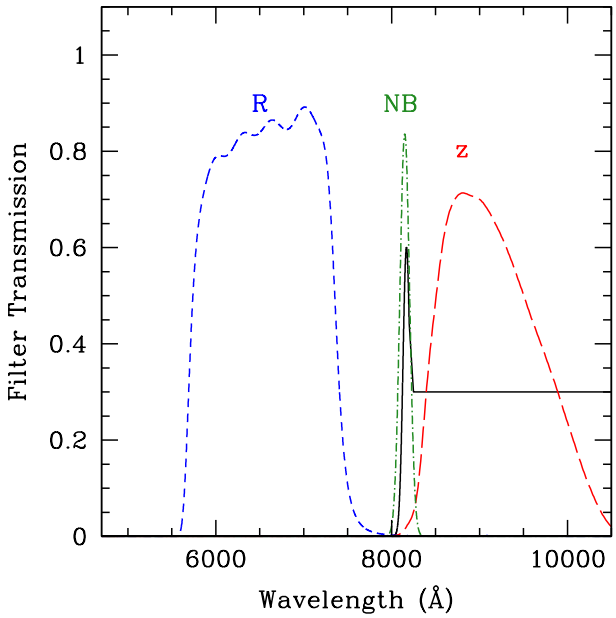

FIGURE 3.1: Set of filters used in the present study, R_SPECIAL (R, *short-dashed blue line*), z_GUNN (z, *long-dashed red line*) and the Narrow Band filter FILT815_13+70 (NB, *dot-dashed green line*). In *solid black line*, a synthetic spectrum of a LAE at the redshift of the quasar studied in this work ($z \sim 5.7$).

in a redshift range of $5.2 \lesssim z \lesssim 6.5$ ($\Delta z \sim 1.3$). The filter throughputs, together with a synthetic LAE spectrum at the redshift of the quasar, are shown in Figure 3.1.

The individual exposure times in each frame are 240s in R, 115s in z and 770s in NB. Each exposure was acquired with a dithering of $\sim 10''$, in order to account for bad pixels and remove cosmic rays. The total exposure times are, respectively, ∼1.13, 2.11 and 8.56 hr in the R, z and NB filter.

We perform a standard data reduction: we subtract from each exposure the bias, we apply the flat field and we subtract the background, then the images are aligned and finally combined; the astrometric solution was derived with `astrometry.net` (Lang et al., 2010). A composite RGB image of the quasar field is shown in Figure 3.2. The seeing values of the stacked images are equal to $0.''78$ in R, $0.''81$ in z and $0.''79$ in NB. In order to circumvent uncertainties due to different apertures or to the angular resolution of the images, we match the Point Spread Function (PSF) of the R and NB images to the one of the z filter frame (the one with the worst seeing), using the IRAF task gauss.

We calculate the photometry using, as reference sources, field stars retrieved from the Pan-STARRS1 catalog (Magnier et al., 2013). We calculate the conversion between the two different filter sets by interpolating spectra of standard stars. The relations found are :

$$R = r_{P1} - 0.277 \times (r_{P1} - i_{P1}) - 0.005 \tag{3.1}$$

$$z = z_{P1} - 0.263 \times (z_{P1} - y_{P1}) - 0.001 \tag{3.2}$$

$$NB = i_{P1} - 0.626 \times (i_{P1} - z_{P1}) + 0.014 \tag{3.3}$$

where r_{P1}, i_{P1}, z_{P1} and y_{P1} are the magnitudes in the Pan-STARRS1 filters. The obtained zero points values are 27.77 ± 0.04 in R, 27.12 ± 0.02 in z and 24.85 ± 0.04 in the NB filter.

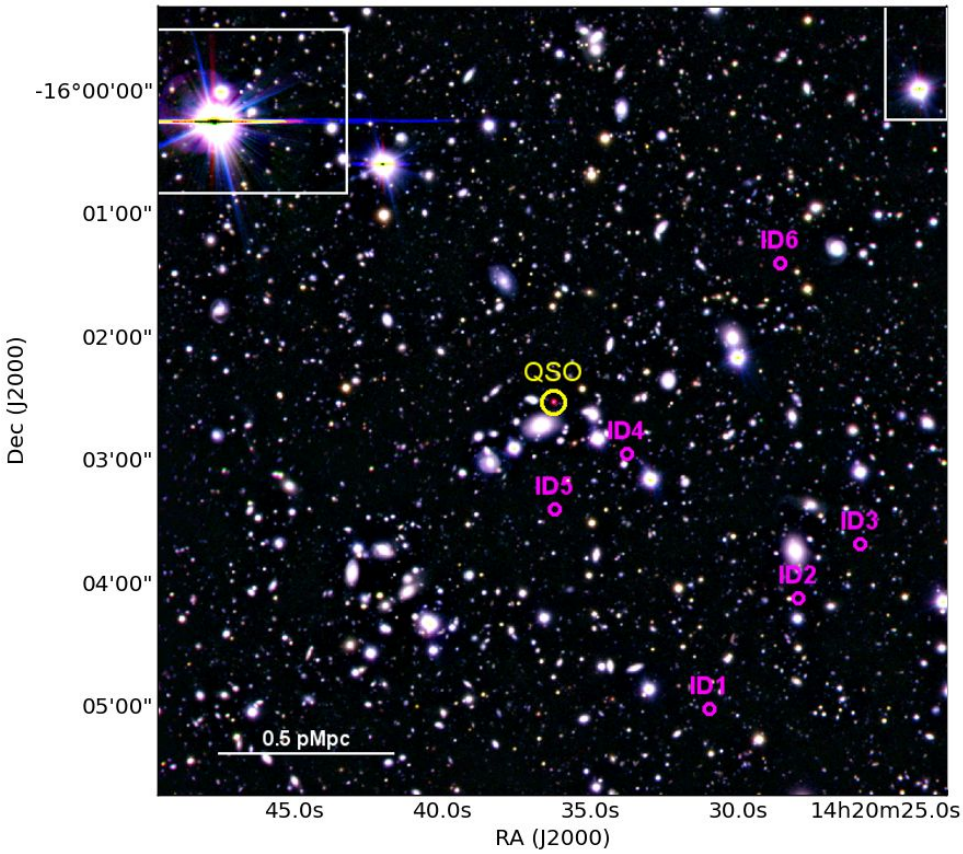

FIGURE 3.2: RGB composite image of the field around the quasar PSOJ215−16. In *magenta* we show the position of the sources only observed in the narrow band, but not detected (at 2σ confidence level) in the R and z filters (see Section 3.2). The position of the quasar and masked regions around bright stars are also shown. The total area analyzed is 37 arcmin^2.

We calculate the noise in our images by computing the standard deviation of flux measurements in circular apertures of 3 pixels radius that were placed randomly in empty regions in the images. This is the radius of the aperture over which we perform our photometry, as discussed below. We achieve limit magnitudes at 5σ level of 26.47, 25.96 and 26.38 mag in the R, z and NB frames.

In order to identify sources from the images, we use the software `SExtractor` (Bertin and Arnouts, 1996) in the double image mode, requiring a minimum detection threshold of 1.8σ. Since we expect LAEs to be strongly detected in the NB filter, we take this frame as the base of our selection. We cut the outskirts of the frames and mask saturated stars, where both the astrometry and the photometry were less reliable. The final effective area is equal to 37 arcmin^2 (i.e. $\sim$206 cMpc^2 at the redshift of the quasar).

We perform the photometry of the sources over an aperture of 3 pixel radius (0.″75). For our frames this is equal to 1.8×seeing: i.e. we encompass more the ∼90% of the flux and, at the same time, maximize the signal-to-noise ratio. We consider only sources with signal-to-noise ratio S/N>4 in the NB filter, and adopt a 2σ upper limit in R and z for non-detections in the broad band images (27.46 in R and 26.95 in z). Sources non detected in the broad bands are allowed in the catalog, and we substitute the R and z values with the respective 2σ limit magnitudes. Finally, we use the 'flags' parameter given by `SExtractor` in order to discard unreliable detections, rejecting sources with flags ≥ 4 (i.e. objects saturated, truncated, or whose aperture data are incomplete or corrupted); the final catalog encompasses 3250 sources.

We extrapolate the cumulative count for the sources detected in our NB frame, in order to estimate the completeness function of our study at the faint end (see Figure 3.3). We compute the logarithmic cumulative number counts of sources detected in NB as a function of NB magnitude. We fit it with a linear relation (in log-mag space) for 21<NB<25, and extrapolate it towards the faint end. The completeness is computed as the ratio between the expected number counts from the logN-logS extrapolation and the actual number of detected sources. Our catalog reaches a completeness of 80% and 50% at NB magnitudes of 26.3 and 27.1, respectively.

3.2 Selection of High Redshift Galaxy Candidates

In this work we follow the color selection defined in Bañados et al., 2013 (hereafter in this chapter 'B13'), and briefly described here.

LAEs are expected to be well detected in the narrow band and to show a break in the continuum emission. More precisely, we required our LAE candidates to satisfy the following criteria:

- (z−NB) > 0.75
  We request the flux density in the NB to be at least twice the one observed in the z filter. This cut implies that we are selecting objects with an equivalent width of the Lyα line in the rest frame greater than 25. (see Section 3.5).

- (R−z) > 1.0
  We expect lower flux at wavelength shorter than the Lyα emission line, i.e. a break in the

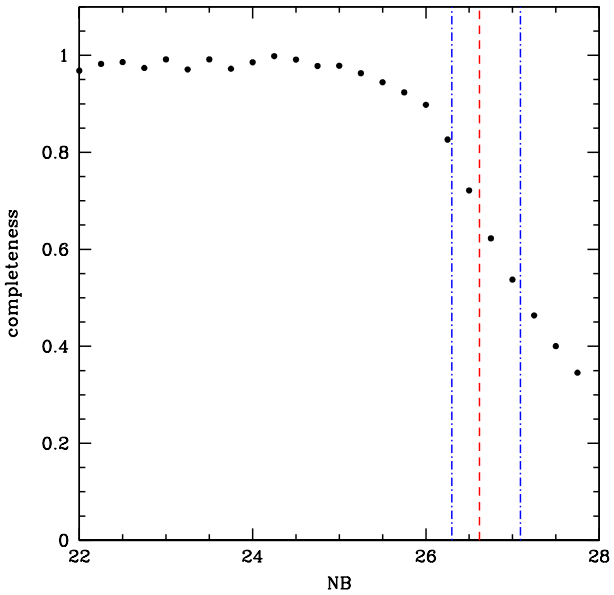

FIGURE 3.3: Detection completeness function for the sources in our catalog, as a function of NB magnitude (see text for details). With a *red, long-dashed line* we show the 4σ limit magnitude estimated from the image noise, which corresponds to a level of completeness of 67%. We show the 80% and 50% completeness levels (at magnitudes of 26.3 and 27.1, respectively), with *blue, dot-dashed lines*.

spectrum, which can be identified by requiring a very red R-z color. In case a source is not detected in R or z, we adopt the 2σ limit magnitudes.

- $|(z - NB)| > 2.5 \times \sqrt{\sigma_z^2 + \sigma_{NB}^2}$
  We want to select only objects with a significant flux excess in the NB. Therefore, we adopt a constrain in order to discard all the objects satisfying our selection criteria only due to their photometric errors.

- NB > 18
  Since LAEs are expected to be faint sources at these redshifts, we impose a lower limit to the observed NB magnitude. However, we note that there are no objects with NB$<$18 that satisfy all the previous criteria.

In Figure 3.4 we show the (z$-$NB) vs (R$-$z) color-color diagram, together with our high redshift galaxies selection. LAEs are expected to fall in the upper right part. In summary, we find no secure detections of LAEs in our field, i.e. no sources fully satisfy all the selection criteria described above. We observe six sources with a detection in the NB, that are not detected in both R and z frame. The ($z_{2\sigma,\mathrm{lim}}$-NB) color ranges from a value of 0.45 to 1.5. In the following analysis, we conservatively consider all these six sources as LAE candidates; however, we stress that, in order to know if these objects would fully satisfy our criteria, deeper R and z band observations are needed.

In Table 3.1 we report their coordinates, the NB magnitudes, the projected distances from the quasar, the estimated Lyα luminosities and the star formation rates (which are within the expectations for typical $z \sim 6$ LAEs, $SFR \sim 6^{+3}_{-2}$ $M_\odot$ yr^{-1}, Ouchi et al. 2008; see Section 3.3). Their postage stamps in the three filters are shown in Figure 3.5.

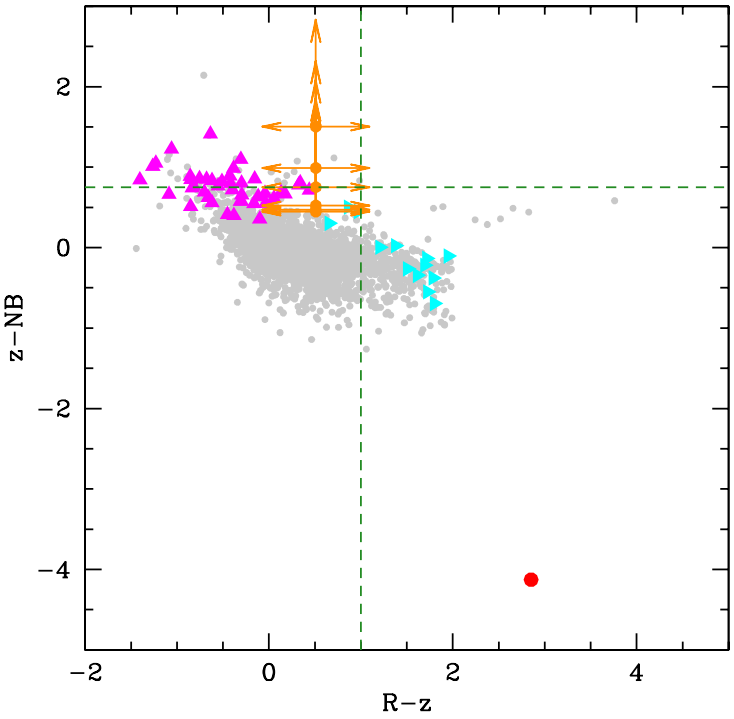

FIGURE 3.4: Color-Color diagram of the sources in our field detected in the NB filter with S/N >4. The sources detected with a significance lower than 2σ, only in the z or in the R filter, are shown as *magenta* and *cyan triangles* respectively. *Orange arrows* indicate objects undetected in both R and z (6 sources). Our selection cuts for LAEs are displayed with *green dashed lines*; LAEs should fall in the upper right panel (see Section 3.2 for the complete set of our criteria). No LAE candidates are securely found in our field. The *red point* in the lower right corner corresponds to the quasar.

TABLE 3.1: Source names, Coordinates, NB magnitudes and projected distances to the quasar of the objects retrieved in our field with a detection in NB (at S/N >4) and a non–detection in the broad bands. Also, we show the luminosities of the Lyα emission line and the star formation rates (SFRs) as estimated in Section 3.3. The errors on the SFRs are derived from the photometric uncertainties on the narrow band magnitudes, and do not account for systematics in the underlying assumptions .

ID J2000	**RA** J2000	**Decl** [AB]	**mag**$_{NB}$ [Å]	**r**$_{angular}$ [arcmin]	**r**$_{comoving}$ [cMpc]	**r**$_{physical}$ [pMpc]	$L_{Ly\alpha}$ 10^{42} [erg s^{-1}]	**SFR** [M$_\odot$ yr^{-1}]
ID1	14:20:31.1	-16:04:59.2	26.50 ± 0.22	2.79	6.58	0.98	$> 1.9 \pm 0.4$	1.2 ± 0.2
ID2	14:20:28.1	-16:04:05.9	25.45 ± 0.09	2.55	6.00	0.89	$> 5.1 \pm 0.4$	3.2 ± 0.3
ID3	14:20:26.0	-16:03:39.7	26.43 ± 0.21	2.74	6.46	0.96	$> 2.1 \pm 0.4$	1.3 ± 0.2
ID4	14:20:33.9	-16:02:55.9	25.96 ± 0.14	0.74	1.75	0.26	$> 3.2 \pm 0.4$	2.0 ± 0.2
ID5	14:20:36.3	-16;03:23.0	26.20 ± 0.17	0.88	2.08	0.31	$> 2.5 \pm 0.4$	1.6 ± 0.2
ID6	14:20:28.7	-16.01:23.8	26.48 ± 0.22	2.14	5.05	0.75	$> 2.0 \pm 0.4$	1.2 ± 0.2

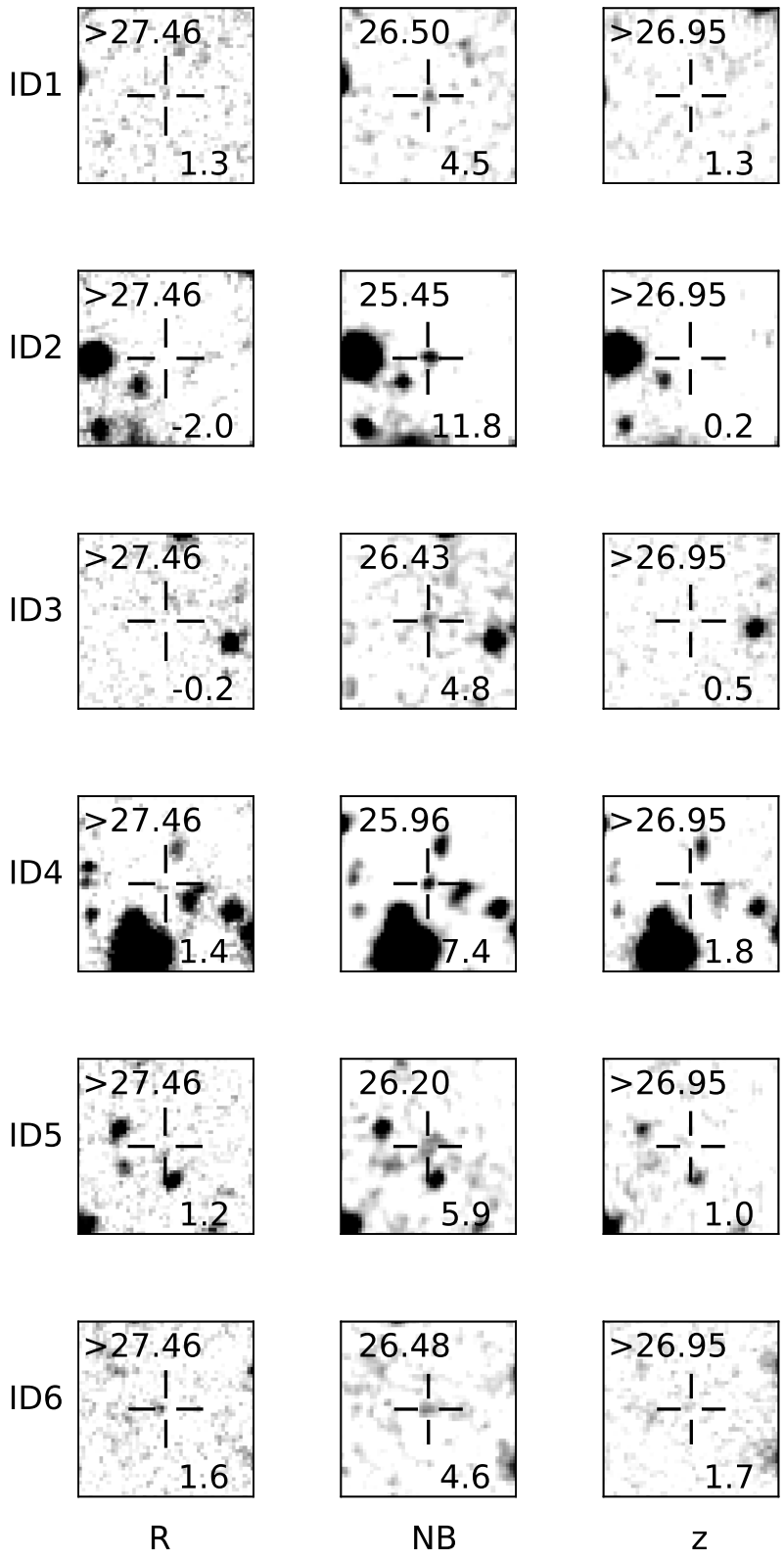

FIGURE 3.5: Postage stamps centered on the sources detected only in the NB, in a region of $12'' \times 12''$. The magnitudes and S/N in the three bands are also reported in top left and bottom right corner, respectively.

3.3 Star Formation Rate Estimates of LAE candidates

We infer here estimates of the star formation rates for our LAE candidates. We use as SFR tracer the luminosity of the Lyα emission line.

We obtain the integrated luminosity of the Lyα line from the flux density observed in the narrow band filter ($f_{\rm NB}$):

$$L_{\rm Ly\alpha} = f_{\rm NB} 4\pi d_L^2 \Delta\nu_{\rm NB} \tag{3.4}$$

where d_L is the luminosity distance at the redshift of the quasar and $\Delta\nu_{\rm NB}$ the width of the narrow band filter. In this estimate, we do not correct for the contribution of the continuum, expected to be very faint (none of our LAE candidates are detected in the broad bands).

From $L_{\rm Ly\alpha}$ we can derive the luminosity of the Hα emission line ($L_{\rm H\alpha}$). Assuming the case-B recombination (Osterbrock 1989), the conversion is given by $L_{\rm Ly\alpha} = 8.7 \times L_{\rm LH\alpha}$. Then, we use the following relation between SFR and $\rm L_{H\alpha}$ (Kennicutt and Evans, 2012):

$$\log \frac{SFR_{\rm Ly\alpha}}{\rm M_\odot \quad yr^{-1}} = \log \frac{L_{\rm H\alpha}}{\rm erg \quad s^{-1}} - 41.27 \tag{3.5}$$

We obtain SFR estimates in the range between (1.2±0.2)−(3.2±0.3) $\rm M_\odot\ yr^{-1}$ (all the SFR values, together with the respective $\rm L_{Ly\alpha}$, are reported in Table 3.1) In all our analysis, we do not consider possible absorption due to the galactic dust. Even if LAEs are thought to be rather dust-poor objects (e.g. Garel et al. 2015), there have been evidence for a non negligible fraction of dusty LAEs (Pentericci et al. 2009). The interstellar neutral gas, its geometry and dynamic, gives also an important contribution to the effective Lyα photon escape fraction. Indeed a higher $L_{\rm H\alpha}/L_{\rm Ly\alpha}$ ratio is expected in case of a lower Lyα photon escape fraction. In addition, we neglect the effect of the significantly neutral intergalactic medium at the high redshift under consideration. All these contributions concur in reducing the estimated SFRs: the values reported here can thus be considered only as upper limits.

3.4 Study of the Environment

In order to study the environment of the quasar PSO J215−16, we compare our findings both to earlier quasar environment studies, and to blank fields (i.e. fields where no quasars are present). In Figure 3.6 we show the cumulative number counts, rescaled to our effective area (37 $\rm arcmin^2$), of LAEs found in two blank fields, Ouchi et al., 2008 and Hu et al., 2010, and in the field of another $z\ \sim$5.7 quasar (see B13). The number counts of the objects found in this work are corrected taking into account the completeness of our catalog at the respective NB magnitude.

Ouchi et al., 2008 and Hu et al., 2010 searched for LAEs at redshift z =5.7 in seven Suprime-Cam fields and in the Subaru/XMM-Newton Deep Survey (SXDS), respectively. The total areas covered in the two studies are ∼1.16 and ∼1 $\rm deg^2$. The difference between the number counts of these two measurements may be ascribed to the fact that Hu et al., 2010 consider only the spectroscopically confirmed sources in their sample, while the sample of Ouchi et al., 2008 is based on the photometric selection, possibly affected by contaminants but also characterized

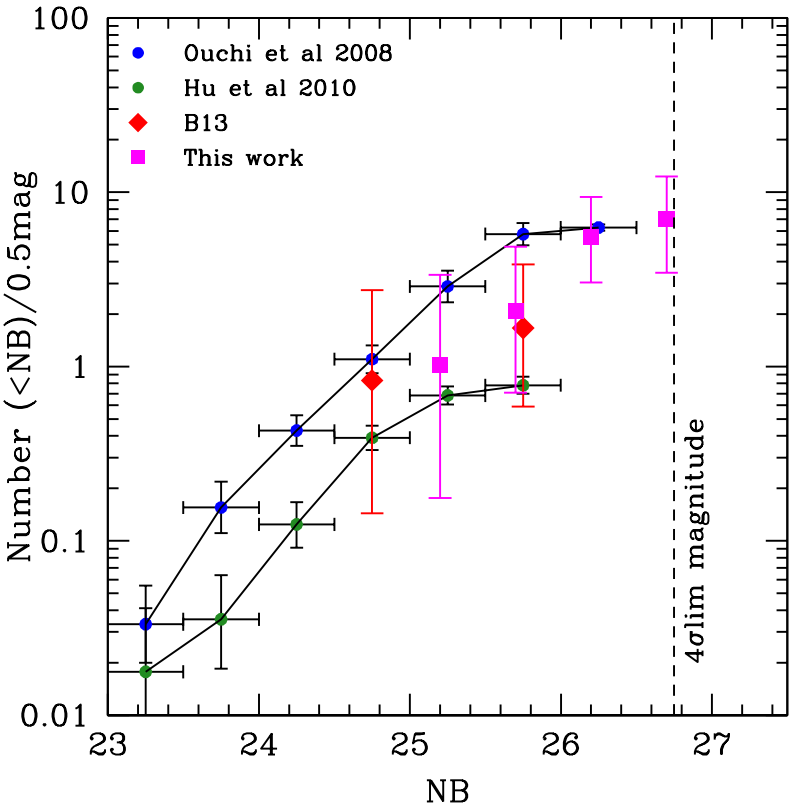

FIGURE 3.6: Cumulative number counts of LAEs observed in two blank fields, i.e. not containing quasars, by Ouchi et al., 2008 and Hu et al., 2010 (*blue* and *green dots*) and in the field of the z=5.7 quasar ULAS J0203+0012 by B13 (*red diamonds*). All the number counts are re-scaled to our effective area. Also, we show the 4σ limit magnitude in this work (*dashed line*). In the present study we retrieve six possible LAE candidates (*magenta squares*, see Section 3.2). The number counts of this work are corrected taking into account our completeness at the corresponding NB magnitudes. We have no evidence for an overdensity around the quasar.
The errors reported are the poissonian noise for small counts (Gehrels 1986).

by a higher completeness level. The present work and B13 are carried out with the same filter set and instrument, and assuming consistent selection criteria. Even if we consider all the sources detected solely in the NB filter in our work as LAE candidates (see Section 3.2), the number counts would be consistent with the blank field measurements and with B13.
There is no evidence for an overdensity of LAEs at the redshift of the quasar.

3.5 Simulation of LAE

We estimate the fraction of LAEs that we expect to detect, based on observations of blank fields, our filters set, and our image depths. We aim to assess, given the set-up of our observations, our ability to recover a population of galaxies that is gravitationally bound to the quasar.

We adopt a distribution of LAEs according to the luminosity function reported by Ouchi et al. (2008, with parameters L*=6.8 $\times 10^{42}$ erg s^{-1}, Φ^* = 7.7$\times 10^{-4}$ Mpc^{-3} and α=-1.5). We then create a synthetic population of LAEs, drawing objects from the luminosity function through the Monte-Carlo method. We modeled the LAEs as composed by a flat, continuum emission ($L_{cont} = L_{Ly\alpha}/EW$) and a Ly$\alpha$ emission line, implemented as a Gaussian function, with FWHM at rest-frame of 200 km s^{-1} (corresponding to typical line widths for LAEs, e.g., Ouchi et al. 2008). We account for the absorption due to the intergalactic medium using the reshift-dependent recipe given by Meiksin, 2006, and assume an exponential distribution of equivalent widths at rest frame (Zheng et al. 2014, $N = e^{-EW/50}$). Our mock spectra are randomly distributed in the redshift range $5.52 < z < 5.88$ and cover down to a luminosity of $L_{Ly\alpha} = 10^{41}$ erg s^{-1}. We then calculate the corresponding synthetic magnitudes in the filters used in this work. We consider the sources detected with our NB image depth, at 4σ magnitude limit. We substitute the z and R broad band magnitudes with their respective 2σ limit magnitudes, in case their values were fainter than our detection limits. We considered the synthetic LAEs detected by our color selection criteria (see Section 3.2), and all the sources not detected in both the broad bands but detected in NB.

In Figure 3.7, we show the EW at rest-frame and Lyα luminosity distributions of all our generated LAEs, of the subsample in the redshift range $5.6 < z < 5.78$ (the window in which we find LAEs in our simulation), and of LAEs recovered by the criteria presented in this study. We recover sources with a minimum EW at rest frame of 25 Å, and a Lyα luminosity of 1.32$\times 10^{42}$ erg s^{-1}. The last value is in agreement with what obtained if one calculates the limit $L_{Ly\alpha}$ by considering that all the flux observed in the NB filter, at our 4σ limit, is due the line emission ($\sim$1.72$\times 10^{42}$ erg s^{-1}, see Section 3.3).

We normalize the total number of simulated sources to the number of objects expected in a blank field, in a cosmological volume equal to the one analyzed here, where we use a line-of-sight depth of 40 cMpc (see Section 3.1). Integrating the LAE luminosity function down to the Lyα luminosity limit considered in the simulation (10^{41}erg s^{-1}) we expect to measure 81.4 sources. Taking into account our depth and selection criteria, we recover 28% of the original sample. Therefore, we expect to observe $\sim$23 LAEs in a field of the same cosmological volume as our study. We actually selected six LAEs candidates in our images; correcting for a completeness level of 67% at our NB magnitude limit (see Figure 3.3), we obtain 8 objects. This

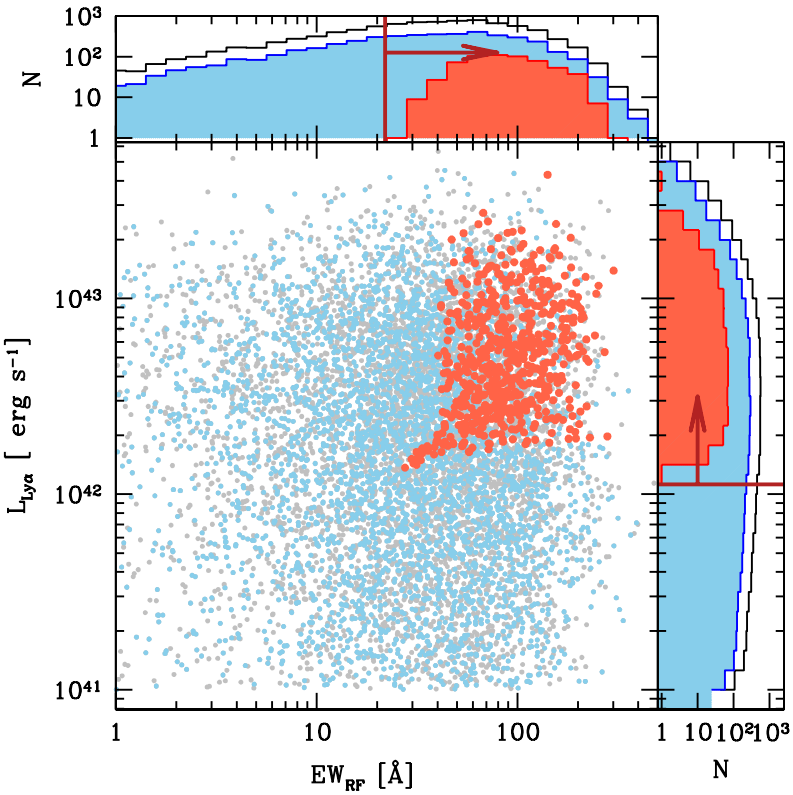

FIGURE 3.7: Equivalent width at rest-frame and Lyα luminosity of all our synthetic templates of LAEs (*grey*), of sources in the redshift range 5.61<z<5.77 (*blue*), and of the ones detected as LAEs by our selection criteria (*red points*). The *upper* and *right* panels show the distribution of EW and Lyα luminosity, respectively. The *red, solid lines* shows the minimum EW and Lyα luminosity retrieved (25 Å and 1.32×10^{42} erg s^{-1}, respectively).

comparison suggests that the field surrounding PSO J215−16 might be less than ∼3 times less dense than the blank field, in agreement with what is shown in Figure 3.6[2].

We report in Figure 3.8 the logarithmic distribution of the LAEs systemic velocities with respect to the quasars, again, for all our simulated sample and for the objects detected as LAEs. The quasar is not located at the center of the redshift range covered by our selection. Nevertheless we can still recover a significant fraction of galaxies even at the red edge. If we assume that LAEs that are gravitationally bound to the quasar are distributed following a Gaussian function centered on the quasar systemic velocity and a width of $\sigma \sim 500$ km s^{-1}, we calculate that, given the shifted position of the quasar, we can recover 56% of the total LAE population. If we assume a velocity dispersion of ∼1000 km s^{-1}, our estimate decreases to 53%. Several studies (e.g. Hashimoto et al. 2013, Song et al. 2014) suggest that the Lyα emission could be redshifted with respect to the systemic velocity of the source by ∼200 km s^{-1}. If this would be the case, we would be affected even more. Nevertheless, we find that the fraction of observed objects in this case would decrease only to 49% and 48% (in case of σ=500 km s^{-1} and 1000 km s^{-1}, respectively). Thus, even in this scenario, we can still recover $\gtrsim$50% of the expected LAEs present in the proximity of PSO J215−16.

[2]We note that Ouchi et al., 2008 states that their completeness level at their last luminosity bin (NB = 26) is estimated to be 50%−60%. Therefore, the last point of the blue curve in Figure 3.6 should be corrected accordingly.

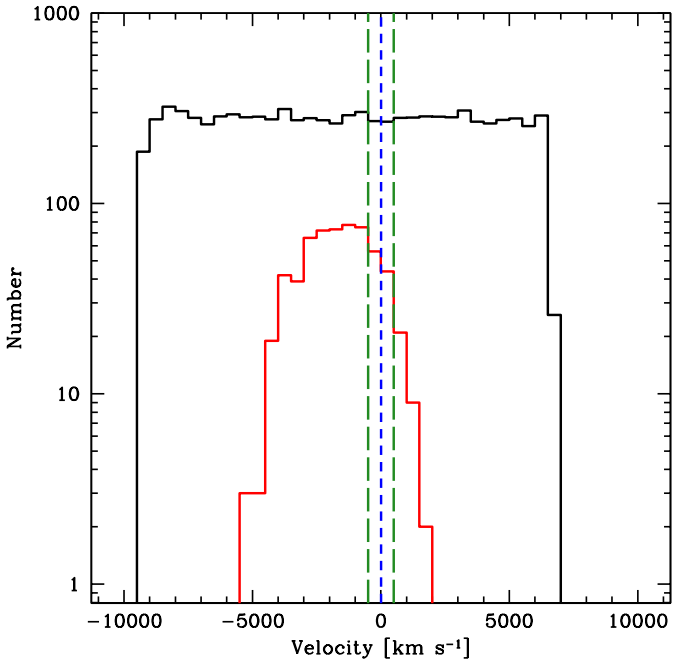

FIGURE 3.8: Velocity distribution of mocked LAEs, with respect to the systemic velocity of PSO J215−16 (*short-dashed, blue line*). In *black* we report the distribution of all the simulated sources, while in *red* only the sources recovered as LAEs. The velocity window encompassing +500 km s^{-1}/-500 km s^{-1} with respect to the quasar is shown with *long-dashed, green lines*. The velocity window is not centered on the redshift of the quasar, but we still recover $\gtrsim$50% of the expected galaxies population gravitationally bound to the quasar.

It is necessary to consider that our observed counts are also affected by Poisson noise and cosmic variance. Trenti and Stiavelli, 2008 provide estimates on the variance of the observed number counts, taking into account both Poisson noise and cosmic variance, and based on a variety of parameters (e.g. the survey volume and completeness, the halo filling factor and expected number of objects)[3]. In our case, we consider a cosmological volume V given by our field of view and a redshift interval of $\Delta z \sim 0.16$, centered on z=5.69 (V∼14900 $cMpc^3$, see Figure 8); an intrinsic number of objects equals to the one recovered by our LAE simulation (23), a completeness of 67% (see Section 2 and Figure 3.3) and a Sheth-Tormen bias calculation. Kovač et al., 2007, studying the clustering properties of LAEs at $z \sim 4.5$, find a value for the duty cycle of high redshift LAEs varying within 6%−50%. We consider here both extreme cases. However, Kovač et al., 2007 consider a sample of LAEs with a minimum EW of 80 Å; since our EW limit is lower (25 Å, see Figure 3.7), we expect that the halo filling factor for our case would be closer to 50%. Then, we expect to observe 15 ± 7 (9) sources in the case of a duty cycle of 6% (50%), where the fractional uncertainty due to cosmic variance and Poisson noise are 36% (49%) and 26% (in both cases), respectively. These results are consistent within 1.3σ, in the first case, and 1σ in the second case with what expected in the present study.

Conversely, we can also obtain a rough estimate of the cosmic variance, for a population of galaxies for which we know the expected number density in a certain volume, following Somerville et al., 2004. They use cold dark matter models to derive the expected bias (b) and

[3] http://casa.colorado.edu/~trenti/CosmicVariance.html

root variance of the dark matter ($\sigma_{\rm DM}$) as a function of galaxy number density and survey volume, respectively (see their Figure 3). We consider our survey volume as reported above, and an expected number density obtained integrating the LAE luminosity function until the Lyα luminosity limit from our simulation ($\sim 10^{-3}$ cMpc^{-3}); we derive a fractional cosmic variance of $\sigma_{\rm v} = b\sigma_{\rm DM}$ $\sim$0.66 for a population of galaxies at z=6. This value is higher than what recovered using the method illustrated by Trenti and Stiavelli, 2008. Indeed, one needs to consider that the cosmic variance is not a trivial quantity to estimate, and depend on several assumptions considered in the models, e.g. the LAEs halo filling factor. Considering the latter value obtained, we would expect to detect 23 ± 15 sources, which, taking into account our completeness, is consistent within 1σ with the observations reported here. Also, considering a clustering scenario, e.g. consistent with the LAE-LAE clustering case (see Ouchi et al. 2003 and Section 3.6), we would obtain 26 ± 18 sources, consistent with the observed ones.

3.6 Clustering

We may also study the environment of PSO J215-16 through a clustering approach. If quasars and galaxies are indeed clustered, the excess of probability to find a galaxy at a distance r from a quasar, with respect to a random distribution of sources, can be estimated through the two-point correlation function (Davis and Peebles, 1983):

$$\xi(\mathrm{r}) = \left(\frac{\mathrm{r}}{r_0}\right)^{-\gamma} \tag{3.6}$$

where r_0 and γ are the correlation length and clustering strength, respectively. In order to account for redshift distortions on the line of sight, we can consider instead the volume-averaged projected correlation function. This is $\xi(\mathrm{r})$ integrated over a line-of-sight distance $d = 2v_{max}/aH(z)$ (with v_{max} maximum velocity from the quasar) and within a radial bin of width $[\mathrm{R_{min}}, \mathrm{R_{max}}]$ (Hennawi et al., 2006):

$$\overline{W}(\mathrm{R_{min}}, \mathrm{R_{max}}) = \frac{\int_{-d/2}^{d/2} \int_{\mathrm{R_{min}}}^{\mathrm{R_{max}}} \xi(\mathrm{r}) 2\pi dR dr}{V} \tag{3.7}$$

where V is the volume of the cylindrical shell:

$$V = \pi(\mathrm{R_{max}^2} - \mathrm{R_{min}^2})d \tag{3.8}$$

Therefore, the number of galaxies that we expect to find around a quasar within a volume V in the presence of clustering is:

$$\mathrm{NC} = \mathrm{N}(1 + \overline{W}(\mathrm{R_{min}}, \mathrm{R_{max}})) \tag{3.9}$$

In case of no clustering, the number of sources expected is:

$$\mathrm{N} = nV \tag{3.10}$$

where n is the number density of galaxies per cMpc^{-3}, above a certain limit in luminosity. In this scenario, N is equal to the number of galaxies found in a blank field within a cosmological volume V.

In this study, we calculate n by integrating the LAE luminosity function (Ouchi et al., 2008) down to the luminosity limit obtained by our simulation (1.32×10^{42}erg s^{-1}, see Section 3.5). We consider a line-of-sight distance given by $v_{max} = 4000$ km s^{-1} (consistent with the interval probed by our NB selection, see Sections 3.1 and 3.5, and Figure 3.8), $R_{min} = 0.001$ cMpc and increasing values of $R = R_{max}$.

In Figure 3.9 we show the number of galaxies expected as function of R in case of no clustering (eq. 3.10), and in different scenarios of quasar-galaxy clustering (eq. 3.9). Since there are currently no studies of LAE-quasar clustering at high redshift, we consider for comparison some other illustrative cases. We take values of r_0 and γ obtained by observations of galaxy-quasar clustering at lower-z and LAE-LAE and quasar-quasar clustering at $z \sim 5$.

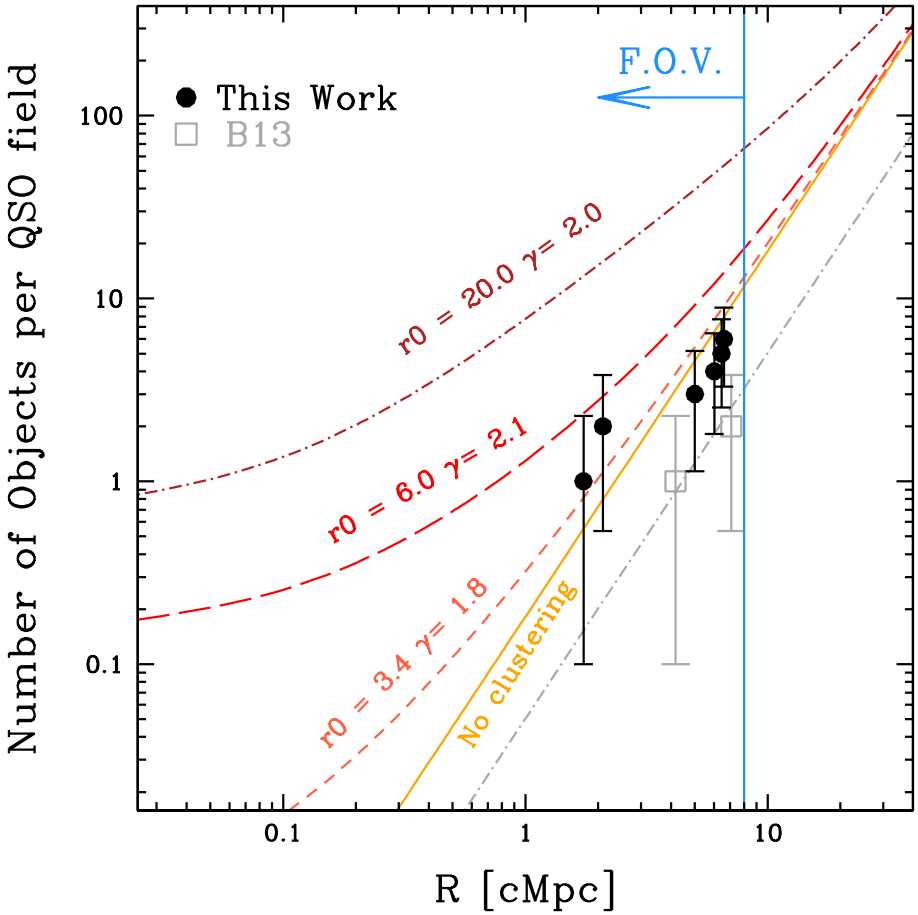

FIGURE 3.9: Expected number of LAEs, given the depth reached in this study, as a function of projected distance from the quasar, in case of no clustering (e.g. a random distribution of sources, *yellow solid line*), and for some illustrative clustering scenarios, taken from observational studies (Zhang et al. 2013, Ouchi et al. 2003 and McGreer et al. 2016, *short-dashed*, *long-dashed* and *dot-short-dashed line*, respectively, see text for details). The counts of LAEs observed in this study are reported (not corrected for completeness). Also, we report the LAEs found by B13, and their expected number of sources in case of no clustering, taking into account the depth of their study (*dot-long-dashed line*). For the sake of clarity, we do not report the respective cases of clustering scenarios. We show the field of view (F.O.V.) encompassed by our study. The errors are the poissonian noise on small counts from Gehrels, 1986. The counts of the observed LAEs are consistent with what expected in a blank field.

Indeed, studies of galaxy-quasar clustering at $z \sim 1$ (Zhang et al. 2013) estimate r_0=6 h^{-1} cMpc and γ=2.1[4]. Ouchi et al., 2003 derive the clustering properties of LAE at $z = 4.86$ from a sample of objects detected in the Subaru Deep Field, for which they obtain $r0 = 3.35$ h^{-1} cMpc and γ=1.8. At high redshift, constraints on the quasar-quasar clustering properties are given by the discovery of a close bright quasar pair, with only 21″separation, at z∼5 (McGreer et al., 2016). The correlation function derived from this pair gives r_0 >20 h^{-1} cMpc and γ=2.0[5]. We show the number of LAEs found in this study. We also report the objects recovered by B13 and the number of sources expected in their study in case of no clustering (since their observations are shallower than the ones presented here, with a Lyα luminosity limit of 3.74×10^{42}erg s^{-1}, the number of background sources expected is lower).

Our number counts are consistent with a scenario of no clustering (i.e. the background counts, in line with what obtained in Section 3.4), and do not show evidence of strong clustering in neither of the two quasar fields.

3.7 Lyman Break Galaxies Analysis

In addition to the LAE selection, we also search for LBGs using the dropout technique. Since LBGs are expected to be characterized by a strong UV continuum, observed in the z filter, we use the catalog obtained taking the z frame as our reference image. We consider all the sources with S/N>4 in z, and we apply only a selection using the broad band filters: we ask for a red R-z color (R-z>2) and, since we expect galaxies at these redshift to be faint, we require z>21. We recover 37 LBG candidates: we report the color-magnitude (R-z) vs z in Figure 3.10. It is worth to notice that, in the selection of LBG candidates, we are mainly limited by the depth of the R image ($R_{2\sigma} = 27.46$) rather than by the z one; indeed, the faintest sources with ($R_{2\sigma}$−z)>2 would have z≤25.46 in our analysis ($z_{5\sigma,\mathrm{lim}} = 25.96$).

For comparison, we refer to the works by Brammer et al., 2012 and Skelton et al., 2014, who compiled catalogs for some well-known extra-galactic fields, completed with spectroscopic and photometric information. We consider four fields, that can be used as comparison blank fields for our study: All-wavelength Extended Groth Strip International Survey (AEGIS), the Cosmic Evolution Survey (COSMOS), the Great Observatories Origins Survey Northen field (GOODS-N) and the UKIRT InfraRed Deep Sky Survey (UKIDSS) Ultra Deep Field (UDS).

We selected LBG candidates from the catalogs imposing the same selection criteria as in the present study. In order to account for the different image depths, we consider only sources with z and R magnitude lower than the limits in our field (z< $z_{5\sigma,\mathrm{lim}} = 25.96$ and R< $R_{2\sigma,\mathrm{lim}} = 27.46$). The GOODS-N and UDS fields are shallower than our images in both R and z and only in the z frame, respectively. In these cases, we take as limits the corresponding values provided by Skelton et al., 2014 ($z_{5\sigma,\mathrm{lim,GOODSN}} = 25.5$, $R_{2\sigma,\mathrm{lim,GOODSN}} = 27.19$ and $z_{5\sigma,\mathrm{lim,UDS}} = 25.9$). We also consider the sample of LBG candidates recovered by B13 around ULAS J0203+0012

[4]We note, however, that the galaxies studied by Zhang et al., 2013 are not selected as LAEs but by considering all the sources in the quasar field recovered in the SDSS-Stripe 82 catalog brighter (in the *i*-band) than a certain threshold value, which depends on the field depth. This selection comprehends also passive and red galaxies.

[5]These values are in agreement with the ones found by Shen et al. (2007, $r0$=25.0 h^{-1} cMpc and γ=2), based on a sample of lower redshift ($z > 3.5$) bright SDSS quasars. However, we note that other quasar clustering studies, such as Eftekharzadeh et al., 2015, suggest much smaller clustering scales, with $r0$=7.59 h^{-1} cMpc (obtained from a lower luminosity, z∼3.4, quasar sample; see also Section 3.8).

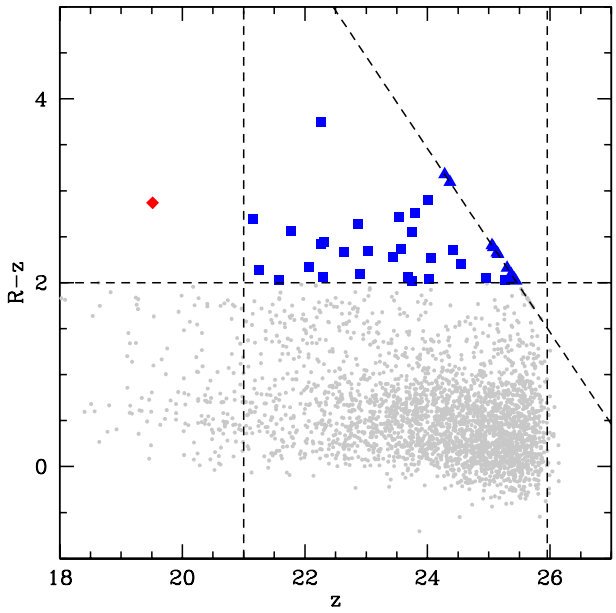

FIGURE 3.10: Color-magnitude diagram (R-z) vs z. In *grey points* all the sources detected in our field, considering the z frame as reference. The LBG candidates found from the z frame (37) are reported in *blue squares*. We show with *vertical dashed lines* the lower limit on the z magnitude (z > 21) and the 5σ upper limit (z=25.96). The *horizontal line* highlights our color criteria. The *diagonal dashed line* displays the 2σ limit magnitude in the R frame. The objects not detected in the R frame at 2σ level are reported in *blue triangles*. The *red diamond* shows the quasar position.

(20 sources), where they used an analogous selection method as the one described here. They reach limit magnitudes in the z and R bands of $z_{5\sigma,\mathrm{lim,B13}} = 25.14$ and $R_{2\sigma,\mathrm{lim,B13}} = 27.29$.

In Table 3.2 we report information on the comparison fields and on our field, i.e. coordinates, effective areas, literature references and characteristics of R and z filters. Although the different fields were imaged with slightly different filter sets, the redshift windows covered are large ($\Delta z \sim 1.2$) and corresponding to the one spanned in the present study[6]. We report the cumulative number counts, scaled to our effective area, of the sources found in the four blank fields and around the quasars (Figure 3.11). The difference between the counts obtained in the UDS field with respect to the counts in the other blank fields may be due to a diverse contribution of contaminant sources. Indeed, the UDS field was imaged through a R filter slightly redder than the ones used in the other fields (see Table 3.2): this might turn into a more conservative selection of high-redshift LBGs. Recent studies suggest also that the UDS field might be intrinsically underdense in z∼6 galaxies with respect to other well-known fields (Bowler et al. 2015, Bouwens et al. 2015b).

[6]With the filters used, in the AEGIS and COSMOS fields we span $5.2 \lesssim z \lesssim 6.3$, $\Delta z \sim 1.1$, in the GOODS-N field $5.2 \lesssim z \lesssim 6.4$, $\Delta z \sim 1.2$, while in the UDS field $5.4 \lesssim z \lesssim 6.5$, $\Delta z \sim 1.1$. In the present study and in B13 we are selecting sources in $5.2 \lesssim z \lesssim 6.5$, $\Delta z \sim 1.3$.

TABLE 3.2: Field names, coordinates, effective areas and technical characteristics for the R and z filters of our comparison fields and the one studied here. The areas analyzed in this study and in B13 differ due to the diverse masking. References from the literature are: (1) Hildebrandt et al., 2009, (2) Erben et al., 2009, (3) Capak et al., 2004, (4) Furusawa et al., 2008, (5) Bañados et al., 2013, (6) This work.

Field	**RA** [J2000.0]	**DEC** [J2000.0]	**Effective Area** [arcmin^2]	$\lambda_{c,R}$ [Å]	$\Delta\lambda_R$ [Å]	$\lambda_{c,z}$ [Å]	$\Delta\lambda_z$ [Å]	**Instrument**	**Reference**
AEGIS	14:18:36.00	+52:39:0.00	88	6245	1232	8872	1719	MegaCam@CFHT	(1), (2)
COSMOS	10:00:31.00	+02:24:0.00	154	6245	1232	8872	1719	MegaCam@CFHT	(1), (2)
GOODS-N	12:35:54.98	+62:11:51.3	93	6276	1379	9028	1411	Suprime-Cam@Subaru	(3)
UDS	02:17:49.00	−05:12:2.00	192	6508	1194	9060	1402	Suprime-Cam@Subaru	(4)
B13	02:03:32.38	00:12:29.06	44	6550	1650	9100	1305	FORS2@VLT	(5)
This work	14:20:36.39	-16:02:29.94	37	6550	1650	9100	1305	FORS2@VLT	(6)

We can compare the cumulative number counts of LBGs in the field of the quasar studied here with the ones found in the comparison blank fields. In order to avoid incompleteness issues in the low-luminosity end, we take only sources with R<$R_{lim,5\sigma}$, considering the GOODSN field, which is the shallowest among our fields ($R_{lim,5\sigma}$=26.2). Taking into account our color selection criterion, we obtain a resulting z magnitude limit of 24.2. At this limit, the counts of the LBG candidates in our quasar field is consistent within 1σ with the counts in the UDS field, and lower than the ones in AEGIS, COSMOS and GOODS-N fields by ∼1.7, 1.3 and 1.1σ respectively. The quasar field analyzed here appears only marginally (∼1.1σ) denser than the one studied in B13. These results are hence in agreement with B13, where no overdensity of LBGs with respect to a blank field was found.

Some general caveats are to be taken into account. Considering our broad selection criteria, both our sample and the ones derived from the comparison fields might be contaminated by red, lower redshift sources. We employ the further information provided in the catalogs of the comparison fields in order to better characterize the sources retrieved by our LBGs selection. We can consider the available photometric redshift estimates, computed with the public code EAZY (Brammer, van Dokkum, and Coppi 2008), which take into account all the photometric information present in the catalog. We take only the objects with a reliable redshift estimate, as based on the quality parameter Q_z ($Q_z < 2.0$, see Brammer, van Dokkum, and Coppi 2008), and for which z_{phot} ≥5.0. Only the 6%, 10%, 4% and 9% of the LBG sample from, respectively, AEGIS, COSMOS, GOODS-N and UDS field could be identified as high-redshift galaxies (see Table 3.3), while the vast majority was better fitted by a z∼1 galaxy model. This simple test shows how the selection criteria used here, without the help of further bands, lead us to a highly contaminated sample.

In summary the LBGs selection also does not reveal a possible overdensity around the quasar. However, due to the wide redshift range considered, an enhancement in the number of LBGs in the quasar field would represent an indication, more than solid evidence, for the presence of an overdensity of galaxies in the proximity of the quasar.

TABLE 3.3: Field names, total number of LBG candidates retrieved by our photometric cuts and number of sources with photometric redshift estimates corresponding to $z_{phot} \geq 5$.

Field	Number LBGs	Number phot LBGs
AEGIS	176	11
COSMOS	257	26
GOODS-N	186	7
UDS	187	17

3.8 Discussion

We do not find evidence for an overdensity of LAEs in an area of ∼37 arcmin^2 centered on the z ∼5.73 quasar PSO J215−16. Here we investigate possible scenarios to explain our findings.

- *The overdensity is more extended than our field of view*

  Overzier et al., 2009 and, more recently, Muldrew, Hatch, and Cooke, 2015, through a

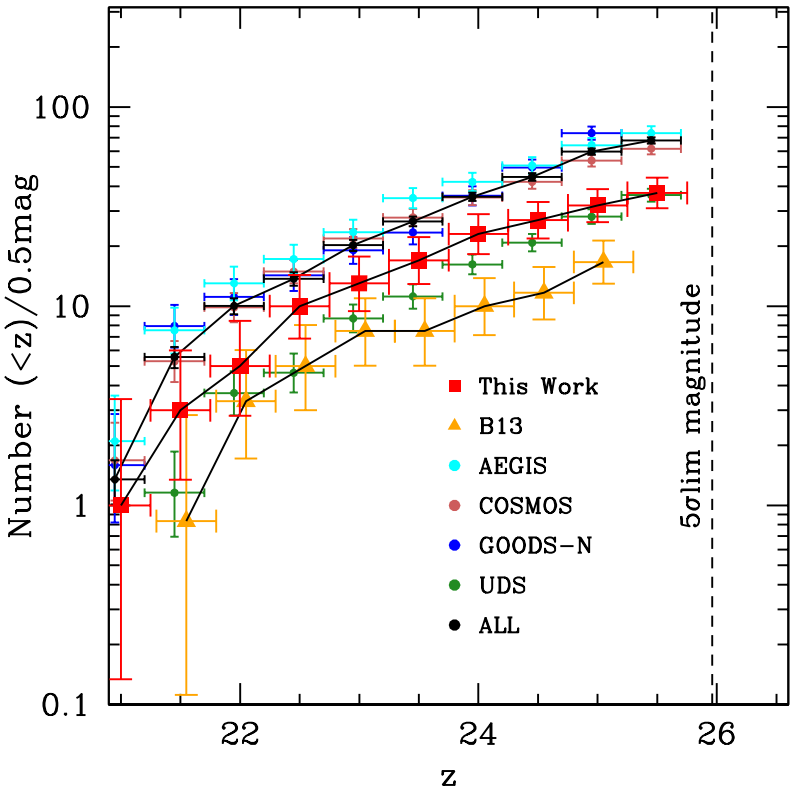

FIGURE 3.11: Cumulative Number Counts of LBGs at z∼6. All the counts are scaled for the effective area in our study. We report the candidates found around the z=5.73 quasar PSO J215−16 (*red squares*) and the quasar ULAS J0203+0012 (*orange triangles*, B13), slightly shifted with respect to the other fields in order to avoid confusion. We show the sources selected, using the same selection criteria and image depth, in four comparison blank fields (AEGIS-*cyan*, COSMOS-*brown*, GOODS-N-*blue* and UDS-*green circles*). The result obtained considering all the blank fields together is shown with *black circles*. The errors are taken from the poisson noise in case of low counts statistics (Gehrels 1986).

combination of N-body simulations and semi-analytical models, find that overdensities of galaxies at z∼6 are expected to be very extended, and can cover regions up to ∼25−30 arcmin radius, corresponding to $\gtrsim$20 pMpc at that redshift. In the present study we cover only a region of ∼1 pMpc transversal radius, and we might be missing a large part of a potential overdensity[7].

From an observational perspective, enhancements in the number of galaxies around quasars have been reported on rather modest scales, comparable to ours or even smaller. However, there are indications, based on LBGs searches, that some quasars are surrounded by overdensities on larger scales, even if a further spectroscopic confirmation is needed (see Section 1.5.4).

In Table 3.4 we show a summary of the findings obtained by diverse studies, where they considered different areas and techniques (see also Section 1.5.4).

In our case, in order to discard or confirm this scenario, we would need further observations covering a wider area (e.g with a radius of $\gtrsim$20 arcmin).

[7]We would like to stress that, in the hypothesis that the quasar occupies the center of a z ∼6 overdensity similar to the one found by Toshikawa et al., 2014 in a blank field, searches in area of ∼2−3 pMpc should still show evidence of an enhancement in the number of galaxies with respect to a blank field.

TABLE 3.4: List of z>5 quasars whose large-scale fields were inspected for the presence of galaxy overdensities. We report the quasars names, redshifts, literature references, instruments used and area covered in each study (in comoving and physical Mpc^2 at z ∼6). The references are coded as: (1) Stiavelli et al., 2005, (2) Willott et al., 2005, (3) Zheng et al., 2006, (4) Kim et al., 2009, (5) Utsumi et al., 2010, (6) Husband et al., 2013, (7) Bañados et al., 2013, (8) Simpson et al., 2014, (9) Morselli et al., 2014, (10) McGreer et al., 2014 , (11) this work. All these studies, except for Bañados et al., 2013 and this work which searched for LAEs, are based on i-dropout selection. We report also whether the fields were found overdense (+), underdense (-) or consistent (0) with respect to a comparison blank field. We note cases in which the same field was found consistent with a blank field when inspected on small scales, while overdense when studied over larger scales (e.g. SDSS J1048+4637 and SDSS J1148+0356). The overdensity reported by Utsumi et al., 2010, even if found with the Subaru SuprimeCam, spreads across an area of ∼ 3Mpc radius, therefore it would have been detected also by searches over smaller fields of view.

Object	Redshift	Ref	Instrument	FoV [cMpc^2]	FoV [pMpc^2]	Overdensity
ULAS J0203+0012	5.72	(7)	VLT FORS2	250	5.6	0
SDSS J0338+0021	5.03	(6)	VLT FORS2	250	5.6	+
SDSS J0836+0054	5.82	(3)	*HST* ACS	65	1.4	+
SDSS J1030+0524	6.28	(1)	*HST* ACS	65	1.4	+
		(2)	GMOS-N	170	3.7	0
		(4)	*HST* ACS	65	1.4	+
		(9)	LBT LBC	3136	64.0	+
SDSS J1048+4637	6.20	(2)	GMOS-N	170	3.7	0
		(4)	*HST* ACS	65	1.4	0
		(9)	LBT LBC	3136	64.0	+
ULAS J1120+0641	7.08	(8)	*HST* ACS	65	1.4	0
SDSS J1148+0356	6.41	(2)	GMOS-N	170	3.7	0
		(4)	*HST* ACS	65	1.4	-
		(9)	LBT LBC	3136	64.0	+
SDSS J1204−0021	5.03	(6)	VLT FORS2	250	5.6	+
SDSS J1306+0356	5.99	(4)	*HST* ACS	65	1.4	-
SDSS J1411+1217	5.95	(9)	LBT LBC	3136	64.0	+
SDSS J1630+4012	6.05	(4)	*HST* ACS	65	1.4	+
CFHQS J2329−0301	6.43	(5)	Subaru SuprimeCam	4600	83.3	+
CFHQS J0050+3445	6.25	(10)	*HST* ACS & WFC3	29	0.6	-
PSO J215.1512−16.0417	5.73	(11)	VLT FORS2	206	4.5	0

- *The ionizing emission from the quasar is preventing structure formation in its immediate proximities*

  Strong radiation from a bright quasar can ionize its nearby regions (up to ∼1−5 pMpc radius around z ∼6 quasars, e.g. Venemans et al. 2015b, Eilers et al. 2017, and Section 2.5.10, Figure 2.19), with an increase in both the temperature and ionized fraction of the IGM, and in the intensity of the local UV radiation field.
  The effects on the visibility of the Lyα radiation in this region are not straightforward to deduce. As a consequence of the increase in the UV background radiation field, a higher Lyα transmission flux value is expected around the quasar with respect to the typical IGM environment at the same redshift (Bruns et al. 2012). However, in addition to the rise in the UV background, also the nearby IGM temperature increases. Thus, the isothermal virial temperature necessary for gas accretion in the dark matter halo is higher, and the mass needed to form a structure increases (Jeans-mass filtering effect, Gnedin 2000). Even if the Lyα transmission flux is supposed to be higher, the formation of galaxies itself is suppressed, especially for objects in the low-mass end (e.g. Shapiro, Iliev, and Raga

2004). Utsumi et al., 2010 invoke this effect in order to explain the absence of galaxies in a region of ∼3 pMpc radius around a z∼6 quasar (see Section 1 and Table 3.4). Given the typical sizes of quasar's ionized regions, and that in our study we cover scales of only ∼2 pMpc, suppression of galaxy formation due to the quasar ionizing radiation might explain the lack of LAEs.

- *The bulk of the overdensity population is composed by dusty/obscured galaxies.*

  Observations find that host galaxies of $z > 5$ quasars contain a considerable amount of dust ($\sim 10^8 - 10^9$ $M_\odot$) and molecular gas ($\sim 10^{10}$ $M_\odot$, e.g. Decarli et al. 2018; see Sections 1.5 and 2.5.9). They are already characterized by a metal-enriched medium, comparable to what is observed at low redshift (e.g. De Rosa et al. 2011; see Section 2.5.8). One might foresee that also the galaxies assembling in the proximity of the quasar might be characterized by a high dust/molecular gas content.
  Indeed, on the theoretical side, Yajima et al., 2015, implementing a 3D radiation transfer code in a high resolution cosmological simulation, show that overdense regions at $z \sim 6$, where quasars are supposedly found, host more evolved, disk-like and massive ($M_* \sim 10^{11}$ $M_\odot$) galaxies, with respect to an average field at the same redshift. They are characterized by a strong dust extinction (i.e. a low UV radiation escape fraction, $f_{esc} \lesssim 0.1$), and a powerful star formation ($SFR \gtrsim 100$ $M_\odot$ yr^{-1}); therefore they are very bright in the IR, with L_{IR} as high as $\sim 4 \times 10^{12}$ $L_\odot$. These massive and highly obscured objects, whose detection in the UV rest-frame might be hindered by absorption and/or strongly dependent on orientation effects, rather than LAEs (i.e. young, dust-poor star forming galaxies), may be a more suited tracer for high redshift, massive overdensities (see Section 1.5.4 and Chapter 4).
  Further studies of the environment of high redshift quasars with sub-mm facilities (in particular ALMA) are starting to test this scenario, allowing us to recover a possible population of dusty galaxies in the quasar field. However, we note that, due to the small field of view of ALMA (with a size of $\sim 20''$, corresponding to $\sim$ 800 ckpc $\sim$ 110 pkpc at $z \sim 6$), we would be able to search only the most proximate region around the quasar. A study of the fields around three z>6.6 quasars with ALMA did not find an excess of dusty galaxies in a region of 65 ckpc radius (Venemans et al. 2016); however, several recent studies spot instead such overdensities of mm–bright galaxies (see Section 1.5.4 and Chapter 4).

- *Quasars at high redshift do not inhabit massive dark matter halos*

  The quasar two-point correlation function at low redshift ($z \lesssim 2.5$), as derived from both the 2dF QSO Redshift Survey (Croom et al. 2005) and the SDSS (Ross et al. 2009) quasar sample, shows that quasars are commonly associated with average-mass dark matter halos (i.e. $M_{DMH} \sim$ (2-3)$\times 10^{12}$ $M_\odot$), far less massive than the most massive halos at the same redshift ($\sim 10^{14} - 10^{15}$ $M_\odot$), independently of the quasar luminosity.
  At higher-z ($3.5 \lesssim z \lesssim 5.4$) the scenario is less clear: based on the SDSS sample, Shen et al., 2007 calculate an average dark matter host halo mass of (4-6)$\times 10^{12}$ $M_\odot$, slightly higher than the results at lower redshifts. However, more recent studies, based on the final SDSS III-BOSS quasar sample, do not find a clear evolution of quasar clustering from $z \sim 0$ to $z \sim 3$ (Eftekharzadeh et al. 2015)[8].

[8] We note that the quasars considered here are less massive than the ones studied by Shen et al., 2007

From a theoretical point of view, there have been studies suggesting that quasars also at high redshift (z$\gtrsim$5) inhabit dark matter halos with average masses (i.e. less massive than the most massive halos at that epoch). In particular, Fanidakis et al., 2013 perform simulations based on the semi-analytical model GALFORM, in order to study the relation between quasars and dark matter halos up to $z \sim$6. They show that, in case of models in which AGN feedback is considered, the masses of the dark matter host halos are roughly $\sim 10^{12}$ $M_{\odot}$, from $z \sim$0 to $z \sim$6: this is an order of magnitude lower than the most massive halos at $z \sim$6 obtained in the same simulation, and is in agreement with observations at low redshift. However, as argued by Simpson et al., 2014, it is worth to notice that the simulations by Fanidakis et al., 2012 fail to create the most massive black holes (M$\gtrsim 10^9$ $M_{\odot}$) at $z \sim$6, while they appear only at $z \sim$4. Therefore, the claims reported here are to be taken with caution, and may not hold in every scenario.

In summary, in this Chapter we studied the environment of the $z \sim$5.73 quasar PSO J215−16 searching for LAEs using broad and narrow-band VLT imaging, on Mpc-scales, i.e. ∼2 pMpc ∼14 cMpc at the redshift of the quasar. This is the second study in which we do not find evidence of an overdensity of Lyα emitting sources in a quasar field, compared to blank fields (see also B13).

Studies on wider areas (>20 arcmin radius, corresponding to ∼8 pMpc ∼ 47 cMpc at the redshift of the quasar), with the support of further, multiwavelength observations (i.e. IR/sub-mm), are required in order to discriminate among these scenarios. However, it is intriguing to note that overdensities of galaxies around radio-loud sources (both radio-loud galaxies and AGN) have been extensively reported (e.g. Venemans et al. 2007, Wylezalek et al. 2013). In the future, it appears to be worthwhile to repeat our experiment on $z > 6$ radio-loud quasars, whose sample has been substantially increased recently (Bañados et al. 2015a), to potentially target the earliest galactic structures (see also Section 5.1.2 for further discussion on this point).

Chapter 4

Highly Obscured Companion Galaxies around $z \sim$6 Quasars

In this chapter, we present new sensitive optical/NIR follow-up observations specifically designed to probe four companion galaxies to $6 \lesssim z \lesssim 6.6$ quasars and obtained from several ground- and space-based facilities. In particular, we aim to observe the bulk of their stellar emission in the rest-frame optical wavelength range, in order to assess their total stellar mass (M_*). We also aim to uncover their rest–frame UV radiation, to probe the contribution from the young stellar population and the budget of the unobscured star formation.

In § 4.1, we describe our sample and report our observations and data reduction. In § 4.2.1, we compare our measured photometry with spectral energy distributions of illustrative cases of local galaxies, and we use a SED fitting code for one source. The relative obscured and unobscured contribution to the star formation rate are examined in § 4.2.2, while in § 4.2.3 we place our findings in the context of observations of star forming galaxies and SMGs at $z \gtrsim$6. Finally, we discuss the case of a source detected solely in the dust continuum emission in § 4.3, and we present our conclusions in § 4.4.

4.1 Observations and Data Reduction

Our sample is composed by three (out of the four) quasar+companion systems presented in Decarli et al., 2017: SDSS J0842+1218, PSO J231.6576–20.8335 and CFHQS J2100−1715 (hereafter J0842, PJ231 and J2100, respectively; see Section 1.5.4). We also consider the quasar PSO J167.6415–13.4960 (hereafter PJ167), whose companion galaxy was recently observed with ALMA by Willott, Bergeron, and Omont (2017; see Section 1.5.4). In the following sections, we will refer to all the respective companions as "quasar_short_name"c. The coordinates, redshifts, spatial and velocity separations of the quasars and respective companion galaxies, obtained from ALMA observations, are reported in Table 4.1.

We also obtained data for a bright source, detected only in the dust continuum emission, close to the quasar VIK J2211−3206 (hereafter J2211; Venemans et al. in prep)[1]. This galaxy is part of the sample of dust continuum emitting sources discovered around several $z \sim$6 quasars that will be discussed by Champagne et al. (in prep), for which no secure redshift confirmation is however available. We present our follow–up data and discuss our constraints on the properties of this source in Section 4.3.

[1]This quasar was also recently independently discovered by Chehade et al., 2018, with the name of VST-ATLAS J332.8017-32.1036.

We collect the available observations of the fields in our sample, either from the literature or obtained with dedicated follow-up campaigns. Details on the observations used here, i.e. dates, instruments/telescopes, exposure times and filters, are shown in Table 4.2.

4.1.1 Optical/NIR Spectroscopy

We observe the companions of PJ231 and J0842, and the quasar PJ231, with the Magellan/FIRE spectrograph (Simcoe et al., 2008) at the Magellan Telescope. The data are reduced following standard techniques, including bias subtraction, flat field and sky subtraction. The wavelength calibration is obtained using sky emission lines as reference (see also Bañados et al. 2014). We use the standard stars HIP43018 and HIP70419 to flux calibrate and correct for telluric contamination in the spectra of J0842c and PJ231/PJ231c, respectively. In order to obtain the absolute flux calibration, we scale the spectrum of PJ231 to match the respective observed J band magnitude (J =19.66±0.05; see Table 2.3 in Section 2.3.2). We use the same factor to scale the spectra of the companions. No clear emission from either of the two companion is detected in the observed spectra (see Figure 4.1). We estimate the 3σ limits on the Lyα broad emission line by considering the 3×mean value of the spectral error vector in a window of 200 Å around the expected location of the emission line, based on the redshift derived from the ALMA [CII] observations. These limits are of 1.4 and 1.0×10^{-17} [erg s^{-1} cm^{-2} Å] for J0842c and PJ231c, respectively.

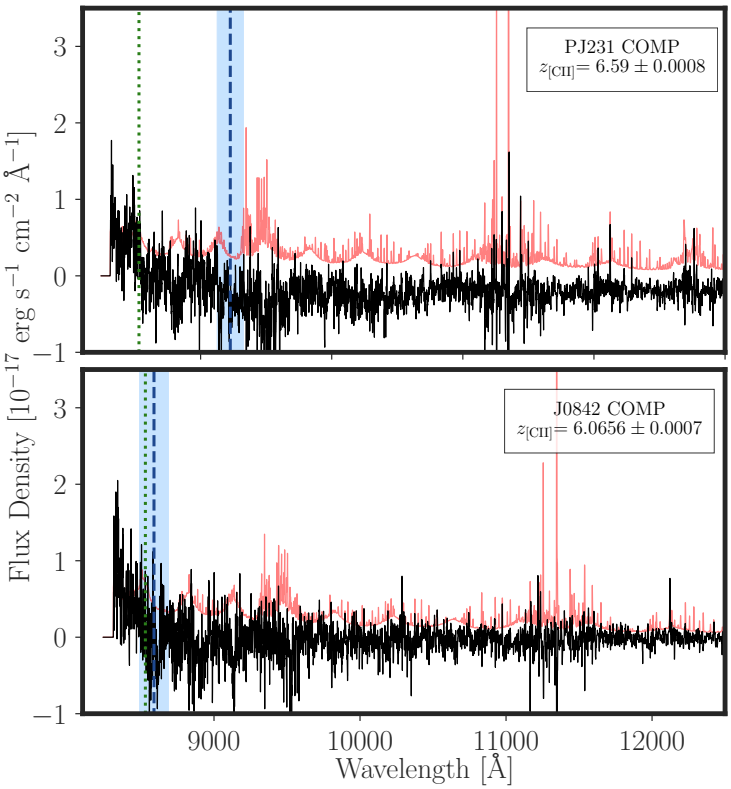

FIGURE 4.1: Spectra of the companions of the quasars PJ231 (*top*) and J0842 (*bottom panel*), acquired with the FIRE spectrograph. The *dashed blue lines* highlight the expected positions of the respective Lyα emission lines, established from the observations of the narrow [CII] emission line with ALMA. The surrounding regions of ±100 Å, used to estimate limits on the Lyα emission line in the companion galaxies, are also shown with *light blue shaded areas*.

TABLE 4.1: Coordinates, redshifts, spatial projected distances and velocity shifts of the quasars and the adjacent galaxies studied in this work. These measurements are obtained from the narrow [CII] emission line and underlying dust continuum observed by ALMA. The analogous quantities for the companion of J2211, detected solely in the dust continuum emission (see Section 4.3) are shown is Table 4.5. References are: (1) Decarli et al., 2017, (2) Decarli et al., 2018 and (3) Willott, Bergeron, and Omont, 2017.

Name	**R.A. (J2000)**	**Decl. (J2000)**	z	z_{err}	$\Delta \mathbf{r}_{\text{projected}}$ [kpc]	$\Delta \mathbf{v}_{\text{line of sight}}$ [km s^{-1}]	**References**
SDSS J0842+1218	08:42:29.43	12:18:50.4	6.0760	0.0006			(1)
SDSS J0842+1218c	08:42:28.95	12:18:55.1	6.0656	0.0007	47.7 ± 0.8	-443	(1)
PSO J167.6415–13.4960	11:10:33.98	-13:29:45.6	6.5148	0.0005			(2)
PSO J167.6415–13.4960c	11:10:34.03	-13:29:46.3	6.5090	–	5.0	-270	(3)
PSO J231.6576–20.8335	15:26:37.84	-20:50:00.8	6.58651	0.00017			(1)
PSO J231.6576–20.8335c	15:26:37.87	-20:50:02.3	6.5900	0.0008	8.4 ± 0.6	+137	(1)
CFHQS J2100−1715	21:00:54.70	-17:15:21.9	6.0806	0.0011			(1)
CFHQS J2100−1715c	21:00:55.45	-17:15:21.7	6.0796	0.0008	60.7 ± 0.7	-41	(1)

TABLE 4.2: Information on the optical/IR spectroscopy and imaging data used in this work. Together with the newly acquired observations presented here, we consider archival data for the quasar J0842, obtained with *Spitzer*/IRAC in the [5.8] and [8.0] channels, and with *HST*/WFC3 in the F105W filter (Leipski et al. 2014; see Section 4.1). We will focus on the dust–continuum detected source close to the quasar VIK J2211−3206 in Section 4.3.

Name	**Date/Program ID**	**Telescope/Instrument**	**Filters/λ range**	**Exp. Time**
SDSS J0842+1218	2016–03–15	Magellan/FIRE	0.82–2.49 μm	4176s
	2017–04–27 / 14876	*HST*/WFC3	F140W	2612s
	2011–01–22 / 12184	*HST*/WFC3	F105W	356s
	2017–02–09 / 13066	*Spitzer*/IRAC	3.6, 4.5 μm	7200s
	2007–11–24 / 40356	*Spitzer*/IRAC	5.8, 8 μm	1000s
PSO J167.6415–13.4960	2017–08–11 / 14876	*HST*/WFC3	F140W	2612s
	2017–04–13 / 13066	*Spitzer*/IRAC	3.6, 4.5 μm	7200s
PSO J231.6576–20.8335	2016–03–15	Magellan/FIRE	0.82–2.49 μm	4788s
	2017–04–01 / 14876	*HST*/WFC3	F140W	2612s
	2016–11–25 / 13066	*Spitzer*/IRAC	3.6, 4.5 μm	7200s
CFHQS J2100−1715	2016–09–18/19 / 334041	LBT/LUCI	*J*	10440s
	2017–05–04 / 14876	*HST*/WFC3	F140W	2612s
	2017–01–14 / 13066	*Spitzer*/IRAC	3.6, 4.5 μm	7200s
VIK J2211−3206	2017–04–28 / 14876	*HST*/WFC3	F140W	2612s
	2017–01–29 / 13066	*Spitzer*/IRAC	3.6,4.5 μm	7200s

4.1.2 IR Photometry

We list here the observations and data reduction of the imaging follow–up data, obtained with ground– and space–based instruments.

LUCI @ LBT

We image the field of J2100 in the J band with the LBT Utility Camera in the Infrared (LUCI1 and LUCI2; Seifert et al. 2003) at the LBT, in binocular mode. We reduce the data following standard techniques, i.e. we subtract the master dark, divide for the master flat field, and median–combine the frames after subtracting the contribution from the background and after aligning them using field stars. We find the final astrometric solution using as reference the GAIA Data Release 1 catalog[2] (DR1; Gaia Collaboration et al. 2016b, 2016). We flux-calibrate the image with respect to the 2MASS Point Source Catalog. The seeing of the reduced image is 0.″98. We calculate the depth of the image by distributing circular regions with radius equal to half of the seeing over the frame, in areas with no sources. We consider as the 1σ error of our image the σ of the gaussian distribution of the fluxes calculated in these apertures. We do not detect, at S/N>3, any emission at the location of the companion, after performing force photometry on an area corresponding to the seeing (see Figure 4.2). The 3σ limit magnitude, that we will consider in the following analysis, is equal to J=26.24.

WFC3 @ *HST*

We obtain new observations of all the targets studied here with the Wide Field Camera 3 (WFC3), on board *HST*, using the F140W filter (λ_c =1.3923 μm and $\Delta\lambda$ =0.384 μm; Program ID:14876, PI: E. Bañados). For the quasar J0842, previous WFC3 observations in the F105W filter (λ_c =1.0552 μm and $\Delta\lambda$ =0.265 μm) were also retrieved from the Hubble Legacy Archive[3] (Program ID:12184,PI: X. Fan). We refer to Table 4.2 for further details on this dataset.

We analyze both the archival and new observations in a consistent way. We consider the reduced data produced by the *HST* pipeline, and we take the zero-point photometry from the WFC3 Handbook[4]. We re-calibrate the images astrometry using the GAIA DR1 catalog. We calculate the depth of the images in an analogous way as performed above for our LUCI data, considering here areas of 0.4″radius (containing the 84% of the flux of a point source[5]). We perform aperture photometry, using this aperture radius, at the positions of the companions. The companion sources of J0842, J2100 and PJ231 are not detected in the F140W filter, and J0842c is not detected in the F105W image. We report all the 3σ limit fluxes in Table 4.3. We show the observations of all the fields studied in this work in the F140W filter in Figure 4.3, and the F105W image of J0842 in Figure 4.4.

In the case of PJ167, the companion is located at a projected distance of only 0.9″, and it is blended with the quasar emission. In order to recover meaningful constraints on the photometry of PJ167c, it is necessary to subtract the quasar contribution, by modeling the image PSF. We use the bright star 2MASS J11103221–1330007, in the proximity of PJ167, in order to

[2]https://www.cosmos.esa.int/web/gaia/dr1
[3]https://hla.stsci.edu/
[4]http://www.stsci.edu/hst/wfc3/analysis/ir_phot_zpt
[5]http://www.stsci.edu/hst/wfc3/analysis/ir_ee

create an empirical PSF model from the same image. This source is located at a distance of only 30″ from the quasar, limiting the errors due to the changes in the shape of the PSF over the field. Its J and H magnitudes, from the 2MASS Point Source Catalog, are 15.249 and 15.105, respectively. The corresponding $J - H$ color of 0.144 is therefore close to that of the quasar ($J - H$=0.216). We shift, scale and subtract the PSF model from the quasar emission using the software GALFIT (version 3.0.5; Peng et al. 2002, 2010). In Figure 4.5 we show the native *HST* image, the PSF star model and the residual frame, in which the bright quasar emission has been subtracted. The companion galaxy is well isolated, and its F140W PSF magnitude, measured with `GALFIT`, is equal to 25.48 $\pm$ 0.17. Diffuse emission, extending from the companion to the quasar, is also tentatively recovered. Additional, high resolution imaging and spectroscopy is needed to securely confirm and characterize such emission.

Summarizing, in the following analysis we adopt the F140W 3σ limit magnitudes for J2100c, PJ231c and J0842c. For this last object, we also measure the 3σ limit magnitude in the F105W band from archival data. We consider the F140W PSF magnitude for PJ167c. All these quantities, converted into fluxes, are reported in Table 4.3.

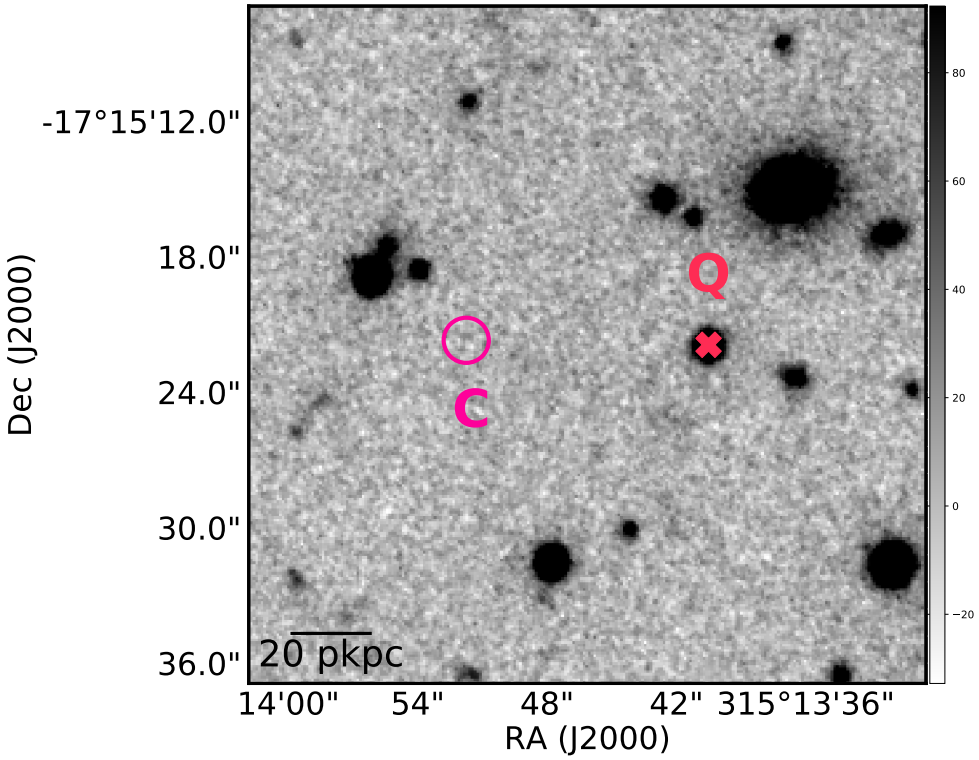

FIGURE 4.2: Postage stamp (30″×30″) of the field around the quasar J2100, imaged in the *J* filter with the LUCI1 and LUCI2 cameras at the LBT (see Section 4.1.2 and Table 4.2). No emission at the location of the companion galaxy (marked with a *red circle* of 1″radius) is recovered at S/N> 3.

IRAC @ *Spitzer*

The fields of all the objects in our sample were recently observed in the [3.6] (λ_c =3.550 μm and $\Delta\lambda$ =0.750 μm) and [4.5] (λ_c =4.493 μm and $\Delta\lambda$ =1.015 μm) filters with the InfraRed Array Camera (IRAC; Fazio et al. 2004; Program ID:13066, PI: C. Mazzucchelli; see Table 4.2). We

also use archival data of J0842 (Program ID:40356, PI: X. Fan), covering the IRAC filters [5.8] (λ_c =5.731 μm and $\Delta\lambda$ =1.425 μm) and [8.0] (λ_c =7.872 μm and $\Delta\lambda$ =2.905 μm; see Table 4.2).

We adopt the reduced data from the *Spitzer* pipeline, and the photometric calibration (i.e. photometric zero point and aperture correction values) specified in the IRAC Instrument Notebook[6]. We refine the astrometric solution re-calibrating the pipeline-reduced images using the GAIA DR1 catalog. Given the limited spatial resolution of the IRAC camera (0.6 arcsec/pixel) and the depth of our [3.6] and [4.5] images, the companion galaxies studied here are blended either with the emission of the much brighter quasar, or with that of foreground sources (see Figure 4.3). Hence, one needs to properly model and remove these emissions.

In order to model the PSF function, which is undersampled in the IRAC data, we re-sample the native images over a grid of 0.12 arcsec/pixel resolution, using the IRAF task *magnify*. In each magnified image, we select a collection of stars in a $1' \times 1'$ window centered on the quasar, in order to minimize the effect of the changes to the PSF shape due to the location on the detector; we use the corresponding *HST*/WFC3 images as reference to pick isolated stars. We obtain the final PSF model for each image by shifting, aligning, scaling and combining the selected stars. The number of stars used ranges between 4 and 9, in case of the [4.5] image of the quasar J2100, and of the [3.6] image of the quasar PJ231, respectively. We use `GALFIT` in order to sample the PSF image to the original resolution, and to model and subtract the emission from the quasar and eventual foreground objects.

In Figure 4.3, we show the postage stamps of the IRAC [3.6] and [4.5] images, and the corresponding images of the residuals. No clear emission from the companion galaxies is detected in the residual images. We quantify the limits on the photometry of the companions as follows. For each image, we run `GALFIT` subtracting at the exact position of the companion a source modeled with a PSF function and scaled to a fixed magnitude, which we vary between 21 and 25, in steps of 0.01 mag. When adopting magnitudes smaller (i.e. brighter fluxes) than the limit magnitude to which our image is sensitive, the subtraction will leave a negative residual. In the residual image, we perform aperture photometry at the companion position in an aperture of 2.4″ radius, and we compare the measured flux with the image 3σ flux limit. This flux limit is measured on the same area used for the force photometry, and by evaluating the background rms in an annulus of radius 14″ and width of 10″ centered on the companion. We assume that the 3σ limit magnitude is the value at which the measured absolute flux in the residual image is equal to the 3σ flux limit. We report these values in Table 4.3.

Finally, we analyze the archival J0842 *Spitzer*/IRAC observations (see Figure 4.4): these observations are much shallower (see Table 4.2), since they were devised to only detect the bright quasar. No foreground objects overlaps the companion location, and we therefore perform aperture photometry on the native images, using the same aperture as in the observations in the [3.6] and [4.5] channels. We measure no detection at S/N>3, and we consider the corresponding 3σ limit fluxes.

To summarize, in Table 4.3 we report the photometric measurements (or limits) for companion galaxies of $z \sim$6 quasars obtained from the observations described above. We also list their fluxes at $\lambda_{\rm obs}$ =1.2 mm from ALMA observations (Decarli et al., 2017).

[6]http://irsa.ipac.caltech.edu/data/SPITZER/docs/ irac/iracinstrumenthandbook/IRAC_Instrument_Handbook.pdf

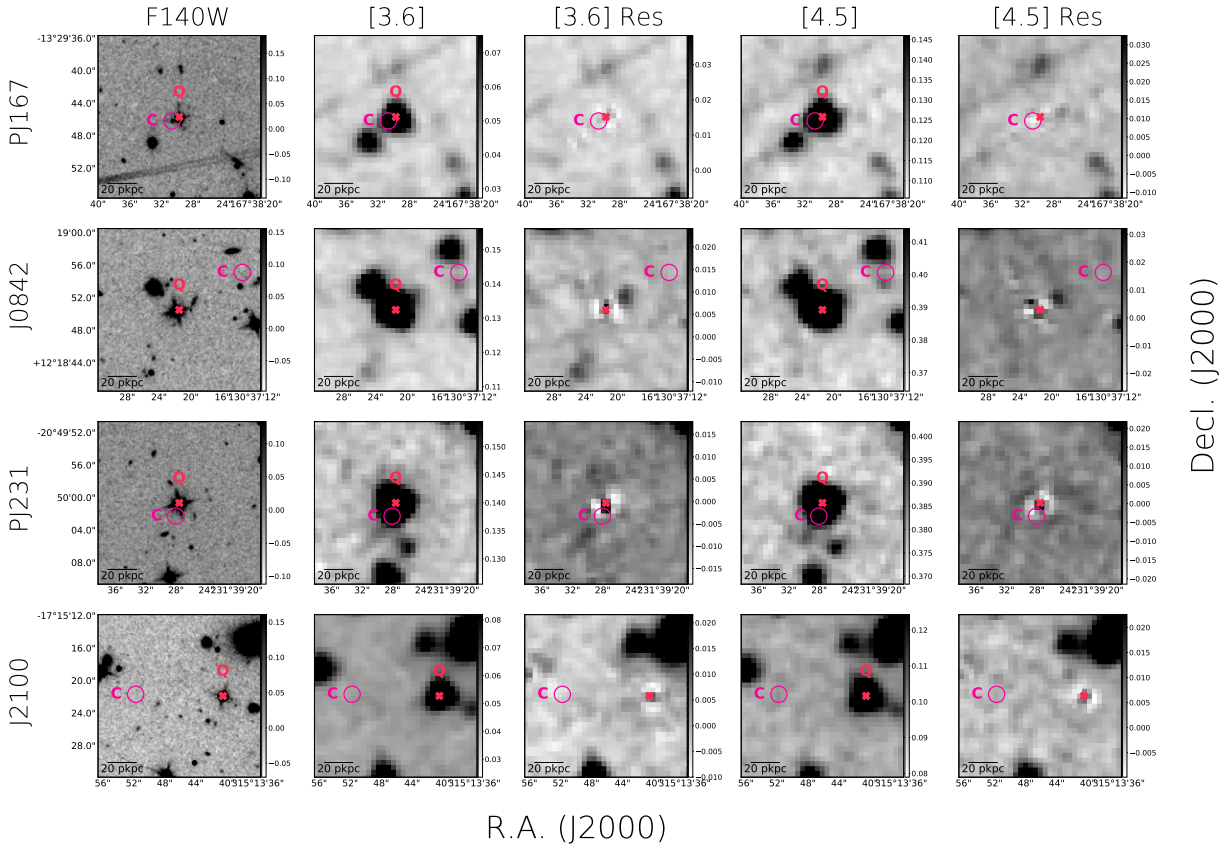

FIGURE 4.3: Postage stamps ($20'' \times 20''$) of the four fields (quasar+companion) considered in this study. We show the observations newly acquired with the *HST*/WFC3 and *Spitzer*/IRAC cameras (see Table 4.2). We also report the IRAC images of the residuals, obtained after removing the emission from the quasar and nearby foreground sources (see Section 4.1.2). The positions of the companions and of the quasars are highlighted with *magenta circles* (of $1''$radius) and *red crosses*, respectively.

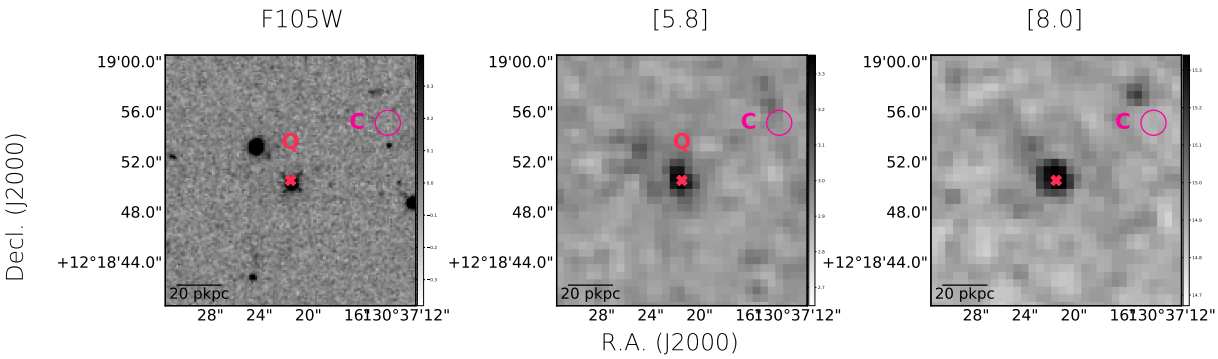

FIGURE 4.4: Archival observations of the field around the quasar J0842 (20″×20″). On the *left* panel, we report the data obtained from the *HST*/WFC3 instrument, in the F105W filter, while on the other two panels we show observations acquired with the *Spitzer*/IRAC camera, in the [5.8] and [8.0] channels (see Section 4.1.2 and Table 4.2 for references). The quasar is pinpointed with a *red cross*, while the companion position is highlighted with a *magenta circle*. These observations were acquired with the aim of studying the bright quasar emission, therefore the flux limits at the companion position are less stringent than the ones newly obtained (see Table 4.3).

FIGURE 4.5: *HST*/WFC3 image, in the F140W filter, of the quasar PJ167. *Left panel*: native postage stamp (5″×5″). *Central panel*: empirical PSF model obtained from a bright star in the field (see Section 4.1.2). *Right panel*: residual image, after the subtraction of the empirical PSF to the data. We note that the companion galaxy observed in the ALMA image is detected and well resolved in the latter frame (*white circle*, of radius 0.″4); additional residual flux, located between the center of the bright quasar and the adjacent galaxy, is also tentatively detected.

TABLE 4.3: Photometric measurement of the companion galaxies to $z \sim 6$ quasars studied in this work (see Section 4.1). The flux measurements at 1.2mm are taken from Decarli et al. 2017; the value for PJ167 is obtained from recent high resolution ALMA data at hands (Decarli et al. in prep.). The limits are intended at 3σ significance.

Name	F_J [μJy]	F_{F105W} [μJy]	F_{F140W} [μJy]	$F_{3.6\text{-}\mathrm{m}}$ [μJy]	$F_{4.5\text{-}\mathrm{m}}$ [μJy]	$F_{5.8\text{-}\mathrm{m}}$ [μJy]	$F_{8.0\text{-}\mathrm{m}}$ [μJy]	$F_{1.2\mathrm{mm}}$ [mJy]
SDSS J0842+1218c	–	<0.154	<0.061	<0.78	<1.06	<9.54	<12.6	0.36 ± 0.12
PSO J167.6415–13.4960c	–	–	0.233 ± 0.040	<0.78	<1.28	–	–	0.156 ± 0.015
PSO J231.6576–20.8335c	–	–	<0.053	<0.64	<2.79	–	–	1.73 ± 0.16
CFHQS J2100−1715c	<0.116	–	<0.083	<0.53	<1.07	–	–	2.05 ± 0.27

4.2 Analysis

In the following section, we characterize the SEDs of four companions to $z \sim 6$ quasars by comparing them with few examples of local galaxies, and by modeling their emission with a SED fitting code. We estimate (or set upper limits to) their unobscured/obscured star formation activity, observed in the rest–frame UV/IR range, respectively. Finally, we place our measurements in the context of observations of star forming galaxies and starbursts at similar redshift.

4.2.1 Spectral Energy Distribution

We study the SEDs of companion galaxies to high redshift quasars by first comparing them with cases of prototypical galaxies in the local universe. We consider SEDs of normal star forming spiral galaxies (M51 and NGC6946), starbursts (M82) and ultraluminous infrared galaxies (ULIRGs; Arp 220), from Silva et al., 1998. M51 is a nearby (D=9.6 Mpc) spiral (Sbc) interacting galaxy, which has been studied in detail over several wavelength and physical scales (e.g. Leroy et al. 2017). NGC6946, found at a distance of 6.72 Mpc, is an intermediate (Scd) spiral galaxy (Degioia-Eastwood et al., 1984). Its size is approximately a third of that of our Galaxy and it hosts roughly half of the stellar mass (e.g. Engargiola 1991). M82 is a prototypical, edge–on starburst (with a galaxy-wide $SFR \sim$ 10–30 $M_\odot$ yr^{-1}; Förster Schreiber et al. 2003), whose intense activity has been most probably triggered by a past interaction with the neighboring galaxy M81 (e.g. Yun, Ho, and Lo 1994). Arp 220 is one of the closest (77 Mpc) and best studied ULIRGs, with a total infrared luminosity of L_{IR} =1.91×10^{12} $M_\odot$ (Armus et al., 2009). It is considered to be the result of a merger which happened ∼3-5 Myr ago (e.g. Joseph and Wright 1985, Baan and Haschick 1995, Scoville et al. 1998, Downes and Eckart 2007), with extreme conditions in its nucleus (e.g. with a dust attenuation of $A_V = 2 \times 10^5$mag; Scoville et al. 2017).

Here, we shift the SEDs of these local galaxies to the redshifts of the companions, and we scale them to match the 1.2mm flux retrieved in the ALMA observations. We plot the SEDs, together with the photometry of the companions presented here, in Figure 4.6. The rest–frame UV/optical observations of PJ231c, J2100c and J0842c are very sensitive, thus they rule out all the galaxy templates considered here, with the exception of Arp 220. On the other hand, the rest-frame UV emission of PJ167c is detected in our *HST*/WFC3 observations (see Section 4.1). Its UV to submm ratio is comparable to that of the starforming galaxy NGC6946, while the limits from our *Spitzer*/IRAC data suggest that it has a lower stellar content.

We compute the star formation rates for PJ231c, J2100c and J0842c assuming that their SEDs are equivalent to that of Arp 220, shifted in redshift and scaled as in Figure 4.6. We derive their star formation rates from the dust emission in the rest-frame infrared region, considering the non-obscured SFR as negligible (see Section 4.2.2). We calculate the total IR luminosity by integrating the emission from 3 μm to 1000 μm, and we measure the SFR as: $SFR = 1.49 \times 10^{-10} L_{\rm IR}$ (Kennicutt and Evans, 2012). The obtained values range between ∼120–700 $M_\odot$ yr^{-1}. We note that, assuming instead a modified black body model, $f_\nu \propto B_\nu(T_d \nu^\beta)$, and adopting typical parameters for high–redshift galaxies ($T_d = 47$ K and $\beta = 1.6$; e.g. Beelen et al. 2006, Venemans et al. 2016; see also Section 2.5.9), one would derive comparable star formation rate values (∼140–800 $M_\odot$ yr^{-1}; see also Decarli et al. 2017).

We can obtain conservative upper limits on the companion stellar masses on the base of their dynamical ($M_{\rm dyn}$) and gas ($M_{\rm gas}$) masses. The former can be obtained from the widths of the [CII] emission lines observed with ALMA (see Decarli et al. 2017). These values, i.e. $M_{\rm dyn} \sim 12 - 27 \times 10^{10}$ M$_\odot$, are reported in Table 4.4. On the other hand, one can estimate $M_{\rm gas}$ from the dust content ($M_{\rm dust}$). We take these values from Decarli et al., 2017: estimates of $M_{\rm dust}$ are measured following the prescription by Downes et al., 1992 (see also Section 2.5.9 and eq. 2.15), while the values of the gas masses are obtained assuming a typical gas–to–dust ratio of $\sim$100 (e.g. Berta et al. 2016). If we subtract the gas content from the total dynamical mass, we can obtain a first order limit on the stellar content of $M_* < 16 - 21 \times 10^{10}$ M$_\odot$ (see Table 4.4). In the following analysis, we utilize these latter values as upper limits on the stellar masses of the companions J0842c, PJ231c and J2100c (see Figures 4.7 and 4.8).

Alternatively, we can compare our photometric measurements with synthetic galaxy templates. We use the SED fitting code MAGPHYS (da Cunha, Charlot, and Elbaz, 2008), which takes advantage of an energy balance technique to combine, all at once, the radiation from the stellar component, the dust attenuation, and the re-emission in the rest-frame IR wavelength range. We consider here the MAPGPHYS–highz extension (da Cunha et al., 2015), which was specifically modified in order to characterize a sample of SMGs at $3 < z < 6$ (see also Section 4.2.3). In particular, this version allows for templates of younger galaxies, with higher dust extinction, and a wider choice of star formation histories. Nevertheless, fitting the companion galaxies presented here with any code do not provide strong constraints, due to the few (and most of the time only one) broad–band detections for each source. This is reflected in strong parameter degeneracies in the fit, and large error bars. Another issue is represented by the potentially inappropriate coverage of the parameter space considered in the fitting machine, which might not be modeling the properties of the peculiar galaxies considered here.

Taking all these points into account, we choose to fit only the companion of PJ167, whose emission is retrieved in more than one broad band. In Figure 4.6, we show the best fit template from MAGPHYS–highz for this galaxy. We take the 50th and 16th/84th percentiles of the marginalized probability distributions as the best fit values and uncertainties of its SFR and stellar mass. The SED of PJ167c is consistent with that of a star forming galaxy, $SFR = 51^{+30}_{-17}$ M$_\odot$ yr^{-1}, with a stellar mass of $M_* = 0.86^{+0.59}_{-0.42} \times 10^9$ M$_\odot$, a moderate dust extinction ($A_V = 0.64^{+0.325}_{-0.25}$ mag) and a dust content of $M_{\rm d} = 5^{+4}_{-2} \times 10^7$ M$_\odot$.

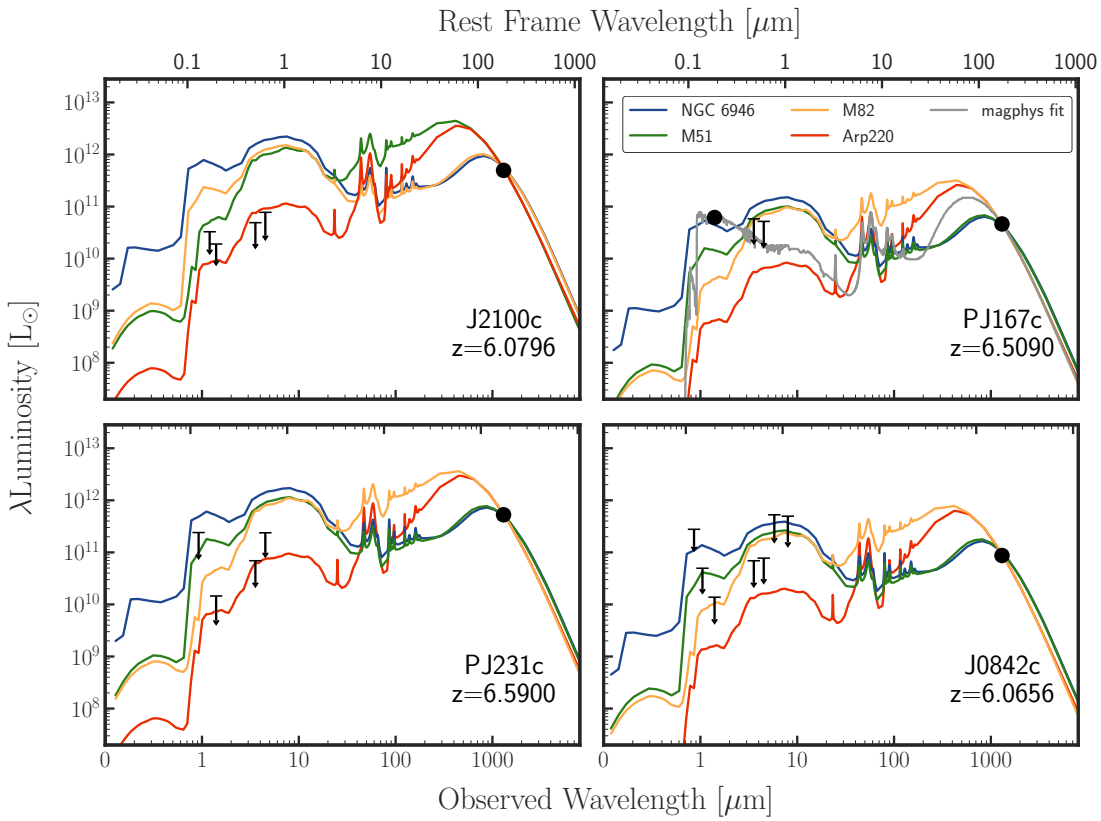

FIGURE 4.6: Spectral Energy Distribution of four companion galaxies adjacent to $z \sim 6$ quasars. The observed photometric measurements (see Tables 4.3) are reported with *down-pointing arrows* (limits at 3σ significance) and *filled black points*. As comparison, we show representative SEDs of various local star forming galaxies (NGC 6946, *blue*; M51, *green*) and starbursts/ULIRG (M82, *orange*; Arp 220, *red line*; Silva et al. 1998), normalized to the ALMA 1.2 mm measurement. The best fit template (*grey line*) of the SED of PJ167c, obtained with the code MAPGPHYS–highz (da Cunha et al., 2015), is also reported. The SEDs of J2100c, J0842c and PJ231c are consistent with being Arp 220 like-galaxies, i.e. intensely forming stars and highly dust obscured, at $z \sim 6$. The *HST*/WFC3 measurement of the rest–frame UV emission of PJ167c suggests that this source is more similar to a "regular" starforming galaxy (e.g. NGC6964), although with a lower stellar mass.

4.2.2 SFR_{UV} vs SFR_{IR}

The rest–frame UV emission of galaxies directly traces young stars, i.e. 10–200 Myr old: It is therefore an excellent probe of recent star formation, but it is also heavily affected by dust attenuation. The energy of the UV photons is indeed absorbed by the dust, and re-emitted in the IR regime. The IR emission therefore is a natural tracer of the obscured star formation (see Kennicutt and Evans 2012 for a review).

We obtain here measurements of (or limits on) the unobscured contribution to the SFR in the companion galaxies, using our *HST*/WFC3 sensitive observations in the F140W filter. We consider the conversion between far UV ($\lambda_{\rm FUV}$ =155 nm) luminosity ($L_{\rm FUV}$) and $SFR_{\rm UV}$ provided by Kennicutt and Evans, 2012:

$$\log\left[\frac{SFR_{\rm UV}}{\rm M_{\odot}yr^{-1}}\right] = \log\left[\frac{L_{\rm FUV}}{\rm ergs^{-1}}\right] - C_{\rm FUV} \tag{4.1}$$

with $C_{\rm FUV}$=43.35. We report in Table 4.4 the estimated values for $SFR_{\rm UV}$. The limits achieved by our data go down to few $\rm M_{\odot}\ yr^{-1}$. PJ167c, the only companion detected in the rest–frame UV, is characterized by an unobscured star formation rate of $\sim$11 $\rm M_{\odot}\ yr^{-1}$. We note that the central wavelength of the broad band filter used here (F140W) corresponds to $\lambda_{\rm rest}$ $\sim$0.18–0.2 μm for z $\sim$6-6.6, i.e. slightly redder than the classically defined FUV. In order to check how this impacts our results, we repeat our star formation rate estimates considering the calibration for the near UV ($\lambda_{\rm NUV}$ =230 nm; $C_{\rm NUV}$=43.17; Kennicutt and Evans 2012). In this case, we measure SFR values only $\sim$ 1.5$\times$ larger. We also consider the best SED fit from MAGPHYS–highz for PJ167c, and we calculate the star formation rate in the exact FUV range. We obtain $SFR_{\rm UV}$ $\sim$8 $\rm M_{\odot}\ yr^{-1}$, consistent, within the errors, with the one measured directly from our *HST* data.

We further consider the contribution from the obscured star formation activity ($SFR_{\rm IR}$). For J2100c, J0842c and PJ231c, we use the values obtained from the Arp 220 SED (see Section 4.2.1 and Table 4.4). In case of PJ167c, we follow the method described in Section 4.2.1, but, instead of Arp 220, we use the best SED from the MAGPHYS–highz fit (see Figure 4.6 and Table 4.4).

An alternative way of measuring the star formation rate is through the luminosity of the [CII] emission line ($\rm L_{[CII]}$, $SFR_{\rm [CII]}$; e.g. De Looze et al. 2011, 2014, Sargsyan et al. 2012b, Herrera-Camus et al. 2015). Here, we follow Decarli et al., 2017, and we derive $L_{\rm [CII]}$ and $SFR_{\rm [CII]}$ with the formula provided by Carilli and Walter, 2013 and De Looze et al., 2014, respectively (see also the discussion in Section 2.5.9, and equations 2.16, 2.17). We obtain star formation rates ranging between $\sim$260–730 $\rm M_{\odot}$, i.e. the same order of magnitude as the ones measured from the dust continuum (see Table 4.4).

In all the companions studied here, with the exception of PJ167c, the SFRs measured in the IR are $\sim$two orders of magnitude larger than the ones observed in the rest–frame UV, with $SFR_{\rm IR}/SFR_{\rm UV} \gtrsim$ 60–200. The contribution of $SFR_{\rm UV}$ to the total star formation budget is therefore negligible. In case of PJ167c, the obscured star formation rate is instead only 6$\times$ higher than the unobscured one.

Another way of performing this comparison is by looking at the fraction of obscured star formation, defined as $f_{\rm obscured} = SFR_{\rm IR}/SFR_{\rm IR+UV}$. Recently, Whitaker et al., 2017 report a tight correlation between this quantity and the stellar mass, irrespective of redshift (up to z <2.5),

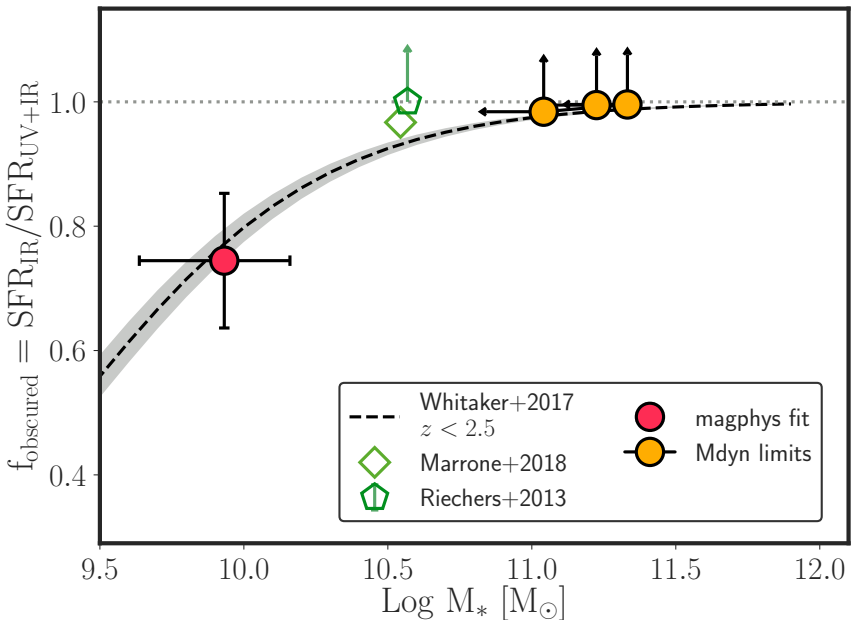

FIGURE 4.7: Fraction of obscured star formation as a function of stellar mass. A tight correlation is observed at lower redshifts (0< z <2.5; *dashed black line*, Whitaker et al. 2017). We show the location of z >6 SMGs observed by Marrone et al. (2018; *big diamond*) and Riechers et al. (2013; *pentagon*). The galaxies studied in this work are reported with *red* (PJ167c, whose physical properties were obtained with the code MAGPHYS–highz) and *yellow circles* (J2100c, PJ231c, J0842c, where we only place upper limits on the stellar masses; see Section 4.2.1). In the latter case, only limits for the unobscured *SFR* could be derived (see Section 4.2.2). The star formation of the companions to high–z quasars studied here is dominated by the obscured component.

in a large sample of star forming galaxies from CANDELS and SDSS. We calculate (limits on) $f_{\rm obscured}$ for the galaxies presented here. We report these values in Table 4.4, and we show them in the context of previous observations in Figure 4.7. As seen before, the star formation activity of the companions is highly dominated by $SFR_{\rm IR}$, with obscured fractions ranging between 0.74–0.99. In particular, taking into account the uncertainties on M_* and $f_{\rm obscured}$, PJ167c is consistent with the expectations from lower−redshift studies. The remaining sources seem to also follow the z <2.5 trend. However, we are here only able to set upper limits on their stellar masses: if M_* were much lower (e.g. $\lesssim 10^{10}$ $M_\odot$), these companions were to significantly diverge from the observations at low−z.

TABLE 4.4: Physical properties of the companion galaxies to $z \sim 6$ quasars studied in this work. We report the unobscured (rest–frame UV) *SFR*s calculated from our *HST*/WFC3 observations (Section 4.2.2), and the obscured (rest–frame IR) contribution from our ALMA data (Section 4.2.1 and 4.2.2). Finally, the dynamical mass estimates and upper limits on the stellar masses are also listed. In case of PJ167c, the reported stellar mass is that derived from MAGPHYS–highz (see Section 4.2.1).

Name	**SFR**$_{\rm UV}$ [$M_\odot$ yr^{-1}]	**SFR**$_{\rm IR}$ [$M_\odot$ yr^{-1}]	**SFR**$_{\rm [CII]}$ [$M_\odot$ yr^{-1}]	$f_{\rm obscured}$ = SFR$_{\rm IR}$/SFR$_{\rm UV+IR}$	**M**$_{\rm dyn}$ [$\times 10^{10}$ $M_\odot$]	**M**$_*$ [$\times 10^{10}$ $M_\odot$]
SDSS J0842+1218c	<2	124 ± 54	260 ± 40	>0.98	12 ± 5	<11
PSO J167.6415–13.4960c	11 ± 3	32 ± 4	–	0.74 ± 0.11	–	$0.86^{+0.59}_{-0.42}$
PSO J231.6576–20.8335c	<3	709 ± 157	730 ± 100	>0.99	22 ± 8	<16.8
CFHQS J2100−1715c	<3	573 ± 73	360 ± 70	>0.99	27 ± 13	<21.5

4.2.3 SFR vs Stellar Mass

A correlation between the SFR and the stellar mass of star forming galaxies ("main sequence", MS) has been observed in a large number of studies, and over a wide redshift range ($0 \lesssim z \lesssim 6$; e.g. Brinchmann et al. 2004, Noeske et al. 2007, Whitaker et al. 2011, Rodighiero et al. 2011; for an in–depth analysis of the literature see Speagle et al. 2014). The tightness (∼0.3–0.2 dex scatter) of this relation has been interpreted as evidence that "regular" star–forming galaxies have smooth star formation histories, in which the majority of the mass is assembled via steady accretion of cool gas from the intergalactic medium on long timescales (e.g. Daddi et al. 2007, Steinhardt et al. 2014). On the other hand, highly starforming galaxies, lying above the MS, are also observed, and are thought to grow mainly via efficient, merger–triggered star formation events (e.g. Santini et al. 2014). The MS normalization is observed to evolve with redshift, and this trend suggests that higher specific star formation rates ($sSFR = SFR/M_*$) are common at early cosmic times (e.g. Whitaker et al. 2014).

We compare the properties of the companion galaxies considered here with those of typical star forming galaxies and SMGs at similar redshifts (see Figure 4.8). We consider the observed MS relation at $z \sim 6$ provided by Salmon et al., 2015 and Speagle et al., 2014, together with predictions from semi-analytical models by Somerville et al. (2008, 2012). Salmon et al., 2015 examine $3.5 \leq z \leq 6.5$ galaxies in the GOODS-S field: we take here SFR and M_* values of their ∼200 $z \sim 6$ galaxies. Speagle et al., 2014 assemble a comprehensive compilation of 25 studies of the MS at $0 \lesssim z \lesssim 6$. After a careful recalibration of the various datasets, they obtain a robust $SFR - M_*$ relation as a function of the age of the universe (t, here in Gyr):

$$\log SFR[M_*, t] = (0.84 - 0.026 \times t)\log M_* - (6.51 - 0.11 \times t) \tag{4.2}$$

They also find that the MS presents a scatter of ∼0.2 dex, irrespective of redshift. We show this relation, calculated at $z = 6$ with the representative 0.2 dex scatter, in Figure 4.8. We consider the semi-analytical model by Somerville et al., 2012, who use N-body simulations and several feedback/accretion recipes to specifically reproduce the GOODS-S field. In particular, we consider the MS relation for this model at z ∼6, as provided by Salmon et al. (2015; see their Table 4). In addition, we report observed SMGs at $4.5 < z < 6.1$ from da Cunha et al., 2015, whose redshifts and physical parameters were obtained with MAGPHYS-highz, and at z ∼4.5 from Gómez-Guijarro et al., 2018, for which recent ALMA mm observations and secure spectroscopic redshifts are available. Finally, we show the massive, extremely starbursting galaxies at $z > 6$ discovered by Riechers et al., 2013 and Marrone et al. (2018; see Section 1.3).

We show in Figure 4.8 the SFR and M_* values obtained with MAGPHYS–highz for PJ167c: This galaxy results to lie on the MS at z ∼6. For the remaining galaxies, i.e. J2100c, J0842c and PJ231c, we only consider the obscured star formation rates and the upper limits on the stellar masses (see Section 4.2.1). These highly conservative constraints place the companions on or below the MS relation. Future, deeper observations in the IR regime, together with further development of current fitting machines (i.e. allowing to probe wider physical parameter spaces), will be fundamental in constraining these galaxies SEDs and stellar masses.

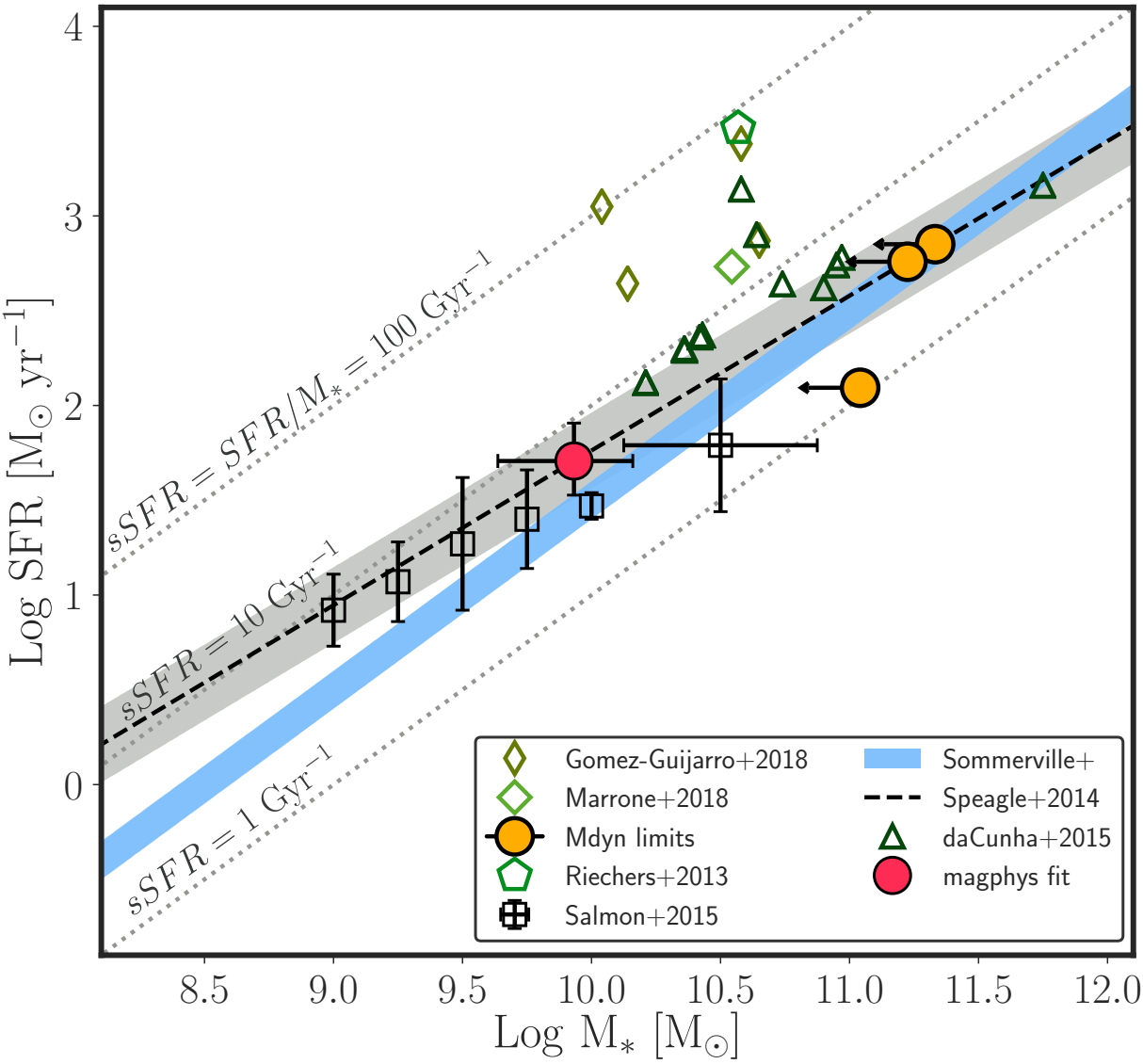

FIGURE 4.8: Star formation rate as a function of stellar mass, in logarithmic space, for a compilation of sources at $z \sim 6$. We here explore how the (currently poorly constrained) stellar masses of the quasars companions affect the locations of these sources with respect to the star forming galaxies main sequence (MS). We report observations of the MS from Salmon et al. (2015; *empty black squares*), the empirically derived MS relation by Speagle et al. (2014; *dashed line and grey region*), and the MS location predicted by semi-analytical models (Somerville et al. 2012; *light blue region*). We show further examples of sub-millimeter galaxies, from $z \sim 4.5 - 6.1$ sources (da Cunha et al. 2015, *triangles*, and Gómez-Guijarro et al. 2018, *small diamonds*) to the extreme starbursts observed at z =6.3 (Riechers et al. 2013; *pentagon*) and at z =6.9 (Marrone et al. 2018; *big diamond*). The companion galaxies reported in this work are shown with *red* and *yellow circles* (labels analogous to Figure 4.7). Finally, we show the location of constant *sSFR*s (*gray dotted lines*). Deeper observations, particularly in the rest-frame optical region, are necessary to securely characterize the properties of the companion galaxies.

4.3 A dust-continuum emitting source adjacent to the quasar VIK J2211−3206

We detect an emission from the dust continuum, but not from the [CII] emission line, from a source in the field of the quasar J2211, at redshift $z_{\rm quasar}$ =6.3394 ± 0.001 (Decarli et al. 2018). No secure redshift value is measured for this neighboring source (hereafter J2211c). It is worthwhile to notice that the detection of one object with flux density comparable to J2211c, over the area covered in the ALMA survey (Decarli et al., 2018), is expected from a comparison with the number counts of 1.2mm–bright sources observed in blank fields (e.g. Aravena et al. 2016). Indeed, if one integrates the luminosity function provided by Fujimoto et al., 2016 down to the flux of J2211c, one obtains an expected number of sources of ∼2.4 in an area of 1 arcmin^2. This amounts to ∼9.8 sources in the effective area spanned by our ALMA Survey (i.e. ∼4 arcmin^2).

We acquire new observations of this field as part of our follow–up campaign of [CII]–bright companions to high–redshift quasars, using *HST*/WFC3 and *Spitzer*/IRAC (see Table 4.2 for details on the observations). We reduce and analyze the data following the procedures reported in Section 4.1. We consider here the case in which J2211c is located at the redshift of the quasar. No emission from the bulk of the stellar population in the rest–frame optical regime is retrieved (at 3σ significance) in the *Spitzer*/IRAC images. However, we measure a tentative (S/N =2.1) emission in the F140W filter with the *HST*/WFC3 camera. We report our photometric measurements/3σ limits in Table 4.5, where we also list the galactic properties (coordinates and mm flux) obtained from ALMA data (Decarli et al. 2017). In Figure 4.9 we show the postage stamps of our follow–up observations.

In analogy to the companions securely physically associated with the quasars, we compare the spectral energy distribution of J2211c with those of local galaxies, and we fit our photometric data with MAGPHYS–highz (see Figure 4.9). From the latter, we find that the SED of J2211c is better reproduced by a galaxy model in between Arp 220/M82 (i.e. a powerful local ULIRG/starburst), with $M_* \sim 3 \times 10^{10}$ M$_\odot$ and SFR ∼130 $M_\odot$ yr^{-1}. We further measure the obscured/unobscured SFR of J2211c, following the same procedure used for PJ167c (see Section 4.2.2). The star formation rate is dominated by the obscured contribution ($SFR_{\rm UV}$ ∼2 $M_\odot$ yr^{-1} and $f_{\rm obscured}$ ∼0.99). We report all these estimates in Table 4.5. The lack of a secure redshift confirmation prevents us from drawing further conclusions on the nature of this source, or from placing it in the context of previous observations.

4.4 Conclusions

In this work, we present sensitive follow-up imaging and spectroscopy of companion galaxies adjacent (i.e. $<$ 60 kpc and $<$450 km s^{-1}) to four $z \sim 6$ quasars, initially discovered by their bright [CII] and infrared emission with ALMA (Decarli et al. 2017, Willott, Bergeron, and Omont 2017).

The data reported here have been acquired with several ground- and space–based facilities (i.e. LBT/LUCI, Magellan/FIRE, *Spitzer*/IRAC and *HST*/WFC3), and are aimed at probing the galaxies stellar content, recovered in the rest–frame UV/optical regime. We perform aperture photometry at the galaxies location (as measured by ALMA), after accounting for both the

TABLE 4.5: Information on VIK J2211−3206c, a source detected only via its dust continuum emission, close to the quasar VIK J2211−3206. Given the lack of any redshift measurement, we are not able to securely identify this galaxy as physically interacting with the quasar. We report here its coordinates and projected spatial separation to the quasar, obtained from ALMA data (Decarli et al. 2018, Champagne et al. in prep), and our *HST*/WFC3 and *Spitzer*/IRAC follow–up photometric measurements/limits (see Figure 4.9). We also list our constraints on its physical properties, given the assumption that J2211c is found at the redshift of the quasar (see Section 4.3 for details).

VIK J2211−3206c	
R.A. (J2000)	22:11:12.11
Decl. (J2000)	-32:06:16.19
$\Delta r_{\rm projected}$ [kpc]	26.8
F140W [mag]	27.39 ± 0.52
$F_{3.6\mu m}$ [μJy]	<3.42
$F_{4.5\mu m}$ [μJy]	<1.80
$F_{\rm mm}$ [mJy]	0.64 ± 0.06
$SFR_{\rm IR}$ [$M_\odot$ yr^{-1}]	257 ± 36
$SFR_{\rm UV}$ [$M_\odot$ yr^{-1}]	2 ± 2
$f_{\rm obscured}$	0.99 ± 0.14
$SFR_{\rm magphys}$ [$M_\odot$ yr^{-1}]	132^{+120}_{-59}
$M_{*,\rm magphys}$ [$\times 10^{10}$ $M_\odot$]	$2.75^{+3.13}_{-1.47}$

bright, point–like, non–thermal quasar radiation and any foreground object. We detect no emission (at $> 3\sigma$ significance level) from the bulk of the companions stellar population, observed at 3-5 μm. In addition, no light from young stars, probed at $\lambda_{\rm obs}$ $\sim$1.4 μm by *HST*/WFC3, is detected in three of the four sources examined, i.e. J2100c, J0842c and PJ231c (see Section 4.1 and Table 4.3). The companion galaxy of the quasar PJ167, instead, is detected in our *HST* observations at 6.4σ.

From a comparison with SEDs of various local galaxies, we find that the companions PJ231c, J2100c and J0842c at $z \sim 6$ are consistent with an Arp 220–like galaxy, i.e. resulting from a recent massive gaseous merger (see Figure 4.6). These objects are heavily dust–obscured and/or they harbor a modest stellar mass. The source PJ167c resembles, instead, a less extreme star forming galaxy (see Figure 4.6). We compute *SFRs* and M_* with the SED fitting code MAGPHYS–highz for PJ167c, whose emission is detected in more than one broad band. We derive the obscured *SFR* of PJ231c, J0842c and J2100c by assuming the SED of Arp 220 scaled at the observed fluxes. We place upper limits on their stellar masses by considering their total dynamical masses, derived from the [CII] emission line widths, and their gas masses, estimated from the dust content (see Table 4.4). We also derive tight constraints on their unobscured star formation rate contribution, as obtained from the sensitive *HST*/WFC3 data. We observe $SFR_{\rm FUV} \lesssim 3$ $M_\odot$ yr^{-1}, i.e. more than two orders of magnitude lower than $SFR_{\rm IR}$, with the exception of PJ167c, whose obscured star formation component is only $\sim$6$\times$ larger than the unobscured value (see Table 4.4 and Figure 4.7). Finally, we find that the companions examined here are comparable with being on the main sequence of star forming galaxies at $z \sim 6$ (see Figure 4.8). However, our constraints/limits, in particular on the stellar masses, are still coarse. This is mainly due to the few detections in the bluer bands.

In the near future, deep observations with upcoming instruments, e.g. the NIRCAM and

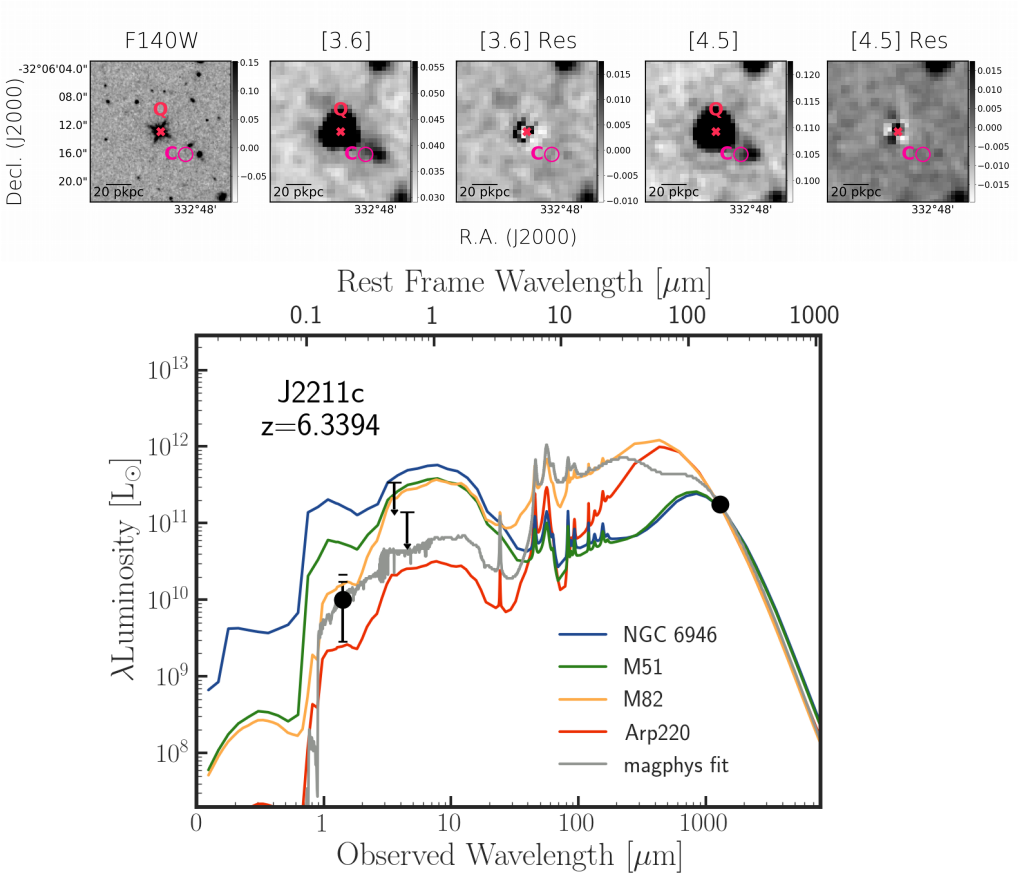

FIGURE 4.9: Source adjacent to the quasar J2211, detected solely in the dust–continuum emission, i.e. with no secure redshift measure. *Top*: Postage stamps ($20'' \times 20''$) of our follow–up observations; labels are as in Figure 4.3. *Bottom*: Spectral Energy Distribution of J2211c. We assume that the source is located at the same redshift of the quasar. We report our photometric measurements/limits and, for comparison, various templates of local galaxies and the best SED fit from MAGPHYS-highz. The labels and templates are as in Figure 4.6. J2211c SED results to be intermediate between the low–z ULIRG Arp220 and the starbursting galaxy M82 (see Section 4.2.1). On the base of our follow–up observations, and considering the predicted density of mm–sources, we are not able to exclude that this source is a fore/background.

NIRSPEC cameras on board the *James Webb Space Telescope*, will enable us to uncover the emission and dynamics of the stellar content of these galaxies (see Section 5.1.4 for further discussion).

Chapter 5

Conclusions and Outlook

In this thesis, we presented a search for the highest redshift quasars, and we analyzed several of their properties, from their central black holes, to their host galaxies and the environments where they live.
In summary:

1. In Chapter 2, we presented our discovery of six new quasars at $z \sim$6.5, from our search based on the PS1 catalog and aided by our imaging and spectroscopy follow–up campaign (Section 2.2).

2. Again in Chapter 2, we analyzed optical/NIR spectra of 15 quasars at $z \gtrsim$6.5, acquired with several facilities (e.g. VLT/FORS2; VLT/X-Shooter, Magellan/FIRE, LBT/MODS; Section 2.3.2), and we presented new NOEMA mm–observations of the host galaxies of four of these quasars (Section 2.3.3).
   The main results from this comprehensive analysis are:

   (a) We inferred evidence for the presence of strong winds/outflows in high–redshift quasar broad line regions, on the base of the large measured blueshifts (∼700–6000 km s^{-1}) of the CIV broad emission line (Section 2.5.4).

   (b) From our fit of the MgII spectral region, we estimated very large masses for the central black holes ($M_{\rm BH} \sim 0.3 - 3 \times 10^9$ M$_\odot$; Section 2.5.6). Quasars at $z \gtrsim$6.5 seem to accrete with a rate comparable to a matched sample at $z \sim$1. The study of a larger number of high–z objects is necessary to test if this trend holds, e.g., at lower luminosities/black hole masses. We assessed the masses of their seeds, given certain assumptions on their radiative efficiency, accretion rate and age, and we placed them in the context of current theoretical models of SMBHs formation and growth (Section 2.5.7).

   (c) We recovered no evolution of the FeII/MgII ratio, proxy of the [metal/α element] abundance ratio, with redshift in quasar BLRs (Section 2.5.8).

   (d) We observed high continuum ($L_{\rm FIR} \sim 10^{12}$ L$_\odot$) and [CII] ($L_{\rm [CII]} \sim 10^9$ L$_\odot$) luminosities, and large star formation rates (>100s M$_\odot$ yr^{-1}), in four quasar host galaxies. Their $L_{\rm [CII]}/L_{\rm FIR}$ ratios, proxy of the conditions of their ISM, are similar to the ones of local ULIRGs (Section 2.5.9).

   (e) We retrieved a shallow evolution of their near zone sizes with redshift, highlighting how these quantities are more strongly correlated with individual quasar properties rather than with the general evolution of the external IGM (Section 2.5.10).

3. In Chapter 3, we presented the second study of the Mpc–scale environment of a $z \sim$5.7 quasar, via observations with broad– and narrow–band filters at VLT/FORS2. We found

no evidence for an enhancement of LAEs in the surroundings of the quasar with respect to a blank field (Section 3.4). This can be explained by several scenarios, e.g. the quasars' ionizing radiation prevents star formation, overdensities are mainly composed by dust–obscured galaxies, or quasars do not live in the most massive dark matter haloes (Section 3.8).

4. In Chapter 4, we presented optical/IR follow–up observations of the gas–rich, companion galaxies discovered by ALMA around four $z \sim 6$ quasars. We reported data from several ground– and space–based facilities, i.e. LBT/LUCI, Magellan/FIRE, *HST*/WFC3 and *Spitzer*/IRAC (Section 4.1). Our sensitive observations showed that three galaxies are very dust enshrouded and/or they host a low stellar content; their SEDs are comparable to the ones of local ULIRGs (Section 4.2.1). The companion to the quasar PSO J167–13 is instead consistent with a less extreme star–forming galaxy.

This thesis pushes forward our knowledge of the highest–redshift quasar population, by presenting a comprehensive analysis of their physical properties.

However, several questions are still left unanswered: How can we push the current redshift frontier even further, and what these discoveries can teach us on the growth and evolution of the first supermassive black holes? How is the gas channeled from the intergalactic medium down to high–redshift quasars? In which environments are the first quasars found, and how our studies depend on the scales and/or wavelength range probed?

In the following section, we sketch potential future directions, aimed at tackling these questions, which take advantage of both state-of-the-art and upcoming observational facilities and surveys.

5.1 Outlook

5.1.1 Pushing the Redshift Frontier of the Quasar Search

We are currently living in the golden age of high–redshift quasar searches, owing to the advent of new, deep, large–area sky surveys, resulting in the recent break of the $z \sim 7$ barrier for the second time (Bañados et al., 2018).

In particular, in the last two years, the HSC survey greatly enlarged the sample of known quasars at $z > 5.5$, with 64 newly discovered objects (already topping the 51 found by SDSS, Jiang et al. 2016), focusing on the low–luminosity regime (i.e. $M_{1450} \sim -22$–24; Matsuoka et al. 2018b; see Section 1.5). These discoveries were performed taking advantage of data covering a sky area of $\sim$650 deg^2. The final sky coverage of the Wide survey will be of 1400 deg^2, of which 27 and 3.5 deg^2 will be imaged with the Deep and UltraDeep layers, respectively. The final number of quasars expected to be discovered by HSC are $\sim$350 at $5.7 < z < 6.5$ (with $M_{1450} < -23$) and $\sim$60 at $6.5 < z < 7.2$ (with $M_{1450} < -24$).

Several new transformational instruments/surveys are also scheduled to come online, in the near (LSST and Euclid), and long–term (WFIRST) future. They will provide a new baseline for the quasar quest, both at lower luminosities and higher redshifts.

The Near Future: LSST and EUCLID

The *Large Synoptic Survey Telescope* (**LSST**; LSST Science Collaboration et al. 2009) will image the sky visible from Cerro Pachon (Chile) multiple times over 10 years time. The main science goals of this survey are determining the nature of Dark Matter and Dark Energy, identifying asteroids/Solar System objects, studying the transient optical sky and understanding the structure and formation of the Milky Way. Thanks to its 3.2 Gigapixels camera, with a large field of view of 9.6 deg^2, LSST will cover a total sky area of 30 000 deg^2 at Decl$<34.5°$. Of the total observing time, 90% will be dedicated to an area of 18 000 deg^2, that will be observed 800 times (Ivezic et al., 2008). The LSST will collect images in 6 broad band filters (*ugrizy*), expecting to reach single epoch depths of (23.9, 25.0, 24.7, 23.3, 22.1), and final co-added images depths of (26.1, 27.4, 26.8, 26.1, 24.9). First light is scheduled for mid 2020, while the full start of science activity is expected for the end of 2022[1]. Together with currently used quasar selection methods (i.e. color/variability criteria), LSST promises to rely on its precise proper motion measurements to very efficiently reject the majority (>70% at $r < 24$) of the contaminant stars in our Galaxy. A total number of 10 million quasars are predicted to be discovered at redshifts up to $\sim$7.2 (Ivezić et al., 2014). In particular, the expected number of new quasars by LSST is of $\sim$3500 at $5.7 < z < 6.5$ and of $\sim$600 at $6.5 < z < 7.2$, down to $M_{1450} = -23, -24$, respectively.

Euclid is an ESA space mission, to be launched in 2020 and to be positioned in L2, aimed at unveiling the nature of Dark Matter and Dark Energy by measuring weak gravitational lensing and galaxy clustering (Laureijs et al., 2011). The satellite will board a 1.2m telescope, equipped with optical and NIR cameras and a NIR spectrograph. During its six years lifetime, Euclid will image 15 000 deg^2 of the sky, with anticipated 5σ depths of 24.0 mag in the YJH filters. The current number density of quasars at $z > 2.2$ is expected to be tripled by EUCLID (Amendola

[1] https://www.lsst.org/about/timeline

et al., 2016). In particular, 55 z >8.1 quasars at $M_{1450} < -24.74$ are predicted to be newly discovered (Laureijs et al., 2011).

In Figure 5.1, we show the quasar parameter space (i.e. black hole masses, redshifts and UV luminosities) that will be explored by LSST and Euclid. In the near future, LSTT and Euclid will allow discoveries, on a wide sky area, of quasars at lower luminosities and higher redshifts, respectively.

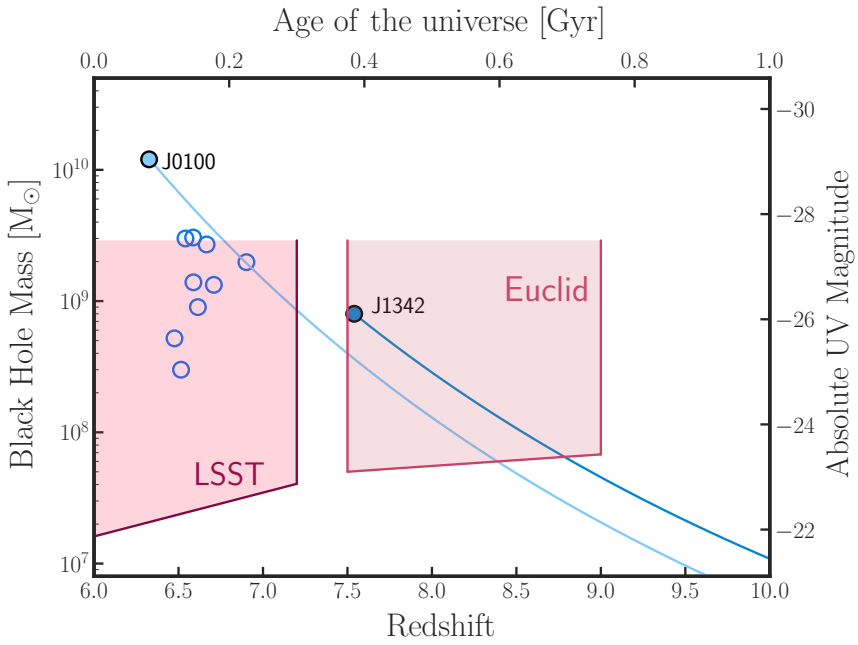

FIGURE 5.1: In the near future, LSST and Euclid will expand the quasar search, on a wide sky area, at lower luminosities/black hole masses and higher redshifts, respectively (*shaded areas*). In particular, we here consider the nominal 5σ depth in the y (LSST) and Y (Euclid) band, and convert them into absolute UV magnitudes and black hole masses (assuming accretion at Eddington rate). The limits at the lowest absolute magnitudes are arbitrary. We show the black hole mass growth, as a function of redshift, calculated from equation 2.13 (assuming constant accretion at Eddington rate and a 10% radiative efficiency), for the quasar at the highest–redshift (J1342; Bañados et al. 2018) and with the largest black hole mass at z >6 (J0100; Wu et al., 2015) known so far. We also report the quasars studied in Chapter 2 at z ∼6.5 (*empty blue circles*).

The Long Term Future: WFIRST

The *Wide Field Infrared Survey Telescope* (**WFIRST**; Spergel et al. 2013) is an approved NASA satellite mission for the coming decade, to be launched in the mid-2020s. As of now, the satellite is designed to be composed by a 2.4m telescope, with a wide field NIR (0.76–2.0 μm) camera and a coronographer. The camera will provide imaging, grism and integral field spectroscopy (IFU) capabilities. WFIRST aims at a plethora of science goals, from the investigation of the early universe and the test of the ΛCDM model, to the discovery of thousands of new exoplanets. In particular, the programmed High Latitude Imaging and Spectroscopy Surveys will produce very deep (down to 26.7 magnitude at 5σ in the Y band) observations of 2000 deg^2 of the sky. The number of predicted new quasars is of ∼2470 at 7< z <8 and of 130 at z >8 for magnitudes H <26.7.

5.1.2 A Multi–scale and Multi–Wavelength Approach on Quasars Environments

As previously discussed in this thesis, current studies of the environments of high–z quasars via UV–based observations have, so far, not provided the unique picture sketched by theoretical models (see Section 1.5.4 and Chapter 3). Very recently (i.e. after the work presented in Chapter 3), new searches for LAEs in the field of two z >6 quasars have been performed. Goto et al., 2017 inspected the surroundings of the quasar CFHQS J2329–0301 at z ∼6.4 with the Suprime-Camera: despite the previously observed, large drop-out overdensity (Utsumi et al., 2010), they found no LAE, suggesting that this field is severely underdense with respect to a blank field. Ota et al., 2018 observed the quasar VIK J0305–3150 (z =6.6145) with the Suprime-Camera: LBGs were found to cluster in large (∼4–20 cMpc), high density (∼3–7σ) regions, while LAEs showed mainly underdensities. The quasar was not located at any particular high density peak, but instead was surrounded by fewer LAEs than what is expected in a blank field.

A drawback of the aforementioned LAE investigations, is that the redshifts of the quasars considered were measured only via broad emission lines in their rest–frame UV spectra[2]. As shown by Venemans et al., 2016 and in Section 2.5.4, such emission lines can be strongly shifted with respect to the systemic redshift of the host galaxy, precisely retrieved by the narrow [CII]/CO emission line, rising from the galactic interstellar medium. The exact redshift of the quasar hosts might therefore shift the Lyα emission line outside the narrow band filter, and a potential overdensity of LAEs might just be missed.

Different from the *radio–quiet* quasars considered so far, *radio–loud* sources were observed to be mostly located in overdense regions, over a wide redshift range ($1.0 \lesssim z \lesssim 5.2$; e.g. Venemans et al. 2007, Wylezalek et al. 2013 and Hennawi et al. 2015). Radio–loud quasars are defined as presenting a *radio-loudness parameter*, i.e. the ratio between radio and optical luminosity, $\mathrm{R} = f_\nu(5\,\mathrm{GHz})\,/\,f_\nu(4400\,) > 10$ (Kellermann et al., 1989). Only a handful of such objects at z >5 are reported in the literature to date, 8 of which are z >5.5 quasars (Bañados et al., 2015a): early studies of their environment are sparse, but promising. In particular, Zheng et al., 2006 and Ajiki et al., 2006 found an overdensity of dropouts around a z∼6 radio-loud quasar, while Venemans et al., 2004 observe an enhancement of sources in the field of the only powerful radio galaxy at z >5. Radio–loud sources might be preferred, with respect to radio–quiet ones, as signposts of the first protoclusters of galaxies.

In order to test whether radio-loud quasars reside in high density environments, we recently secured broad– and narrow–band observations, at VLT/FORS2, of the field around the quasar PSOJ135.3860+16.2518 (Bañados et al., 2015a). This source is the only radio–loud quasar at z >5.5 with observations of the CO emission line which precisely locate the Lyα emission of its host galaxy within the narrow band filter response, at a redshift of z=5.719±0.0004.

On the other hand, studies in the rest–frame IR range suggested that high–redshift quasars are indeed highly clustered (e.g. Decarli et al. 2017; see also Section 1.5.4 and Chapter 4). The discrepancy with UV–based studies (but see also the work by Farina et al. 2017) could be due to several reasons. For instance, dusty galaxies, not sensibly emitting in the UV range, might prefer to live close to quasars, or the small–scale environment present an enhancement of sources

[2]The redshift of the quasar VIK J0305–3150 is based on the narrow [CII] emission line. However, the Lyα line at this redshift falls very close to one of the edges of the narrow band filter used in the environment study. Half (or more) of the LAEs surrounding the quasar could potentially have Lyα emission that falls outside the filter response.

with respect to the large–scale one. Distinguishing among these scenarios is still hard, mainly due to the lack of comprehensive studies that securely locate galaxies associated with high–z quasars over a large range of wavelength (from rest–frame UV to IR), and scales (from several kpc, e.g. the ALMA field, to Mpc).

In order to build a first, comprehensive, multi-wavelength and multi-scale study of quasars environments, we have very recently submitted a proposal to image a large sample (34) of $z \sim$6 quasars with ALMA. These observations are intended to set the search for any possible gas–rich companion galaxy: based on the previous ALMA survey (Decarli et al. 2017, 2018) we would expect to recover 7 ± 3 new overdensities. The targeted quasars are located in suitable redshift ranges for optical/NIR follow–up studies with narrow band filters, which will recover the ionized gas from any companion system, and probe the Mpc-scale environment.

5.1.3 Gas Accretion onto the First Quasars

Quasars' host galaxies have been so far studied via the cool gas and dust emission observed in the rest–frame IR. Observations of the stellar component and of the predicted ionized gas surrounding the quasars (Lyα halo) are currently extremely hard. This is due both to the presence of the bright central, non–thermal engine (e.g. Decarli et al., 2012, see Section 1.5), and to the rapid dimming of the surface brightness with redshift ($\propto (1+z)^{-4}$; e.g. Farina et al. 2017). While waiting for the transformational capabilities of *JWST* (see Section 5.1.4), a couple of peculiar quasars at $z >$6.5 can already help us now in the investigation of the dynamics, composition and distribution of the ionized gas fueling these sources in the first Gyr of the universe.

The quasar PSO J323.1382+12.1277 (PJ323+12; discovered as part of this work, see Chapter 2), at $z \sim$6.6, represents an ideal laboratory to effectively study, for the first time at these redshifts, both the stellar radiation from the host galaxy and the Lyα halo. A diffuse Lyα emission surrounding the quasar, extended up to several kpc, is detected in the 2D spectrum acquired with VLT/FORS2 (see Figure 5.2). A foreground galaxy (at $z \sim 1-2$), with a line-of-sight separation from the quasar of only $\sim$1.4", is likely acting as a gravitational lens, greatly magnifying the emission from the quasar host and its surrounding (see Section 2.4). PJ323+12 is the first case of a potentially gravitationally lensed quasar at $z >$5. This scenario is sustained by our $K-$band observations, acquired with the Magellan/Fourstar camera, in which the quasar image appears extended/irregular at 0.7" resolution (see Figure 5.2). Future imaging and spectroscopic observations, with e.g. *HST*, will be crucial in assessing the dynamics of the Lyα halo, and the stellar and ionized gas emission from the quasar host galaxy.

Also the quasar PSO J167.6415-13.4960 (PJ167–13; Venemans et al. 2015b), at $z \sim$6.5, studied in both Chapter 2 and 4, represents an interesting case. As reported in Section 4.1.2, our *HST*/WFC3 observations spot a tentative, extended, UV–bright emission connecting the quasar to its proximate companion galaxy (see also Figure 4.5). While ALMA data provide detailed information on the cool gas and dust in the system, additional deep and spatially resolved observations are needed to characterize the luminosity, structure and kinematics of the ionized component. With this aim, we recently submitted a proposal to collect sensitive MUSE observations of the field around this quasar, using the newly offered wide-field AO mode. These observations would provide us the opportunity to characterize the extended emission, to search for further LAEs in the surroundings, and to map any potential large–scale Lyα halo.

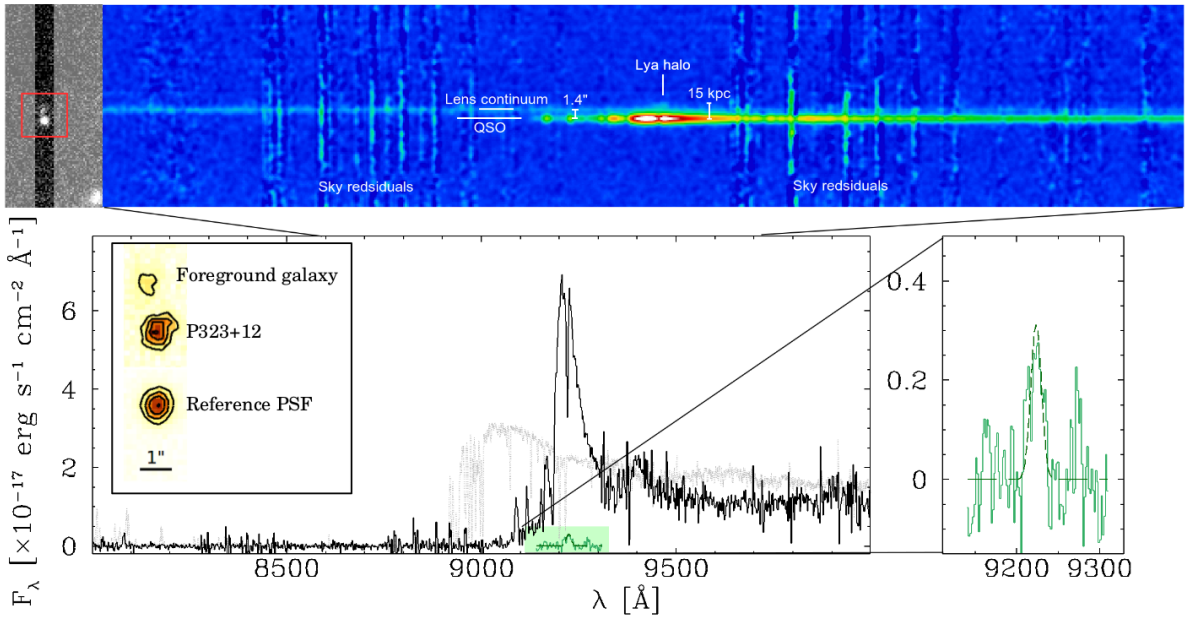

FIGURE 5.2: The quasar PJ323+12 offers an unprecedented opportunity to study the stellar light and diffuse gas around a quasar at $z \sim 6.6$. A foreground galaxy (*top panel, left inset*) might act as a gravitational lens, greatly magnifying the emission from the quasar and the surroundings. Both our 2D (*top panel*) and 1D (*bottom panel, right inset*) spectra reveal the presence of a spatially–resolved Lyα emission. Evidence in support of such scenario are provided by recent $K-$band observations, in which the QSO presents an extended morphology (*bottom panel, left inset*). Future, sensitive imaging, grism and IFU observations, which can be provided by *HST* and, in the near future, by *JWST*, will be crucial in characterizing this unique source.

5.1.4 A JWST View on High–z Quasars

The *James Webb Space Telescope* (**JWST**) is NASA's next decade premier observatory, scheduled to be launched in 2020. With its unprecedented capabilities in the NIR regime, *JWST* is expected to revolutionize our view of the universe over a wide range of science cases, from our own Solar System, to exoplanets, and galaxies in the very early universe. In particular, *JWST* will provide a wealth of unparalleled information on high–redshift quasars.

Imaging observations acquired with the *Near Infrared Camera* (NIRCam; 0.6–5.0 μm) and the *Mid-Infrared Instrument* (MIRI; 5–28 μm) will reveal, for the first time, the *stellar light* in the *quasar host galaxies* (see Figure 5.3). Such observations will shed light on the galaxies morphologies, stellar masses, extinction and unobscured *SFR*s. Moreover, the IFU capabilities of the *Near Infrared Spectrograph* (NIRSpec; 0.6–5.3 μm) will permit a 3D tomography (i.e. morphology/kinematics) of quasar host galaxies, by imaging several emission lines, such as [OII], Hβ and [OIII].

Our knowledge of the *quasar physics* and of the *central massive black hole* will also be pushed to a new frontier. NIRCam and MIRI imaging will provide a high–quality and comprehensive (up to rest frame $\lambda = 3$ μm) SED of the highest redshift quasars (see Figure 5.3). This will allow us to check for any systematic difference with respect to lower–redshift sources, and firstly precisely study the contribution from the dusty torus at high$-z$. Moreover, observations with NIRSpec and MIRI Medium Resolution Spectrometer (MRS) will characterize the metallicities,

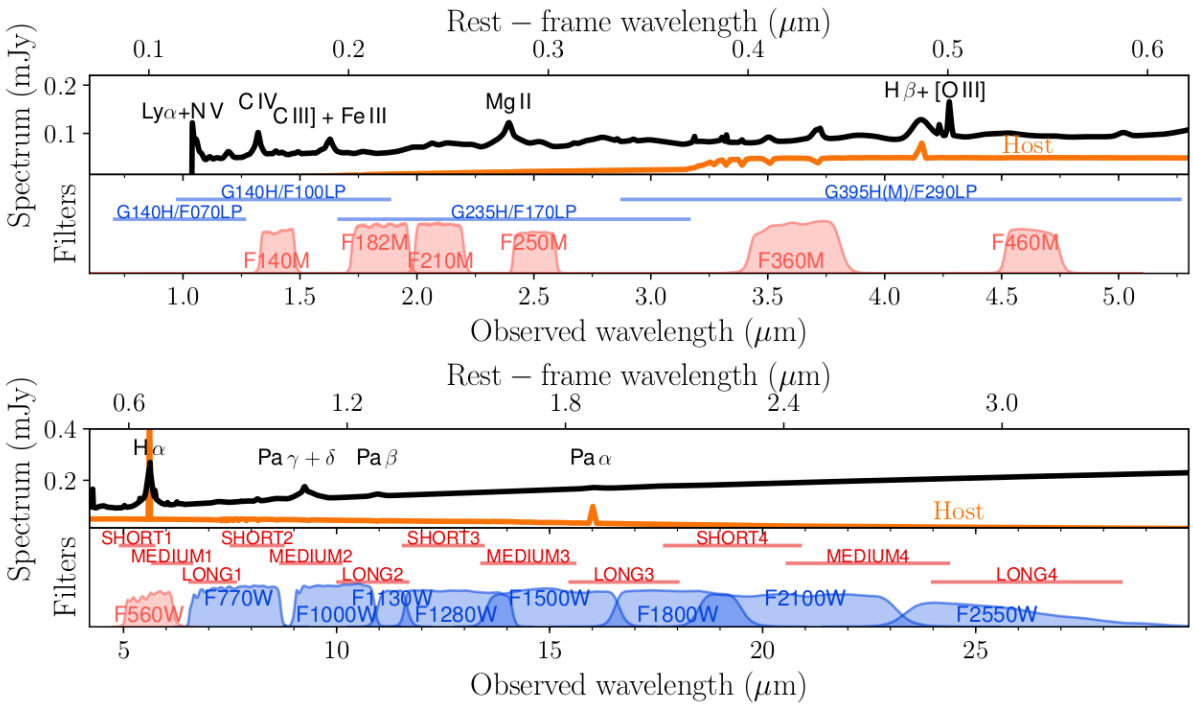

FIGURE 5.3: Spectral Energy distribution of a quasar and its host galaxy at z =7.54. The broad band filter response curves of the NIRCam and MIRI cameras on board *JWST* are overplotted. *JWST* will, for the first time at z >6, constrain the entire UV-to-optical quasar's SED, and it will pin down the contribution from the stellar emission in the host galaxy.

kinematics and extinction of the BLRs, from the UV to the rest–frame optical regime. We will be able to obtain precise black hole mass estimates from the Hβ emission line (e.g. Park et al. 2012; see Sections 1.4.3 and 2.5.1). The simultaneous $M_{\rm BH}$ measurements, using several broad emission lines (e.g. CIV, MgII, Hβ, Hα), will inform us on whether the scaling relations/line correlations observed at lower$-z$ still hold in the early universe (e.g. Shen et al. 2008).

The high S/N quasar spectra obtained with NIRSpec and MIRI MRS will also enable systematic searches for *metal absorption systems* along the line of sight. These systems are essential in the study of galaxy evolution, and in locating any emission from the first, metal–free Pop III stars (e.g. Becker et al. 2012, Kulkarni et al. 2013 and Ma et al. 2017). Complementary NIRSpec IFU and NIRCam imaging observations will permit the identification of the emitting counterparts of the systems previously identified in absorption.

JWST offers exceptional tools to study the *environment* of high–redshift quasars. Analogously to quasars host galaxies, observations with NIRCam, NIRSpec and MIRI will unveil the nature of the gas–rich companion galaxies to high$-z$ quasars studied in Chapter 4, whose rest–frame optical stellar emission remains elusive so far. Moreover, NIRCam is equipped with a set of narrow band filters ideal to detect the Hα emission line at z ∼6.1-6.2. Two of the quasar+companion systems discovered by ALMA are located in within the filter response, together with a large number of known quasars (see Figure 5.4). Thanks to observations with a combination of broad and narrow band filters, we will be able to characterize any ionized diffuse emission around the quasars and the companions, and to probe the larger scale environment by searching for Hα Emitters (HAE).

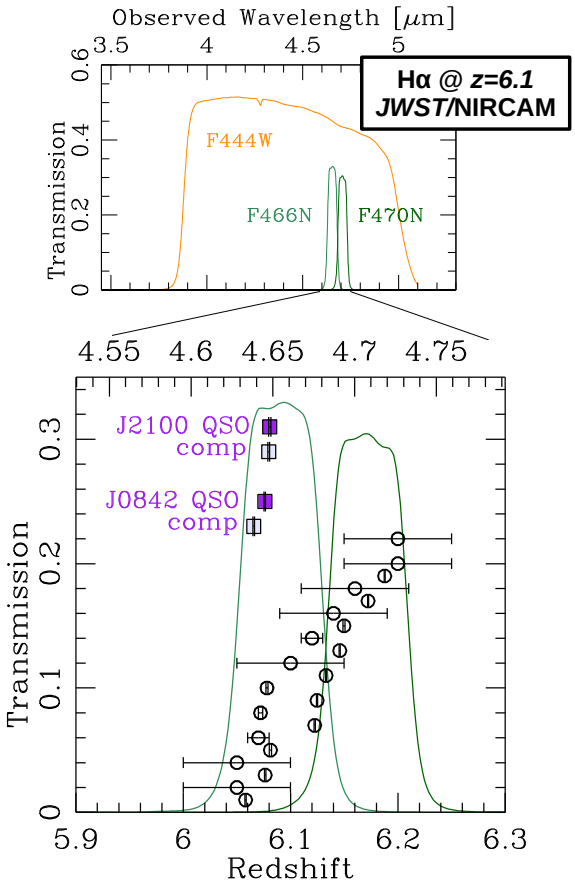

FIGURE 5.4: The *JWST*/NIRCam instrument offers a unique combination of broad and narrow band filters, thanks to which any emission from the quasar hosts or any companion galaxy will be detected. A number of known $z \sim 6.1$ quasars, and two quasar+companion systems (Decarli et al. 2017, see Chapter 4) are located at suitable redshifts for such studies.

The unique capabilities of *JWST* will open a new, exciting window on the early universe, and will enable detailed and panchromatic investigations of massive galaxies and supermassive black holes in the first Gyr of cosmic history.

Acknowledgements

I wish to thank my supervisor, Fabian Walter, for his precious support, guidance and enthusiasm through my PhD.

I would like to thank the members of Team HQ: Roberto Decarli, for your endless patience and support in me, in all aspects, from papers to proposals to future decisions; Emanuele Farina, for all the observing nights spent together, the scientific discussions (the pinky plot) and the merendellas; Eduardo Bañados, for sharing your (incredible!) knowledge of and passion for quasars; Bram Venemans, for patiently and kindly guiding me through data reduction/analysis and database mining.

I thank Christian Fendt, our IMPRS coordinator, who, especially in the beginning of my PhD, helped me navigating the German and MPIA system. I also would like to thank my fellow members of the 10th IMPRS generation, for the nice time at the annual retreat(s) and the supportive feedback during our scientific activities.

I will never be able to deeply, wholeheartedly thank the many people that made my time in Heidelberg truly memorable.
I start by thanking the regular faces at "coffee after lunch", Bert, Iskren, Morgan, Nikolay, Allison, for the shared coffee and laughter. I thank my officemates, Sara, Richard, Michael, Aiara and Irina, for sharing with me the everyday life, including the hot summer days in the green house. Thanks to Nadine, who always listened and encouraged me, and for simply being there, especially in the most difficult moments.

I thank the extended Gym(?) group: Peter, Gym tonight?; Reza, and his musical tastes; Christina, for all the scientific and psychological support; Maria, for your appreciation of my driving skills, and because you always make me laugh, even in my particularly grumpy moments; Sara, I can't even start to put in words how your very presence was essential for me; Thank you for your time and your smile at volleyball, in the office, even at the hospital: I consider myself honored to be your friend.

I thank the "Italian Gang": Gabriele and his jokes and great risotto; Laura, for the PS1 discussions, and the burger and chips nights; Chiara, for being an amazing person, for sustaining, understanding and hugging me when I truly needed; Alessandra, for our efficient shopping, for your patience, support, words of wisdom, and for helping me navigating through my paranoia: your support was crucial for me.

I thank my flatmate Anna, for the biscuits, ice cream, laughter and time with you and your kind family: Thank you for being kind and supportive. I thank my volleyball team mates "Schnelleshelles", because the time in the Gym was a ray of sunshine: Arjen, Sara, Arno, Ralph, Steffen, Claudia, Adrian, Laurent, Karin, Chrissi.

Finiró in italiano. Ringrazio i miei amici di sempre, della (ora!)gente che telegrammano: Bormio, Fulvio, Teo, Lucio, Marta, Carlo, Ricca, Carli. Nonostante i vari impegni, e il non costante contatto, le nostre cene/risottate mi fanno tornare indietro nel tempo. Ringrazio i "Panda", Luca e Francesca, perche' ci conosciamo da piu di meta' delle nostre vite, e il resto potete estrapolarlo. Ringrazio Nikita, perché il tuo sostegno, pratico e psicologico, e la tua presenza, mi hanno aiutato ad essere qui, e ad essere la persona che sono oggi.

Ringrazio la mia famiglia: i miei genitori, perche' mi hanno supportata e sopportata sempre, e

i buongiorno e messaggi quotidiani sono stati per me piú importanti di quanto anche loro possano pensare; mio fratello, per essere il mio riferimento informatico, per avermi incoraggiato e ospitato, e sempre fatto ridere; Milena, per la tua dolcezza, i tuoi biscotti e il tuo sorriso; i miei nonni, che sono la mia bussola interna, qualsiasi cosa succeda.

Infine, come sempre, ringrazio te, Clara.

Appendix A

Filters Description

We list here in Table A.1 the broad band filters used throughout this work, both from public surveys and follow–up efforts.

TABLE A.1: List of broad band filters used in this thesis and their characteristics (Telescope/Survey, central wavelength and width).

Filter name	**Instrument/Survey**	λ_c [μm]	$\Delta\lambda$ [μm]
$g_{\rm P1}$	PS1	0.487	0.117
$r_{\rm P1}$	PS1	0.622	0.132
$i_{\rm P1}$	PS1	0.755	0.124
$z_{\rm P1}$	PS1	0.868	0.097
$y_{\rm P1}$	PS1	0.963	0.062
$g_{\rm decam}$	DECaLS	0.475	0.152
$r_{\rm decam}$	DECaLS	0.640	0.143
$z_{\rm decam}$	DECaLS	0.928	0.147
R_SPECIAL	VLT/FORS2	0.655	0.165
z_GUNN	VLT/FORS2	0.910	0.131
FILT815_13+70	VLT/FORS2	0.815	0.13
Y	UKIDSS/VHS	1.000	0.120
J	UKIDSS/VHS	1.250	0.213
H	UKIDSS/VHS	1.650	0.307
K	UKIDSS/VHS	2.150	0.390
$z_{\rm O2K}$	CAHA 3.5m/Omega2000	0.908	0.158
$Y_{\rm O2K}$	CAHA 3.5m/Omega2000	1.039	0.205
$J_{\rm O2K}$	CAHA 3.5m/Omega2000	1.234	0.164
$I_{\rm E}$	NTT/EFOSC2	0.793	0.126
$Z_{\rm E}$	NTT/EFOSC2	>0.840	–
$J_{\rm S}$	NTT/SofI	1.247	0.290
$i_{\rm w}$	CAHA 3.5m/CAFOS	0.762	0.139
$i_{\rm MMT}$	MMT/MMTCam	0.769	0.130
$Y_{\rm retro}$	su Pont/Retrocam	1.000	0.120
$J_{\rm LUCI}$	LBT/LUCI	1.247	0.305
$g_{\rm G}$	MPG 2.2m/GROND	0.459	0.137
$r_{\rm G}$	MPG 2.2m/GROND	0.622	0.156
$i_{\rm G}$	MPG 2.2m/GROND	0.764	0.094
$z_{\rm G}$	MPG 2.2m/GROND	0.899	0.128
$J_{\rm G}$	MPG 2.2m/GROND	1.240	0.229
$H_{\rm G}$	MPG 2.2m/GROND	1.647	0.264
$K_{\rm G}$	MPG 2.2m/GROND	2.171	0.303
F105W	*HST*/WFC3	1.0552	0.265
F140W	*HST*/WFC3	1.3923	0.384
$W1$	ALLWISE	3.353	0.663
$W2$	ALLWISE	4.603	1.042
$W3$	ALLWISE	11.56	5.506
[3.6]	*Spitzer*/IRAC	3.550	0.750
[4.5]	*Spitzer*/IRAC	4.493	1.015
[5.8]	*Spitzer*/IRAC	5.731	1.425
[8.0]	*Spitzer*/IRAC	7.872	2.905

Appendix B

Spectroscopically Rejected Objects

We report in Table B.1 the Galactic contaminants found in our spectroscopic follow-up observations, which satisfied our selection criteria considering the PS1 PV3 database information (three sources). We list names, coordinates, z_{P1} , y_{P1} , Y and J magnitudes. An accurate spectral classification of the sources is beyond the scope of this work.

TABLE B.1: Objects spectroscopically confirmed to not be high redshift quasars.

Name	**R.A.(J2000)**	**Decl. (J2000)**	z_{P1}	y_{P1}	Y	J
PSO229.40365−22.37078	229.403651	-22.3707877	>22.36	20.36 ± 0.14	–	20.95 ± 0.27
PSO267.27554+15.6457	267.2755422	15.64579622	22.48 ± 0.31	20.69 ± 0.13	–	20.31 ± 0.18
PSO357.24231+25.77427	357.2423123	25.77427024	>22.81	20.72 ± 0.13	21.52 ± 0.2	21.16 ± 0.14

Appendix C

Acronyms

AEGIS	All-wavelength Extended Groth Strip International Survey
AGN	Active Galactic Nucleus
ALLWISE	all-sky Wide-field Infrared Survey Explorer
ALMA	Atacama Large Millimeter Array
BAL	Broad Absorption Line
BLR	Broad Line Region
CFHQS	Canada-France High-z Quasar Survey
COSMOS	Cosmic Evolution Survey
CMB	Cosmic Microwave Background
DBSP	Double Spectrograph for the Palomar 200-inch Telescope
DeCALS	Dark Energy Camera Legacy Survey
DES	Dark Energy Survey
DLA	Damped Lyman Alpha system
EFOSC2	ESO Faint Object Spectrograph and Camera 2
ESO	European Southern Observatory
EoR	Epoch of Reionization
EW	Equivalent Width
FIR	Far Infrared

FIRE Folded-port InfraRed Echellette

FORS2 FOcal Reducer/low dispersion Spectrograph 2

FOV Field of View

FWHM Full Width at Half Maximum

GOODS Great Observatories Origins Deep Survey

GNT Gemini North Telescope

GNIRS Gemini Near IR Spectrograph

GRB Gamma-Ray Burst

GROND Gamma-Ray Burst Optical Near-Infrared Detector

HAE Hα Emitters

HSC Hyper-Suprime Camera

HST Hubble Space Telescope

IGM Intergalactic Medium

IR Infrared

IRAC Infrared Array Camera for the Spitzer Space Telescope

IRAM Institute de Radioastronomie Millimétrique

ISM Interstellar Medium

JCMT James Clerk Maxwell Telescope

JWST James Webb Telescope

LAE Lyα Emitters

LBG Lyman Break Galaxies

LBT Large Binocular Telescope

LF	Luminosity Function
LRIS	Low Resolution Imaging Spectrometer
LSST	Large Synoptic Survey Telescope
LUCI	LBT Utility Camera in the Infrared
MMT	Multiple Mirror Telescope
MODS	Multi-Object Double Spectrograph
MPG	Max Planck Gesellschaft
MUSE	Multi Unit Spectrograph Explorer
NIR	Near-Infrared
NOEMA	NOrthern Extended Millimeter Array
NTT	New Technology Telescope
Pan-STARRS1 **PS1**	Panoramic Survey Telescope & Rapid Response System 1
PdBI	Plateau de Bure Interferometer
PSF	Point Spread Function
RM	Reverberation Mapping
SDF	Subaru Deep Field
SDF	Spectral Energy Distribution
SDSS	Sloan Digital Sky Survey
SFR	Star Formation Rate
SMBH	Supermassive Black Hole
SMG	Submillimeter Galaxies

SN	Supernova
SoFI	infrared spectrograph and imaging camera Son of ISAAC
S/N	Signal-to-noise ratio
TIR	Total Infrared
UDS	UKIDSS Ultra Deep Survey
UKIDSS	UKIRT InfraRed Deep Sky Survey
UHS	UKIRT Hemisphere Survey
ULIRG	Ultra Luminous Infrared Galaxy
UV	Ultraviolet
VHS	VISTA Hemisphere Survey
VIKING	Visible and Infrared Survey Telescope Kilo-Degree Infrared Galaxy
VISTA	Visible and Infrared Survey Telescope for Astronomy
VLT	Very Large Telescope
WEL	Weak Emission Line
WFC3	Wide Field Camera 3
WFIRST	Wide-Field Infrared Telescope
ΛCDM	Lambda Cold Dark Matter

Bibliography

Ajiki, M. et al. (2006). "New Corroborative Evidence for the Overdensity of Galaxies around the Radio-Loud Quasar SDSS J0836+0054 at z = 5.8". In: *PASJ* 58, pp. 499–502. DOI: 10.1093/pasj/58.3.499. eprint: astro-ph/0603298.

Alam, S. et al. (2015). "The Eleventh and Twelfth Data Releases of the Sloan Digital Sky Survey: Final Data from SDSS-III". In: *ApJS* 219, 12, p. 12. DOI: 10.1088/0067-0049/219/1/12. arXiv: 1501.00963 [astro-ph.IM].

Alexander, T. and P. Natarajan (2014). "Rapid growth of seed black holes in the early universe by supra-exponential accretion". In: *Science* 345, pp. 1330–1333. DOI: 10.1126/science.1251053. arXiv: 1408.1718.

Alvarez, M. A., J. H. Wise, and T. Abel (2009). "Accretion onto the First Stellar-Mass Black Holes". In: *ApJL* 701, pp. L133–L137. DOI: 10.1088/0004-637X/701/2/L133. arXiv: 0811.0820.

Amendola, L. et al. (2016). "Cosmology and Fundamental Physics with the Euclid Satellite". In: *ArXiv e-prints*. arXiv: 1606.00180.

Angulo, R. E. et al. (2012). "The journey of QSO haloes from z $\sim$ 6 to the present". In: *MNRAS* 425, pp. 2722–2730. DOI: 10.1111/j.1365-2966.2012.21783.x. arXiv: 1203.5339.

Appenzeller, I. and G. Rupprecht (1992). "FORS - the focal reducer for the VLT." In: *The Messenger* 67, pp. 18–21.

Appenzeller, I. et al. (1998). "Successful commissioning of FORS1 - the first optical instrument on the VLT." In: *The Messenger* 94, pp. 1–6.

Aravena, M. et al. (2016). "The ALMA Spectroscopic Survey in the Hubble Ultra Deep Field: Search for [CII] Line and Dust Emission in 6". In: *ApJ* 833, 71, p. 71. DOI: 10.3847/1538-4357/833/1/71. arXiv: 1607.06772.

Armus, L. et al. (2009). "GOALS: The Great Observatories All-Sky LIRG Survey". In: *PASP* 121, p. 559. DOI: 10.1086/600092. arXiv: 0904.4498.

Bañados, E. et al. (2013). "The Galaxy Environment of a QSO at z $\sim$ 5.7". In: *ApJ* 773, 178, p. 178. DOI: 10.1088/0004-637X/773/2/178. arXiv: 1306.6642 [astro-ph.CO].

Bañados, E. et al. (2014). "Discovery of Eight z $\sim$ 6 Quasars from Pan-STARRS1". In: *AJ* 148, 14, p. 14. DOI: 10.1088/0004-6256/148/1/14. arXiv: 1405.3986.

Bañados, E. et al. (2015a). "Bright [C II] 158 μm Emission in a Quasar Host Galaxy at z = 6.54". In: *ApJL* 805, L8, p. L8. DOI: 10.1088/2041-8205/805/1/L8. arXiv: 1504.05216.

Bañados, E. et al. (2015b). "Constraining the Radio-loud Fraction of Quasars at z $>$ 5.5". In: *ApJ* 804, 118, p. 118. DOI: 10.1088/0004-637X/804/2/118. arXiv: 1503.04214.

Bañados, E. et al. (2016). "The Pan-STARRS1 Distant z$>$5.6 Quasar Survey: More than 100 Quasars within the First Gyr of the Universe". In: *ApJS* 227, 11, p. 11. DOI: 10.3847/0067-0049/227/1/11. arXiv: 1608.03279.

Bañados, E. et al. (2018). "An 800-million-solar-mass black hole in a significantly neutral Universe at a redshift of 7.5". In: *Nature* 553, pp. 473–476. DOI: 10.1038/nature25180. arXiv: 1712.01860.

Baade, W. and R. Minkowski (1954). "Identification of the Radio Sources in Cassiopeia, Cygnus A, and Puppis A." In: *ApJ* 119, p. 206. DOI: 10.1086/145812.

Baan, W. A. and A. D. Haschick (1995). "Nuclear Antics of IC 4553 (ARP 220)". In: *ApJ* 454, p. 745. DOI: 10.1086/176526.

Bailer-Jones, C. A., P. Bizenberger, and C. Storz (2000). "Achieving a wide-field near-infrared camera for the Calar Alto 3.5-m telescope". In: *Optical and IR Telescope Instrumentation and Detectors*. Ed. by M. Iye and A. F. Moorwood. Vol. 4008. PSPIE, pp. 1305–1316. DOI: 10.1117/12.395447. eprint: astro-ph/0003072.

Baldwin, J. A. (1977). "Luminosity Indicators in the Spectra of Quasi-Stellar Objects". In: *ApJ* 214, pp. 679–684. DOI: 10.1086/155294.

Balmaverde, B. et al. (2017). "Primordial environment of supermassive black holes. II. Deep Y- and J-band images around the z 6.3 quasar SDSS J1030+0524". In: *A&A* 606, A23, A23. DOI: 10.1051/0004-6361/201730683. arXiv: 1706.02317.

Barnett, R. et al. (2017). "Observations of the Lyman series forest towards the redshift 7.1 quasar ULAS J1120+0641". In: *A&A* 601, A16, A16. DOI: 10.1051/0004-6361/201630258. arXiv: 1702.03687.

Barth, A. J. et al. (2003). "Iron Emission in the z = 6.4 Quasar SDSS J114816.64+525150.3". In: *ApJL* 594, pp. L95–L98. DOI: 10.1086/378735. eprint: astro-ph/0308005.

Becker, G. D. et al. (2012). "Iron and α-element Production in the First One Billion Years after the Big Bang". In: *ApJ* 744, 91, p. 91. DOI: 10.1088/0004-637X/744/2/91. arXiv: 1111.4843.

Becker, G. D. et al. (2015). "Evidence of patchy hydrogen reionization from an extreme Lyα trough below redshift six". In: *MNRAS* 447, pp. 3402–3419. DOI: 10.1093/mnras/stu2646. arXiv: 1407.4850.

Beelen, A. et al. (2006). "350 μm Dust Emission from High-Redshift Quasars". In: *ApJ* 642, pp. 694–701. DOI: 10.1086/500636. eprint: astro-ph/0603121.

Begelman, M. C. and M. Volonteri (2017). "Hyperaccreting black holes in galactic nuclei". In: *MNRAS* 464, pp. 1102–1107. DOI: 10.1093/mnras/stw2446. arXiv: 1609.07137 [astro-ph.HE].

Bentz, M. C. et al. (2013). "The Low-luminosity End of the Radius-Luminosity Relationship for Active Galactic Nuclei". In: *ApJ* 767, 149, p. 149. DOI: 10.1088/0004-637X/767/2/149. arXiv: 1303.1742.

Berta, S. et al. (2016). "Measures of galaxy dust and gas mass with Herschel photometry and prospects for ALMA". In: *A&A* 587, A73, A73. DOI: 10.1051/0004-6361/201527746. arXiv: 1511.05147.

Bertin, E. and S. Arnouts (1996). "SExtractor: Software for source extraction." In: *A&AS* 117, pp. 393–404. DOI: 10.1051/aas:1996164.

Best, W. M. J. et al. (2013). "A Search for L/T Transition Dwarfs with Pan-STARRS1 and WISE: Discovery of Seven Nearby Objects Including Two Candidate Spectroscopic Variables". In: *ApJ* 777, 84, p. 84. DOI: 10.1088/0004-637X/777/2/84. arXiv: 1309.0503 [astro-ph.SR].

Best, W. M. J. et al. (2015). "A Search for L/T Transition Dwarfs with Pan-STARRS1 and WISE. II. L/T Transition Atmospheres and Young Discoveries". In: *ApJ* 814, 118, p. 118. DOI: 10.1088/0004-637X/814/2/118. arXiv: 1612.02824 [astro-ph.SR].

Bian, W.-H. and Y.-H. Zhao (2003). "Accretion Rates and the Accretion Efficiency in AGNs". In: *PASJ* 55, pp. 599–603. DOI: 10.1093/pasj/55.3.599.

Blain, A. W. et al. (2002). "Submillimeter galaxies". In: *PhR* 369, pp. 111–176. DOI: 10.1016/S0370-1573(02)00134-5. eprint: astro-ph/0202228.

Bond, J. R., W. D. Arnett, and B. J. Carr (1984). "The evolution and fate of Very Massive Objects". In: *ApJ* 280, pp. 825–847. DOI: 10.1086/162057.

Bondi, H. (1952). "On spherically symmetrical accretion". In: *MNRAS* 112, p. 195. DOI: 10.1093/mnras/112.2.195.

Bouwens, R. J. et al. (2015a). "Reionization After Planck: The Derived Growth of the Cosmic Ionizing Emissivity Now Matches the Growth of the Galaxy UV Luminosity Density". In: *ApJ* 811, 140, p. 140. DOI: 10.1088/0004-637X/811/2/140. arXiv: 1503.08228.

Bouwens, R. J. et al. (2015b). "UV Luminosity Functions at Redshifts z $\sim$ 4 to z $\sim$ 10: 10,000 Galaxies from HST Legacy Fields". In: *ApJ* 803, 34, p. 34. DOI: 10.1088/0004-637X/803/1/34. arXiv: 1403.4295.

Bowler, R. A. A. et al. (2015). "The galaxy luminosity function at z $\simeq$ 6 and evidence for rapid evolution in the bright end from z $\simeq$ 7 to 5". In: *MNRAS* 452, pp. 1817–1840. DOI: 10.1093/mnras/stv1403. arXiv: 1411.2976.

Brammer, G. B., P. G. van Dokkum, and P. Coppi (2008). "EAZY: A Fast, Public Photometric Redshift Code". In: *ApJ* 686, 1503-1513, pp. 1503–1513. DOI: 10.1086/591786. arXiv: 0807.1533.

Brammer, G. B. et al. (2012). "3D-HST: A Wide-field Grism Spectroscopic Survey with the Hubble Space Telescope". In: *ApJS* 200, 13, p. 13. DOI: 10.1088/0067-0049/200/2/13. arXiv: 1204.2829.

Brenneman, L. W. et al. (2011). "The Spin of the Supermassive Black Hole in NGC 3783". In: *ApJ* 736, 103, p. 103. DOI: 10.1088/0004-637X/736/2/103. arXiv: 1104.1172 [astro-ph.HE].

Brinchmann, J. et al. (2004). "The physical properties of star-forming galaxies in the low-redshift Universe". In: *MNRAS* 351, pp. 1151–1179. DOI: 10.1111/j.1365-2966.2004.07881.x. eprint: astro-ph/0311060.

Brisbin, D. et al. (2015). "Strong C^+ Emission in Galaxies at z $\sim$ 1-2: Evidence for Cold Flow Accretion Powered Star Formation in the Early Universe". In: *ApJ* 799, 13, p. 13. DOI: 10.1088/0004-637X/799/1/13. arXiv: 1411.1332.

Bruns, L. R. et al. (2012). "Clustering of Lyα emitters around luminous quasars at z= 2-3: an alternative probe of reionization on galaxy formation". In: *MNRAS* 421, pp. 2543–2552. DOI: 10.1111/j.1365-2966.2012.20479.x. arXiv: 1105.3524.

Burgasser, A. J. (2014). "The SpeX Prism Library: 1000+ low-resolution, near-infrared spectra of ultracool M, L, T and Y dwarfs". In: *Astronomical Society of India Conference Series*. Vol. 11. Astronomical Society of India Conference Series. arXiv: 1406.4887 [astro-ph.SR].

Buzzoni, B. et al. (1984). "The ESO Faint Object Spectrograph and Camera (EFOSC)". In: *The Messenger* 38, pp. 9–13.

Calderone, G. et al. (2017). "QSFIT: automatic analysis of optical AGN spectra". In: *MNRAS* 472, pp. 4051–4080. DOI: 10.1093/mnras/stx2239. arXiv: 1612.01580 [astro-ph.HE].

Calzetti, D. et al. (2000). "The Dust Content and Opacity of Actively Star-forming Galaxies". In: *ApJ* 533, pp. 682–695. DOI: 10.1086/308692. eprint: astro-ph/9911459.

Capak, P. et al. (2004). "A Deep Wide-Field, Optical, and Near-Infrared Catalog of a Large Area around the Hubble Deep Field North". In: *AJ* 127, pp. 180–198. DOI: 10.1086/380611. eprint: astro-ph/0312635.

Carilli, C. L. and F. Walter (2013). "Cool Gas in High-Redshift Galaxies". In: *ARA&A* 51, pp. 105–161. DOI: 10.1146/annurev-astro-082812-140953. arXiv: 1301.0371.

Carilli, C. L. et al. (2010). "Ionization Near Zones Associated with Quasars at z $\sim$ 6". In: *ApJ* 714, pp. 834–839. DOI: 10.1088/0004-637X/714/1/834. arXiv: 1003.0016.

Carnall, A. C. et al. (2015). "Two bright z > 6 quasars from VST ATLAS and a new method of optical plus mid-infrared colour selection". In: *MNRAS* 451, pp. L16–L20. DOI: 10.1093/mnrasl/slv057. arXiv: 1502.07748.

Chambers, K. C. et al. (2016). "The Pan-STARRS1 Surveys". In: *ArXiv e-prints*. arXiv: 1612.05560 [astro-ph.IM].

Chapman, S. C. et al. (2005). "A Redshift Survey of the Submillimeter Galaxy Population". In: *ApJ* 622, pp. 772–796. DOI: 10.1086/428082. eprint: astro-ph/0412573.

Chehade, B. et al. (2018). "Two more, bright, z > 6 quasars from VST ATLAS and WISE". In: *MNRAS*. DOI: 10.1093/mnras/sty690. arXiv: 1803.01424.

Chen, S.-F. S. et al. (2017). "Mg II Absorption at 2 < Z < 7 with Magellan/Fire. III. Full Statistics of Absorption toward 100 High-redshift QSOs". In: *ApJ* 850, 188, p. 188. DOI: 10.3847/1538-4357/aa9707. arXiv: 1612.02829.

Chiang, Y.-K., R. Overzier, and K. Gebhardt (2013). "Ancient Light from Young Cosmic Cities: Physical and Observational Signatures of Galaxy Proto-clusters". In: *ApJ* 779, 127, p. 127. DOI: 10.1088/0004-637X/779/2/127. arXiv: 1310.2938.

Ciardi, B. and A. Ferrara (2005). "The First Cosmic Structures and Their Effects". In: *SSRv* 116, pp. 625–705. DOI: 10.1007/s11214-005-3592-0. eprint: astro-ph/0409018.

Cool, R. J. et al. (2006). "The Discovery of Three New z>5 Quasars in the AGN and Galaxy Evolution Survey". In: *AJ* 132, pp. 823–830. DOI: 10.1086/505535. eprint: astro-ph/0605030.

Cox, P. et al. (2011). "Gas and Dust in a Submillimeter Galaxy at z = 4.24 from the Herschel Atlas". In: *ApJ* 740, 63, p. 63. DOI: 10.1088/0004-637X/740/2/63. arXiv: 1107.2924.

Croom, S. M. et al. (2005). "The 2dF QSO Redshift Survey - XIV. Structure and evolution from the two-point correlation function". In: *MNRAS* 356, pp. 415–438. DOI: 10.1111/j.1365-2966.2004.08379.x. eprint: astro-ph/0409314.

da Cunha, E., S. Charlot, and D. Elbaz (2008). "A simple model to interpret the ultraviolet, optical and infrared emission from galaxies". In: *MNRAS* 388, pp. 1595–1617. DOI: 10.1111/j.1365-2966.2008.13535.x. arXiv: 0806.1020.

da Cunha, E. et al. (2015). "An ALMA Survey of Sub-millimeter Galaxies in the Extended Chandra Deep Field South: Physical Properties Derived from Ultraviolet-to-radio Modeling". In: *ApJ* 806, 110, p. 110. DOI: 10.1088/0004-637X/806/1/110. arXiv: 1504.04376.

Daddi, E. et al. (2007). "Multiwavelength Study of Massive Galaxies at z ∼ 2. I. Star Formation and Galaxy Growth". In: *ApJ* 670, pp. 156–172. DOI: 10.1086/521818. arXiv: 0705.2831.

Davies, F. B. et al. (2018). "Quantitative Constraints on the Reionization History from the IGM Damping Wing Signature in Two Quasars at z > 7". In: *ArXiv e-prints*. arXiv: 1802.06066.

Davis, M. and P. J. E. Peebles (1983). "A survey of galaxy redshifts. V - The two-point position and velocity correlations". In: *ApJ* 267, pp. 465–482. DOI: 10.1086/160884.

De Breuck, C. et al. (2011). "Enhanced [CII] emission in a z = 4.76 submillimetre galaxy". In: *A&A* 530, L8, p. L8. DOI: 10.1051/0004-6361/201116868. arXiv: 1104.5250.

De Looze, I. et al. (2011). "The reliability of [C II] as an indicator of the star formation rate". In: *MNRAS* 416, pp. 2712–2724. DOI: 10.1111/j.1365-2966.2011.19223.x. arXiv: 1106.1643 [astro-ph.CO].

De Looze, I. et al. (2014). "The applicability of far-infrared fine-structure lines as star formation rate tracers over wide ranges of metallicities and galaxy types". In: *A&A* 568, A62, A62. DOI: 10.1051/0004-6361/201322489. arXiv: 1402.4075.

De Rosa, G. et al. (2011). "Evidence for Non-evolving Fe II/Mg II Ratios in Rapidly Accreting z ∼ 6 QSOs". In: *ApJ* 739, 56, p. 56. DOI: 10.1088/0004-637X/739/2/56. arXiv: 1106.5501.

De Rosa, G. et al. (2014). "Black Hole Mass Estimates and Emission-line Properties of a Sample of Redshift z $>$ 6.5 Quasars". In: *ApJ* 790, 145, p. 145. DOI: 10.1088/0004-637X/790/2/145. arXiv: 1311.3260.

Decarli, R. et al. (2008). "On the geometry of broad emission region in quasars". In: *MNRAS* 387, pp. 1237–1247. DOI: 10.1111/j.1365-2966.2008.13320.x. arXiv: 0804.1875.

Decarli, R. et al. (2010). "The quasar MBH-Mhost relation through cosmic time - II. Evidence for evolution from z = 3 to the present age". In: *MNRAS* 402, pp. 2453–2461. DOI: 10.1111/j.1365-2966.2009.16049.x. arXiv: 0911.2988.

Decarli, R. et al. (2012). "Hubble Space Telescope Narrowband Search for Extended Lyα Emission around Two z $>$ 6 Quasars". In: *ApJ* 756, 150, p. 150. DOI: 10.1088/0004-637X/756/2/150. arXiv: 1207.2155.

Decarli, R. et al. (2017). "Rapidly star-forming galaxies adjacent to quasars at redshifts exceeding 6". In: *Nature* 545, pp. 457–461. DOI: 10.1038/nature22358. arXiv: 1705.08662.

— (2018). "An ALMA [C II] Survey of 27 Quasars at z $>$ 5.94". In: *ApJ* 854, 97, p. 97. DOI: 10.3847/1538-4357/aaa5aa. arXiv: 1801.02641.

Degioia-Eastwood, K. et al. (1984). "Massive star formation in NGC 6946". In: *ApJ* 278, pp. 564–574. DOI: 10.1086/161823.

Devecchi, B. and M. Volonteri (2009). "Formation of the First Nuclear Clusters and Massive Black Holes at High Redshift". In: *ApJ* 694, pp. 302–313. DOI: 10.1088/0004-637X/694/1/302. arXiv: 0810.1057.

Díaz-Santos, T. et al. (2013). "Explaining the [C II]157.7 μm Deficit in Luminous Infrared Galaxies–First Results from a Herschel/PACS Study of the GOALS Sample". In: *ApJ* 774, 68, p. 68. DOI: 10.1088/0004-637X/774/1/68. arXiv: 1307.2635.

Díaz-Santos, T. et al. (2017). "A Herschel/PACS Far-infrared Line Emission Survey of Local Luminous Infrared Galaxies". In: *ApJ* 846, 32, p. 32. DOI: 10.3847/1538-4357/aa81d7. arXiv: 1705.04326.

Downes, D. and A. Eckart (2007). "Black hole in the West nucleus of Arp 220". In: *A&A* 468, pp. L57–L61. DOI: 10.1051/0004-6361:20077301. arXiv: 0706.2599.

Downes, D. et al. (1992). "Submillimeter spectrum and dust mass of the primeval galaxy IRAS 10214 + 4724". In: *ApJL* 398, pp. L25–L27. DOI: 10.1086/186568.

Dubbeldam, M. et al. (2000). "Integral field unit for the Gemini near-infrared spectrograph". In: *Optical and IR Telescope Instrumentation and Detectors*. Ed. by M. Iye and A. F. Moorwood. Vol. 4008. PSPIE, pp. 1181–1192. DOI: 10.1117/12.395437.

Dunlop, J. S. (2013). "Observing the First Galaxies". In: *The First Galaxies*. Ed. by T. Wiklind, B. Mobasher, and V. Bromm. Vol. 396. Astrophysics and Space Science Library, p. 223. DOI: 10.1007/978-3-642-32362-1_5. arXiv: 1205.1543.

Dunne, L., D. L. Clements, and S. A. Eales (2000). "Constraining the radio-submillimetre redshift indicator using data from the SCUBA Local Universe Galaxy Survey". In: *MNRAS* 319, pp. 813–820. DOI: 10.1046/j.1365-8711.2000.03882.x. eprint: astro-ph/0002436.

Edge, D. O. et al. (1959). "A survey of radio sources at a frequency of 159 Mc/s." In: *MmRAS* 68, pp. 37–60.

Eftekharzadeh, S. et al. (2015). "Clustering of intermediate redshift quasars using the final SDSS III-BOSS sample". In: *MNRAS* 453, pp. 2779–2798. DOI: 10.1093/mnras/stv1763. arXiv: 1507.08380.

Eilers, A.-C. et al. (2017). "Implications of z $\sim$ 6 Quasar Proximity Zones for the Epoch of Reionization and Quasar Lifetimes". In: *ApJ* 840, 24, p. 24. DOI: 10.3847/1538-4357/aa6c60. arXiv: 1703.02539.

Engargiola, G. (1991). "Origins of the 12-200 micron flux in NGC 6946 - Starlight and continuum dust emission from an SC galaxy". In: *ApJS* 76, pp. 875–910. DOI: 10.1086/191583.

Erben, T. et al. (2009). "CARS: the CFHTLS-Archive-Research Survey. I. Five-band multi-colour data from 37 sq. deg. CFHTLS-wide observations". In: *A&A* 493, pp. 1197–1222. DOI: 10.1051/0004-6361:200810426. arXiv: 0811.2239.

Fan, X., C. L. Carilli, and B. Keating (2006). "Observational Constraints on Cosmic Reionization". In: *ARA&A* 44, pp. 415–462. DOI: 10.1146/annurev.astro.44.051905.092514. eprint: astro-ph/0602375.

Fan, X. et al. (2000). "The Discovery of a Luminous Z=5.80 Quasar from the Sloan Digital Sky Survey". In: *AJ* 120, pp. 1167–1174. DOI: 10.1086/301534. eprint: astro-ph/0005414.

Fan, X. et al. (2003). "A Survey of z>5.7 Quasars in the Sloan Digital Sky Survey. II. Discovery of Three Additional Quasars at z>6". In: *AJ* 125, pp. 1649–1659. DOI: 10.1086/368246. eprint: astro-ph/0301135.

Fan, X. et al. (2006). "Constraining the Evolution of the Ionizing Background and the Epoch of Reionization with z$\sim$6 Quasars. II. A Sample of 19 Quasars". In: *AJ* 132, pp. 117–136. DOI: 10.1086/504836. eprint: astro-ph/0512082.

Fanidakis, N. et al. (2012). "The evolution of active galactic nuclei across cosmic time: what is downsizing?" In: *MNRAS* 419, pp. 2797–2820. DOI: 10.1111/j.1365-2966.2011.19931.x. arXiv: 1011.5222.

Fanidakis, N. et al. (2013). "The most luminous quasars do not live in the most massive dark matter haloes at any redshift". In: *MNRAS* 436, pp. 315–326. DOI: 10.1093/mnras/stt1567. arXiv: 1305.2199.

Farina, E. P. et al. (2017). "Mapping the Lyα Emission around a z $\sim$ 6.6 QSO with MUSE: Extended Emission and a Companion at a Close Separation". In: *ApJ* 848, 78, p. 78. DOI: 10.3847/1538-4357/aa8df4. arXiv: 1709.06096.

Farrah, D. et al. (2013). "Far-infrared Fine-structure Line Diagnostics of Ultraluminous Infrared Galaxies". In: *ApJ* 776, 38, p. 38. DOI: 10.1088/0004-637X/776/1/38. arXiv: 1308.4165.

Fazio, G. G. et al. (2004). "The Infrared Array Camera (IRAC) for the Spitzer Space Telescope". In: *ApJS* 154, pp. 10–17. DOI: 10.1086/422843. eprint: astro-ph/0405616.

Finkelstein, K. D. et al. (2015a). "Probing the Physical Properties of z = 4.5 Lyman Alpha Emitters with Spitzer". In: *ApJ* 813, 78, p. 78. DOI: 10.1088/0004-637X/813/1/78. arXiv: 1509.06381.

Finkelstein, S. L. et al. (2009). "Lyman Alpha Galaxies: Primitive, Dusty, or Evolved?" In: *ApJ* 691, pp. 465–481. DOI: 10.1088/0004-637X/691/1/465. arXiv: 0806.3269.

Finkelstein, S. L. et al. (2013). "A galaxy rapidly forming stars 700 million years after the Big Bang at redshift 7.51". In: *Nature* 502, pp. 524–527. DOI: 10.1038/nature12657. arXiv: 1310.6031.

Finkelstein, S. L. et al. (2015b). "The Evolution of the Galaxy Rest-frame Ultraviolet Luminosity Function over the First Two Billion Years". In: *ApJ* 810, 71, p. 71. DOI: 10.1088/0004-637X/810/1/71. arXiv: 1410.5439.

Flewelling, H. A. et al. (2016). "The Pan-STARRS1 Database and Data Products". In: *ArXiv e-prints*. arXiv: 1612.05243 [astro-ph.IM].

Förster Schreiber, N. M. et al. (2003). "The Nature of Starburst Activity in M82". In: *ApJ* 599, pp. 193–217. DOI: 10.1086/379097. eprint: astro-ph/0309357.

Fudamoto, Y. et al. (2017). "The most distant, luminous, dusty star-forming galaxies: redshifts from NOEMA and ALMA spectral scans". In: *MNRAS* 472, pp. 2028–2041. DOI: 10.1093/mnras/stx1956. arXiv: 1707.08967.

Fujimoto, S. et al. (2016). "ALMA Census of Faint 1.2 mm Sources Down to $\sim$ 0.02 mJy: Extragalactic Background Light and Dust-poor, High-z Galaxies". In: *ApJS* 222, 1, p. 1. DOI: 10.3847/0067-0049/222/1/1. arXiv: 1505.03523.

Furlanetto, S. R. and S. P. Oh (2008). "The History and Morphology of Helium Reionization". In: *ApJ* 681, 1-17, pp. 1–17. DOI: 10.1086/588546. arXiv: 0711.1542.

Furusawa, H. et al. (2008). "Subaru/XMM-Newton Deep Survey (SXDS) - Optical Imaging Survey and Photometric Catalogs". In: *Panoramic Views of Galaxy Formation and Evolution*. Ed. by T. Kodama, T. Yamada, and K. Aoki. Vol. 399. Astronomical Society of the Pacific Conference Series, p. 131.

Gaia Collaboration et al. (2016a). "Gaia Data Release 1. Summary of the astrometric, photometric, and survey properties". In: *A&A* 595, A2, A2. DOI: 10.1051/0004-6361/201629512. arXiv: 1609.04172 [astro-ph.IM].

Gaia Collaboration et al. (2016b). "The Gaia mission". In: *A&A* 595, A1, A1. DOI: 10.1051/0004-6361/201629272. arXiv: 1609.04153 [astro-ph.IM].

Garel, T. et al. (2015). "The UV, Lyman α, and dark matter halo properties of high-redshift galaxies". In: *MNRAS* 450, pp. 1279–1294. DOI: 10.1093/mnras/stv374. arXiv: 1503.06635.

Gehrels, N. (1986). "Confidence limits for small numbers of events in astrophysical data". In: *ApJ* 303, pp. 336–346. DOI: 10.1086/164079.

Genzel, R., F. Eisenhauer, and S. Gillessen (2010). "The Galactic Center massive black hole and nuclear star cluster". In: *Reviews of Modern Physics* 82, pp. 3121–3195. DOI: 10.1103/RevModPhys.82.3121. arXiv: 1006.0064.

Ghisellini, G., ed. (2013). *Radiative Processes in High Energy Astrophysics*. Vol. 873. Lecture Notes in Physics, Berlin Springer Verlag. DOI: 10.1007/978-3-319-00612-3. arXiv: 1202.5949 [astro-ph.HE].

Giallongo, E. et al. (2015). "Faint AGNs at z $>$ 4 in the CANDELS GOODS-S field: looking for contributors to the reionization of the Universe". In: *A&A* 578, A83, A83. DOI: 10.1051/0004-6361/201425334. arXiv: 1502.02562.

Gnedin, N. Y. (2000). "Effect of Reionization on Structure Formation in the Universe". In: *ApJ* 542, pp. 535–541. DOI: 10.1086/317042. eprint: astro-ph/0002151.

Gómez-Guijarro, C. et al. (2018). "Starburst to Quiescent from HST/ALMA: Stars and Dust Unveil Minor Mergers in Submillimeter Galaxies at z $\sim$ 4.5". In: *ApJ* 856, 121, p. 121. DOI: 10.3847/1538-4357/aab206. arXiv: 1802.07751.

González, V. et al. (2011). "Evolution of Galaxy Stellar Mass Functions, Mass Densities, and Mass-to-light Ratios from z $\sim$ 7 to z $\sim$ 4". In: *ApJL* 735, L34, p. L34. DOI: 10.1088/2041-8205/735/2/L34. arXiv: 1008.3901.

Goto, T. et al. (2017). "No Ly α emitters detected around a QSO at z = 6.4: Suppressed by the QSO?" In: *MNRAS* 470, pp. L117–L121. DOI: 10.1093/mnrasl/slx088. arXiv: 1706.04620.

Graciá-Carpio, J. et al. (2011). "Far-infrared Line Deficits in Galaxies with Extreme L_{FIR}/M_{H_{2}} Ratios". In: *ApJL* 728, L7, p. L7. DOI: 10.1088/2041-8205/728/1/L7. arXiv: 1101.0628.

Grandi, S. A. (1982). "The 3000 A bump in quasars". In: *ApJ* 255, pp. 25–38. DOI: 10.1086/159799.

Greenstein, J. L. (1963). "Red-Shift of the Unusual Radio Source: 3C 48". In: *Nature* 197, pp. 1041–1042. DOI: 10.1038/1971041a0.

Greig, B. et al. (2017). "Are we witnessing the epoch of reionisation at z = 7.1 from the spectrum of J1120+0641?" In: *MNRAS* 466, pp. 4239–4249. DOI: 10.1093/mnras/stw3351. arXiv: 1606.00441.

Greiner, J. et al. (2008). "GROND–a 7-Channel Imager". In: *PASP* 120, p. 405. DOI: 10.1086/587032. arXiv: 0801.4801.

Grier, C. J. et al. (2013). "The Structure of the Broad-line Region in Active Galactic Nuclei. I. Reconstructed Velocity-delay Maps". In: *ApJ* 764, 47, p. 47. DOI: 10.1088/0004-637X/764/1/47. arXiv: 1210.2397.

Grier, C. J. et al. (2017). "The Sloan Digital Sky Survey Reverberation Mapping Project: Hα and Hβ Reverberation Measurements from First-year Spectroscopy and Photometry". In: *ApJ* 851, 21, p. 21. DOI: 10.3847/1538-4357/aa98dc. arXiv: 1711.03114.

Gullberg, B. et al. (2015). "The nature of the [C II] emission in dusty star-forming galaxies from the SPT survey". In: *MNRAS* 449, pp. 2883–2900. DOI: 10.1093/mnras/stv372. arXiv: 1501.06909.

Haehnelt, M. G. and M. J. Rees (1993). "The formation of nuclei in newly formed galaxies and the evolution of the quasar population". In: *MNRAS* 263, pp. 168–178. DOI: 10.1093/mnras/263.1.168.

Hashimoto, T. et al. (2013). "Gas Motion Study of Lyα Emitters at z $\sim$ 2 Using FUV and Optical Spectral Lines". In: *ApJ* 765, 70, p. 70. DOI: 10.1088/0004-637X/765/1/70. arXiv: 1206.2316.

Hazard, C., M. B. Mackey, and A. J. Shimmins (1963). "Investigation of the Radio Source 3C 273 By The Method of Lunar Occultations". In: *Nature* 197, pp. 1037–1039. DOI: 10.1038/1971037a0.

Hazard, C. et al. (2018). "The Sequence of Events that led to the 1963 Publications in Nature of 3C 273, the First Quasar and the First Extragalactic Radio Jet". In: *PASA* 35, e006, e006. DOI: 10.1017/pasa.2017.62.

Helou, G. et al. (1988). "IRAS observations of galaxies in the Virgo cluster area". In: *ApJS* 68, pp. 151–172. DOI: 10.1086/191285.

Hennawi, J. F. et al. (2006). "Binary Quasars in the Sloan Digital Sky Survey: Evidence for Excess Clustering on Small Scales". In: *AJ* 131, pp. 1–23. DOI: 10.1086/498235. eprint: astro-ph/0504535.

Hennawi, J. F. et al. (2015). "Quasar quartet embedded in giant nebula reveals rare massive structure in distant universe". In: *Science* 348, pp. 779–783. DOI: 10.1126/science.aaa5397. arXiv: 1505.03786.

Herrera-Camus, R. et al. (2015). "[C II] 158 μm Emission as a Star Formation Tracer". In: *ApJ* 800, 1, p. 1. DOI: 10.1088/0004-637X/800/1/1. arXiv: 1409.7123.

Herrera-Camus, R. et al. (2018). "SHINING, A Survey of Far Infrared Lines in Nearby Galaxies. I: Survey Description, Observational Trends, and Line Diagnostics". In: *ArXiv e-prints*. arXiv: 1803.04419.

Hildebrandt, H. et al. (2009). "CARS: the CFHTLS-Archive-Research Survey. II. Weighing dark matter halos of Lyman-break galaxies at z = 3-5". In: *A&A* 498, pp. 725–736. DOI: 10.1051/0004-6361/200811042. arXiv: 0903.3951.

Hodge, J. A. et al. (2013). "An ALMA Survey of Submillimeter Galaxies in the Extended Chandra Deep Field South: Source Catalog and Multiplicity". In: *ApJ* 768, 91, p. 91. DOI: 10.1088/0004-637X/768/1/91. arXiv: 1304.4266.

Hopkins, P. F. et al. (2008). "A Cosmological Framework for the Co-Evolution of Quasars, Supermassive Black Holes, and Elliptical Galaxies. I. Galaxy Mergers and Quasar Activity". In: *ApJS* 175, 356-389, pp. 356–389. DOI: 10.1086/524362. arXiv: 0706.1243.

Hu, E. M. et al. (2010). "An Atlas of z = 5.7 and z = 6.5 Lyα Emitters". In: *ApJ* 725, pp. 394–423. DOI: 10.1088/0004-637X/725/1/394. arXiv: 1009.1144.

Hubble, E. (1929). "A Relation between Distance and Radial Velocity among Extra-Galactic Nebulae". In: *Proceedings of the National Academy of Science* 15, pp. 168–173. DOI: 10.1073/pnas.15.3.168.

Hughes, D. H. et al. (1998). "High-redshift star formation in the Hubble Deep Field revealed by a submillimetre-wavelength survey". In: *Nature* 394, pp. 241–247. DOI: 10.1038/28328. eprint: astro-ph/9806297.

Husband, K. et al. (2013). "Are z $\sim$ 5 quasars found in the most massive high-redshift overdensities?" In: *MNRAS* 432, pp. 2869–2877. DOI: 10.1093/mnras/stt642. arXiv: 1304.3726.

Ivezic, Z. et al. (2008). "LSST: from Science Drivers to Reference Design and Anticipated Data Products". In: *ArXiv e-prints*. arXiv: 0805.2366.

Ivezić, Ž. et al. (2014). "Optical selection of quasars: SDSS and LSST". In: *Multiwavelength AGN Surveys and Studies*. Ed. by A. M. Mickaelian and D. B. Sanders. Vol. 304. IAU Symposium, pp. 11–17. DOI: 10.1017/S1743921314003159. arXiv: 1312.3963 [astro-ph.IM].

Ivison, R. J. et al. (2000). "The diversity of SCUBA-selected galaxies". In: *MNRAS* 315, pp. 209–222. DOI: 10.1046/j.1365-8711.2000.03376.x. eprint: astro-ph/9911069.

Ivison, R. J. et al. (2010). "Herschel and SCUBA-2 imaging and spectroscopy of a bright, lensed submillimetre galaxy at z = 2.3". In: *A&A* 518, L35, p. L35. DOI: 10.1051/0004-6361/201014548. arXiv: 1005.1071.

Iwamuro, F. et al. (2002). "Fe II/Mg II Emission-Line Ratios of QSOs within $0 < z < 5.3$". In: *ApJ* 565, pp. 63–77. DOI: 10.1086/324540.

Iwamuro, F. et al. (2004). "Fe II/Mg II Emission-Line Ratios of QSOs. II. $z > 6$ Objects". In: *ApJ* 614, pp. 69–74. DOI: 10.1086/423610. eprint: astro-ph/0408517.

Jiang, L. et al. (2007). "Gemini Near-Infrared Spectroscopy of Luminous z $\sim$ 6 Quasars: Chemical Abundances, Black Hole Masses, and Mg II Absorption". In: *AJ* 134, p. 1150. DOI: 10.1086/520811. arXiv: 0707.1663.

Jiang, L. et al. (2016). "The Final SDSS High-redshift Quasar Sample of 52 Quasars at z>5.7". In: *ApJ* 833, 222, p. 222. DOI: 10.3847/1538-4357/833/2/222. arXiv: 1610.05369.

Joseph, R. D. and G. S. Wright (1985). "Recent star formation in interacting galaxies. II - Super starburst in merging galaxies". In: *MNRAS* 214, pp. 87–95. DOI: 10.1093/mnras/214.2.87.

Kaiser, N. et al. (2002). "Pan-STARRS: A Large Synoptic Survey Telescope Array". In: *Survey and Other Telescope Technologies and Discoveries*. Ed. by J. A. Tyson and S. Wolff. Vol. 4836. PSPIE, pp. 154–164. DOI: 10.1117/12.457365.

Kaiser, N. et al. (2010). "The Pan-STARRS wide-field optical/NIR imaging survey". In: *Ground-based and Airborne Telescopes III*. Vol. 7733. PSPIE, 77330E. DOI: 10.1117/12.859188.

Kashikawa, N. et al. (2015). "The Subaru High-z Quasar Survey: Discovery of Faint z $\sim$ 6 Quasars". In: *ApJ* 798, 28, p. 28. DOI: 10.1088/0004-637X/798/1/28. arXiv: 1410.7401.

Kaspi, S. et al. (2005). "The Relationship between Luminosity and Broad-Line Region Size in Active Galactic Nuclei". In: *ApJ* 629, pp. 61–71. DOI: 10.1086/431275. eprint: astro-ph/0504484.

Kawamata, R. et al. (2016). "Precise Strong Lensing Mass Modeling of Four Hubble Frontier Field Clusters and a Sample of Magnified High-redshift Galaxies". In: *ApJ* 819, 114, p. 114. DOI: 10.3847/0004-637X/819/2/114. arXiv: 1510.06400.

Kellermann, K. I. et al. (1989). "VLA observations of objects in the Palomar Bright Quasar Survey". In: *AJ* 98, pp. 1195–1207. DOI: 10.1086/115207.

Kennicutt, R. C. and N. J. Evans (2012). "Star Formation in the Milky Way and Nearby Galaxies". In: *ARA&A* 50, pp. 531–608. DOI: 10.1146/annurev-astro-081811-125610. arXiv: 1204.3552.

Kim, S. et al. (2009). "The Environments of High-Redshift Quasi-Stellar Objects". In: *ApJ* 695, pp. 809–817. DOI: 10.1088/0004-637X/695/2/809. arXiv: 0805.1412.

Kim, Y. et al. (2015). "Discovery of a Faint Quasar at z $\sim$ 6 and Implications for Cosmic Reionization". In: *ApJL* 813, L35, p. L35. DOI: 10.1088/2041-8205/813/2/L35. arXiv: 1511.01585.

Kovač, K. et al. (2007). "Clustering of Lyα Emitters at z $\sim$ 4.5". In: *ApJ* 668, pp. 15–22. DOI: 10.1086/520668. arXiv: 0706.0893.

Kulkarni, G. et al. (2013). "Chemical Enrichment of Damped Lyα Systems as a Direct Constraint on Population III Star Formation". In: *ApJ* 772, 93, p. 93. DOI: 10.1088/0004-637X/772/2/93. arXiv: 1301.4201.

Kurk, J. D. et al. (2007). "Black Hole Masses and Enrichment of z $\sim$ 6 SDSS Quasars". In: *ApJ* 669, pp. 32–44. DOI: 10.1086/521596. arXiv: 0707.1662.

Kurk, J. D. et al. (2009). "Near-Infrared Spectroscopy of SDSS J0303 - 0019: A Low-luminosity, High-Eddington-Ratio Quasar at z $\sim$ 6". In: *ApJ* 702, pp. 833–837. DOI: 10.1088/0004-637X/702/2/833. arXiv: 0907.0435.

Lang, D. (2014). "unWISE: Unblurred Coadds of the WISE Imaging". In: *AJ* 147, 108, p. 108. DOI: 10.1088/0004-6256/147/5/108. arXiv: 1405.0308 [astro-ph.IM].

Lang, D. et al. (2010). "Astrometry.net: Blind Astrometric Calibration of Arbitrary Astronomical Images". In: *AJ* 139, pp. 1782–1800. DOI: 10.1088/0004-6256/139/5/1782. arXiv: 0910.2233 [astro-ph.IM].

Langer, W. D. and J. L. Pineda (2015). "[C ii] emission from galactic nuclei in the presence of X-rays". In: *A&A* 580, A5, A5. DOI: 10.1051/0004-6361/201525950. arXiv: 1505.02777.

Lapi, A. et al. (2006). "Quasar Luminosity Functions from Joint Evolution of Black Holes and Host Galaxies". In: *ApJ* 650, pp. 42–56. DOI: 10.1086/507122. eprint: astro-ph/0603819.

Latif, M. A. and A. Ferrara (2016). "Formation of Supermassive Black Hole Seeds". In: *PASA* 33, e051, e051. DOI: 10.1017/pasa.2016.41. arXiv: 1605.07391.

Latif, M. A. and D. R. G. Schleicher (2015). "The formation of supermassive black holes in rapidly rotating disks". In: *A&A* 578, A118, A118. DOI: 10.1051/0004-6361/201525855. arXiv: 1411.5902.

Laureijs, R. et al. (2011). "Euclid Definition Study Report". In: *ArXiv e-prints*. arXiv: 1110.3193 [astro-ph.CO].

Lawrence, A. et al. (2007). "The UKIRT Infrared Deep Sky Survey (UKIDSS)". In: *MNRAS* 379, pp. 1599–1617. DOI: 10.1111/j.1365-2966.2007.12040.x. eprint: astro-ph/0604426.

Leighly, K. M. (2004). "Hubble Space Telescope STIS Ultraviolet Spectral Evidence of Outflow in Extreme Narrow-Line Seyfert 1 Galaxies. II. Modeling and Interpretation". In: *ApJ* 611, pp. 125–152. DOI: 10.1086/422089. eprint: astro-ph/0402452.

Leipski, C. et al. (2014). "Spectral Energy Distributions of QSOs at z $>$ 5: Common Active Galactic Nucleus-heated Dust and Occasionally Strong Star-formation". In: *ApJ* 785, 154, p. 154. DOI: 10.1088/0004-637X/785/2/154. arXiv: 1402.5976.

Leroy, A. K. et al. (2017). "Cloud-scale ISM Structure and Star Formation in M51". In: *ApJ* 846, 71, p. 71. DOI: 10.3847/1538-4357/aa7fef. arXiv: 1706.08540.

Lira, P. et al. (2018). "Reverberation Mapping of High-z, High-luminosity Quasars". In: *Frontiers in Astronomy and Space Sciences* 4, 71, p. 71. DOI: 10.3389/fspas.2017.00071. arXiv: 1801.03866.

Lodieu, N., S. Boudreault, and V. J. S. Béjar (2014). "Spectroscopy of Hyades L dwarf candidates". In: *MNRAS* 445, pp. 3908–3918. DOI: 10.1093/mnras/stu2059. arXiv: 1410.0192 [astro-ph.SR].

Loeb, A. and R. Barkana (2001). "The Reionization of the Universe by the First Stars and Quasars". In: *ARA&A* 39, pp. 19–66. DOI: 10.1146/annurev.astro.39.1.19. eprint: astro-ph/0010467.

Longair, M. S. (2008). *Galaxy Formation*.

LSST Science Collaboration et al. (2009). "LSST Science Book, Version 2.0". In: *ArXiv e-prints*. arXiv: 0912.0201 [astro-ph.IM].

Lupi, A. et al. (2016). "Growing massive black holes through supercritical accretion of stellar-mass seeds". In: *MNRAS* 456, pp. 2993–3003. DOI: 10.1093/mnras/stv2877. arXiv: 1512.02651.

Ma, Q. et al. (2017). "Metal enrichment signatures of the first stars on high-z DLAs". In: *MNRAS* 472, pp. 3532–3542. DOI: 10.1093/mnras/stx1839. arXiv: 1707.07580.

Mace, G. N. (2014). "Investigating Low-Mass Binary Stars And Brown Dwarfs with Near-Infrared Spectroscopy". PhD thesis. University of California, Los Angeles.

Madau, P., F. Haardt, and M. Dotti (2014). "Super-critical Growth of Massive Black Holes from Stellar-mass Seeds". In: *ApJL* 784, L38, p. L38. DOI: 10.1088/2041-8205/784/2/L38. arXiv: 1402.6995.

Magdis, G. E. et al. (2011). "GOODS-Herschel: Gas-to-dust Mass Ratios and CO-to-H_2 Conversion Factors in Normal and Starbursting Galaxies at High-z". In: *ApJL* 740, L15, p. L15. DOI: 10.1088/2041-8205/740/1/L15. arXiv: 1109.1140.

Magnier, E. A. et al. (2013). "The Pan-STARRS 1 Photometric Reference Ladder, Release 12.01". In: *ApJS* 205, 20, p. 20. DOI: 10.1088/0067-0049/205/2/20. arXiv: 1303.3634 [astro-ph.IM].

Magnier, E. A. et al. (2016). "The Pan-STARRS Data Processing System". In: *ArXiv e-prints*. arXiv: 1612.05240 [astro-ph.IM].

Mainzer, A. et al. (2011). "Preliminary Results from NEOWISE: An Enhancement to the Wide-field Infrared Survey Explorer for Solar System Science". In: *ApJ* 731, 53, p. 53. DOI: 10.1088/0004-637X/731/1/53. arXiv: 1102.1996 [astro-ph.EP].

Maiolino, R. et al. (2003). "Early Star Formation Traced by the Highest Redshift Quasars". In: *ApJL* 596, pp. L155–L158. DOI: 10.1086/379600. eprint: astro-ph/0307264.

Maiolino, R. et al. (2005). "First detection of [CII]158 μm at high redshift: vigorous star formation in the early universe". In: *A&A* 440, pp. L51–L54. DOI: 10.1051/0004-6361:200500165. eprint: astro-ph/0508064.

Maiolino, R. et al. (2009). "Strong [CII] emission at high redshift". In: *A&A* 500, pp. L1–L4. DOI: 10.1051/0004-6361/200912265. arXiv: 0904.3793.

Malhotra, S. et al. (2001). "Far-Infrared Spectroscopy of Normal Galaxies: Physical Conditions in the Interstellar Medium". In: *ApJ* 561, pp. 766–786. DOI: 10.1086/323046. eprint: astro-ph/0106485.

Marconi, A. et al. (2008). "The Effect of Radiation Pressure on Virial Black Hole Mass Estimates and the Case of Narrow-Line Seyfert 1 Galaxies". In: *ApJ* 678, 693-700, pp. 693–700. DOI: 10.1086/529360. arXiv: 0802.2021.

Marocco, F. et al. (2015). "A large spectroscopic sample of L and T dwarfs from UKIDSS LAS: peculiar objects, binaries, and space density". In: *MNRAS* 449, pp. 3651–3692. DOI: 10.1093/mnras/stv530. arXiv: 1503.05082 [astro-ph.SR].

Marrone, D. P. et al. (2018). "Galaxy growth in a massive halo in the first billion years of cosmic history". In: *Nature* 553, pp. 51–54. DOI: 10.1038/nature24629. arXiv: 1712.03020.

Matsuoka, Y. et al. (2016). "Subaru High-z Exploration of Low-luminosity Quasars (SHELLQs). I. Discovery of 15 Quasars and Bright Galaxies at $5.7 < z < 6.9$". In: *ApJ* 828, 26, p. 26. DOI: 10.3847/0004-637X/828/1/26. arXiv: 1603.02281.

Matsuoka, Y. et al. (2018a). "Subaru High-z Exploration of Low-Luminosity Quasars (SHELLQs). II. Discovery of 32 quasars and luminous galaxies at $5.7 < z \leq 6.8$". In: *PASJ* 70, S35, S35. DOI: 10.1093/pasj/psx046. arXiv: 1704.05854.

Matsuoka, Y. et al. (2018b). "Subaru High-z Exploration of Low-Luminosity Quasars (SHELLQs). IV. Discovery of 41 Quasars and Luminous Galaxies at $5.7 < z < 6.9$". In: *ArXiv e-prints*. arXiv: 1803.01861.

Matteucci, F. and L. Greggio (1986). "Relative roles of type I and II supernovae in the chemical enrichment of the interstellar gas". In: *A&A* 154, pp. 279–287.

Matthews, J. H., C. Knigge, and K. S. Long (2017). "Quasar emission lines as probes of orientation: implications for disc wind geometries and unification". In: *MNRAS* 467, pp. 2571–2584. DOI: 10.1093/mnras/stx231. arXiv: 1701.07037.

Mazzucchelli, C. et al. (2017a). "No Overdensity of Lyman-Alpha Emitting Galaxies around a Quasar at $z \sim 5.7$". In: *ApJ* 834, 83, p. 83. DOI: 10.3847/1538-4357/834/1/83. arXiv: 1611.02870.

Mazzucchelli, C. et al. (2017b). "Physical Properties of 15 Quasars at $z \gtrsim 6.5$". In: *ApJ* 849, 91, p. 91. DOI: 10.3847/1538-4357/aa9185. arXiv: 1710.01251.

McGreer, I. D., A. Mesinger, and V. D'Odorico (2015). "Model-independent evidence in favour of an end to reionization by $z \approx 6$". In: *MNRAS* 447, pp. 499–505. DOI: 10.1093/mnras/stu2449. arXiv: 1411.5375.

McGreer, I. D. et al. (2006). "Discovery of a z = 6.1 Radio-Loud Quasar in the NOAO Deep Wide Field Survey". In: *ApJ* 652, pp. 157–162. DOI: 10.1086/507767. eprint: astro-ph/0607278.

McGreer, I. D. et al. (2014). "Close Companions to Two High-redshift Quasars". In: *AJ* 148, 73, p. 73. DOI: 10.1088/0004-6256/148/4/73. arXiv: 1404.2297.

McGreer, I. D. et al. (2016). "A Constraint on Quasar Clustering at z = 5 from a Binary Quasar". In: *AJ* 151, 61, p. 61. DOI: 10.3847/0004-6256/151/3/61. arXiv: 1601.03056.

McLeod, D. J. et al. (2015). "New redshift $z \simeq 9$ galaxies in the Hubble Frontier Fields: implications for early evolution of the UV luminosity density". In: *MNRAS* 450, pp. 3032–3044. DOI: 10.1093/mnras/stv780. arXiv: 1412.1472.

McMahon, R. G. et al. (2013). "First Scientific Results from the VISTA Hemisphere Survey (VHS)". In: *The Messenger* 154, pp. 35–37.

McQuinn, M. (2016). "The Evolution of the Intergalactic Medium". In: *ARA&A* 54, pp. 313–362. DOI: 10.1146/annurev-astro-082214-122355. arXiv: 1512.00086.

Mechtley, M. et al. (2012). "Near-infrared Imaging of a z = 6.42 Quasar Host Galaxy with the Hubble Space Telescope Wide Field Camera 3". In: *ApJL* 756, L38, p. L38. DOI: 10.1088/2041-8205/756/2/L38. arXiv: 1207.3283 [astro-ph.CO].

Meiksin, A. (2006). "Colour corrections for high-redshift objects due to intergalactic attenuation". In: *MNRAS* 365, pp. 807–812. DOI: 10.1111/j.1365-2966.2005.09756.x. eprint: astro-ph/0512435.

Meisner, A. M., D. Lang, and D. J. Schlegel (2016). "Full-depth Coadds of the WISE and NEOWISE-Reactivation Data". In: *American Astronomical Society Meeting Abstracts #227*. Vol. 227. American Astronomical Society Meeting Abstracts, p. 140.03.

Mesinger, A. (2018). "Reionization and Cosmic Dawn: theory and simulations". In: *ArXiv e-prints*. arXiv: 1801.02649.

Miralda-Escudé, J. (1998). "Reionization of the Intergalactic Medium and the Damping Wing of the Gunn-Peterson Trough". In: *ApJ* 501, pp. 15–22. DOI: 10.1086/305799. eprint: astro-ph/9708253.

Miyoshi, M. et al. (1995). "Evidence for a black hole from high rotation velocities in a sub-parsec region of NGC4258". In: *Nature* 373, pp. 127–129. DOI: 10.1038/373127a0.

Moorwood, A., J.-G. Cuby, and C. Lidman (1998). "SOFI sees first light at the NTT." In: *The Messenger* 91, pp. 9–13.

Morganson, E. et al. (2012). "The First High-redshift Quasar from Pan-STARRS". In: *AJ* 143, 142, p. 142. DOI: 10.1088/0004-6256/143/6/142. arXiv: 1109.6241.

Morselli, L. et al. (2014). "Primordial environment of super massive black holes: large-scale galaxy overdensities around z $\sim$ 6 quasars with LBT". In: *A&A* 568, A1, A1. DOI: 10.1051/0004-6361/201423853. arXiv: 1406.3961.

Mortlock, D. J. et al. (2009). "Discovery of a redshift 6.13 quasar in the UKIRT infrared deep sky survey". In: *A&A* 505, pp. 97–104. DOI: 10.1051/0004-6361/200811161. arXiv: 0810.4180.

Mortlock, D. J. et al. (2011). "A luminous quasar at a redshift of z = 7.085". In: *Nature* 474, pp. 616–619. DOI: 10.1038/nature10159. arXiv: 1106.6088 [astro-ph.CO].

Muldrew, S. I., N. A. Hatch, and E. A. Cooke (2015). "What are protoclusters? - Defining high-redshift galaxy clusters and protoclusters". In: *MNRAS* 452, pp. 2528–2539. DOI: 10.1093/mnras/stv1449. arXiv: 1506.08835.

Murphy, E. J. et al. (2011). "Calibrating Extinction-free Star Formation Rate Diagnostics with 33 GHz Free-free Emission in NGC 6946". In: *ApJ* 737, 67, p. 67. DOI: 10.1088/0004-637X/737/2/67. arXiv: 1105.4877.

Namikawa, T. (2018). "Constraints on patchy reionization from Planck CMB temperature trispectrum". In: *PhRvD* 97.6, 063505, p. 063505. DOI: 10.1103/PhysRevD.97.063505. arXiv: 1711.00058.

Noeske, K. G. et al. (2007). "Star Formation in AEGIS Field Galaxies since z=1.1: The Dominance of Gradually Declining Star Formation, and the Main Sequence of Star-forming Galaxies". In: *ApJL* 660, pp. L43–L46. DOI: 10.1086/517926. eprint: astro-ph/0701924.

Nomoto, K. et al. (1997). "Nucleosynthesis in type II supernovae". In: *Nuclear Physics A* 616, pp. 79–90. DOI: 10.1016/S0375-9474(97)00076-6. eprint: astro-ph/9706024.

Oesch, P. A. et al. (2016). "A Remarkably Luminous Galaxy at z=11.1 Measured with Hubble Space Telescope Grism Spectroscopy". In: *ApJ* 819, 129, p. 129. DOI: 10.3847/0004-637X/819/2/129. arXiv: 1603.00461.

Oke, J. B. and J. E. Gunn (1982). "An Efficient Low Resolution and Moderate Resolution Spectrograph for the Hale Telescope". In: *PASP* 94, p. 586. DOI: 10.1086/131027.

Oke, J. B. et al. (1995). "The Keck Low-Resolution Imaging Spectrometer". In: *PASP* 107, p. 375. DOI: 10.1086/133562.

Onken, C. A. et al. (2004). "Supermassive Black Holes in Active Galactic Nuclei. II. Calibration of the Black Hole Mass-Velocity Dispersion Relationship for Active Galactic Nuclei". In: *ApJ* 615, pp. 645–651. DOI: 10.1086/424655. eprint: astro-ph/0407297.

Ono, Y. et al. (2010). "Stellar Populations of Lyα Emitters at z $\sim$ 6-7: Constraints on the Escape Fraction of Ionizing Photons from Galaxy Building Blocks". In: *ApJ* 724, pp. 1524–1535. DOI: 10.1088/0004-637X/724/2/1524. arXiv: 1004.0963.

Ono, Y. et al. (2012). "Spectroscopic Confirmation of Three z-dropout Galaxies at z = 6.844-7.213: Demographics of Lyα Emission in z $\sim$ 7 Galaxies". In: *ApJ* 744, 83, p. 83. DOI: 10.1088/0004-637X/744/2/83. arXiv: 1107.3159.

Osterbrock, D. E. (1989). *Astrophysics of gaseous nebulae and active galactic nuclei*.

Ota, K. et al. (2018). "Large Scale Environment of a $z = 6.61$ Luminous Quasar Probed by Lyα Emitters and Lyman Break Galaxies". In: *ArXiv e-prints*. arXiv: 1802.08912.

Ouchi, M. et al. (2003). "Subaru Deep Survey. II. Luminosity Functions and Clustering Properties of Lyα Emitters at z=4.86 in the Subaru Deep Field". In: *ApJ* 582, pp. 60–68. DOI: 10.1086/344476. eprint: astro-ph/0202204.

Ouchi, M. et al. (2008). "The Subaru/XMM-Newton Deep Survey (SXDS). IV. Evolution of Lyα Emitters from z = 3.1 to 5.7 in the 1 deg^2 Field: Luminosity Functions and AGN". In: *ApJS* 176, 301-330, pp. 301–330. DOI: 10.1086/527673. arXiv: 0707.3161.

Ouchi, M. et al. (2018). "Systematic Identification of LAEs for Visible Exploration and Reionization Research Using Subaru HSC (SILVERRUSH). I. Program strategy and clustering properties of $\sim$2000 Lyα emitters at z = 6-7 over the 0.3-0.5 Gpc^2 survey area". In: *PASJ* 70, S13, S13. DOI: 10.1093/pasj/psx074. arXiv: 1704.07455.

Overzier, R. A. et al. (2009). "ΛCDM predictions for galaxy protoclusters - I. The relation between galaxies, protoclusters and quasars at z $\sim$ 6". In: *MNRAS* 394, pp. 577–594. DOI: 10.1111/j.1365-2966.2008.14264.x. arXiv: 0810.2566.

Pacucci, F., M. Volonteri, and A. Ferrara (2015). "The growth efficiency of high-redshift black holes". In: *MNRAS* 452, pp. 1922–1933. DOI: 10.1093/mnras/stv1465. arXiv: 1506.04750.

Palanque-Delabrouille, N. et al. (2013). "The one-dimensional Lyα forest power spectrum from BOSS". In: *A&A* 559, A85, A85. DOI: 10.1051/0004-6361/201322130. arXiv: 1306.5896 [astro-ph.CO].

Pâris, I. et al. (2011). "A principal component analysis of quasar UV spectra at z $\sim$ 3". In: *A&A* 530, A50, A50. DOI: 10.1051/0004-6361/201016233. arXiv: 1104.2024.

Pâris, I. et al. (2014). "The Sloan Digital Sky Survey quasar catalog: tenth data release". In: *A&A* 563, A54, A54. DOI: 10.1051/0004-6361/201322691. arXiv: 1311.4870.

Pâris, I. et al. (2017). "The Sloan Digital Sky Survey Quasar Catalog: Twelfth data release". In: *A&A* 597, A79, A79. DOI: 10.1051/0004-6361/201527999. arXiv: 1608.06483.

Park, D. et al. (2012). "The Lick AGN Monitoring Project: Recalibrating Single-epoch Virial Black Hole Mass Estimates". In: *ApJ* 747, 30, p. 30. DOI: 10.1088/0004-637X/747/1/30. arXiv: 1111.6604.

Peng, C. Y. et al. (2002). "Detailed Structural Decomposition of Galaxy Images". In: *AJ* 124, pp. 266–293. DOI: 10.1086/340952. eprint: astro-ph/0204182.

— (2010). "Detailed Decomposition of Galaxy Images. II. Beyond Axisymmetric Models". In: *AJ* 139, pp. 2097–2129. DOI: 10.1088/0004-6256/139/6/2097. arXiv: 0912.0731.

Pentericci, L. et al. (2009). "The physical properties of Lyα emitting galaxies: not just primeval galaxies?" In: *A&A* 494, pp. 553–561. DOI: 10.1051/0004-6361:200810722. arXiv: 0811.1861.

Perlmutter, S. et al. (1999). "Measurements of Ω and Λ from 42 High-Redshift Supernovae". In: *ApJ* 517, pp. 565–586. DOI: 10.1086/307221. eprint: astro-ph/9812133.

Peterson, B. M. and K. Horne (2004). "Echo mapping of active galactic nuclei". In: *Astronomische Nachrichten* 325, pp. 248–251. DOI: 10.1002/asna.200310207. eprint: astro-ph/0407538.

Peterson, B. M. et al. (2004). "Central Masses and Broad-Line Region Sizes of Active Galactic Nuclei. II. A Homogeneous Analysis of a Large Reverberation-Mapping Database". In: *ApJ* 613, pp. 682–699. DOI: 10.1086/423269. eprint: astro-ph/0407299.

Pezzulli, E., R. Valiante, and R. Schneider (2016). "Super-Eddington growth of the first black holes". In: *MNRAS* 458, pp. 3047–3059. DOI: 10.1093/mnras/stw505. arXiv: 1603.00475.

Pirzkal, N. et al. (2007). "Optical-to-Mid-Infrared Observations of Lyα Galaxies at z∼5 in the Hubble Ultra Deep Field: A Young and Low-Mass Population". In: *ApJ* 667, pp. 49–59. DOI: 10.1086/519485. eprint: astro-ph/0612513.

Planck Collaboration et al. (2016). "Planck 2015 results. XIII. Cosmological parameters". In: *A&A* 594, A13, A13. DOI: 10.1051/0004-6361/201525830. arXiv: 1502.01589.

Pogge, R. W. et al. (2010). "The multi-object double spectrographs for the Large Binocular Telescope". In: *Ground-based and Airborne Instrumentation for Astronomy III*. Vol. 7735. PSPIE, 77350A. DOI: 10.1117/12.857215.

Porciani, C. and P. Norberg (2006). "Luminosity- and redshift-dependent quasar clustering". In: *MNRAS* 371, pp. 1824–1834. DOI: 10.1111/j.1365-2966.2006.10813.x. eprint: astro-ph/0607348.

Reed, S. L. et al. (2015). "DES J0454-4448: discovery of the first luminous z ≥ 6 quasar from the Dark Energy Survey". In: *MNRAS* 454, pp. 3952–3961. DOI: 10.1093/mnras/stv2031. arXiv: 1504.03264.

Reed, S. L. et al. (2017). "Eight new luminous z ≥ 6 quasars discovered via SED model fitting of VISTA, WISE and Dark Energy Survey Year 1 observations". In: *MNRAS* 468, pp. 4702–4718. DOI: 10.1093/mnras/stx728. arXiv: 1701.04852.

Reynolds, C. S. (2014). "Measuring Black Hole Spin Using X-Ray Reflection Spectroscopy". In: *SSRv* 183, pp. 277–294. DOI: 10.1007/s11214-013-0006-6. arXiv: 1302.3260 [astro-ph.HE].

Richards, G. T. et al. (2002). "Broad Emission-Line Shifts in Quasars: An Orientation Measure for Radio-Quiet Quasars?" In: *AJ* 124, pp. 1–17. DOI: 10.1086/341167. eprint: astro-ph/0204162.

Richards, G. T. et al. (2011). "Unification of Luminous Type 1 Quasars through C IV Emission". In: *AJ* 141, 167, p. 167. DOI: 10.1088/0004-6256/141/5/167. arXiv: 1011.2282.

Riechers, D. A. et al. (2013). "A dust-obscured massive maximum-starburst galaxy at a redshift of 6.34". In: *Nature* 496, pp. 329–333. DOI: 10.1038/nature12050. arXiv: 1304.4256 [astro-ph.CO].

Riess, A. G. et al. (1998). "Observational Evidence from Supernovae for an Accelerating Universe and a Cosmological Constant". In: *AJ* 116, pp. 1009–1038. DOI: 10.1086/300499. eprint: astro-ph/9805201.

Roberts-Borsani, G. W. et al. (2016). "z ≳ 7 Galaxies with Red Spitzer/IRAC [3.6]-[4.5] Colors in the Full CANDELS Data Set: The Brightest-Known Galaxies at z ∼ 7-9 and a Probable Spectroscopic Confirmation at z = 7.48". In: *ApJ* 823, 143, p. 143. DOI: 10.3847/0004-637X/823/2/143. arXiv: 1506.00854.

Rockosi, C. et al. (2010). "The low-resolution imaging spectrograph red channel CCD upgrade: fully depleted, high-resistivity CCDs for Keck". In: *Ground-based and Airborne Instrumentation for Astronomy III*. Vol. 7735. PSPIE, 77350R. DOI: 10.1117/12.856818.

Rodighiero, G. et al. (2011). "The Lesser Role of Starbursts in Star Formation at z = 2". In: *ApJL* 739, L40, p. L40. DOI: 10.1088/2041-8205/739/2/L40. arXiv: 1108.0933.

Ross, N. P. et al. (2009). "Clustering of Low-redshift (z <= 2.2) Quasars from the Sloan Digital Sky Survey". In: *ApJ* 697, pp. 1634–1655. DOI: 10.1088/0004-637X/697/2/1634. arXiv: 0903.3230.

Ryden, B. (2003). *Introduction to cosmology*.

Salmon, B. et al. (2015). "The Relation between Star Formation Rate and Stellar Mass for Galaxies at 3.5 <= z <= 6.5 in CANDELS". In: *ApJ* 799, 183, p. 183. DOI: 10.1088/0004-637X/799/2/183. arXiv: 1407.6012.

Sameshima, H. et al. (2009). "Ultraviolet FeII emission in z $\sim$ 2 quasars". In: *MNRAS* 395, pp. 1087–1091. DOI: 10.1111/j.1365-2966.2009.14605.x. arXiv: 0902.2057 [astro-ph.CO].

Sandage, A. (1965). "The Existence of a Major New Constituent of the Universe: the Quasistellar Galaxies." In: *ApJ* 141, p. 1560. DOI: 10.1086/148245.

Santini, P. et al. (2014). "The evolution of the dust and gas content in galaxies". In: *A&A* 562, A30, A30. DOI: 10.1051/0004-6361/201322835. arXiv: 1311.3670.

Sargsyan, L. et al. (2012a). "[C II] 158 μm Luminosities and Star Formation Rate in Dusty Starbursts and Active Galactic Nuclei". In: *ApJ* 755, 171, p. 171. DOI: 10.1088/0004-637X/755/2/171. arXiv: 1206.5435.

— (2012b). "[C II] 158 μm Luminosities and Star Formation Rate in Dusty Starbursts and Active Galactic Nuclei". In: *ApJ* 755, 171, p. 171. DOI: 10.1088/0004-637X/755/2/171. arXiv: 1206.5435.

Sarkar, P. et al. (2009). "The scale of homogeneity of the galaxy distribution in SDSS DR6". In: *MNRAS* 399, pp. L128–L131. DOI: 10.1111/j.1745-3933.2009.00738.x. arXiv: 0906.3431.

Schlegel, D. J., D. P. Finkbeiner, and M. Davis (1998). "Maps of Dust Infrared Emission for Use in Estimation of Reddening and Cosmic Microwave Background Radiation Foregrounds". In: *ApJ* 500, pp. 525–553. DOI: 10.1086/305772. eprint: astro-ph/9710327.

Schmidt, B. P. et al. (1998). "The High-Z Supernova Search: Measuring Cosmic Deceleration and Global Curvature of the Universe Using Type IA Supernovae". In: *ApJ* 507, pp. 46–63. DOI: 10.1086/306308. eprint: astro-ph/9805200.

Schmidt, G. D., R. J. Weymann, and C. B. Foltz (1989). "A moderate-resolution, high-throughput CCD channel for the Multiple Mirror Telescope spectrograph". In: *PASP* 101, pp. 713–724. DOI: 10.1086/132495.

Schmidt, K. B. et al. (2014). "The Luminosity Function at z $\sim$ 8 from 97 Y-band Dropouts: Inferences about Reionization". In: *ApJ* 786, 57, p. 57. DOI: 10.1088/0004-637X/786/1/57. arXiv: 1402.4129.

Schmidt, M. (1963). "3C 273 : A Star-Like Object with Large Red-Shift". In: *Nature* 197, p. 1040. DOI: 10.1038/1971040a0.

— (1966). "Redshifts of Fourteen Quasi-Stellar Radio Sources". In: *ApJ* 144, p. 443. DOI: 10.1086/148627.

Schneider, D. P. et al. (2003). "The Sloan Digital Sky Survey Quasar Catalog. II. First Data Release". In: *AJ* 126, pp. 2579–2593. DOI: 10.1086/379174. eprint: astro-ph/0308443.

Scoville, N. et al. (2017). "ALMA Resolves the Nuclear Disks of Arp 220". In: *ApJ* 836, 66, p. 66. DOI: 10.3847/1538-4357/836/1/66. arXiv: 1605.09381.

Scoville, N. Z. et al. (1998). "NICMOS Imaging of the Nuclei of Arp 220". In: *ApJL* 492, pp. L107–L110. DOI: 10.1086/311099. eprint: astro-ph/9801006.

Seifert, W. et al. (2003). "LUCIFER: a Multi-Mode NIR Instrument for the LBT". In: *Instrument Design and Performance for Optical/Infrared Ground-based Telescopes*. Ed. by M. Iye and A. F. M. Moorwood. Vol. 4841. PSPIE, pp. 962–973. DOI: 10.1117/12.459494.

Selsing, J. et al. (2016). "An X-Shooter composite of bright $1 < z < 2$ quasars from UV to infrared". In: *A&A* 585, A87, A87. DOI: 10.1051/0004-6361/201527096. arXiv: 1510.08058.

Sesana, A. et al. (2014). "Linking the Spin Evolution of Massive Black Holes to Galaxy Kinematics". In: *ApJ* 794, 104, p. 104. DOI: 10.1088/0004-637X/794/2/104. arXiv: 1402.7088.

Shapiro, P. R., I. T. Iliev, and A. C. Raga (2004). "Photoevaporation of cosmological minihaloes during reionization". In: *MNRAS* 348, pp. 753–782. DOI: 10.1111/j.1365-2966.2004.07364.x. eprint: astro-ph/0307266.

Shapiro, S. L. (2005). "Spin, Accretion, and the Cosmological Growth of Supermassive Black Holes". In: *ApJ* 620, pp. 59–68. DOI: 10.1086/427065. eprint: astro-ph/0411156.

Shen, Y. et al. (2007). "Clustering of High-Redshift (z >= 2.9) Quasars from the Sloan Digital Sky Survey". In: *AJ* 133, pp. 2222–2241. DOI: 10.1086/513517. eprint: astro-ph/0702214.

Shen, Y. et al. (2008). "Biases in Virial Black Hole Masses: An SDSS Perspective". In: *ApJ* 680, 169-190, pp. 169–190. DOI: 10.1086/587475. arXiv: 0709.3098.

Shen, Y. et al. (2011). "A Catalog of Quasar Properties from Sloan Digital Sky Survey Data Release 7". In: *ApJS* 194, 45, p. 45. DOI: 10.1088/0067-0049/194/2/45. arXiv: 1006.5178 [astro-ph.CO].

Shen, Y. et al. (2015). "The Sloan Digital Sky Survey Reverberation Mapping Project: No Evidence for Evolution in the M• -σ_* Relation to z$\sim$ 1". In: *ApJ* 805, 96, p. 96. DOI: 10.1088/0004-637X/805/2/96. arXiv: 1502.01034.

Shen, Y. et al. (2016). "The Sloan Digital Sky Survey Reverberation Mapping Project: First Broad-line Hβ and Mg II Lags at z $\gtrsim$ 0.3 from Six-month Spectroscopy". In: *ApJ* 818, 30, p. 30. DOI: 10.3847/0004-637X/818/1/30. arXiv: 1510.02802.

Shibuya, T. et al. (2012). "The First Systematic Survey for Lyα Emitters at z = 7.3 with Red-sensitive Subaru/Suprime-Cam". In: *ApJ* 752, 114, p. 114. DOI: 10.1088/0004-637X/752/2/114. arXiv: 1112.3997.

Silva, L. et al. (1998). "Modeling the Effects of Dust on Galactic Spectral Energy Distributions from the Ultraviolet to the Millimeter Band". In: *ApJ* 509, pp. 103–117. DOI: 10.1086/306476.

Simcoe, R. A. et al. (2008). "FIRE: a near-infrared cross-dispersed echellette spectrometer for the Magellan telescopes". In: *Ground-based and Airborne Instrumentation for Astronomy II*. Vol. 7014. PSPIE, 70140U. DOI: 10.1117/12.790414.

Simpson, C. et al. (2014). "No excess of bright galaxies around the redshift 7.1 quasar ULAS J1120+0641". In: *MNRAS* 442, pp. 3454–3461. DOI: 10.1093/mnras/stu1116. arXiv: 1406.0851.

Skelton, R. E. et al. (2014). "3D-HST WFC3-selected Photometric Catalogs in the Five CANDELS/3D-HST Fields: Photometry, Photometric Redshifts, and Stellar Masses". In: *ApJS* 214, 24, p. 24. DOI: 10.1088/0067-0049/214/2/24. arXiv: 1403.3689.

Skrzypek, N. et al. (2015). "Photometric brown-dwarf classification. I. A method to identify and accurately classify large samples of brown dwarfs without spectroscopy". In: *A&A* 574, A78, A78. DOI: 10.1051/0004-6361/201424570. arXiv: 1411.7578 [astro-ph.IM].

Smith, H. J. and D. Hoffleit (1963). "Light Variations in the Superluminous Radio Galaxy 3C273". In: *Nature* 198, pp. 650–651. DOI: 10.1038/198650a0.

Sokasian, A., T. Abel, and L. Hernquist (2002). "The epoch of helium reionization". In: *MNRAS* 332, pp. 601–616. DOI: 10.1046/j.1365-8711.2002.05291.x. eprint: astro-ph/0112297.

Somerville, R. S. et al. (2004). "Cosmic Variance in the Great Observatories Origins Deep Survey". In: *ApJL* 600, pp. L171–L174. DOI: 10.1086/378628. eprint: astro-ph/0309071.

Somerville, R. S. et al. (2008). "A semi-analytic model for the co-evolution of galaxies, black holes and active galactic nuclei". In: *MNRAS* 391, pp. 481–506. DOI: 10.1111/j.1365-2966.2008.13805.x. arXiv: 0808.1227.

Somerville, R. S. et al. (2012). "Galaxy properties from the ultraviolet to the far-infrared: Λ cold dark matter models confront observations". In: *MNRAS* 423, pp. 1992–2015. DOI: 10.1111/j.1365-2966.2012.20490.x. arXiv: 1104.0669.

Song, M. et al. (2014). "The HETDEX Pilot Survey. V. The Physical Origin of Lyα Emitters Probed by Near-infrared Spectroscopy". In: *ApJ* 791, 3, p. 3. DOI: 10.1088/0004-637X/791/1/3. arXiv: 1406.4503.

Speagle, J. S. et al. (2014). "A Highly Consistent Framework for the Evolution of the Star-Forming "Main Sequence" from z $\sim$ 0-6". In: *ApJS* 214, 15, p. 15. DOI: 10.1088/0067-0049/214/2/15. arXiv: 1405.2041.

Spergel, D. et al. (2013). "Wide-Field InfraRed Survey Telescope-Astrophysics Focused Telescope Assets WFIRST-AFTA Final Report". In: *ArXiv e-prints*. arXiv: 1305.5422 [astro-ph.IM].

Springel, V. et al. (2005). "Simulations of the formation, evolution and clustering of galaxies and quasars". In: *Nature* 435, pp. 629–636. DOI: 10.1038/nature03597. eprint: astro-ph/0504097.

Stacey, G. J. et al. (2010). "A 158 μm [C II] Line Survey of Galaxies at z $\sim$ 1-2: An Indicator of Star Formation in the Early Universe". In: *ApJ* 724, pp. 957–974. DOI: 10.1088/0004-637X/724/2/957. arXiv: 1009.4216.

Steidel, C. C. et al. (1996). "Spectroscopic Confirmation of a Population of Normal Star-forming Galaxies at Redshifts Z $>$ 3". In: *ApJL* 462, p. L17. DOI: 10.1086/310029. eprint: astro-ph/9602024.

Steinhardt, C. L. et al. (2014). "Star Formation at 4 $<$ z $<$ 6 from the Spitzer Large Area Survey with Hyper-Suprime-Cam (SPLASH)". In: *ApJL* 791, L25, p. L25. DOI: 10.1088/2041-8205/791/2/L25. arXiv: 1407.7030.

Stern, D. et al. (2000). "Discovery of a Color-selected Quasar at Z = 5.50". In: *ApJL* 533, pp. L75–L78. DOI: 10.1086/312614. eprint: astro-ph/0002338.

Stern, D. et al. (2003). "Gemini-South+FLAMINGOS Demonstration Science: Near-Infrared Spectroscopy of the z = 5.77 Quasar SDSS J083643.85+005453.3". In: *ApJL* 596, pp. L39–L42. DOI: 10.1086/379206. eprint: astro-ph/0309468.

Stiavelli, M. et al. (2005). "Evidence of Primordial Clustering around the QSO SDSS J1030+0524 at z=6.28". In: *ApJL* 622, pp. L1–L4. DOI: 10.1086/429406. eprint: astro-ph/0502223.

Straatman, C. M. S. et al. (2014). "A Substantial Population of Massive Quiescent Galaxies at z $\sim$ 4 from ZFOURGE". In: *ApJL* 783, L14, p. L14. DOI: 10.1088/2041-8205/783/1/L14. arXiv: 1312.4952.

Stubbs, C. W. et al. (2010). "Precise Throughput Determination of the PanSTARRS Telescope and the Gigapixel Imager Using a Calibrated Silicon Photodiode and a Tunable Laser: Initial Results". In: *ApJS* 191, pp. 376–388. DOI: 10.1088/0067-0049/191/2/376. arXiv: 1003.3465 [astro-ph.IM].

Suzuki, N. (2006). "Quasar Spectrum Classification with Principal Component Analysis (PCA): Emission Lines in the Lyα Forest". In: *ApJS* 163, pp. 110–121. DOI: 10.1086/499272.

Tang, J.-J. et al. (2017). "A quasar discovered at redshift 6.6 from Pan-STARRS1". In: *MNRAS* 466, pp. 4568–4572. DOI: 10.1093/mnras/stw3287. arXiv: 1612.06148.

Toft, S. et al. (2014). "Submillimeter Galaxies as Progenitors of Compact Quiescent Galaxies". In: *ApJ* 782, 68, p. 68. DOI: 10.1088/0004-637X/782/2/68. arXiv: 1401.1510.

Tonry, J. L. et al. (2012). "The Pan-STARRS1 Photometric System". In: *ApJ* 750, 99, p. 99. DOI: 10.1088/0004-637X/750/2/99. arXiv: 1203.0297 [astro-ph.IM].

Toshikawa, J. et al. (2014). "A First Site of Galaxy Cluster Formation: Complete Spectroscopy of a Protocluster at z = 6.01". In: *ApJ* 792, 15, p. 15. DOI: 10.1088/0004-637X/792/1/15. arXiv: 1407.1851.

Trakhtenbrot, B., M. Volonteri, and P. Natarajan (2017). "On the Accretion Rates and Radiative Efficiencies of the Highest-redshift Quasars". In: *ApJL* 836, L1, p. L1. DOI: 10.3847/2041-8213/836/1/L1. arXiv: 1611.00772.

Trakhtenbrot, B. et al. (2017). "ALMA Observations Show Major Mergers Among the Host Galaxies of Fast-growing, High-redshift#8203 Supermassive#8203 Black Holes". In: *ApJ* 836, 8, p. 8. DOI: 10.3847/1538-4357/836/1/8. arXiv: 1612.00010.

Tremaine, S. et al. (2002). "The Slope of the Black Hole Mass versus Velocity Dispersion Correlation". In: *ApJ* 574, pp. 740–753. DOI: 10.1086/341002. eprint: astro-ph/0203468.

Trenti, M. and M. Stiavelli (2008). "Cosmic Variance and Its Effect on the Luminosity Function Determination in Deep High-z Surveys". In: *ApJ* 676, 767-780, pp. 767–780. DOI: 10.1086/528674. arXiv: 0712.0398.

Urry, C. M. and P. Padovani (1995). "Unified Schemes for Radio-Loud Active Galactic Nuclei". In: *PASP* 107, p. 803. DOI: 10.1086/133630. eprint: astro-ph/9506063.

Utsumi, Y. et al. (2010). "A Large Number of z $>$ 6 Galaxies Around a QSO at z = 6.43: Evidence for a Protocluster?" In: *ApJ* 721, pp. 1680–1688. DOI: 10.1088/0004-637X/721/2/1680. arXiv: 1008.0857.

Valiante, R. et al. (2016). "From the first stars to the first black holes". In: *MNRAS* 457, pp. 3356–3371. DOI: 10.1093/mnras/stw225. arXiv: 1601.07915.

Valtchanov, I. et al. (2011). "Physical conditions of the interstellar medium of high-redshift, strongly lensed submillimetre galaxies from the Herschel-ATLAS". In: *MNRAS* 415, pp. 3473–3484. DOI: 10.1111/j.1365-2966.2011.18959.x. arXiv: 1105.3924 [astro-ph.CO].

van Dokkum, P. G. et al. (2008). "Confirmation of the Remarkable Compactness of Massive Quiescent Galaxies at z $\sim$ 2.3: Early-Type Galaxies Did not Form in a Simple Monolithic Collapse". In: *ApJL* 677, L5, p. L5. DOI: 10.1086/587874. arXiv: 0802.4094.

Vanden Berk, D. E. et al. (2001). "Composite Quasar Spectra from the Sloan Digital Sky Survey". In: *AJ* 122, pp. 549–564. DOI: 10.1086/321167. eprint: astro-ph/0105231.

Vanzella, E. et al. (2011). "Spectroscopic Confirmation of Two Lyman Break Galaxies at Redshift Beyond 7". In: *ApJL* 730, L35, p. L35. DOI: 10.1088/2041-8205/730/2/L35. arXiv: 1011.5500.

Venemans, B. P. et al. (2004). "Discovery of six Lyα emitters near a radio galaxy at z $\sim$ 5.2". In: *A&A* 424, pp. L17–L20. DOI: 10.1051/0004-6361:200400041. eprint: astro-ph/0408520.

Venemans, B. P. et al. (2007). "The discovery of the first luminous z $\sim$ 6 quasar in the UKIDSS Large Area Survey". In: *MNRAS* 376, pp. L76–L80. DOI: 10.1111/j.1745-3933.2007.00290.x. eprint: astro-ph/0612162.

Venemans, B. P. et al. (2012). "Detection of Atomic Carbon [C II] 158 μm and Dust Emission from a z = 7.1 Quasar Host Galaxy". In: *ApJL* 751, L25, p. L25. DOI: 10.1088/2041-8205/751/2/L25. arXiv: 1203.5844.

Venemans, B. P. et al. (2013). "Discovery of Three z $>$ 6.5 Quasars in the VISTA Kilo-Degree Infrared Galaxy (VIKING) Survey". In: *ApJ* 779, 24, p. 24. DOI: 10.1088/0004-637X/779/1/24. arXiv: 1311.3666.

Venemans, B. P. et al. (2015a). "First discoveries of z $\sim$ 6 quasars with the Kilo-Degree Survey and VISTA Kilo-Degree Infrared Galaxy survey". In: *MNRAS* 453, pp. 2259–2266. DOI: 10.1093/mnras/stv1774. arXiv: 1507.00726.

Venemans, B. P. et al. (2015b). "The Identification of Z-dropouts in Pan-STARRS1: Three Quasars at 6.5$<$ z$<$ 6.7". In: *ApJL* 801, L11, p. L11. DOI: 10.1088/2041-8205/801/1/L11. arXiv: 1502.01927.

Venemans, B. P. et al. (2016). "Bright [C II] and Dust Emission in Three z $>$ 6.6 Quasar Host Galaxies Observed by ALMA". In: *ApJ* 816, 37, p. 37. DOI: 10.3847/0004-637X/816/1/37. arXiv: 1511.07432.

Venemans, B. P. et al. (2017). "Copious Amounts of Dust and Gas in a z = 7.5 Quasar Host Galaxy". In: *ApJL* 851, L8, p. L8. DOI: 10.3847/2041-8213/aa943a. arXiv: 1712.01886.

Vernet, J. et al. (2011). "X-shooter, the new wide band intermediate resolution spectrograph at the ESO Very Large Telescope". In: *A&A* 536, A105, A105. DOI: 10.1051/0004-6361/201117752. arXiv: 1110.1944 [astro-ph.IM].

Vestergaard, M. (2004). "Black-Hole Mass Measurements". In: *AGN Physics with the Sloan Digital Sky Survey*. Ed. by G. T. Richards and P. B. Hall. Vol. 311. Astronomical Society of the Pacific Conference Series, p. 69. eprint: astro-ph/0401436.

Vestergaard, M. and P. S. Osmer (2009). "Mass Functions of the Active Black Holes in Distant Quasars from the Large Bright Quasar Survey, the Bright Quasar Survey, and the Color-selected Sample of the SDSS Fall Equatorial Stripe". In: *ApJ* 699, pp. 800–816. DOI: 10.1088/0004-637X/699/1/800. arXiv: 0904.3348 [astro-ph.CO].

Vestergaard, M. and B. J. Wilkes (2001). "An Empirical Ultraviolet Template for Iron Emission in Quasars as Derived from I Zwicky 1". In: *ApJS* 134, pp. 1–33. DOI: 10.1086/320357. eprint: astro-ph/0104320.

Volonteri, M. (2010). "Formation of supermassive black holes". In: *A&ARv* 18, pp. 279–315. DOI: 10.1007/s00159-010-0029-x. arXiv: 1003.4404.

Volonteri, M. and M. J. Rees (2005). "Rapid Growth of High-Redshift Black Holes". In: *ApJ* 633, pp. 624–629. DOI: 10.1086/466521. eprint: astro-ph/0506040.

Volonteri, M. et al. (2016). "The evolution of high-redshift massive black holes". In: *Galaxies at High Redshift and Their Evolution Over Cosmic Time*. Ed. by S. Kaviraj. Vol. 319. IAU Symposium, pp. 72–79. DOI: 10.1017/S1743921315010005. arXiv: 1511.02588.

Wagg, J. et al. (2010). "[CII] line emission in BRI 1335-0417 at z = 4.4". In: *A&A* 519, L1, p. L1. DOI: 10.1051/0004-6361/201015424. arXiv: 1008.1578.

Wagg, J. et al. (2012). "[C II] Line Emission in Massive Star-forming Galaxies at z = 4.7". In: *ApJL* 752, L30, p. L30. DOI: 10.1088/2041-8205/752/2/L30. arXiv: 1205.3498.

Walter, F. et al. (2003). "Molecular gas in the host galaxy of a quasar at redshift z = 6.42". In: *Nature* 424, pp. 406–408. DOI: 10.1038/nature01821. eprint: astro-ph/0307410.

Walter, F. et al. (2009). "A kiloparsec-scale hyper-starburst in a quasar host less than 1gigayear after the Big Bang". In: *Nature* 457, pp. 699–701. DOI: 10.1038/nature07681. arXiv: 0902.0662 [astro-ph.GA].

Walter, F. et al. (2012). "The intense starburst HDF 850.1 in a galaxy overdensity at z $\approx$ 5.2 in the Hubble Deep Field". In: *Nature* 486, pp. 233–236. DOI: 10.1038/nature11073. arXiv: 1206.2641.

Walton, D. J. et al. (2015). "Broad Iron Emission from Gravitationally Lensed Quasars Observed by Chandra". In: *ApJ* 805, 161, p. 161. DOI: 10.1088/0004-637X/805/2/161. arXiv: 1503.05255 [astro-ph.HE].

Wang, F. et al. (2016). "A Survey of Luminous High-redshift Quasars with SDSS and WISE. I. Target Selection and Optical Spectroscopy". In: *ApJ* 819, 24, p. 24. DOI: 10.3847/0004-637X/819/1/24. arXiv: 1602.04659.

Wang, F. et al. (2017). "First Discoveries of z $>$ 6 Quasars with the DECam Legacy Survey and UKIRT Hemisphere Survey". In: *ApJ* 839, 27, p. 27. DOI: 10.3847/1538-4357/aa689f. arXiv: 1703.07490.

Wang, R. et al. (2011). "Far-infrared and Molecular CO Emission from the Host Galaxies of Faint Quasars at z $\sim$ 6". In: *AJ* 142, 101, p. 101. DOI: 10.1088/0004-6256/142/4/101. arXiv: 1107.5065.

Wang, R. et al. (2013). "Star Formation and Gas Kinematics of Quasar Host Galaxies at z $\sim$ 6: New Insights from ALMA". In: *ApJ* 773, 44, p. 44. DOI: 10.1088/0004-637X/773/1/44. arXiv: 1302.4154.

Waters, C. Z. et al. (2016). "Pan-STARRS Pixel Processing: Detrending, Warping, Stacking". In: *ArXiv e-prints*. arXiv: 1612.05245 [astro-ph.IM].

Whitaker, K. E. et al. (2011). "The NEWFIRM Medium-band Survey: Photometric Catalogs, Redshifts, and the Bimodal Color Distribution of Galaxies out to z $\sim$ 3". In: *ApJ* 735, 86, p. 86. DOI: 10.1088/0004-637X/735/2/86. arXiv: 1105.4609.

Whitaker, K. E. et al. (2014). "Constraining the Low-mass Slope of the Star Formation Sequence at 0.5 $<$ z $<$ 2.5". In: *ApJ* 795, 104, p. 104. DOI: 10.1088/0004-637X/795/2/104. arXiv: 1407.1843.

Whitaker, K. E. et al. (2017). "The Constant Average Relationship between Dust-obscured Star Formation and Stellar Mass from z = 0 to z = 2.5". In: *ApJ* 850, 208, p. 208. DOI: 10.3847/1538-4357/aa94ce. arXiv: 1710.06872.

Willott, C. J., J. Bergeron, and A. Omont (2015). "Star Formation Rate and Dynamical Mass of 10^8 Solar Mass Black Hole Host Galaxies At Redshift 6". In: *ApJ* 801, 123, p. 123. DOI: 10.1088/0004-637X/801/2/123. arXiv: 1501.07538.

— (2017). "A Wide Dispersion in Star Formation Rate and Dynamical Mass of 10^8 Solar Mass Black Hole Host Galaxies at Redshift 6". In: *ApJ* 850, 108, p. 108. DOI: 10.3847/1538-4357/aa921b. arXiv: 1710.02212.

Willott, C. J., A. Omont, and J. Bergeron (2013). "Redshift 6.4 Host Galaxies of 10^8 Solar Mass Black Holes: Low Star Formation Rate and Dynamical Mass". In: *ApJ* 770, 13, p. 13. DOI: 10.1088/0004-637X/770/1/13. arXiv: 1302.1587.

Willott, C. J. et al. (2005). "Imaging of SDSS z $>$ 6 Quasar Fields: Gravitational Lensing, Companion Galaxies, and the Host Dark Matter Halos". In: *ApJ* 626, pp. 657–665. DOI: 10.1086/430168. eprint: astro-ph/0503202.

Willott, C. J. et al. (2007). "Four Quasars above Redshift 6 Discovered by the Canada-France High-z Quasar Survey". In: *AJ* 134, pp. 2435–2450. DOI: 10.1086/522962. arXiv: 0706.0914.

Willott, C. J. et al. (2009). "Six More Quasars at Redshift 6 Discovered by the Canada-France High-z Quasar Survey". In: *AJ* 137, pp. 3541–3547. DOI: 10.1088/0004-6256/137/3/3541. arXiv: 0901.0565 [astro-ph.GA].

Willott, C. J. et al. (2010a). "Eddington-limited Accretion and the Black Hole Mass Function at Redshift 6". In: *AJ* 140, pp. 546–560. DOI: 10.1088/0004-6256/140/2/546. arXiv: 1006.1342.

Willott, C. J. et al. (2010b). "The Canada-France High-z Quasar Survey: Nine New Quasars and the Luminosity Function at Redshift 6". In: *AJ* 139, pp. 906–918. DOI: 10.1088/0004-6256/139/3/906. arXiv: 0912.0281.

Wright, E. L. et al. (2010). "The Wide-field Infrared Survey Explorer (WISE): Mission Description and Initial On-orbit Performance". In: *AJ* 140, 1868-1881, pp. 1868–1881. DOI: 10.1088/0004-6256/140/6/1868. arXiv: 1008.0031 [astro-ph.IM].

Wu, K. K. S., O. Lahav, and M. J. Rees (1999). "The large-scale smoothness of the Universe". In: *Nature* 397, pp. 225–230. DOI: 10.1038/16637. eprint: astro-ph/9804062.

Wu, X.-B. et al. (2015). "An ultraluminous quasar with a twelve-billion-solar-mass black hole at redshift 6.30". In: *Nature* 518, pp. 512–515. DOI: 10.1038/nature14241. arXiv: 1502.07418.

Wuyts, S. et al. (2010). "On Sizes, Kinematics, M/L Gradients, and Light Profiles of Massive Compact Galaxies at z $\sim$ 2". In: *ApJ* 722, pp. 1666–1684. DOI: 10.1088/0004-637X/722/2/1666. arXiv: 1008.4127.

Wyithe, J. S. B. and A. Loeb (2003). "Self-regulated Growth of Supermassive Black Holes in Galaxies as the Origin of the Optical and X-Ray Luminosity Functions of Quasars". In: *ApJ* 595, pp. 614–623. DOI: 10.1086/377475. eprint: astro-ph/0304156.

Wylezalek, D. et al. (2013). "Galaxy Clusters around Radio-loud Active Galactic Nuclei at 1.3 $<$ z $<$ 3.2 as Seen by Spitzer". In: *ApJ* 769, 79, p. 79. DOI: 10.1088/0004-637X/769/1/79. arXiv: 1304.0770.

Yajima, H. et al. (2015). "Observational properties of simulated galaxies in overdense and average regions at redshifts z $\simeq$ 6-12". In: *MNRAS* 451, pp. 418–432. DOI: 10.1093/mnras/stv974. arXiv: 1411.2626.

Yun, M. S., P. T. P. Ho, and K. Y. Lo (1994). "A high-resolution image of atomic hydrogen in the M81 group of galaxies". In: *Nature* 372, pp. 530–532. DOI: 10.1038/372530a0.

Zavala, J. A. et al. (2017). "The SCUBA-2 Cosmology Legacy Survey: the EGS deep field - I. Deep number counts and the redshift distribution of the recovered cosmic infrared background at 450 and 850 μ m". In: *MNRAS* 464, pp. 3369–3384. DOI: 10.1093/mnras/stw2630. arXiv: 1610.03551.

Zeimann, G. R. et al. (2011). "Discovery of a Radio-selected z $\sim$ 6 Quasar". In: *ApJ* 736, 57, p. 57. DOI: 10.1088/0004-637X/736/1/57. arXiv: 1105.2047.

Zhang, S. et al. (2013). "Quasar-Galaxy Clustering through Projected Galaxy Counts at z = 0.6-1.2". In: *ApJ* 773, 175, p. 175. DOI: 10.1088/0004-637X/773/2/175. arXiv: 1307.1951.

Zheng, W. et al. (2006). "An Overdensity of Galaxies near the Most Distant Radio-loud Quasar". In: *ApJ* 640, pp. 574–578. DOI: 10.1086/500167. eprint: astro-ph/0511734.

Zheng, Z.-Y. et al. (2014). "Lyα equivalent width distribution of Lyα emitting galaxies at redshift z $\sim$ 4.5". In: *MNRAS* 439, pp. 1101–1109. DOI: 10.1093/mnras/stu054. arXiv: 1310.4835 [astro-ph.CO].

Zitrin, A. et al. (2015). "Lymanα Emission from a Luminous z = 8.68 Galaxy: Implications for Galaxies as Tracers of Cosmic Reionization". In: *ApJL* 810, L12, p. L12. DOI: 10.1088/2041-8205/810/1/L12. arXiv: 1507.02679.